World Journal of

Radiology

World Journal of Radiology

A peer-reviewed, online, open-access journal of Radiology

Editorial Board

2014-2017

World Journal of Radiology

Contents

Monthly Volume 6 Number 7 July 28, 2014

Contents

Contents

ABOUT COVER

Editorial Board Member of *World Journal of Radiology*, Edward Araujo Júnior, PhD, Associate Professor, Department of Obstetrics, Paulista School of Medicine - Federal University of Sao Paulo, Sao Paulo, SP 05303000, Brazil

AIM AND SCOPE

World Journal of Radiology (*World J Radiol*, *WJR*, online ISSN 1949-8470, DOI: 10.4329) is a peer-reviewed open access academic journal that aims to guide clinical practice and improve diagnostic and therapeutic skills of clinicians.

WJR covers topics concerning diagnostic radiology, radiation oncology, radiologic physics, neuroradiology, nuclear radiology, pediatric radiology, vascular/interventional radiology, medical imaging achieved by various modalities and related methods analysis. The current columns of *WJR* include editorial, frontier, diagnostic advances, therapeutics advances, field of vision, mini-reviews, review, topic highlight, medical ethics, original articles, case report, clinical case conference (clinicopathological conference), and autobiography.

We encourage authors to submit their manuscripts to *WJR*. We will give priority to manuscripts that are supported by major national and international foundations and those that are of great basic and clinical significance.

INDEXING/ABSTRACTING

World Journal of Radiology is now indexed in PubMed Central, PubMed, Digital Object Identifier, and Directory of Open Access Journals.

EDITORS FOR THIS ISSUE

Responsible Assistant Editor: *Xiang Li*   Responsible Science Editor: *Ling-Ling Wen*
Responsible Electronic Editor: *Ya-Jing Lu*   Proofing Editorial Office Director: *Xiu-Xia Song*
Proofing Editor-in-Chief: *Lian-Sheng Ma*

TOPIC HIGHLIGHT

FDG-PET/CT response evaluation during EGFR-TKI treatment in patients with NSCLC

Matthijs H van Gool, Tjeerd S Aukema, Koen J Hartemink, Renato A Valdés Olmos, Harm van Tinteren, Houke M Klomp

Matthijs H van Gool, Koen J Hartemink, Houke M Klomp, Department of Surgical Oncology, The Netherlands Cancer Institute, Antoni van Leeuwenhoek Hospital, 1066 CX Amsterdam, The Netherlands
Tjeerd S Aukema, Renato A Valdés Olmos, Department of Nuclear Medicine, The Netherlands Cancer Institute, Antoni van Leeuwenhoek Hospital, 1066 CX Amsterdam, The Netherlands
Harm van Tinteren, Department of Biometrics, The Netherlands Cancer Institute, Antoni van Leeuwenhoek Hospital, 1066 CX Amsterdam, The Netherlands
Author contributions: All authors contributed equally on this manuscript in accordance with the standard proposed by the International Committee of Medical Journal Editors.
Correspondence to: Houke M Klomp, MD, PhD, Department of Surgical Oncology, The Netherlands Cancer Institute, Antoni van Leeuwenhoek Hospital, Plesmanlaan 121, 1066 CX Amsterdam, The Netherlands. h.klomp@nki.nl
Telephone: +31-20-5122554 Fax: +31-20-5129111
Received: January 23, 2014 Revised: April 28, 2014
Accepted: May 16, 2014
Published online: July 28, 2014

Abstract

Over recent years, [18F]-fluorodeoxyglucose positron emission tomography acquired together with low dose computed tomography (FDG-PET/CT) has proven its role as a staging modality in patients with non-small cell lung cancer (NSCLC). The purpose of this review was to present the evidence to use FDG-PET/CT for response evaluation in patients with NSCLC, treated with epidermal growth factor receptor (EGFR)-tyrosine kinase inhibitors (TKI). All published articles from 1 November 2003 to 1 November 2013 reporting on 18F-FDG-PET response evaluation during EGFR-TKI treatment in patients with NSCLC were collected. In total 7 studies, including data of 210 patients were eligible for analyses. Our report shows that FDG-PET/CT response during EGFR-TKI therapy has potential in targeted treatment for NSCLC. FDG-PET/CT response is associated with clinical and radiologic response and with survival. Furthermore FDG-PET/CT response monitoring can be performed as early as 1-2 wk after initiation of EGFR-TKI treatment. Patients with substantial decrease of metabolic activity during EGFR-TKI treatment will probably benefit from continued treatment. If metabolic response does not occur within the first weeks of EGFR-TKI treatment, patients may be spared (further) unnecessary toxicity of ineffective treatment. Refining FDG-PET response criteria may help the clinician to decide on continuation or discontinuation of targeted treatment.

Core tip: Our report shows that response monitoring using [18F]-fluorodeoxyglucose positron emission tomography (FDG-PET) acquired together with low dose computed tomography has potential in targeted treatment for non-small cell lung cancer and can be performed as early as 1-2 wk after initiation of treatment. Patients with substantial decrease of metabolic activity during epidermal growth factor receptor-tyrosine kinase inhibitors treatment will probably benefit from continued treatment. Refining FDG-PET response criteria may help the clinician to decide on continuation or discontinuation of targeted treatment.

van Gool MH, Aukema TS, Hartemink KJ, Valdés Olmos RA, van Tinteren H, Klomp HM. FDG-PET/CT response evaluation during EGFR-TKI treatment in patients with NSCLC. *World J*

INTRODUCTION

Over recent years, [18F]-fluorodeoxyglucose positron emission tomography acquired together with low dose computed tomography (FDG-PET/CT) has proven its role as a staging modality in patients with non-small cell lung cancer (NSCLC)[1-3]. In addition, *FDG-PET/CT* has been evaluated as a method to monitor tumor response to chemotherapy. Several studies demonstrated that FDG-PET/CT is able to predict response to treatment in various malignancies, *i.e.,* breast cancer[4,5], malignant lymphoma[6,7] and colorectal cancer[8]. Diagnostic CT has been the clinical standard for response evaluation in NSCLC. There is an ongoing discussion on the performance of FDG-PET/CT as compared to CT[9-11].

With advances in molecular research, molecular-targeted agents such as epidermal growth factor receptor (EGFR)-tyrosine kinase inhibitors (TKI) have emerged for the treatment of (advanced) NSCLC. EGFR-TKIs are able to induce swift responses in selected groups of NSCLC patients and TKI treatment is associated with survival benefit when given as second-line treatment in unselected patients[12]. It blocks the tyrosine kinase domain of the EGFR, thereby inhibiting downstream signaling pathways involved in cell proliferation, angiogenesis, invasion and metastasis and prevention of apoptosis. They can be orally administered, have a relatively favorable toxicity profile, and are registered for the treatment of patients with advanced (chemotherapy-refractory) NSCLC[13].

The probability of response to EGFR–TKIs is considerably higher in patients with EGFR-mutated tumors[14-16]. However, prediction of response is suboptimal by mutation analysis only[17,18]. It is known, that several patients without apparent sensitizing EGFR mutations do benefit from erlotinib therapy[19]. This may be due to heterogeneity within the tumor or the limitations of biopsy analysis not always showing relevant mutations. On the other hand, patients who do not respond to EGFR-TKI's, despite the presence of activating mutations, could be spared unnecessary toxicity and costs. Therefore early decision making as to the effect of treatment is essential.

In this perspective, we present the evidence to use FDG-PET/CT for response evaluation in patients with NSCLC, treated with EGFR-TKI.

SEARCH

Study eligibility and identification

We performed a systematic computerized search of the of PubMed and Medline databases (last search: 01 November 2013) and the Cochrane library (Issue 10, 31 October 2013) to identify all published articles from 01 November 2003 to 01 November 2013 reporting on 18F-FDG-PET response evaluation during EGFR-TKI treatment in patients with NSCLC, using the algorithm: [(Non-Small Cell Lung Carcinoma OR NSCLC) AND (Epidermal Growth Factor Receptor OR EGFR) AND (Diagnostic Imaging) AND (18-FDG PET)]. We also hand-searched journals known to publish data relevant to our search, the reference lists of all articles we recovered and those of relevant review articles were also cross-referenced. Experts in the field were contacted to broaden our yield of potentially eligible articles. Whenever several reports pertained to overlapping groups of patients, we retained only the report with the largest number of events or largest patient population (where appropriate) to avoid duplication of information.

Inclusion and exclusion criteria

The inclusion criteria were as follows: (1) histologically proven NSCLC; (2) use of 18F-FDG as a tracer; (3) use of an 18F-FDG-PET/CT scanning apparatus in humans; (4) use of EGFR-TKI; and (5) articles reported in English.

Studies examining EGFR-targeted agents in combination with other agents were considered eligible, as were single agent anti-EGFR studies, whether they were single arm non-randomised studies, phase Ⅱ or Ⅲ randomised studies, prospective studies, or retrospective studies. Abstracts, meeting proceedings and case reports, defined as studies reporting on fewer than five patients, were excluded. When datasets were incomplete for required data, corresponding authors were contacted; however, no additional data were obtained by this process. Our literature search was limited to published studies.

Data extraction

The following information was manually extracted from each recovered article: first author, journal and year of publication, number of patients screened, EGFR mutational rate, stage of disease correlations with clinicopathologic and demographic data (*i.e.*, smoking status, history, gender, histologic type), and also for data to treatment outcome [*i.e.*, CR, PR CR + PR, stable disease (SD), progressive disease (PD), and nonassessable patients] with the TKIs gefitinib and erlotinib when administered as single agent, *i.e.*, monotherapy TKI. No stratification has been made according to TKI with respect to response data. Information recorded about each recovered reference is listed in Table 1. Data extraction was done independently by two of the authors (MG and TA) and discrepancies were resolved by consensus including a third author (HK).

RESEARCH

During the search period, a total of 20 articles of potential interest have been screened for 18F-FDG-PET/CT response evaluation during EGFR-TKI treatment in patients with NSCLC. Of these, 13 were excluded because

Ref.	Year of publication	n	Age, yr	M/F	Study type	Study protocol FDG response	Stage of disease	Histology	EGFR Selection
Riely *et al*[20]	2007	13	56	2/11	Prospective	21 d after stopping and 21 d after restarting	IV	Adenocarcinoma 11 (85) Other (including NOS) 2 (15)	Only EGFR mutated tumors
Aukema *et al*[21]	2010	23	63	8/15	Prospective	After 7 d	I - III	Adenocarcinoma 17 (73) Other 6 (26)	No selection
Mileshkin *et al*[11]	2011	51	61	30/21	Prospective	After 14 d and 56 d	III - IV	Adenocarcinoma 37 (72) Squamous cell carcinoma 8 (16) Large-cell carcinoma 1 (2) Other (including NOS) 5 (10)	No selection
Zander *et al*[22]	2011	34	61	17/17	Prospective	After 7 d and 42 d	IV	Adenocarcinoma 26 (76) Squamous cell carcinoma 4 (12) Large cell carcinoma 1 (3) Bronchioloalveolar carcinoma 3 (9)	No selection
Benz *et al*[23]	2011	22	64	6/16	Prospective	After 14 d and 78 d	III - IV	Adenocarcinoma 17 (78) Squamous cell carcinoma 3 (14) Other (including NOS) 1 (4) Large cell carcinoma 1 (4)	No selection
O'Brien *et al*[24]	2012	47	63	18/29	Prospective	After 42 d	III - IV	Adenocarcinoma 28 (60) Squamous cell carcinoma 6 (13) Bronchioalveolar carcinoma 7 (14) Other (including NOS) 6 (13)	No selection
Takahashi *et al*[25]	2012	20	69	5/15	Prospective	After 2 d and 28 d	III - IV	Adenocarcinoma 20 (100)	No selection

Table 1 Patient characteristics n(%)

FDG: [18F]-fluorodeoxyglucose; EGFR: Epidermal growth factor receptor.

they did not meet the defined inclusion criteria. In total, data of 210 patients were eligible for analyses[11,20-25]. The characteristics of eligible studies are summarised in Table 1.

FDG-PET/CT and response

The majority of studies used European Organization for Research and Treatment of Cancer (EORTC) criteria to determine response[26] (Tables 2 and 3). Cut-off values to determine response varied from 15% to 30% change in SUVmax between baseline and response FDG-PET/CT scan. Median cut-off value was 15%. Time between initiation of EGFR-TKI therapy and response FDG-PET/CT scan varied from 2-78 d[11,14,20-25].

FDG-PET/CT vs diagnostic CT

Four studies analysed FDG-PET and CT according to Response Evaluation Criteria in Solid Tumors (RECIST) criteria for response (Tables 2 and 3). There was a large variety in days between initiation of EGFR-TKI therapy and response FDG-PET/CT scan (2-56 d) and response CT scan (28-84 d). However all studies showed that FDG-PET response correlated with CT response. The majority of patients with response on FDG-PET/CT scan also showed response on CT-scan. In addition, zero patients with progressive disease on FDG-PET/CT scan had a response on CT-scan[11,14,22,24,25].

FDG-PET/CT and progression free survival

Four studies reported on progression free survival (PFS)[11,22,23,25] (Tables 2 and 3). In general, patients with metabolic response showed a prolonged progression

free survival varying from 3.0 to 8.7 mo. Mileshkin *et al*[11] showed that response at FDG-PET/CT on day 14 was associated with improved PFS using EORTC criteria and Wahl *et al*[27] using Response Criteria in Solid Tumors (PERCIST). In addition Zander *et al*[22] reported the same association on day 7. Takahashi *et al*[25] found no significant relation at 2 d using a cut-off value of 30%, however when a cutoff value of 20% was used, metabolic responders had significantly longer PFS compared with metabolic non-responders.

FDG-PET/CT and overall survival

Five studies reported on metabolic response and overall survival (OS)[11,22-25] (Tables 2 and 3). Metabolic response was associated with improved OS. Both Mileshkin *et al*[11] and Zander *et al*[22] reported early FDG-PET/CT response (resp. 14 d, 7 d) to be significantly associated with longer OS. Metabolic response as shown during later FDG-PET/CT evaluation (resp. 56 d, 42 d) was also associated with longer survival, although this trend was not statistically significant. Similarly O' Brien *et al*[24] reported that responders on FDG-PET/CT scan at 42 d lived longer than patients with metabolic stable disease. Takahashi et al did not find significant survival differences between metabolic responders and non-responders.

FDG-PET/CT EGFR

Forty-eight patients (23%) had an EGFR mutant tumor (Table 4). In one study patients were selected based on EGFR mutation. As shown before, patients with an EGFR mutant tumor were more likely to respond to EGFR therapy and thus to have response on FDG-

Table 2	Early [18F]-fluorodeoxyglucose positron emission tomography acquired together with low dose computed tomography reponse results \< 21 d								
Ref.	Year of publication	*n*	SUV	Response criteria	FDG response time	Cut-off value	FDG response, *n* (%)	FDG-PET/CT *vs* RECIST	PFS	OS
Riely *et al*[20]	2007	13	Max	EORTC	21 d	15%	PR 6 (46)			
							SD 7 (54)			
Aukema *et al*[21]	2010	22	Max	EORTC	7 d	25%	PR 6 (26)			
							SD 16 (70)			
							PD 1 (4)			
Mileshkin *et al*[11]	2011	51	Max	EORTC	14 d	15%	PR 13 (26)	FDG PR: PR 4 SD 7 PD 2	R 5.5 mo	R 11.6 mo
							SD 17 (33)	FDG SD: PR 0 SD 12 PD 5	NR 2.5 mo	NR 7.6 mo
							PD 21 (41)	FDG PD: PR 0 SD 7 PD 14		
Zander *et al*[22]	2011	34	Peak	EORTC	7 d	30%	PR 8 (24)	FDG PR: PR/SD 6 PD 2	R 7.8 mo	R 16.1mo
							SD/PD 26 (76)	FDG SD/PD: PR/SD 5 PD 21	NR 1.5 mo	NR 3.4mo
Benz *et al*[23]	2011	22	Max	PRECIST	14 d	30%	PR 6 (27)		R 11.1 mo	R 16.4 mo
							SD 7 (32)		NR 2.4 mo	NR 14.7 mo
							PD 9 (41)			
Takahashi *et al*[25]	2012	20	Max	EORTC	2 d	25%	PR 10 (50)	FDG PR: PR 8 SD 2 PD 0	R 10.4 mo	
							SD 8 (40)	FDG SD: PR 2 SD 5 PD 1	NR 1.7 mo	
							PD 2 (10)	FDG PD: PR 0 SD 1 PD 1		

FDG: [18F]-fluorodeoxyglucose positron emission tomography acquired together with low dose computed tomography; RECIST: Response Evaluation Criteria in Solid Tumors; PFS: Progression free survival; EORTC: European Organization for Research and Treatment of Cancer.

Table 3	Late [18F]-fluorodeoxyglucose positron emission tomography acquired together with low dose computed tomography response > 21 d								
Ref.	Year of publication	*n*	SUV	Response criteria	Cut-off value	FDG response time	FDG Response *n* (%)	FDG-PET *vs* RECIST	PFS	OS
Mileshkin *et al*[11]	2011	51	Max	EORTC	15%	56 d	PR 8 (16)	FDG PR: PR 4 SD 4 PD 0	R 6.5 mo	R 11.9 mo
							SD 12 (23)	FDG SD: PR 0 SD 11 PD 1	NR 2.7 mo	NR 7.6 mo
							PD 31 (61)	FDG PD: PR 0 SD 11 PD 20		
Zander *et al*[22]	2011	34	Peak	EORTC		42 d	n/a	n/a		
Benz *et al*[23]	2011	22	Max	PRECIST		78 d	n/a	n/a		
O'Brien *et al*[24]	2012	47	Max	EORTC	25%	42 d	PR 15 (32)	FDG PR: PR 11 SD 2 PD 2		
							SD 8 (17)	FDG SD: PR 0 SD 4 PD 4		
							PD 15 (32)	FDG PD: PR 0 SD 2 PD 7		
							NE 9 (19)			
Takahashi *et al*[25]	2012	20	Max	EORTC		28 d	n/a	n/a		

FDG: [18F]-fluorodeoxyglucose positron emission tomography acquired together with low dose computed tomography; RECIST: Response Evaluation Criteria in Solid Tumors; PFS: Progression free survival; EORTC: European Organization for Research and Treatment of Cancer; n/a: Not applicable.

PET[11,23,25].

DISCUSSION

This review summarizes the available data regarding the potential of FDG-PET/CT to predict or monitor treatment efficacy and the relation of metabolic data to clinical outcome in NSCLC patients who are treated with EGFR-TKIs. Our report shows that FDG-PET/CT response during EGFR-TKI therapy is associated with clinical and radiologic response and with survival. FDG-PET shows informative results as early as 7-14 d after initiation of treatment .

This report includes a heterogeneous group of NSCLC subtypes. Over time, it has been come clear that adenocarcinomas are more likely to respond to EGFR-TKI treatment[28]. However, histological classification of squamous-cell and adenocarcinoma is challenging[29]. This difficulty increases in the preoperative setting where attempts at tumor classification in small diagnostic samples are hampered by the paucity of tumor cells and the absence of tissue architecture[30]. Although the efficacy of EGFR–TKIs is higher in patients with EGFR-mutated tumors, prediction of response is not optimal by mutation analysis only. It is known, that several patients without sensitizing EGFR mutations do benefit from EGFR-TKI therapy. This may be due to heterogeneity within the tumor and biopsies will not always show relevant mutations[31]. Tumor response monitoring is of value since unnecessary toxicity and additional cost of administering ineffective treatment can be avoided, especially if monitoring is feasible and informative early during treatment.

For categorization of metabolic response, varying response criteria were used (EORTC, PRECIST). Different cut-off values were used between studies, resulting in suboptimal comparison. However overall, results

Table 4 Epidermal growth factor receptor							
Ref.	Year of publication	*n*	EGFR selection	EGFR mutation (*n*)	Cut-off value	FDG	PFS
Riely *et al*[20]	2007	13	Only EGFR mutated tumors	8	n/a		
Aukema *et al*[21]	2010	22	No selection	4	25%		
Milishkin *et al*[11]	2011	51	No selection	4	> 15%	EGFR + PR 3 PD 2 SD 0 EGFR - PR SD PD	
Zander *et al*[22]	2011	34	No selection	4			EGFR + 6.4 mo EGFR - 1.6 mo
Benz *et al*[23]	2011	22	No selection	5			
O'Brien *et al*[24]	2012	47	No selection	11			
Takahashi *et al*[25]	2012	20	No selection	12		EGFR+ PR 8 SD 3 PD 1 EGFR- PR SD PD	

EGFR: Epidermal growth factor receptor; FDG: [^{18}F]-fluorodeoxyglucose positron emission tomography acquired together with low dose computed tomography; PFS: Progression free survival; n/a: Not applicable.

suggest that any significant metabolic response on FDG-PET/CT is associated with radiologic response later on and longer survival. For example, Mileshkin *et al*[11] and Benz *et al*[23] show similar distributions of response relations using different cut-off values 15% *vs* 30% and different response criteria. As natural variability (repeatability) of FDG-PET is also relevant for implementation of response assessment, lower cut-off values (15%-20%) may increase false positive results for identification of response[9].

Furthermore there is no consensus regarding the optimal timing in performing FDG-PET/CT after initiation of treatment. Several authors suggest that in advanced NSCLC metabolic response on FDG-PET/CT scan as early as 1-2 wk after chemotherapy can predict progression free survival and overall survival[17,26-29]. In this review with studies on EGFR-TKI's, Mileshkin *et al*[11] and Zander *et al*[22] found significant associations of early response (day 14, day 7) with survival data. Other authors report the same trend. However, changing FDG-uptake on PET (early) during treatment may reflect all kinds of tissue reactions, as tumor regression (or progression) but also senescence, fibrosis formation, and inflammatory reactions as macrophage infiltration.

Several authors in this report use RECIST criteria as golden standard for response evaluation. However early diagnostic CT for response evaluation in EGFR-TKI therapy has severe limitations. EGFR-TKI therapy is expected to induce response *via* cytostasis rather than objective morphologic response[32]. RECIST is further confounded by structural abnormalities, before and after treatment, which may not actually contain tumor[33]. In this report all early FDG-PET-CT responses were associated with CT responses (according to RECIST), when CT was performed after a period of 28-84 d presuming that morphologic response have took place[11,22,24,25].

Presumably, in patients with NSCLC treated with EGFR-TKI's, the potential value of FDG-PET/CT response monitoring is best described by its possibilities of early response identification. If metabolic response does not occur within the first weeks of EGFR-TKI treatment, patients may be spared (further) unnecessary toxicity of ineffective treatment. Furthermore, even disregarding EGFR mutation, metabolic response during EGFR-TKI treatment is associated with favorable (progression free) survival[11,22-25].

Concluding, our report shows that response monitoring using FDG-PET/CT has potential in targeted treatment for NSCLC and can be performed as early as 1-2 wk after initiation of treatment. Patients with substantial decrease of metabolic activity during EGFR-TKI treatment will probably benefit from continued treatment. Refining FDG-PET response criteria may help the clinician to decide on continuation or discontinuation of targeted treatment.

REFERENCES

1 **Lardinois D**, Weder W, Hany TF, Kamel EM, Korom S, Seifert B, von Schulthess GK, Steinert HC. Staging of non-small-cell lung cancer with integrated positron-emission tomography and computed tomography. *N Engl J Med* 2003; **348**: 2500-2507 [PMID: 12815135 DOI: 10.1056/NEJMoa022136]

2 **Antoch G**, Stattaus J, Nemat AT, Marnitz S, Beyer T, Kuehl H, Bockisch A, Debatin JF, Freudenberg LS. Non-small cell lung cancer: dual-modality PET/CT in preoperative staging. *Radiology* 2003; **229**: 526-533 [PMID: 14512512 DOI: 10.1148/radiol.2292021598]

3 **van Tinteren H**, Smit EF, Hoekstra OS. FDG-PET in addition to conventional work-up in non-small-cell lung cancer. *J Clin Oncol* 2005; **23**: 1591; author reply 1591-1592 [PMID: 15735147 DOI: 10.1200/JCO.2005.05.201]

4 **Dose SJ**, Bader M, Jenicke L, Hemminger G, Janicke F, Avril N. Early prediction of response to chemotherapy in metastatic breast cancer using sequential 18F-FDG PET. *J Nucl Med* 2005; **46**: 1144-1150

5 **Smith IC**, Welch AE, Hutcheon AW, Miller ID, Payne S, Chilcott F, Waikar S, Whitaker T, Ah-See AK, Eremin O, Heys SD, Gilbert FJ, Sharp PF. Positron emission tomography using [F-18]-fluorodeoxy-D-glucose to predict the pathologic response of breast cancer to primary chemotherapy. *J Clin Oncol* 2000; **18**: 1676-1688

6 **MacManus MP**, Seymour JF, Hicks RJ. Overview of early response assessment in lymphoma with FDG-PET. *Cancer Imaging* 2007; **7**: 10-18 [PMID: 17766210 DOI: 10.1102/1470-7330.2007.0004]

7 **Terasawa T**, Lau J, Bardet S, Couturier O, Hotta T, Hutchings M, Nihashi T, Nagai H. Fluorine-18-fluorodeoxyglu-

cose positron emission tomography for interim response assessment of advanced-stage Hodgkin's lymphoma and diffuse large B-cell lymphoma: a systematic review. *J Clin Oncol* 2009; **27**: 1906-1914 [PMID: 19273713 DOI: 10.1200/JCO.2008.16.0861]

8 **de Geus-Oei LF**, van Laarhoven HW, Visser EP, Hermsen R, van Hoorn BA, Kamm YJ, Krabbe PF, Corstens FH, Punt CJ, Oyen WJ. Chemotherapy response evaluation with FDG-PET in patients with colorectal cancer. *Ann Oncol* 2008; **19**: 348-352 [PMID: 17962202 DOI: 10.1093/annonc/mdm470]

9 **Hoekstra CJ,** Stroobants SG, Smit EF, Vansteenkiste J, van TH, Postmus PE, Golding RP, Biesma B, Schramel FJ, van ZN, Lammertsma AA, Hoekstra OS. Prognostic relevance of response evaluation using [18F]-2-fluoro-2-deoxy-D-glucose positron emission tomography in patients with locally advanced non-small-cell lung cancer. *J Clin Oncol* 2005; **23**: 8362-8370

10 **Tanvetyanon T**, Eikman EA, Sommers E, Robinson L, Boulware D, Bepler G. Computed tomography response, but not positron emission tomography scan response, predicts survival after neoadjuvant chemotherapy for resectable non-small-cell lung cancer. *J Clin Oncol* 2008; **26**: 4610-4616

11 **Mileshkin L**, Hicks RJ, Hughes BG, Mitchell PL, Charu V, Gitlitz BJ, Macfarlane D, Solomon B, Amler LC, Yu W, Pirzkall A, Fine BM. Changes in 18F-fluorodeoxyglucose and 18F-fluorodeoxythymidine positron emission tomography imaging in patients with non-small cell lung cancer treated with erlotinib. *Clin Cancer Res* 2011; **17**: 3304-3315 [PMID: 21364032 DOI: 10.1158/1078-0432.CCR-10-2763]

12 **Shepherd FA**, Rodrigues Pereira J, Ciuleanu T, Tan EH, Hirsh V, Thongprasert S, Campos D, Maoleekoonpiroj S, Smylie M, Martins R, van Kooten M, Dediu M, Findlay B, Tu D, Johnston D, Bezjak A, Clark G, Santabárbara P, Seymour L. Erlotinib in previously treated non-small-cell lung cancer. *N Engl J Med* 2005; **353**: 123-132 [PMID: 16014882 DOI: 10.1056/NEJMoa050753]

13 **Johnson JR**, Cohen M, Sridhara R, Chen YF, Williams GM, Duan J, Gobburu J, Booth B, Benson K, Leighton J, Hsieh LS, Chidambaram N, Zimmerman P, Pazdur R. Approval summary for erlotinib for treatment of patients with locally advanced or metastatic non-small cell lung cancer after failure of at least one prior chemotherapy regimen. *Clin Cancer Res* 2005; **11**: 6414-6421 [PMID: 16166415 DOI: 10.1158/1078-0432.CCR-05-0790]

14 **Paez JG**, Jänne PA, Lee JC, Tracy S, Greulich H, Gabriel S, Herman P, Kaye FJ, Lindeman N, Boggon TJ, Naoki K, Sasaki H, Fujii Y, Eck MJ, Sellers WR, Johnson BE, Meyerson M. EGFR mutations in lung cancer: correlation with clinical response to gefitinib therapy. *Science* 2004; **304**: 1497-1500 [PMID: 15118125 DOI: 10.1126/science.1099314]

15 **Lynch TJ**, Bell DW, Sordella R, Gurubhagavatula S, Okimoto RA, Brannigan BW, Harris PL, Haserlat SM, Supko JG, Haluska FG, Louis DN, Christiani DC, Settleman J, Haber DA. Activating mutations in the epidermal growth factor receptor underlying responsiveness of non-small-cell lung cancer to gefitinib. *N Engl J Med* 2004; **350**: 2129-2139 [PMID: 15118073 DOI: 10.1056/NEJMoa040938]

16 **Lara-Guerra H**, Waddell TK, Salvarrey MA, Joshua AM, Chung CT, Paul N, Boerner S, Sakurada A, Ludkovski O, Ma C, Squire J, Liu G, Shepherd FA, Tsao MS, Leighl NB. Phase II study of preoperative gefitinib in clinical stage I non-small-cell lung cancer. *J Clin Oncol* 2009; **27**: 6229-6236 [PMID: 19884551 DOI: 10.1200/JCO.2009.22.3370]

17 **Yu J**, Kane S, Wu J, Benedettini E, Li D, Reeves C, Innocenti G, Wetzel R, Crosby K, Becker A, Ferrante M, Cheung WC, Hong X, Chiriac LR, Sholl LM, Haack H, Smith BL, Polakiewicz RD, Tan Y, Gu TL, Loda M, Zhou X, Comb MJ. Mutation-specific antibodies for the detection of EGFR mutations in non-small-cell lung cancer. *Clin Cancer Res* 2009; **15**: 3023-3028 [PMID: 19366827 DOI: 10.1158/1078-0432.

CCR-08-2739]

18 **Kawahara A**, Yamamoto C, Nakashima K, Azuma K, Hattori S, Kashihara M, Aizawa H, Basaki Y, Kuwano M, Kage M, Mitsudomi T, Ono M. Molecular diagnosis of activating EGFR mutations in non-small cell lung cancer using mutation-specific antibodies for immunohistochemical analysis. *Clin Cancer Res* 2010; **16**: 3163-3170 [PMID: 20423982 DOI: 10.1158/1078-0432.CCR-09-3239]

19 **Gridelli C**, De Marinis F, Di Maio M, Cortinovis D, Cappuzzo F, Mok T. Gefitinib as first-line treatment for patients with advanced non-small-cell lung cancer with activating Epidermal Growth Factor Receptor mutation: implications for clinical practice and open issues. *Lung Cancer* 2011; **72**: 3-8 [PMID: 21216488 DOI: 10.1016/j.lungcan.2010.12.009]

20 **Riely GJ**, Kris MG, Zhao B, Akhurst T, Milton DT, Moore E, Tyson L, Pao W, Rizvi NA, Schwartz LH, Miller VA. Prospective assessment of discontinuation and reinitiation of erlotinib or gefitinib in patients with acquired resistance to erlotinib or gefitinib followed by the addition of everolimus. *Clin Cancer Res* 2007; **13**: 5150-5155 [PMID: 17785570 DOI: 10.1158/1078-0432.CCR-07-0560]

21 **Aukema TS**, Kappers I, Olmos RA, Codrington HE, van Tinteren H, van Pel R, Klomp HM. Is 18F-FDG PET/CT useful for the early prediction of histopathologic response to neoadjuvant erlotinib in patients with non-small cell lung cancer? *J Nucl Med* 2010; **51**: 1344-1348 [PMID: 20720059 DOI: 10.2967/jnumed.110.076224]

22 **Zander T**, Scheffler M, Nogova L, Kobe C, Engel-Riedel W, Hellmich M, Papachristou I, Toepelt K, Draube A, Heukamp L, Buettner R, Ko YD, Ullrich RT, Smit E, Boellaard R, Lammertsma AA, Hallek M, Jacobs AH, Schlesinger A, Schulte K, Querings S, Stoelben E, Neumaier B, Thomas RK, Dietlein M, Wolf J. Early prediction of nonprogression in advanced non-small-cell lung cancer treated with erlotinib by using [(18)F]fluorodeoxyglucose and [(18)F]fluorothymidine positron emission tomography. *J Clin Oncol* 2011; **29**: 1701-1708 [PMID: 21422426 DOI: 10.1200/JCO.2010.32.4939]

23 **Benz MR**, Herrmann K, Walter F, Garon EB, Reckamp KL, Figlin R, Phelps ME, Weber WA, Czernin J, Allen-Auerbach MS. (18)F-FDG PET/CT for monitoring treatment responses to the epidermal growth factor receptor inhibitor erlotinib. *J Nucl Med* 2011; **52**: 1684-1689 [PMID: 22045706 DOI: 10.2967/jnumed.111.095257]

24 **O'Brien ME**, Myerson JS, Coward JI, Puglisi M, Trani L, Wotherspoon A, Sharma B, Cook G, Ashley S, Gunapala R, Chua S, Popat S. A phase II study of ¹⁸F-fluorodeoxyglucose PET-CT in non-small cell lung cancer patients receiving erlotinib (Tarceva); objective and symptomatic responses at 6 and 12 weeks. *Eur J Cancer* 2012; **48**: 68-74 [PMID: 22119198]

25 **Takahashi R**, Hirata H, Tachibana I, Shimosegawa E, Inoue A, Nagatomo I, Takeda Y, Kida H, Goya S, Kijima T, Yoshida M, Kumagai T, Kumanogoh A, Okumura M, Hatazawa J, Kawase I. Early [18F]fluorodeoxyglucose positron emission tomography at two days of gefitinib treatment predicts clinical outcome in patients with adenocarcinoma of the lung. *Clin Cancer Res* 2012; **18**: 220-228 [PMID: 22019513 DOI: 10.1158/1078-0432.CCR-11-0868]

26 **Young H**, Baum R, Cremerius U, Herholz K, Hoekstra O, Lammertsma AA, Pruim J, Price P. Measurement of clinical and subclinical tumour response using [18F]-fluorodeoxyglucose and positron emission tomography: review and 1999 EORTC recommendations. European Organization for Research and Treatment of Cancer (EORTC) PET Study Group. *Eur J Cancer* 1999; **35**: 1773-1782 [PMID: 10673991]

27 **Wahl RL**, Jacene H, Kasamon Y, Lodge MA. From RECIST to PERCIST: Evolving Considerations for PET response criteria in solid tumors. *J Nucl Med* 2009; **50** Suppl 1: 122S-150S [PMID: 19403881 DOI: 10.2967/jnumed.108.057307]

28 **Besse B**, Ropert S, Soria JC. Targeted therapies in lung cancer. *Ann Oncol* 2007; **18** Suppl 9: ix135-ix142 [PMID:

17631566 DOI: 10.1093/annonc/mdm308]

29   **Stang A**, Pohlabeln H, Müller KM, Jahn I, Giersiepen K, Jöckel KH. Diagnostic agreement in the histopathological evaluation of lung cancer tissue in a population-based case-control study. *Lung Cancer* 2006; **52**: 29-36 [PMID: 16476504 DOI: 10.1016/j.lungcan.2005.11.012]

30   **Field RW**, Smith BJ, Platz CE, Robinson RA, Neuberger JS, Brus CP, Lynch CF. Lung cancer histologic type in the surveillance, epidemiology, and end results registry versus independent review. *J Natl Cancer Inst* 2004; **96**: 1105-1107 [PMID: 15265973 DOI: 10.1093/jnci/djh189]

31   **Soria JC**, Mok TS, Cappuzzo F, Jänne PA. EGFR-mutated oncogene-addicted non-small cell lung cancer: current trends and future prospects. *Cancer Treat Rev* 2012; **38**: 416-430 [PMID: 22119437 DOI: 10.1016/j.ctrv.2011.10.003]

32   **Tuma RS**. Sometimes size doesn't matter: reevaluating RECIST and tumor response rate endpoints. *J Natl Cancer Inst* 2006; **98**: 1272-1274 [PMID: 16985244 DOI: 10.1093/jnci/djj403]

33   **Vansteenkiste J**, Fischer BM, Dooms C, Mortensen J. Positron-emission tomography in prognostic and therapeutic assessment of lung cancer: systematic review. *Lancet Oncol* 2004; **5**: 531-540 [PMID: 15337482 DOI: 10.1016/S1470-2045(04)01564-5]

TOPIC HIGHLIGHT

WJR 6th Anniversary Special Issues (6): CT

Coronary venous system in cardiac computer tomography: Visualization, classification and role

Rafal Mlynarski, Agnieszka Mlynarska, Maciej Sosnowski

Rafal Mlynarski, Agnieszka Mlynarska, Maciej Sosnowski, Unit of Noninvasive Cardiovascular Diagnostics, Medical University of Silesia, Upper-Silesian Cardiology Center, Katowice 40-635, Poland
Rafal Mlynarski, Agnieszka Mlynarska, Department of Electrocardiology, Medical University of Silesia, Upper-Silesian Cardiology Center, Katowice 40-635, Poland
Maciej Sosnowski, 2nd Chair and Division of Cardiology, Medical University of Silesia, Upper-Silesian Cardiology Center, Katowice 40-635, Poland
Author contributions: All authors who wrote this paper had substantial contribution to conception and design and final approval of the version to be published.
Correspondence to: Rafal Mlynarski, MD, PhD, Department of Electrocardiology, Medical University of Silesia, Upper-Silesian Cardiology Center, ul. Ziolowa 45/47, Katowice 40-635, Poland. rafal_mlynarski@mp.pl
Telephone: +48-60-6484161 Fax: +48-32-2524098
Received: December 31, 2013 Revised: February 28, 2014
Accepted: May 16, 2014
Published online: July 28, 2014

Abstract

The role of the coronary venous system was underestimated for many years. In the last 20 years, a few percutaneous cardiology techniques in which the anatomy of the coronary venous system was significant were developed and are in use. The most important seems to be cardiac resynchronization therapy, which is an invasive method for the treatment of heart failure. Unfortunately, one of the major problems is the significant anatomical variability of the coronary venous system. The description of the selected anatomical structures is only useful in selected cases such as, for example, the obstruction of selected vessels, a huge Thebesian valve, *etc.* The 3D images can add significant value; however, their usefulness is limited due to the different points of view that are obtained during intra-operational fluoroscopy. After summarizing all of the articles and guidelines, it can be recommended that the visualization of the coronary venous system be performed in certain patients before cardiac resynchronization. The best option is to use tomography with retrospective gating with the optimal reconstruction of cardiac veins that occurs during the diastolic phases.

Core tip: In the article role of the analysis of coronary venous system in cardiac computed tomography (CT) was presented. In the last 20 years, a few percutaneous cardiology techniques in which the anatomy of the coronary venous system was significant were developed and are in use. The description of the selected anatomical structures in CT is useful in selected cases such as, for example, the obstruction of selected coronary veins, a huge Thebesian valve, *etc.*

Mlynarski R, Mlynarska A, Sosnowski M. Coronary venous system in cardiac computer tomography: Visualization, classification and role. *World J Radiol* 2014; 6(7): 399-408 Available from: URL: http://www.wjgnet.com/1949-8470/full/v6/i7/399.htm DOI: http://dx.doi.org/10.4329/wjr.v6.i7.399

INTRODUCTION

The role of the coronary venous system was not appreciated for many years. In the last 20 years, the number of percutaneous cardiology techniques in which the anatomy of the coronary venous system was significant were developed and are in use. The most important seems to
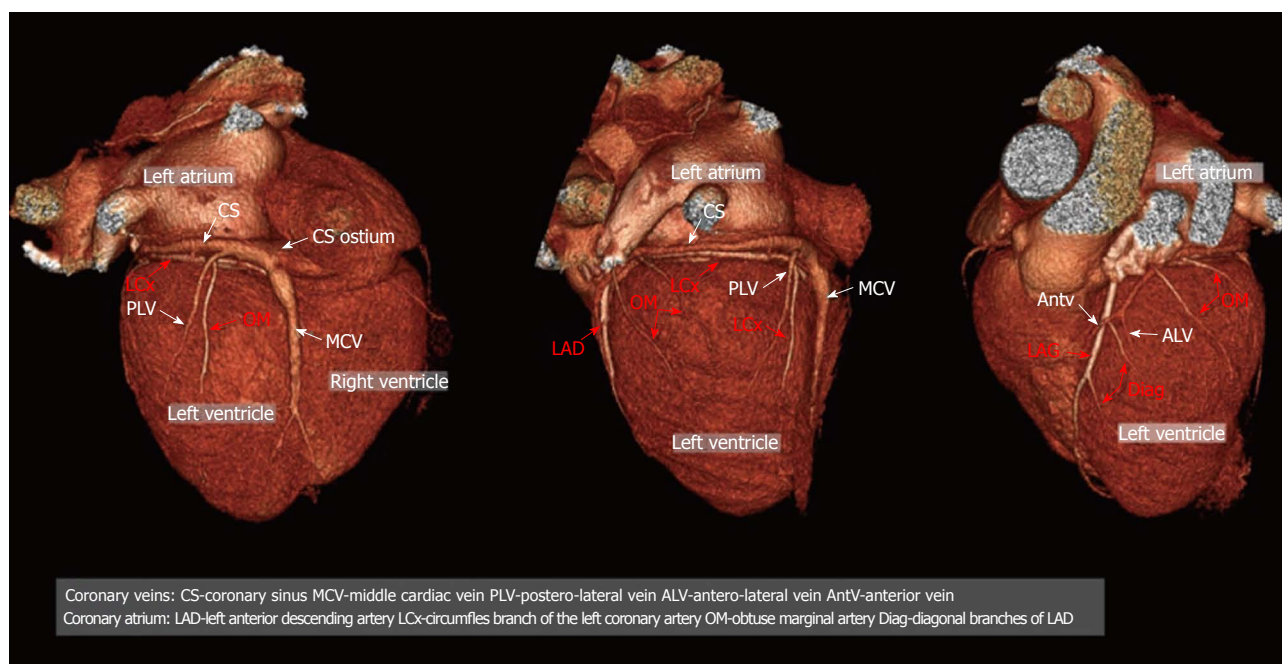
Figure 1 Example of the three-dimensional (3D) anatomy of coronary vessels (arteries and veins). Posterior, lateral antero-lateral view of the heart; 3D volume rendering projections. CS: Coronary sinus; MCV: Middle cardiac vein; PLV: Postero-lateral vein; ALV: Antero-lateral vein; AntV: Anterior vein; LAD: Left anterior descending artery; LCx: Circumfles branch of the left coronary artery; OM: Obtuse marginal artery; Diag: Diagonal branches of LAD.

be cardiac resynchronization therapy (CRT), which is an invasive method for the treatment of heart failure[1-5]. The most recent European guidelines for this method were published in 2012 and 2013[6,7]. In this method, an additional left ventricle (LV) lead is placed in the target coronary vein on the surface of the left ventricle. Proper implantation provides the possibility of pacing the left ventricle together with the classic pacing of the right ventricle and usually the right atrium The most important challenge of left ventricle lead implantation is the precise placement in the area where the electrical parameters are assumed to be optimal[8-10]. The lead is implanted *via* the right atrium by the cannulation of the coronary sinus (CS) ostium to the coronary sinus and the great cardiac vein to the lateral or posterolateral veins (typically), which are called the target veins[11,12]. Unfortunately, one of the major problems is the significant anatomical variability of the coronary venous system[13,14].

ANATOMY OF THE CORONARY VENOUS SYSTEM

The coronary sinus ostium is located in the posteroseptal area of the right atrium and is the final part of the coronary venous system. The coronary sinus usually begins in the place where the vein of Marshall (which is sometimes called the oblique vein of the left atrium) is typically connected to the great cardiac vein[9,15-18]. The vein of Marshall is a small vein that courses on the surface of the right atrium with the ligament of the left vena cava. Sometimes, the valve of Vieussens also occurs[19,20]. The role of the coronary sinus is to collect veins and join

them together; it collects blood from the myocardium and delivers deoxygenated blood to the right atrium. The coronary sinus runs transversely in the right atrioventricular groove on the posterior side of the heart close to the distal part of circumflex branch of the left coronary artery[21-24]. The first branch, which is the beginning of the great cardiac vein is the anterior vein, is sometimes called the anterior interventricular vein and runs parallel to the left descending artery[25].

The area between the anterior vein and the middle cardiac vein is a place where more veins occur in different variants. Depending on the area of drainage, they are called the anterolateral, lateral, posterolateral and posterior veins. There are no strict borders on the left ventricle in the nomenclature of veins. Their number and locations depends on many factors (this will be the subject of a separate paragraph in this article due to its important function in many invasive cardiovascular procedures). Another border of the coronary venous system is the middle cardiac vein. The middle cardiac vein begins close to the apex of the heart and goes into the posterior interventricular groove and finally enters the coronary sinus close to the coronary sinus ostium[15,26,27]. A three-dimensional (3D)/2D reconstructions of the coronary venous system in cardiac computed tomography (CT) are presented in Figures 1 and 2.

COMPUTED TOMOGRAPHY

Since the beginning of cardiac CT, different authors have tried to examine the coronary venous system. At the very beginning, the papers usually had only anatomical merit. One of the first was Christiaens *et al*[25]. The authors
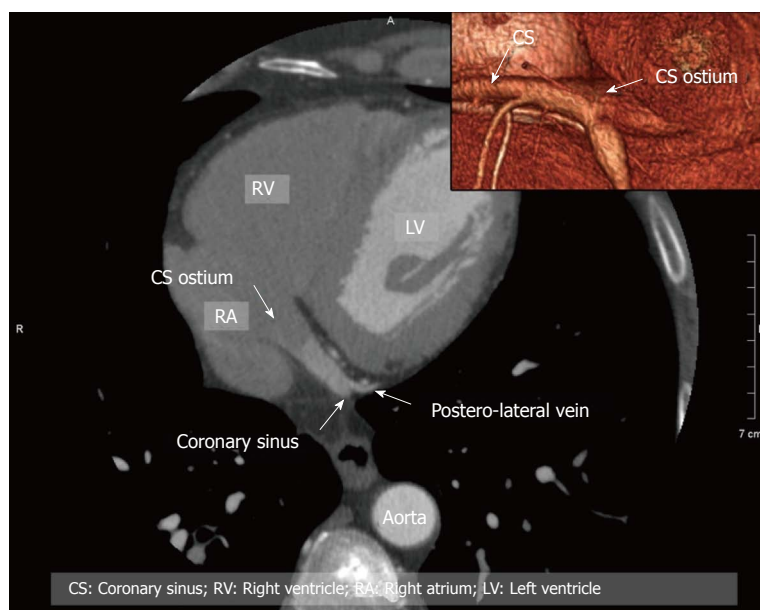
Figure 2 Example of anatomy of coronary vessels in two-dimensional (2D)/3D with reference to the coronary sinus. CS: Coronary sinus; RV: Right ventricle; RA: Right atrium; LV: Left ventricle.

examined 50 consecutive patients using 16-row MDCT (Siemens, Sensation 16). They were able to measure the coronary sinus in two directions, which were 12.2 ± 3.6 in the antero-posterior and 15.3 ± 3.7 in supero-inferior direction with a detailed analysis of the profile of the coronary sinus branches. The first paper that described the anatomical variants was the paper of Jongbloed *et al*[28]. They examined 38 patients using 16-slice CT (Toshiba, Aquilion 16) in which the insertion and continuity of the main tributaries, the number of antero and posterolateral tributaries and the distances between the main tributaries were evaluated. Another study using a 16-slice scanner was the study of Abbara *et al*[29]. The authors used a 16-slice scanner (Siemens, Sensation 16). The authors concluded the feasibility of CT coronary venous imaging especially in the planning of transvenous procedures where the cannulation of the coronary sinus is necessary. In this paper, the authors used an image-quality scale using both conspicuity and contrast-to-noise ratio (CNR), which is very precise; however, this was seldom used in papers that described the coronary venous system. The paper of Tada *et al*[30] discussed the examination of 70 patients using an 8-slice detector. The authors stressed that the venous flow shows an aphasic pattern during the cardiac cycle. This can be a crucial element for the image quality of the coronary venous system. In the paper of Tada, the CVS was greater on the reconstructions that were performed during systole. It can be seen that the images reconstructed in the diastolic phases can cause an underestimate CVS and its tributaries that is similar to the coronary arteries. Another paper describing the coronary venous system in cardiac CT using the latest generation scanner is a paper by Genc *et al*[31]. The authors prospectively examined 357 subjects who had undergone a cardiac CT due to coronary artery disease using a 128-slice Dual Source ECG-gated MDCT (Siemens). All of the veins were visualized in all of the included patients including at least one target vein for cardiac

resynchronization. The posterior cardiac vein and the left marginal vein were visualized in approximately 87%, and the small cardiac vein in 20%. The results obtained by Genc *et al*[31] suggested more detailed images when compared to the older scanners (16-64 slices); however, for a pre-procedural clinical analysis/visualization any of the cardiac CT scanners should be acceptable; however, a more detailed post-processing and analysis of the images is recommended.

The above-mentioned papers influenced the evolution of the imaging the coronary veins and were a prelude to later papers.

The challenge is how to visualize the coronary venous system in cardiac CT. In our earlier research, we documented that the optimal phases for reconstruction should be performed during diastolic phases 30%-50% RR. It can be easily performed on scanners with retrospective gating despite the higher dose of radiation[32]. In Figures 3 and 4 we present the influence of the phase of reconstruction on the visualization of heart vessels-veins and arteries.

IMAGES AND CARDIAC RESYNCHRONISATION

A description of the selected anatomical structures is only useful in selected cases such as, for example, the obstruction of selected vessels, a huge Thebesian valve, *etc*. The images do have added value; however, their usefulness is limited due to the different points of view that are obtained during intra-operational fluoroscopy in comparison with 3D visualizations that are performed using cardiac CT. We attempted to resolve this problem in 2009. The results of our research were published in the PACE journal[33]. We determined that the key features that images must have are: (1) that they be similar in quality to intra-operative fluoroscopy; (2) that they give a
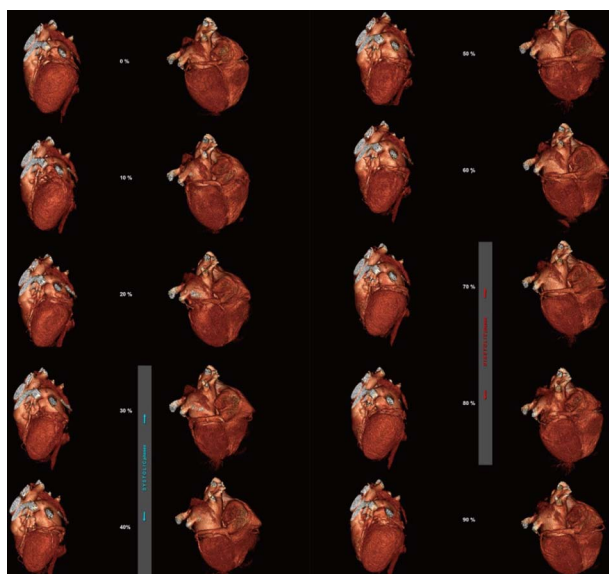
Figure 3 Influence of the phase of reconstruction on the quality of reconstructions of the coronary arteries and veins. Posterior and antero-lateral view of the heart; three-dimensional Volume rendering.
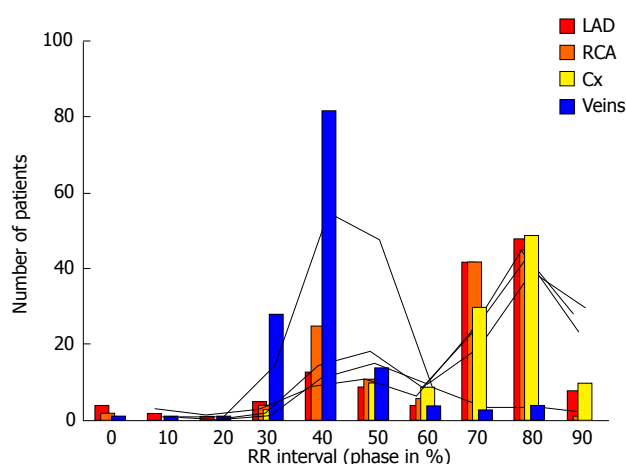
Figure 4 Influence of the phase of reconstruction on the quality of reconstructions of the coronary arteries and veins. LAD: Left anterior descending artery; Cx: Circumfles

Figure 5 Proposed scheme of reconstruction necessary to fulfill cardiac re-synchronization therapy requirements[15]. RA: Right atrium; CS: Coronary sinus;.

semitransparent view of the heart; (3) that they show the semitransparent bones, sternum and vertebral column as a position reference for the implanting physician; (4) that they provide the anterior-posterior (AP), left anterior oblique (LAO) and right anterior oblique (RAO) views; and (5) that they show 3D views in order to evaluate all of the important anatomical aspects.

The cardiac veins are indicated using markers (3D arrows) that are added to the image during post-processing. Finally, the heart is corrected in order to fulfill AP, LAO and RAO-Figure 5[33]. By using this solution in 83 patients (74%), it was possible to obtain very similar images to those that were obtained during the CRT implantation procedure within all three views. In 24% patients, it was not possible to obtain the AP view with the coronary sinus and its ostium due to the large amount of contrast

agent in the right heart. We were also able to visualize the coronary venous system with the vein of Marshall (23%) and the Thebesian valve in 41% of the patients. After seven years of experience with this method, in most cases we are able to obtain proper images. One prospective randomized trial in which Girsky *et al*[34] examined the usefulness of venous cardiac CT angiography for the facilitation of CRT implantation was also published. The authors included 26 patients who had full qualification for CRT-D implantation. The images of eight patients were analyzed using electron-beam CT and 18 patients using 64-slice CT. According to the methods described, the authors used prospective gating to reduce the radiation. They also used a two-second delay for imaging the coronary veins as a modification of routine coronary arteries visualization. According to their results, the CT images helped to decrease the time required for the cannulation of the coronary sinus and the total length of the procedures. A significant reduction in the utilization of a contrast agent, fluoroscopy and some of the equipment that was used was also observed.

There are a few technical-anatomical challenges during the implantation of a left ventricle lead. According to the Blendea and Singh[35], these can include: (1) Lack of successful coronary sinus cannulation caused by the Thebesian valve or a strange (narrow) angle of entrance from the right atrium; (2) Valve of Vieussens on the border of the coronary sinus and the great cardiac vein; (3) Accidental placement of the LV lead into the vein of Marshall, which is unacceptable for LV pacing; (4) Coronary sinus spasm or stenosis; and (5) Lack of target veins-posterolateral, lateral or sometimes anterolateral.

Images generated by cardiac CT can facilitate placement preparation of the procedure, shorten the time of implantation or lower the exposure to X-ray.

THEBESIAN VALVE

The Thebesian valve is the part of the cardiac anatomy that can present problems during coronary sinus cannulation. It is a semicircular fold membrane of the right atrium at the orifice of the coronary sinus, and it is a cau-
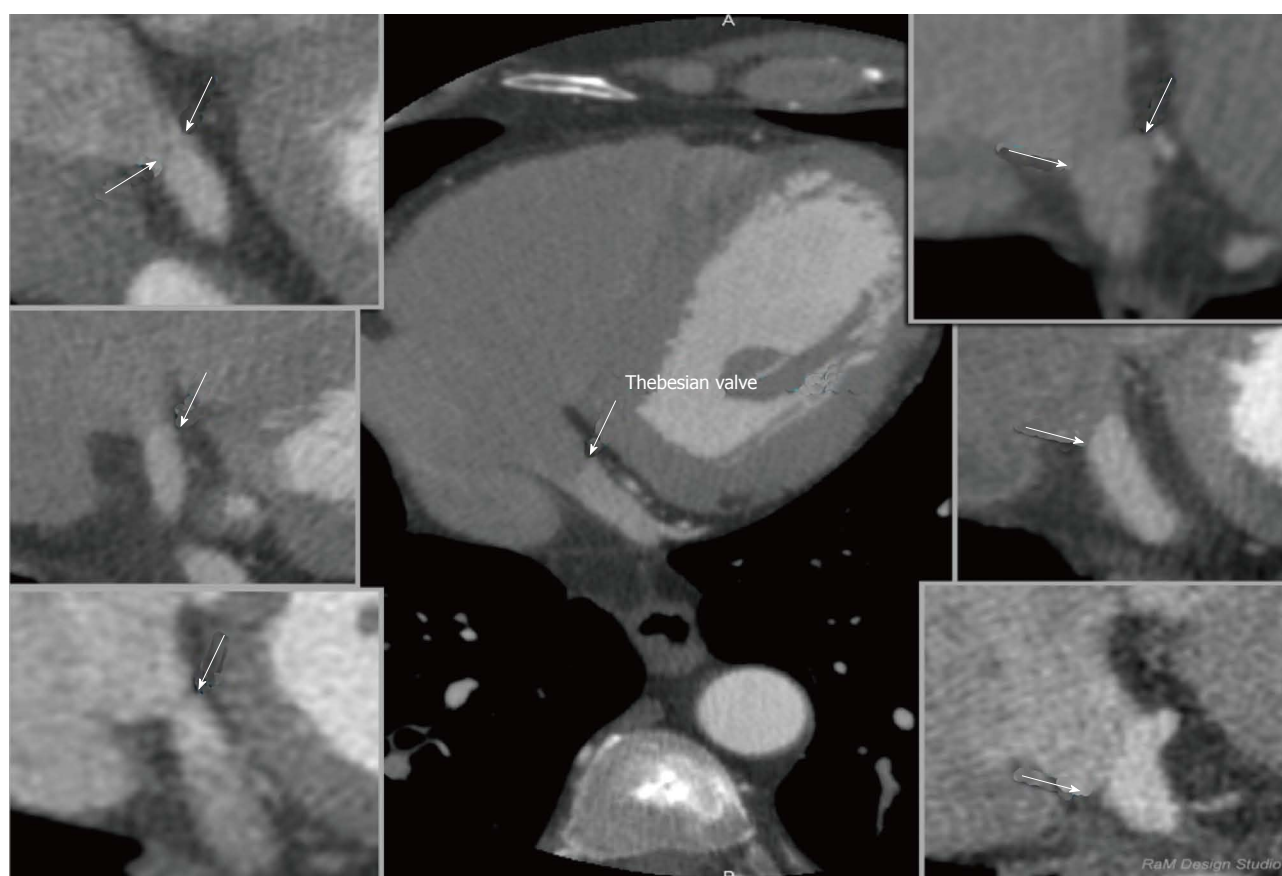
Figure 6 Examples of thebesian valves in cardiac computed tomography; two-dimensional multi-planar reformatting projections.

dal remnant of the embryonic sinoatrial valve. It is situated at the base of the superior vena cava and sometimes is called the coronary sinus guard dog[36,37]. The valve may have a different size, shape or structure or it can be completely absent[38-43]. One of the largest researches that evaluated the Thebesian valve in autopsied hearts was presented in the paper by Mak *et al*[36]. A wide variety of Thebesian valve morphologies were observed in the 75 hearts that were examined, ranging from the absence of the valve to cases in which the valve completely occluded the CS ostium. A Thebesian valve was present in the majority of the hearts that were examined (55/75 hearts-73%). In a study of 50 human CSs of the heart, Silver and Rowley showed that the Thebesian valve covered the ostium in 41% of the cases, including 20% that were totally covered and in 26% of hearts that had an increased weight[44]. In contrast, El-Maasarany *et al*[45] obtained different results. In their study, the valve was present in 87.5% (35/40)-in those cases it was a thin semilunar fold. In four of the 40 patients (10%), the valve had the form of a narrow circular rim surrounding the ostium. The valve was absent in only one case. These differences between the researches indicate the huge anatomical variability of the coronary venous system. Based on our research we proposed a tomographic classification of the Thebesian valve[46]. Our paper was the first in which a heart failure subgroup (EF < 40%) was examined. This might be of special significance since this group is a po-

tential target for cardiac resynchronization. In this group, the prevalence of the Thebesian valve appeared to be significantly lower as compared to groups with a preserved (41%-60%) or normal (approximately 60%) ejection fraction. However, there were no significant differences in the angle of entrance or in the CS diameter between the groups. The prevalence of the valve in heart failure patients is probably caused by atrial enlargement and the stretching of the CS as well as the Thebesian valve. In fact, the Thebesian valve can be relatively well described in MSCT. None of the authors have suggested that any special techniques are required for performing MSCT to visualize the Thebesian valve. A precise evaluation of a standard cardiac scan should be enough to describe this valve. An example of the visualization of Thebesian valve is presented in Figure 6.

INFLUENCE OF CARDIAC PATHOLOGIES ON THE CORONARY VENOUS SYSTEM

Most percutaneous cardiological procedures are performed in patients with different pathologies of the heart. The question of whether those pathologies significantly influence the coronary venous system is interesting. Computed tomography of the heart is an ideal tool to perform such research. In 2007 Chen *et al*[47] examined 23 consecutive patients with chronic systolic heart failure and an ejec-
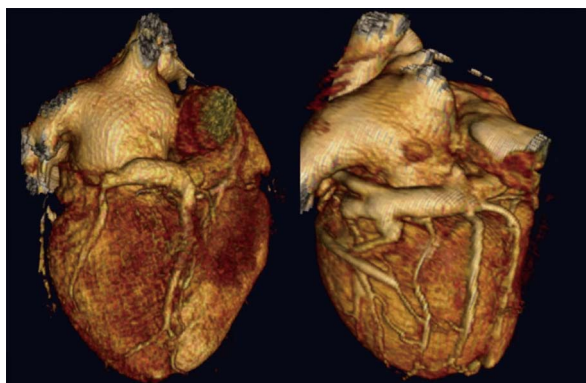
Figure 7 Example of coronary venous system in patients after CABG; three-dimensional Volume rendering.

Figure 8 Mutual relations between coronary sinus/great cardiac vein and circumflex branch of left coronary artery-twisted variant which is very risky for LCx compression by PMA device; three-dimensional Volume rendering. CS: Coronary sinus; GCV: Great cardiac vein; LCx: Circumflex branch.

tion fraction < 40%. The authors concluded that heart failure extends the total length between the PIV and AIV as compared to the control group. Similar results were also obtained by our team[48]. During MSCT of patients with heart failure, the average number of visible veins per case was 3.44 in the HF group and 2.72 in patients with a normal ejection fraction ($P = 0.0246$). The statistical correlation between a reduction in ejection fraction and an increase in the number of veins was found ($r = $ -0.2446, $P < 0.05$). We also examined the influence of heart failure on the variants of the coronary venous system and found that for two of the seven common variants of the coronary venous system at least two target veins (posterolateral and lateral) were presented for cardiac resynchronization. We concluded that an association possibly exists between a failing heart and cardiac venous retention.

Another important question is whether there are some problems with performing MSCT in heart failure patients. First of all, we have to look at the volume of contrast agent because renal impairment often coexists in HF patients, secondly because the use of beta blockers to stabilize the heart rhythm are often contraindicated in these patients and finally these patients often have a problem holding their breath, which is necessary in order to avoid any motion artifacts[49]. Another important observation is the coronary venous system in patients after bypass grafts[50]. We documented that the average number of visible coronary veins in the CABG group was significantly higher (5.3 ± 1.3), while in the control group, it was 3.1 ± 1.1 ($P = 0.001$). An example of such an image is presented in Figure 7.

PERCUTANEOUS MITRAL ANNULOPLASTY

Percutaneous mitral annuloplasty (PMA) is another method in which the visualization of the coronary venous system is important. In this technique devices are implanted into the coronary sinus and the great cardiac vein in order to reduce mitral ischemic regurgitation[51-55]. Its safety and usefulness were evaluated in human stud-

ies such as the AMADEUS trial[56,57]. Why is knowledge about the anatomy so important? In selected patients, a close relationship between the left circumflex artery (LCx) and the coronary sinus can cause the LCx to be accidently occluded during the placement of a device-an example is presented in Figure 8. Computed tomography allows the visualization of the relationships between the mitral valve (MV), the LCx and CS and therefore the risk of occluding the LCx can be minimized[58-60]. Mutual relations between coronary sinus / great cardiac vein and the circumflex branch of left coronary artery-potential role before percutaneous mitral annuloplasty are presented in Figure 9. Several studies have confirmed the considerable anatomical variability in the relative positions of the LCx, the CS and the MV. For example, Maselli *et al*[61] examined the hearts of 61 patients who had died of non-cardiological causes. In the era of non-invasive procedures, visualization using MSCT can play a vital role. One of the earliest studies was that of Maselli *et al*[61] in 2007. The authors analyzed 105 consecutive patients who had been referred for MSCT coronary angiography. Patients were divided into three groups depending on the presence of CAD and heart failure. They concluded that the LCx, CS and mitral valve could be analyzed. Another study evaluating the relationship of the coronary sinus and great cardiac vein to the mitral annulus is a paper by del Valle-Fernandez *et al*[62]. The authors reviewed 390 CT angiograms in order to evaluate patients with a coronary sinus that was more than 200 Hounsfield units in phases 40%, 75% and 0% RR, the absence of a mitral prosthesis and without any anomalies or diseases of the mitral valve. A 64-slice scanner was used in this research and 56 patients were chosen for the final analysis. The authors were able to precisely evaluate the anatomical relationship between the mitral annulus and the coronary sinus. They concluded that the distance between the CS and the mitral annulus varies along the cardiac cycle. The authors also found that the LCx lies between the CS and the mitral annulus in 86% of the subjects that were included.
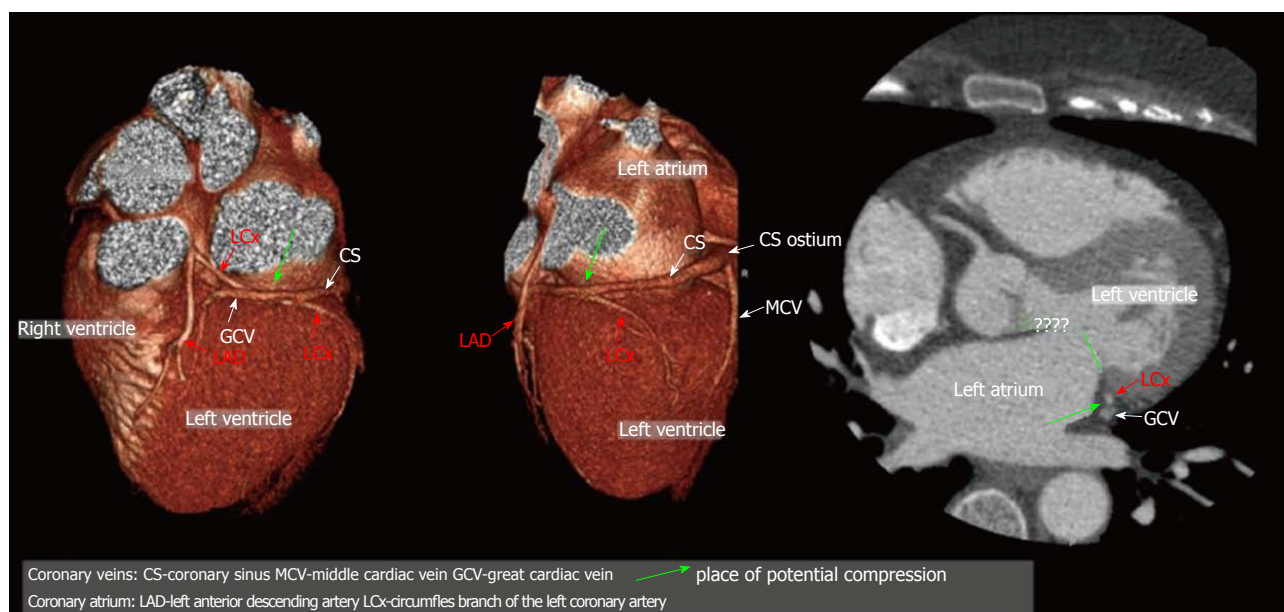
Figure 9 Mutual relations between coronary sinus/great cardiac vein and circumflex branch of left coronary artery - potential role before percutaneous mitral annuloplasty; three-dimensional Volume rendering. CS: Coronary sinus; MCV: Middle cardiac vein; PLV: Postero-lateral vein; ALV: Antero-lateral vein; AntV: Anterior vein; LAD: Left anterior descending artery; LCx: Circumfles branch of the left coronary artery.

PLACE ON INTERNATIONAL GUIDELINES

Most papers have had a huge influence on the creation of clinical guidelines-in the 2010 version of the appropriate use criteria for cardiac CT, noninvasive coronary vein mapping prior to the placement of a biventricular pacemaker received an A (8), which means that it is highly recommended[63]. When the imaging technology was evaluated and the images started to have an acceptable quality and became more common, creating clinical-practical guidelines was only a matter of time. The most important seem to be the 2012 EHRA/HRS expert consensus statement on cardiac resynchronization therapy in heart failure: implant and follow-up recommendations and management[64]. In this document some key elements of using CT before cardiac resynchronization were outlined including the statement that cardiac CT angiography provides a detailed assessment of the coronary arteries and can image and quantify the coronary venous system, including branch vein variability and potential obstacles to placement prior to a CRT procedure in individual patients. There are also limited data suggesting that pre-procedural knowledge about the 3D coronary venous anatomy can facilitate CRT by decreasing the length of the procedure, the time that the patient is receiving radiation and the utilization of guide catheters. The authors also stressed that the target population for cardiac resynchronization-the heart failure population-is not the overall population and can cause some difficulties such as the necessity of using a contrast agent during CT, the ability to do a breath-hold, proper renal function and sometimes the necessity of using intravenous B-Blockers to control the rhythm, which can be contraindicated in the heart failure population.

LIMITATIONS OF COMPUTED TOMOGRAPHY BEFORE ELECTROPHYSIOLOGY PROCEDURES

As was written previously, and underlined in the guidelines, CT is not an examination for the entire population. There are some limitations that apply mostly to patients with heart failure who are potentially qualified for CRT such as: (1) Necessity of a breath hold-elderly patient with advanced heart failure can have problems with this and this can cause motion artifacts; (2) Heart rhythm below 65/min-a higher value than 65/min sometimes requires the administration of Beta Blockers, which can be contraindicated in this population; and (3) During procedures like CRT a large amount of contrast agent, which is also used during CT, is used. This can cause significant problems in the population who suffer from renal failure-prophylaxis of contrast-induced nephropathy should be implemented.

Some physicians are also afraid of the dosage of radiation, which is substantial during CT. Fortunately, progress in the manufacture of CT scanners means that this dosage is continuously decreased by the new techniques that are used in the latest scanners. An example of this is the visualization of the pulmonary veins with a low dosage by using a dual source CT[65]. To date there are no data to support a direct link between CT imaging and a future risk of developing cancer; however, health care practitioners should make every effort to minimize their patients' radiation exposure[66].

CONCLUSION

After summarizing all of the articles and guidelines, it can

be recommended that the visualization of the coronary venous system be considered in certain patients before cardiac resynchronization. The best option is to use tomography with a retrospective ECG gating. Typically, the optimal reconstruction of cardiac veins is during the diastolic phases (30%-40% and 50%) and in our opinion this might complement the standard reconstruction for coronary arteries. If a candidate for CRT had an MSCT examination with retrospective gating performed earlier, it is possible to refer to this exam and reconstruct the coronary venous system without exposing the patient to additional radiation. However, it is necessary to remember that because some diseases or the progress of some diseases can significantly influence the coronary venous tree anatomy, the period between the MSCT exam and CRT should not be too long. In most cardiac resynchronization centers, CRT is almost a routine procedure-it is difficult to recommend MSCT visualization as a routine procedure because intra-operational fluoroscopy is usually enough for the proper implantation of a left ventricle lead. However, in certain cases where difficulties in cannulation are expected, a pre-procedural MSCT should be considered.

Considering and recommending MSCT before percutaneous mitral annuloplasty is too early because of the lack of experience with this method, even in cases in which some device had received a CE mark. However, in such a situation, parallel reconstruction during the systolic (70%-80%) and diastolic phases (30%-40%-50%) should be considered in order to define the anatomical relation between the mitral valve, the coronary sinus and the circumflex branch of the left coronary artery with the highest precision.

REFERENCES

1   **Sohaib SM**, Whinnett ZI, Ellenbogen KA, Stellbrink C, Quinn TA, Bogaard MD, Bordachar P, van Gelder BM, van Geldorp IE, Linde C, Meine M, Prinzen FW, Turcott RG, Spotnitz HM, Wichterle D, Francis DP. Cardiac resynchronisation therapy optimisation strategies: systematic classification, detailed analysis, minimum standards and a roadmap for development and testing. *Int J Cardiol* 2013; **170**: 118-131 [PMID: 24239155 DOI: 10.1016/j.ijcard.2013.10.069]

2   **Guha K**, Konstantinou D, Mantziari L, Modi BN, Chandrasekaran B, Khalique Z, McDonagh T, Sharma R. The impact of age on clinical outcomes following cardiac resynchronisation therapy. *J Interv Card Electrophysiol* 2014; **39**: 95-102 [PMID: 24293176]

3   **Nayar V**, Hiari N, Prasad R, Belham MR, Dutka DP, Pugh PJ. Eligibility for cardiac resynchronisation therapy among patients with heart failure, according to UK NICE guideline criteria. *Int J Cardiol* 2013; **168**: 4401-4402 [PMID: 23706281 DOI: 10.1016/j.ijcard.2013.05.041]

4   **Witte KK**. Cardiac resynchronisation therapy for chronic heart failure: predicting and measuring 'response'. *Heart* 2013; **99**: 293-294 [PMID: 23349344 DOI: 10.1136/heartjnl-2012-303359]

5   **Kloch Badełek M**, Klocek M, Czarnecka D, Wojciechowska W, Wiliński J, Kawecka Jaszcz K. Impact of cardiac resynchronisation therapy on physical ability and quality of life in patients with chronic heart failure. *Kardiol Pol* 2012; **70**:
581-588 [PMID: 22718376]

6   **McMurray JJ**, Adamopoulos S, Anker SD, Auricchio A, Böhm M, Dickstein K, Falk V, Filippatos G, Fonseca C, Gomez-Sanchez MA, Jaarsma T, Køber L, Lip GY, Maggioni AP, Parkhomenko A, Pieske BM, Popescu BA, Rønnevik PK, Rutten FH, Schwitter J, Seferovic P, Stepinska J, Trindade PT, Voors AA, Zannad F, Zeiher A, Bax JJ, Baumgartner H, Ceconi C, Dean V, Deaton C, Fagard R, Funck-Brentano C, Hasdai D, Hoes A, Kirchhof P, Knuuti J, Kolh P, McDonagh T, Moulin C, Popescu BA, Reiner Z, Sechtem U, Sirnes PA, Tendera M, Torbicki A, Vahanian A, Windecker S, McDonagh T, Sechtem U, Bonet LA, Avraamides P, Ben Lamin HA, Brignole M, Coca A, Cowburn P, Dargie H, Elliott P, Flachskampf FA, Guida GF, Hardman S, Iung B, Merkely B, Mueller C, Nanas JN, Nielsen OW, Orn S, Parissis JT, Ponikowski P. ESC guidelines for the diagnosis and treatment of acute and chronic heart failure 2012: The Task Force for the Diagnosis and Treatment of Acute and Chronic Heart Failure 2012 of the European Society of Cardiology. Developed in collaboration with the Heart Failure Association (HFA) of the ESC. *Eur J Heart Fail* 2012; **14**: 803-869 [PMID: 22828712 DOI: 10.1093/eurjhf/hfs105]

7   **Brignole M**, Auricchio A, Baron-Esquivias G, Bordachar P, Boriani G, Breithardt OA, Cleland J, Deharo JC, Delgado V, Elliott PM, Gorenek B, Israel CW, Leclercq C, Linde C, Mont L, Padeletti L, Sutton R, Vardas PE, Zamorano JL, Achenbach S, Baumgartner H, Bax JJ, Bueno H, Dean V, Deaton C, Erol C, Fagard R, Ferrari R, Hasdai D, Hoes AW, Kirchhof P, Knuuti J, Kolh P, Lancellotti P, Linhart A, Nihoyannopoulos P, Piepoli MF, Ponikowski P, Sirnes PA, Tamargo JL, Tendera M, Torbicki A, Wijns W, Windecker S, Kirchhof P, Blomstrom-Lundqvist C, Badano LP, Aliyev F, Bänsch D, Baumgartner H, Bsata W, Buser P, Charron P, Daubert JC, Dobreanu D, Faerestrand S, Hasdai D, Hoes AW, Le Heuzey JY, Mavrakis H, McDonagh T, Merino JL, Nawar MM, Nielsen JC, Pieske B, Poposka L, Ruschitzka F, Tendera M, Van Gelder IC, Wilson CM. 2013 ESC Guidelines on cardiac pacing and cardiac resynchronization therapy: the Task Force on cardiac pacing and resynchronization therapy of the European Society of Cardiology (ESC). Developed in collaboration with the European Heart Rhythm Association (EHRA). *Eur Heart J* 2013; **34**: 2281-2329 [PMID: 23801822 DOI: 10.1093/eurheartj/eht150]

8   **Buss SJ**, Schulz F, Wolf D, Hosch W, Galuschky C, Schummers G, Giannitsis E, Kauczor HU, Zugck C, Becker R, Hardt SE, Katus HA, Korosoglou G. Quantitative analysis of left ventricular dyssynchrony using cardiac computed tomography versus three-dimensional echocardiography. *Eur Radiol* 2012; **22**: 1303-1309 [PMID: 22270144 DOI: 10.1007/s00330-011-2375-0]

9   **Giazitzoglou E**, Katritsis DG. Antegrade visualisation of the coronary sinus for left ventricular pacing. *Hellenic J Cardiol* 2008; **49**: 102-105 [PMID: 18459468]

10   **Cazeau S**, Alonso C, Jauvert G, Lazarus A, Ritter P. Cardiac resynchronization therapy. *Europace* 2004; **5** Suppl 1: S42-S48 [PMID: 15450279]

11   **Riedlbauchová L**, Cihák R, Bytesník J, Vancura V, Frídl P, Hosková L, Kautzner J. Optimization of right ventricular lead position in cardiac resynchronisation therapy. *Eur J Heart Fail* 2006; **8**: 609-614 [PMID: 16504581]

12   **Randhawa A**, Saini A, Aggarwal A, Rohit MK, Sahni D. Variance in coronary venous anatomy: a critical determinant in optimal candidate selection for cardiac resynchronization therapy. *Pacing Clin Electrophysiol* 2013; **36**: 94-102 [PMID: 23106173 DOI: 10.1111/pace.12026]

13   **Blendea D**, Shah RV, Auricchio A, Nandigam V, Orencole M, Heist EK, Reddy VY, McPherson CA, Ruskin JN, Singh JP. Variability of coronary venous anatomy in patients undergoing cardiac resynchronization therapy: a high-speed rotational venography study. *Heart Rhythm* 2007; **4**: 1155-1162

[PMID: 17765613]

14   **Mlynarski R**, Mlynarska A, Sosnowski M. Anatomical variants of coronary venous system on cardiac computed tomography. *Circ J* 2011; **75**: 613-618 [PMID: 21242643]

15   **Noheria A**, DeSimone CV, Lachman N, Edwards WD, Gami AS, Maleszewski JJ, Friedman PA, Munger TM, Hammill SC, Hayes DL, Packer DL, Asirvatham SJ. Anatomy of the coronary sinus and epicardial coronary venous system in 620 hearts: an electrophysiology perspective. *J Cardiovasc Electrophysiol* 2013; **24**: 1-6 [PMID: 23066703 DOI: 10.1111/j.1540-8167.2012.02443.x]

16   **Macedo PG**, Kapa S, Mears JA, Fratianni A, Asirvatham SJ. Correlative anatomy for the electrophysiologist: ablation for atrial fibrillation. Part I: pulmonary vein ostia, superior vena cava, vein of Marshall. *J Cardiovasc Electrophysiol* 2010; **21**: 721-730 [PMID: 20158562 DOI: 10.1111/j.1540-8167.2010.01728.x]

17   **Kim SY**, Hong YJ, Lee HJ, Hur J, Choi BW, Kim YJ. Anomalous great cardiac vein draining into the right atrium combined with a single left coronary artery. *Int J Cardiovasc Imaging* 2013; **29** Suppl 1: 53-56 [PMID: 23443338 DOI: 10.1007/s10554-013-0195-9]

18   **Goldberg SP**, Fonseca BM, Younoszai AK, Campbell DN. An unusual location of a persistent vein of Marshall. *Ann Thorac Surg* 2009; **88**: 305 [PMID: 19559259 DOI: 10.1016/j.athoracsur.2008.10.015]

19   **Strohmer B**. Valve of Vieussens: an obstacle for left ventricular lead placement. *Can J Cardiol* 2008; **24**: e63 [PMID: 18787728]

20   **Hasdemir C**, Alp A, Can LH. Successful balloon dilatation of the valve of Vieussens for left ventricular lead placement. *Pacing Clin Electrophysiol* 2009; **32**: 828-829 [PMID: 19545352 DOI: 10.1111/j.1540-8159.2009.02376.x]

21   **Gokhroo RK**, Bisht DS, Padmanabhan D, Gupta S. Coronary sinus anatomy: ajmer working group classification. *J Invasive Cardiol* 2014; **26**: 71-74 [PMID: 24486664]

22   **Kawata H**, Mulpuru S, Phan H, Patel J, Gadiyaram V, Chen L, Sawhney N, Feld G, Birgersdotter-Green U. Gender difference in coronary sinus anatomy and left ventricular lead pacing parameters in patients with cardiac resynchronization therapy. *Circ J* 2013; **77**: 1424-1429 [PMID: 23459446]

23   **Alikhani Z**, Li J, Merchan JA, Nijhof N, Mendel J, Orlov MV. Coronary sinus anatomy by computerized tomography, overlaid on live fluoroscopy can be successfully used to guide left ventricular lead implantation: a feasibility study. *J Interv Card Electrophysiol* 2013; **36**: 217-222 [PMID: 23196855 DOI: 10.1007/s10840-012-9736-8]

24   **Osman F**, Kundu S, Tuan J, Pathmanathan RK. Use of coronary venous angioplasty to facilitate optimal placement of left ventricular lead during CRT. *Pacing Clin Electrophysiol* 2009; **32**: 281-282 [PMID: 19170924 DOI: 10.1111/j.1540-8159.2008.02217.x]

25   **Christiaens L**, Ardilouze P, Ragot S, Mergy J, Allal J. Prospective evaluation of the anatomy of the coronary venous system using multidetector row computed tomography. *Int J Cardiol* 2008; **126**: 204-208 [PMID: 17493696]

26   **Bali HK**, Chattree KK, Bali SK, Chauhan HK, Shukla CP. Collateral approach for LV lead implantation in a case with abnormal venous anatomy. *Indian Heart J* 2013; **65**: 607-610 [PMID: 24206886 DOI: 10.1016/j.ihj.2013.08.022]

27   **Gilard M**, Mansourati J, Etienne Y, Larlet JM, Truong B, Boschat J, Blanc JJ. Angiographic anatomy of the coronary sinus and its tributaries. *Pacing Clin Electrophysiol* 1998; **21**: 2280-2284 [PMID: 9825333]

28   **Jongbloed MR**, Lamb HJ, Bax JJ, Schuijf JD, de Roos A, van der Wall EE, Schalij MJ. Noninvasive visualization of the cardiac venous system using multislice computed tomography. *J Am Coll Cardiol* 2005; **45**: 749-753 [PMID: 15734621]

29   **Abbara S**, Cury RC, Nieman K, Reddy V, Moselewski F, Schmidt S, Ferencik M, Hoffmann U, Brady TJ, Achenbach S. Noninvasive evaluation of cardiac veins with 16-MDCT angiography. *AJR Am J Roentgenol* 2005; **185**: 1001-1006 [PMID: 16177423]

30   **Tada H**, Naito S, Koyama K, Taniguchi K. Three-dimensional computed tomography of the coronary venous system. *J Cardiovasc Electrophysiol* 2003; **14**: 1385 [PMID: 14678120]

31   **Genc B**, Solak A, Sahin N, Gur S, Kalaycioglu S, Ozturk V. Assessment of the coronary venous system by using cardiac CT. *Diagn Interv Radiol* 2013; **19**: 286-293 [PMID: 23337097 DOI: 10.5152/dir.2013.012]

32   **Mlynarski R**, Sosnowski M, Wlodyka A, Chromik K, Kargul W, Tendera M. Optimal image reconstruction intervals for noninvasive visualization of the cardiac venous system with a 64-slice computed tomography. *Int J Cardiovasc Imaging* 2009; **25**: 635-641 [PMID: 19415522 DOI: 10.1007/s10554-009-9463-0]

33   **Mlynarski R**, Sosnowski M, Wlodyka A, Kargul W, Tendera M. A user-friendly method of cardiac venous system visualization in 64-slice computed tomography. *Pacing Clin Electrophysiol* 2009; **32**: 323-329 [PMID: 19272061 DOI: 10.1111/j.1540-8159.2008.02239.x]

34   **Girsky MJ**, Shinbane JS, Ahmadi N, Mao S, Flores F, Budoff MJ. Prospective randomized trial of venous cardiac computed tomographic angiography for facilitation of cardiac resynchronization therapy. *Pacing Clin Electrophysiol* 2010; **33**: 1182-1187 [PMID: 20579305 DOI: 10.1111/j.1540-8159.2010.02821.x]

35   **Blendea D**, Singh JP. Lead positioning strategies to enhance response to cardiac resynchronization therapy. *Heart Fail Rev* 2011; **16**: 291-303 [PMID: 21184174 DOI: 10.1007/s10741-010-9212-4]

36   **Mak GS**, Hill AJ, Moisiuc F, Krishnan SC. Variations in Thebesian valve anatomy and coronary sinus ostium: implications for invasive electrophysiology procedures. *Europace* 2009; **11**: 1188-1192 [PMID: 19587062 DOI: 10.1093/europace/eup179]

37   **Kautzner J**. Thebesian valve: the guard dog of the coronary sinus? *Europace* 2009; **11**: 1136-1137 [PMID: 19706637 DOI: 10.1093/europace/eup227]

38   **Ghosh SK**, Raheja S, Tuli A. Obstructive Thebesian valve: anatomical study and implications for invasive cardiologic procedures. *Anat Sci Int* 2014; **89**: 85-94 [PMID: 24043316]

39   **Cao M**, Chang P, Garon B, Shinbane JS. Cardiac resynchronization therapy: double cannulation approach to coronary venous lead placement via a prominent thebesian valve. *Pacing Clin Electrophysiol* 2013; **36**: e70-e73 [PMID: 22432962 DOI: 10.1111/j.1540-8159.2012.03362.x]

40   **Loukas M**, Clarke P, Tubbs RS, Kolbinger W. Adam Christian Thebesius, a historical perspective. *Int J Cardiol* 2008; **129**: 138-140 [PMID: 17692957]

41   **Kuroda M**, Takahashi T, Mita N, Kagaya S, Miyoshi S, Saito S. Difficult cannulation of the coronary sinus due to a large Thebesian valve. *Anesth Analg* 2013; **116**: 563-566 [PMID: 23400976 DOI: 10.1213/ANE.0b013e31827bc77e]

42   **Parikh MG**, Halleran SM, Bharati S, Trohman RG. Successful percutaneous cardiac resynchronization despite an occlusive Thebesian valve. *Pediatr Cardiol* 2011; **32**: 1223-1227 [PMID: 21805325 DOI: 10.1007/s00246-011-0066-x]

43   **Anh DJ**, Eversull CS, Chen HA, Mofrad P, Mourlas NJ, Mead RH, Zei PC, Hsia HH, Wang PJ, Al-Ahmad A. Characterization of human coronary sinus valves by direct visualization during biventricular pacemaker implantation. *Pacing Clin Electrophysiol* 2008; **31**: 78-82 [PMID: 18181913 DOI: 10.1111/j.1540-8159.2007.00928.x]

44   **Silver MA**, Rowley NE. The functional anatomy of the human coronary sinus. *Am Heart J* 1988; **115**: 1080-1084 [PMID: 2966548]

45   **El-Maasarany S**, Ferrett CG, Firth A, Sheppard M, Henein MY. The coronary sinus conduit function: anatomical study (relationship to adjacent structures). *Europace* 2005; **7**:

475-481 [PMID: 16087113]

46   **Mlynarski R**, Mlynarska A, Tendera M, Sosnowski M. Coronary sinus ostium: the key structure in the heart's anatomy from the electrophysiologist's point of view. *Heart Vessels* 2011; **26**: 449-456 [PMID: 21240507 DOI: 10.1007/s00380-010-0075-3]

47   **Chen JJ**, Lee WJ, Wang YC, Tsai CT, Lai LP, Hwang JJ, Lin JL. Morphologic and topologic characteristics of coronary venous system delineated by noninvasive multidetector computed tomography in chronic systolic heart failure patients. *J Card Fail* 2007; **13**: 482-488 [PMID: 17675063]

48   **Mlynarska A**, Mlynarski R, Sosnowski M. Coronary venous retention-a feature in heart failure as evidenced by mean of cardiac computed tomography. *Pacing Clin Electrophysiol* 2012; **35**: 1472-1479 [PMID: 23035935 DOI: 10.1111/pace.12000]

49   **Mangalat D,** Kalogeropoulos A, Georgiopoulou V, Stillman A, Butler J. Value of Cardiac CT in Patients With Heart Failure. *Curr Cardiovasc Imaging Rep* 2009; **2**: 410-417 [PMID: 20369033]

50   **Mlynarski R**, Mlynarska A, Sosnowski M. Association between changes in coronary artery circulation and cardiac venous retention: a lesson from cardiac computed tomography. *Int J Cardiovasc Imaging* 2013; **29**: 885-890 [PMID: 23076605 DOI: 10.1007/s10554-012-0139-9]

51   **Siminiak T**, Dankowski R, Baszko A, Lee C, Firek L, Ka⌊mucki P, Szyszka A, Groothuis A. Percutaneous direct mitral annuloplasty using the Mitralign Bident system: description of the method and a case report. *Kardiol Pol* 2013; **71**: 1287-1292 [PMID: 24399585 DOI: 10.5603/KP.2013.0325]

52   **Sack S**. [Percutaneous mitral annuloplasty with the VIACOR coronary sinus system for the treatment of functional mitral regurgitation in heart failure patients. Development and results]. *Herz* 2009; **34**: 468-476 [PMID: 19784565 DOI: 10.1007/s00059-009-3287-5]

53   **Masson JB**, Webb JG. Percutaneous mitral annuloplasty. *Coron Artery Dis* 2009; **20**: 183-188 [PMID: 19339881 DOI: 10.1097/MCA.0b013e328326c6e6]

54   **Lansac E**, Di Centa I, Al Attar N, Messika-Zeitoun D, Raffoul R, Vahanian A, Nataf P. Percutaneous mitral annuloplasty through the coronary sinus: an anatomic point of view. *J Thorac Cardiovasc Surg* 2008; **135**: 376-381 [PMID: 18242272 DOI: 10.1016/j.jtcvs.2007.05.071]

55   **Feldman T**. Percutaneous mitral annuloplasty: not always a cinch. *Catheter Cardiovasc Interv* 2007; **69**: 1062-1063 [PMID: 17525966]

56   **Siminiak T**, Hoppe UC, Schofer J, Haude M, Herrman JP, Vainer J, Firek L, Reuter DG, Goldberg SL, Van Bibber R. Effectiveness and safety of percutaneous coronary sinus-based mitral valve repair in patients with dilated cardiomyopathy (from the AMADEUS trial). *Am J Cardiol* 2009; **104**: 565-570 [PMID: 19660613 DOI: 10.1016/j.amjcard.2009.04.021]

57   **Schofer J**, Siminiak T, Haude M, Herrman JP, Vainer J, Wu JC, Levy WC, Mauri L, Feldman T, Kwong RY, Kaye DM, Duffy SJ, Tübler T, Degen H, Brandt MC, Van Bibber R, Goldberg S, Reuter DG, Hoppe UC. Percutaneous mitral annuloplasty for functional mitral regurgitation: results of the CARILLON Mitral Annuloplasty Device European Union Study. *Circulation* 2009; **120**: 326-333 [PMID: 19597051 DOI: 10.1161/CIRCULATIONAHA.109.849885]

58   **Gopal A**, Shah A, Shareghi S, Bansal N, Nasir K, Gopal

D, Budoff MJ, Shavelle DM. The role of cardiovascular computed tomographic angiography for coronary sinus mitral annuloplasty. *J Invasive Cardiol* 2010; **22**: 67-73 [PMID: 20124591]

59   **Tops LF**, Van de Veire NR, Schuijf JD, de Roos A, van der Wall EE, Schalij MJ, Bax JJ. Noninvasive evaluation of coronary sinus anatomy and its relation to the mitral valve annulus: implications for percutaneous mitral annuloplasty. *Circulation* 2007; **115**: 1426-1432 [PMID: 17353434]

60   **M⌊ynarski R**, M⌊ynarska A, Wilczek J, Sosnowski M. Optimal visualization of heart vessels before percutaneous mitral annuloplasty. *Cardiol J* 2012; **19**: 459-465 [PMID: 23042308]

61   **Maselli D**, Guarracino F, Chiaramonti F, Mangia F, Borelli G, Minzioni G. Percutaneous mitral annuloplasty: an anatomic study of human coronary sinus and its relation with mitral valve annulus and coronary arteries. *Circulation* 2006; **114**: 377-380 [PMID: 16864726 DOI: 10.1161/CIRCINTERVENTIONS.109.873281]

62   **del Valle-Fernández R**, Jelnin V, Panagopoulos G, Ruiz CE. Insight into the dynamics of the coronary sinus/great cardiac vein and the mitral annulus: implications for percutaneous mitral annuloplasty techniques. *Circ Cardiovasc Interv* 2009; **2**: 557-564 [PMID: 20031774]

63   **Taylor AJ**, Cerqueira M, Hodgson JM, Mark D, Min J, O'Gara P, Rubin GD. ACCF/SCCT/ACR/AHA/ASE/ASNC/NASCI/SCAI/SCMR 2010 Appropriate Use Criteria for Cardiac Computed Tomography. A Report of the American College of Cardiology Foundation Appropriate Use Criteria Task Force, the Society of Cardiovascular Computed Tomography, the American College of Radiology, the American Heart Association, the American Society of Echocardiography, the American Society of Nuclear Cardiology, the North American Society for Cardiovascular Imaging, the Society for Cardiovascular Angiography and Interventions, and the Society for Cardiovascular Magnetic Resonance. *J Cardiovasc Comput Tomogr* 2010; **4**: 407.e1-407.33 [PMID: 21232696 DOI: 10.1016/j.jacc.2010.07.005]

64   **Daubert JC**, Saxon L, Adamson PB, Auricchio A, Berger RD, Beshai JF, Breithard O, Brignole M, Cleland J, DeLurgio DB, Dickstein K, Exner DV, Gold M, Grimm RA, Hayes DL, Israel C, Leclercq C, Linde C, Lindenfeld J, Merkely B, Mont L, Murgatroyd F, Prinzen F, Saba SF, Shinbane JS, Singh J, Tang AS, Vardas PE, Wilkoff BL, Zamorano JL, Anand I, Blomström-Lundqvist C, Boehmer JP, Calkins H, Cazeau S, Delgado V, Estes NA, Haines D, Kusumoto F, Leyva P, Ruschitzka F, Stevenson LW, Torp-Pedersen CT. 2012 EHRA/HRS expert consensus statement on cardiac resynchronization therapy in heart failure: implant and follow-up recommendations and management. *Europace* 2012; **14**: 1236-1286 [PMID: 22930717 DOI: 10.1093/europace/eus222]

65   **Thai WE**, Wai B, Lin K, Cheng T, Heist EK, Hoffmann U, Singh JP, Truong QA. Pulmonary venous anatomy imaging with low-dose, prospectively ECG-triggered, high-pitch 128-slice dual-source computed tomography. *Circ Arrhythm Electrophysiol* 2012; **5**: 521-530 [PMID: 22586259 DOI: 10.1161/CIRCEP.111.968313]

66   **Shapiro BP**, Young PM, Kantor B, Choe YH, McCollough CH, Gerber TC. Radiation dose reduction in CT coronary angiography. *Curr Cardiol Rep* 2010; **12**: 59-67 [PMID: 20425185 DOI: 10.1007/s11886-009-0074-0]

TOPIC HIGHLIGHT

Clinical significance of visceral adiposity assessed by computed tomography: A Japanese perspective

Miwa Ryo, Ken Kishida, Tadashi Nakamura, Tohru Yoshizumi, Tohru Funahashi, Iichiro Shimomura

Miwa Ryo, Ken Kishida, Tadashi Nakamura, Tohru Yoshizumi, Tohru Funahashi, Iichiro Shimomura, Department of Metabolic Medicine, Graduate School of Medicine, Osaka University, Suita, Osaka 565-0871, Japan

Miwa Ryo, Osaka Health Support Center, Sumitomo Mitsui Banking Corporation, Osaka 541-0041, Japan

Ken Kishida, Department of Hemodialysis, Kishida Clinic, Toyonaka, Osaka 560-0021, Japan

Tadashi Nakamura, Department of Internal Medicine, Kawasaki Hospital, Kobe, Hyogo 652-0042, Japan

Tohru Yoshizumi, Department of Radiology, Kawasaki Hospital, Kobe, Hyogo 652-0042, Japan

Tohru Funahashi, Department of Metabolism and Atherosclerosis, Graduate School of Medicine, Osaka University, Suita, Osaka 565-0871, Japan

Author contributions: Ryo M, Kishida K, Nakamura T, Yoshizumi T, Funahashi T and Shimomura I contributed to this work.

Correspondence to: Miwa Ryo, MD, PhD, Department of Metabolic Medicine, Graduate School of Medicine, Osaka University, 2-2 B-5, Yamada-oka, Suita, Osaka 565-0871, Japan. ryomw@gaia.eonet.ne.jp

Telephone: +81-6-68793732   Fax: +81-6-68793739

Received: December 27, 2013   Revised: February 11, 2014

Accepted: April 25, 2014

Published online: July 28, 2014

Abstract

Abdominal obesity, rather than total amount of fat, is linked to obesity-related disorders. Visceral adiposity is an important component of obesity-related disorders in Japanese individuals with a mild degree of adiposity compared with Western subjects. In 1983, our group reported techniques for body fat analysis using computed tomography (CT) and established the concept of visceral fat obesity in which intra-abdominal fat accumulation is an important factor in the development of obesity-related complications, such as diabetes, lipid disorders, hypertension and atherosclerosis. Our group also established ideal imaging conditions for determining abdominal fat area at the umbilical level CT scan.

Visceral fat area (VFA) measured in a single slice at L4 level correlated significantly with the total abdominal visceral fat volume measured on multislice CT scan. In a large-scale study of a Japanese population, the mean number of obesity-related cardiovascular risk factors (hypertension, low high-density lipoprotein cholesterolemia and/or hypertriglyceridemia, and hyperglycemia) was greater than 1.0 at 100 cm^2 of VFA, irrespective of gender, age and body mass index. Our group also demonstrated that reduction of visceral fat accumulation subsequent to voluntary lifestyle modification, "Hokenshido", correlated with a decrease in the number of obesity-related cardiovascular risk factors. It is important to select the most appropriate subjects from the general population (*e.g.*, non-obese subjects with a cluster of risk factors for the metabolic syndrome) that are most suitable for body weight reduction, with the goal of preventing atherosclerotic cardiovascular diseases.

Core tip: Accumulation of intra-abdominal visceral fat correlates with atherogenic and metabolic abnormalities, collectively known as the metabolic syndrome. Visceral adiposity is an important component of the syndrome in Japanese individuals with mild adiposity compared with Western subjects. A computed tomography (CT) scan allows the separate analysis of subcutaneous fat and visceral fat, and the visceral fat area (VFA) from a single CT slice L4 level correlates with total visceral fat volume. A VFA cut-off value of 100 cm^2 is used for risk assessment of obesity-related disorders.

Ryo M, Kishida K, Nakamura T, Yoshizumi T, Funahashi T, Shimomura I. Clinical significance of visceral adiposity assessed by

ABDOMINAL OBESITY RATHER THAN TOTAL AMOUNT OF FAT CORRELATES WITH OBESITY-RELATED DISORDERS

Obesity is generally defined as excess storage of energy in the form of fat. Clinical evidence indicates that regional body fat distribution correlates with morbidity and mortality in obese subjects. In 1947, Vague[1] was the first to report a link between adipose tissue distribution and complications in obese subjects. Subsequent clinical studies demonstrated that abdominal obesity [increased waist to hip (W/H) ratio], rather than total amount of fat, is linked to obesity-related disorders[1-5]. A high W/H ratio (an expression of upper body or abdominal obesity) became an index used to predict risks associated with fat accumulation. In comparison, "waist" originally comprised both abdominal subcutaneous fat and intra abdominal visceral fat.

SEPARATE ANALYSIS OF SUBCUTANEOUS FAT AND INTRA-ABDOMINAL VISCERAL FAT

In 1983, our group introduced a new method for fat analysis using a computed tomography (CT) scan, which allowed the separate measurement of subcutaneous fat and intra-abdominal visceral fat[6]. We divided the human body into 11 cylindrical parts (head, forearm, upper arm, chest, abdomen, thigh, calf) for the measurement. Intraperitoneal fat, with a density similar to the subcutaneous fat layer, is considered the visceral fat area (representing fat accumulation predominantly in the mesenteric and omental regions). These respective areas (cm^2) are measured by tracing object contours on the films of each individual scan using the computerized planimetric method. CT scans at the level of the umbilicus show great variability in fat distribution. Two different types of fat distribution patterns are found among obese subjects with similar waist circumferences and body mass indices. In one group of subjects, subcutaneous fat is rather scanty; fat accumulates in the intraperitoneal compartment. In the other group of subjects, fat accumulates exclusively in the subcutaneous area. Lean body mass comprising muscles and bones did not increase with obesity, at least in the abdomen.

VISCERAL FAT OBESITY

The average ratio of visceral fat to subcutaneous fat at the level of the umbilicus (V/S ratio) in obese subjects is about 0.4. Accordingly, we defined obese subjects with V/S ratio of $\geq$ 0.4 as visceral fat obesity, whereas obese subjects with V/S ratio of < 0.4 were considered subcutaneous fat obesity[7,8]. Comparison of the metabolic features of subjects with visceral fat obesity and those with subcutaneous fat obesity showed significantly higher or otherwise greater fasting plasma glucose level, area under the plasma glucose concentration curve after oral glucose loading, triglyceride level, and total cholesterol level in the former group, when either all or sex-matched obese subjects were examined, although BMI or the duration of obesity was not different between the two groups[7,8].

STANDARD METHOD FOR MEASUREMENT OF VISCERAL FAT AND SUBCUTANEOUS FAT

A CT scan and magnetic resonance imaging (MRI) at the umbilical level are the standard techniques used for the assessment of visceral fat accumulation[6-12]. The MRI findings significantly correlate with those of a CT scan. MRI offers the advantage of lack of radiation exposure, although it is more expensive. Several studies have demonstrated that visceral fat area (VFA) measured in a single slice obtained at the level of the umbilicus (approximately the level of L4 and L5) correlates significantly with total visceral abdominal fat volume[6,9,10].

Accurate and standardized techniques are required to implement the use of CT in clinical practice for measurement of VFA. Our group established the imaging conditions necessary for measurement of abdominal fat area at the umbilical level from a CT scan taken in the supine position[11]. The VFA was measured by drawing a line within the muscle wall surrounding the abdominal cavity. The subcutaneous fat area (SFA) was calculated by subtracting the visceral fat area from the total fat area. Fat areas measured by this method correlated closely with those obtained by the computed planimetric method. Thus, VFA measured on a single CT slice at the L4 level correlated strongly with total abdominal visceral fat volume measured by multislice CT ($r = 0.94$, $P < 0.0001$) (Figure 1).

VFA but not SFA value varies considerably (approximately 20%) with respiration and site of obtained CT scan (Figure 2). During inspiration, the downward movement of the diaphragm results in the compression of the abdominal cavity and extension of visceral fat. These changes cause overestimation of VFA and/or inclusion of the lower part of the kidney in the slice. For accurate measurement of VFA, it is important that measurement is made in late expiration. In subjects with a low position umbilicus, the umbilicus CT slices can also include the pelvic cavity. To avoid errors in measurements in such subjects, the slice position must be adjusted to a much higher level (L4 level).

To take VFA measurement from the research bench to daily clinical practice, our group also developed com-
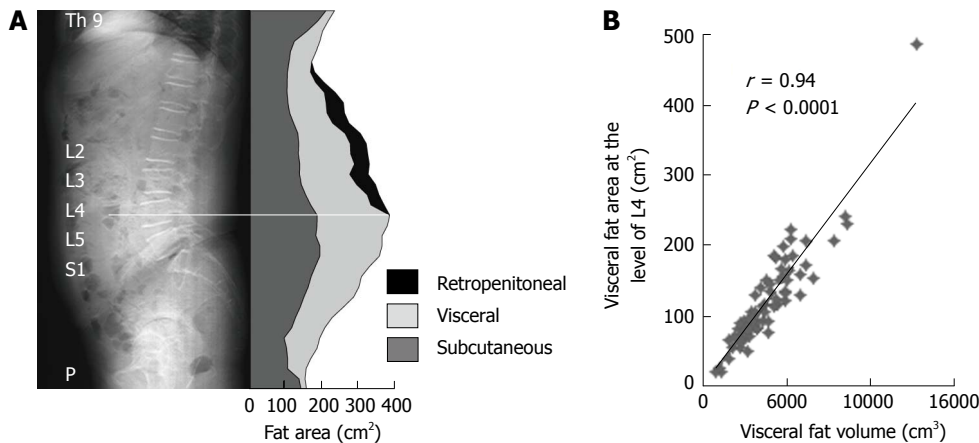
Figure 1 Correlation between visceral fat volume and visceral fat area measured by multislice computed tomography. A: Abdominal fat distribution; B; Correlation between abdominal visceral fat volume and visceral fat area from a single slice at the level of L4. Number = 75 (males 55, females 20); age: 53 ± 1 yr (range, 18-81 yr), body mass index: 25.4 ± 3.9 kg/cm^2 (18.9-38.8 kg/cm^2). Slice thickness was 10 mm, and images were obtained from Th 8/9 to the pubis. Fat area measurement application: Advanced area calculation, GE Healthcare Co.
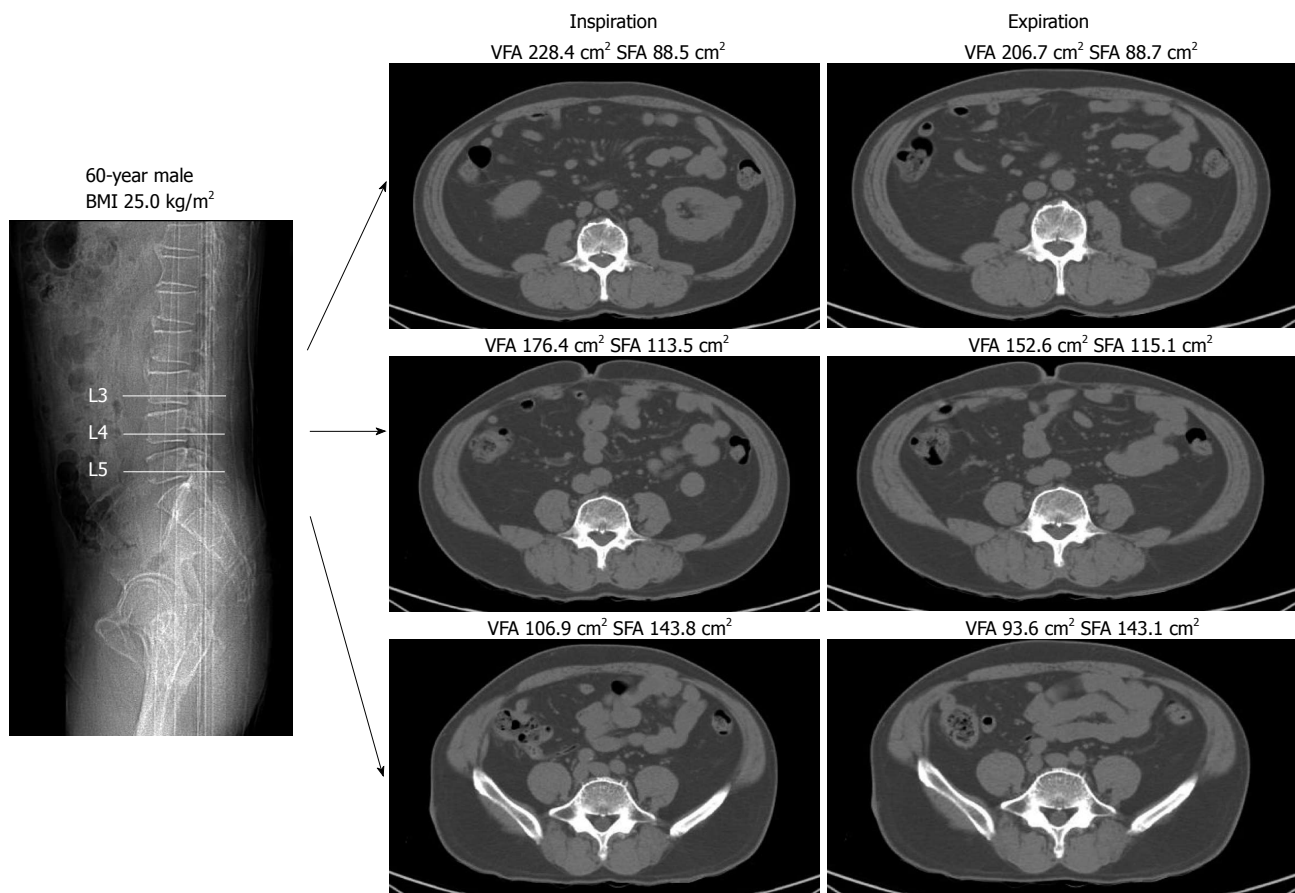
Figure 2 Measurement of visceral fat area varies with respiratory phase and level of computed tomography scan. Fat area measurement application: Advanced area calculation, GE Healthcare Co. VFA: Visceral fat area; SFA: Subcutaneous fat area; BMI: Body mass index.

mercial software that measures both VFA and SFA from a single slice CT scan. These investigations were confirmed in the subsequent generation of CT scanners and the Japanese guidelines of obesity treatment 2011 (Japan Society for the Study of Obesity, in Japanese) defined the imaging conditions for assessment of abdominal fat in multislice CT scan (Table 1).

With regard to the radiation dose, the dose-length product (mGy·cm) is determined by multiplying CT dose index volume (mGy) by scan length (cm)[13]. The effective dose (0.015 mSv/mGy·cm) is computed by multiplying the dose-length product by a conversion factor for the abdomen[13]. The mean ± SD of the radiation dose used in the standard protocol for assessment of abdominal fat measured in 37 subjects (men 20, women 17) was 26.6 ± 4.4 for men and 25.6 ± 4.2 mGy/slice for women, while

Table 1 Parameters used for computed tomography imaging of abdominal fat: Multislice computed tomography	
Scan position	Umbilicus. Scan around the level of L4 to avoid the kidney and/or the ilium in view. Take 3-5 slices in comparative scans after weight reduction
Tube voltage	120 kVp
Tube current	Preferred AEC. SD 8-10
Slice thickness	5-10 mm
FOV	Include whole circumference of the abdominal without deficiency
Respiratory phase	Late expiration
Reconstruction conditions	Displaying conditions common for plain CT scan of the abdomen

CT: Computed tomography; AEC: Automatic exposure control; FOV: Field of view.

the respective effective dose was 0.42 ± 0.07 and 0.41 ± 0.06 mSv/slice.

The above data indicate that radiation exposure for measurement of VFA and SFA is inevitable. Therefore, an alternative simple, rapid, noninvasive and convenient technique to evaluate visceral fat accumulation is desirable in routine clinical practice. To date, the abdominal bioelectrical impedance analysis (BIA) method represents a simple, rapid, noninvasive and convenient technique that can specifically measure VFA[14]. The voltage recorded at the flank to the flow of current between the umbilicus and the back correlates significantly with VFA and is unaffected by SFA. The VFA measured by abdominal BIA correlates significantly with VFA determined by CT scan. Routine measurement of VFA by the BIA method should provide more information on the importance of visceral fat.

RELATIONSHIP BETWEEN VISCERAL FAT AND METABOLIC RISK ACCUMULATION AND CARDIOVASCULAR DISEASE

Analysis of abdominal fat on CT scan showed that body fat distribution, especially excess accumulation of visceral fat, rather than the amount of total fat, correlates with diabetogenic, atherogenic, prothrombotic and proinflammatory metabolic abnormalities or the "metabolic syndrome", which is associated with increased risk of atherosclerotic cardiovascular diseases (ACVD)[15-17].

Using a different approach, other investigators showed that ACVD can be predicted by measuring the carotid intima-media thickness (IMT) by ultrasonography (United States)[18]. Interestingly, however, the Multicultural Community Health Assessment Trial demonstrated that visceral adiposity measured by CT correlates with the ultrasound-measured carotid IMT, plaque area and total area (IMT area plus plaque area) after adjusting for demographics, family history, smoking and percent body fat[19].

The importance of CT-based adiposity indexes in ACVD was further confirmed in the Framingham Heart study (*n* = 3086; men = 1574, women = 1512; mean age 50.2 years; median follow-up 5.0 years), which showed a significant correlation between visceral adiposity and cardiovascular diseases (HR = 1.44; 95%CI: 1.08-1.92; *P* = 0.01) and cancer (HR = 1.43; 95%CI: 1.12-1.84; *P* =

0.005), even after adjustment for clinical risk factors and BMI. In contrast, the amount of subcutaneous adipose tissue did not correlate with ACVD[20].

DIAGNOSTIC CRITERIA OF VISCERAL FAT ACCUMULATION IN JAPAN

The Japanese Visceral Fat Syndrome (J-VFS) Study Committee of the Ministry of Health and Welfare of Japan was subsequently organized to establish the diagnostic criteria of obesity disease and the importance of visceral fat accumulation in obesity-related cardiovascular multiple risk factors[21]. Their study included 1193 subjects (men 775, women 418; 55 ± 12 years of age, mean ± SD). In that study, the mean number of obesity-related cardiovascular risk factors (hypertension, low high-density lipoprotein cholesterolemia and/or hypertriglyceridemia, and hyperglycemia) was greater than 1.0 at 100 cm^2 of VFA in both men and women[21]. They also demonstrated that among the various anthropometric parameters measured in their study, waist circumference showed the closest relationship with VFA in both men and women. The regression line obtained from simple correlation analyses indicated that waist circumference that corresponds to 100 cm^2 of VFA was 84.4 cm for men and 92.5 cm in women. The cut-off point of VFA of 100 cm^2 as indicative of risk of obesity-related disorders in Japanese corresponds to waist circumferences of 85 cm in men and 90 cm in women[21]. The J-VFS study also reported a significant increase in the mean number of cardiovascular risk factors with increases in CT-measured VFA and was more than 1.0 at approximately 100 cm^2 for VFA in both men and women. The area under the receiver-operating characteristic curve analysis indicated that VFA (men 0.741, women 0.763) was a significantly better indicator of clustering of risk factors (≥ 1) than SFA (men 0.636, women 0.689). Furthermore, larger VFA values and smaller SFA values were recorded in men than in women at similar BMI categories[22] (Figure 3A and B).

The Visceral Fat Accumulation and Coronary Artery Disease Investigation in Japanese (VACATION-J) study was organized by the Ministry of Health, Labor and Welfare and included 12443 Japanese (men 10080, women 2363)[23-26]. The results showed that the mean number of obesity-related cardiovascular risk factors increased
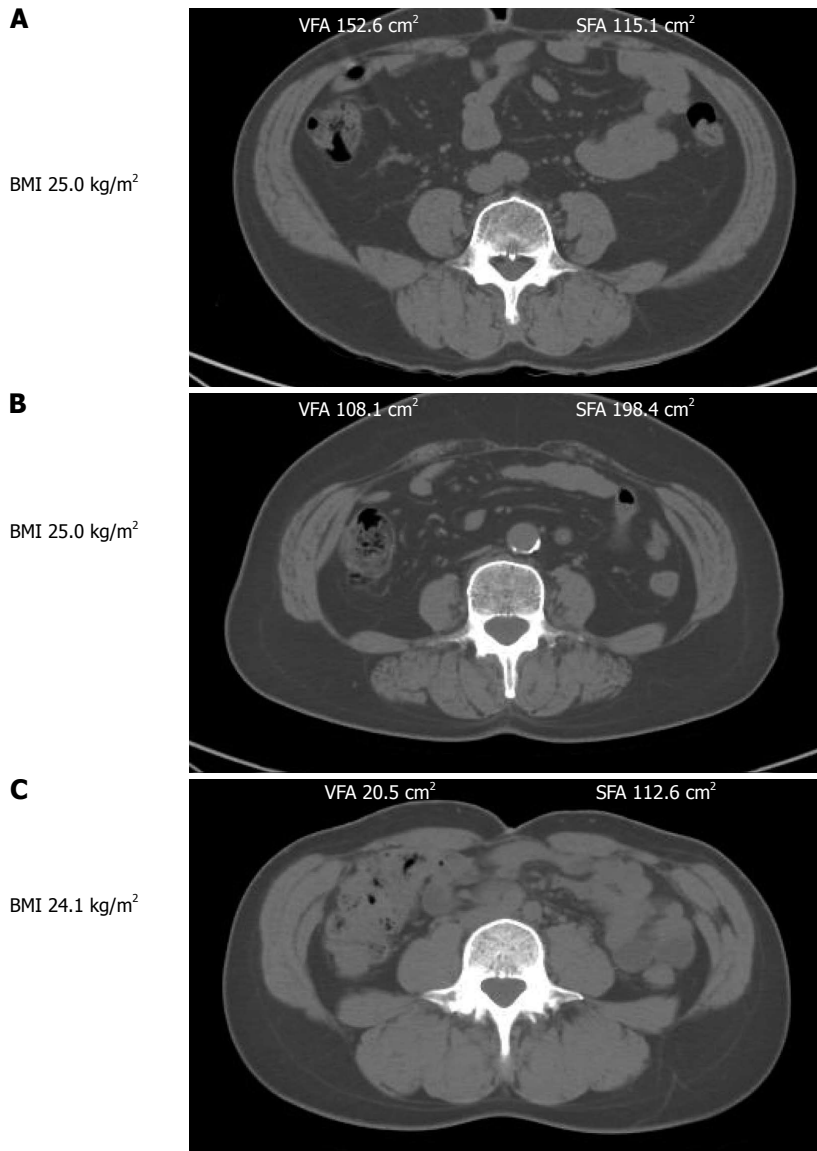
Figure 3 Differences in fat distribution based on sex and age. CT scans of the abdomen in three representative subjects. A: A 60-year-old male; B: A 60-year-old female; C: A 40-year-old female. Fat area measurement application: Advanced area calculation, GE Healthcare Co. CT: Computed tomography; BMI: Body mass index.

with increase in VFA but not with increase in SFA. VFA showed a normal distribution pattern in both men and old women, with a median value of 85-120 cm^2. However, the VFA was markedly smaller (median: 59.8 cm^2) (Figure 3C) and cardiovascular risk factors were fewer in younger women aged under 55 years[23]. The average number of cardiovascular risk factors exceeded 1.0 at VFA around 100 cm^2 for all groups in men and women, irrespective of age. Thus, VFA of approximately 100 cm^2 equates with the presence of more than 1.0 cardiovascular risk factors in Japanese, irrespective of gender, age and BMI[23]. In obese Japanese subjects, obesity-related risk factors did not increase with increase in SFA[23], suggesting a protective effect for subcutaneous fat[27,28]. Considered together, the above studies suggest that "Hokenshido" designed to reduce visceral fat might target Japanese subjects with VFA ≥ 100 cm^2 (waist circumference of 85 cm for men and 90 cm for women) at risk of ACVD.

HEALTH EDUCATION GUIDANCE "HOKENSHIDO" REDUCES METABOLIC SYNDROME

"Hokenshido", a voluntary lifestyle modification, is a unique and original health education guidance used in Japan[26,29,30]. The Industrial Safety and Health Law of Japan stipulates that all workers must undergo annual health check-ups in the workplace. This includes anthropometry and laboratory measurements, testing visual acuity, audiometry, sphygmomanometry and chest X-ray. Other adult Japanese usually undergo annual public or private health check-ups. After the health check-up, physicians or public health nurses identify subjects at high risk of ACVD based on the presence of multiple risk factors, with and without visceral fat accumulation. Public health nurses and/or dietitians provide "Hokenshido" to subjects at high risk in a group setup and/or one-to-

one meetings. "Hokenshido" consists of education about the relationship between visceral fat accumulation and ACVD and interviews, including counseling, about eating habits, alcohol intake and physical activity. Through "Hokenshido", the guided subjects image their own condition of vascular damage and identify problematic habits that need to be changed. "Hokenshido" allows subjects to understand the value of voluntary lifestyle modification with the aim of reducing visceral fat, consequently resulting in reduction of cardiovascular risks.

Using the health promotion program, we conducted a prospective cohort study (UMIN 000002391) of Amagasaki Visceral Fat Study based on visceral adiposity[29-40]. The study included 3174 employees [men 2440 (age 46 ± 11 years), women 734 (43 ± 10 years)] who underwent an annual health checkup. Application of "Hokenshido" resulted in reduction in the prevalence of the metabolic syndrome from 20.8% to 14.4% in men and from 3.0% to 1.9% in women in three consecutive years. Among subjects with the metabolic syndrome at baseline, the mean decrease in waist circumference was 2.5 cm in men and 3.9 cm in women after three consecutive years[29]. Furthermore, the decrease in visceral fat (measured by BIA) correlated with the decrease in the number of metabolic risk factors in men[31].

VISCERAL FAT REDUCTION EFFECTIVELY REDUCES CARDIOVASCULAR RISK

What is the pathological relationship between visceral fat and ACVD? Visceral fat comprises metabolically active adipose tissue. It provides fatty acids and glycerol to the liver *via* the portal vein and secretes adipocytokines and other vasoactive substances that can increase the likelihood of developing the metabolic syndrome. Excess visceral fat accumulation results in adipocyte dysfunction, *i.e.*, overproduction of plasminogen activator inhibitor type 1 and tumor necrosis factor alpha and underproduction of defensive adipocytokines, such as adiponectin[41-44].

We have demonstrated through both the VACA-TION-J Study[23-26] and Amagasaki Visceral Fat Study[29-40] that a decrease in accumulated visceral fat (measured by CT or BIA) achieved within one year correlates with a decrease in the number of metabolic risk factors (hypertension, dyslipidemia and hyperglycemia)[24,31] and an increase in serum adiponectin level[32]. During 4 years follow-up of cardiovascular events in 3228 employees (men 2486, women 742), providing risk factor-oriented "Hokenshido" to subjects with visceral fat accumulation resulted in a significant decrease in the cumulative incidence of cardiovascular events in subjects who showed visceral fat reduction (-20.7 ± 16.1 cm^2), compared to those who showed an increase in visceral fat (12.7 ± 14.6 cm^2) (P = 0.0049)[39].

Considered together, the above results suggest that reducing the amount of visceral fat is beneficial as it improves obesity-related disorders, possibly preventing ACVD. Based on this clinical and scientific background,

it is important to select the most appropriate subjects from the general population, including nonobese overweight subjects with a cluster of risk factors known as the metabolic syndrome, for body weight reduction in order to prevent ACVD. Health promotion programs should be useful in reducing visceral fat accumulation with subsequent improvement in cardiovascular risks (*e.g.*, glucose intolerance, dyslipidemia, hypertension, increased systemic oxidative stress and hypoadiponectinemia)[32], as well as reducing the number of obesity-related cardiovascular risk factors[24,31] to prevent cardiovascular events[39].

REFERENCES

1   **Vague J**. La differenciation sexuelle, featuer determinant des formes del'obesite. *Presse Med* 1947; **55**: 339-340
2   **Kissebah AH**, Vydelingum N, Murray R, Evans DJ, Hartz AJ, Kalkhoff RK, Adams PW. Relation of body fat distribution to metabolic complications of obesity. *J Clin Endocrinol Metab* 1982; **54**: 254-260 [PMID: 7033275 DOI: 10.1210/jcem-54-2-254]
3   **Bjorntorp P**. Obesity and the risk of cardiovascular disease. *Ann Intern Med* 1985; **17**: 3-9
4   **Kaplan NM**. The deadly quartet. Upper-body obesity, glucose intolerance, hypertriglyceridemia, and hypertension. *Arch Intern Med* 1989; **149**: 1514-1520 [DOI: 10.1001/archinte.1989.00390070054005]
5   **Després JP**, Moorjani S, Lupien PJ, Tremblay A, Nadeau A, Bouchard C. Regional distribution of body fat, plasma lipoproteins, and cardiovascular disease. *Arteriosclerosis* 1990; **10**: 497-511 [PMID: 2196040 DOI: 10.1161/01.ATV.10.4.497]
6   **Tokunaga K**, Matsuzawa Y, Ishikawa K, Tarui S. A novel technique for the determination of body fat by computed tomography. *Int J Obes* 1983; **7**: 437-445 [PMID: 6642855]
7   **Matsuzawa Y**, Fujioka S, Tokunaga K, Tarui S. A novel classification: visceral fat obesity and subcutaneous fat obesity. *Adv Obes Res* 1987; 92-96
8   **Fujioka S**, Matsuzawa Y, Tokunaga K, Tarui S. Contribution of intra-abdominal fat accumulation to the impairment of glucose and lipid metabolism in human obesity. *Metabolism* 1987; **36**: 54-59 [DOI: 10.1016/0026-0495(87)90063-1]
9   **Sjöström L**, Kvist H, Cederblad A, Tylén U. Determination of total adipose tissue and body fat in women by computed tomography, 40K, and tritium. *Am J Physiol* 1986; **250**: E736-E745 [PMID: 3717334]
10   **Kvist H**, Chowdhury B, Sjöström L, Tylén U, Cederblad A. Adipose tissue volume determination in males by computed tomography and 40K. *Int J Obes* 1988; **12**: 249-266
11   **Yoshizumi T**, Nakamura T, Yamane M, Islam AH, Menju M, Yamasaki K, Arai T, Kotani K, Funahashi T, Yamashita S, Matsuzawa Y. Abdominal fat: standardized technique for measurement at CT. *Radiology* 1999; **211**: 283-286 [PMID: 10189485 DOI: 10.1148/radiology.211.1.r99ap15283]
12   **Seidell JC**, Bakker CJ, van der Kooy K. Imaging techniques for measuring adipose-tissue distribution--a comparison between computed tomography and 1.5-T magnetic resonance. *Am J Clin Nutr* 1990; **51**: 953-957 [PMID: 2349931]
13   The 2007 Recommendations of the International Commission

on Radiological Protection. ICRP publication 103. *Ann ICRP* 2007; **37**: 1-332 [PMID:18082557]

14   **Ryo M**, Maeda K, Onda T, Katashima M, Okumiya A, Nishida M, Yamaguchi T, Funahashi T, Matsuzawa Y, Nakamura T, Shimomura I. A new simple method for the measurement of visceral fat accumulation by bioelectrical impedance. *Diabetes Care* 2005; **28**: 451-453 [PMID: 15677816 DOI: 10.2337/diacare.28.2.451]

15   **Alberti KG**, Zimmet P, Shaw J. Metabolic syndrome--a new world-wide definition. A Consensus Statement from the International Diabetes Federation. *Diabet Med* 2006; **23**: 469-480 [PMID: 16681555 DOI: 10.1111/j.1464-5491.2006.01858.x]

16   **Després JP**, Lemieux I, Bergeron J, Pibarot P, Mathieu P, Larose E, Rodés-Cabau J, Bertrand OF, Poirier P. Abdominal obesity and the metabolic syndrome: contribution to global cardiometabolic risk. *Arterioscler Thromb Vasc Biol* 2008; **28**: 1039-1049 [PMID: 18356555 DOI: 10.1161/ATVBAHA.107.159228]

17   **Després JP**, Lemieux I. Abdominal obesity and metabolic syndrome. *Nature* 2006; **444**: 881-887 [PMID: 17167477 DOI: 10.1038/nature05488]

18   **Lorenz MW**, Markus HS, Bots ML, Rosvall M, Sitzer M. Prediction of clinical cardiovascular events with carotid intima-media thickness: a systematic review and meta-analysis. *Circulation* 2007; **115**: 459-467 [PMID: 17242284 DOI: 10.1161/CIRCULATIONAHA.106.628875]

19   **Lear SA**, Humphries KH, Kohli S, Frohlich JJ, Birmingham CL, Mancini GB. Visceral adipose tissue, a potential risk factor for carotid atherosclerosis: results of the Multicultural Community Health Assessment Trial (M-CHAT). *Stroke* 2007; **38**: 2422-2429 [PMID: 17673711 DOI: 10.1161/STROKEAHA.107.484113]

20   **Britton KA**, Massaro JM, Murabito JM, Kreger BE, Hoffmann U, Fox CS. Body fat distribution, incident cardiovascular disease, cancer, and all-cause mortality. *J Am Coll Cardiol* 2013; **62**: 921-925 [PMID: 23850922 DOI: 10.1016/j.jacc.2013.06.027]

21   Examination Committee of Criteria for "Obesity Disease" in Japan; Japan Society for the Study of Obesity. New criteria for "obesity disease" in Japan. *Circ J* 2002; **66**: 987-992

22   **Ryo M**, Funahashi T, Nakamura T, Kihara S, Kotani K, Tokunaga K, Matsuzawa Y, Shimomura I. Fat accumulation and obesity-related cardiovascular risk factors in middle-aged Japanese men and women. *Intern Med* 2014; **53**: 299-305 [PMID: 24531085 DOI: 10.2169/internalmedicine.53.9476]

23   **Hiuge-Shimizu A**, Kishida K, Funahashi T, Ishizaka Y, Oka R, Okada M, Suzuki S, Takaya N, Nakagawa T, Fukui T, Fukuda H, Watanabe N, Yoshizumi T, Nakamura T, Matsuzawa Y, Yamakado M, Shimomura I. Absolute value of visceral fat area measured on computed tomography scans and obesity-related cardiovascular risk factors in large-scale Japanese general population (the VACATION-J study). *Ann Med* 2012; **44**: 82-92 [PMID: 20964583 DOI: 10.3109/07853890.2010.526138]

24   **Hiuge-Shimizu A**, Kishida K, Funahashi T, Ishizaka Y, Oka R, Okada M, Suzuki S, Takaya N, Nakagawa T, Fukui T, Fukuda H, Watanabe N, Yoshizumi T, Ohira T, Nakamura T, Matsuzawa Y, Yamakado M, Shimomura I. Reduction of visceral fat correlates with the decrease in the number of obesity-related cardiovascular risk factors in Japanese with Abdominal Obesity (VACATION-J Study). *J Atheroscler Thromb* 2012; **19**: 1006-1018 [PMID: 22785136 DOI: 10.5551/jat.12963]

25   **Hiuge-Shimizu A**, Kishida K, Funahashi T, Okutsu M, Kametani R, Kobayashi H, Nozaki Y, Nomura A, Yokoi H, Yoshizumi T, Ohira T, Nakamura T, Matsuzawa Y, Sumitsuji S, Shimomura I. Coexistence of visceral fat and multiple risk factor accumulations is strongly associated with coronary artery disease in Japanese (the VACATION-J study). *J Atheroscler Thromb* 2012; **19**: 657-663 [PMID: 22472215 DOI: 10.5551/jat.13037]

26   **Kishida K**, Funahashi T, Matsuzawa Y, Shimomura I. Visceral obesity and cardiometabolic risks: lessons from the VACATION-J study. *Clin Lipidol* 2012; **7**: 579-586 [DOI: 10.2217/clp.12.54]

27   **Fox CS**, Massaro JM, Hoffmann U, Pou KM, Maurovich-Horvat P, Liu CY, Vasan RS, Murabito JM, Meigs JB, Cupples LA, D'Agostino RB, O'Donnell CJ. Abdominal visceral and subcutaneous adipose tissue compartments: association with metabolic risk factors in the Framingham Heart Study. *Circulation* 2007; **116**: 39-48 [PMID: 17576866 DOI: 10.1161/CIRCULATIONAHA.106.675355]

28   **Porter SA**, Massaro JM, Hoffmann U, Vasan RS, O'Donnel CJ, Fox CS. Abdominal subcutaneous adipose tissue: a protective fat depot? *Diabetes Care* 2009; **32**: 1068-1075 [PMID: 19244087]

29   **Ryo M**, Nakamura T, Funahashi T, Noguchi M, Kishida K, **Okauchi Y**, Nishizawa H, Ogawa T, Kojima S, Ohira T, Okita K, Iwahashi H, Imagawa A, Matsuzawa Y, Shimomura I. Health education "Hokenshido" program reduced metabolic syndrome in the Amagasaki Visceral Fat Study. Three-year follow-up study of 3,174 Japanese employees. *Intern Med* 2012; **50**:1643-1648 [DOI: 10.2169/internalmedicine.50.5039]

30   **Kishida K**, Funahashi T, Shimomura I. Clinical significance of visceral fat reduction through health education in preventing atherosclerotic cardiovascular disease - Lesson from the Amagasaki Visceral Fat Study: A Japanese perspective. *Nutr Metab* 2011; **8**: 57 [DOI: 10.1186/1743-7075-8-57]

31   **Okauchi Y**, Nishizawa H, Funahashi T, Ogawa T, Noguchi M, Ryo M, Kihara S, Iwahashi H, Yamagata K, Nakamura T, Shimomura I, Matsuzawa Y. Reduction of visceral fat is associated with decrease in the number of metabolic risk factors in Japanese men. *Diabetes Care* 2007; **30**: 2392-2394 [PMID: 17563343 DOI: 10.2337/dc07-0218]

32   **Okauchi Y**, Kishida K, Funahashi T, Noguchi M, Ogawa T, Ryo M, Okita K, Iwahashi H, Imagawa A, Nakamura T, Matsuzawa Y, Shimomura I. Changes in serum adiponectin concentrations correlate with changes in BMI, waist circumference, and estimated visceral fat area in middle-aged general population. *Diabetes Care* 2009; **32**: e122 [PMID: 19793996 DOI: 10.2337/dc09-1130]

33   **Tamba S**, Nishizawa H, Funahashi T, Okauchi Y, Ogawa T, Noguchi M, Fujita K, Ryo M, Kihara S, Iwahashi H, Yamagata K, Nakamura T, Shimomura I, Matsuzawa Y. Relationship between the serum uric acid level, visceral fat accumulation and serum adiponectin concentration in Japanese men. *Intern Med* 2008; **47**: 1175-1180 [PMID: 18591837 DOI: 10.2169/internalmedicine.47.0603]

34   **Fukuda-Akita E**, Okita K, Okauchi Y, Ryo M, Nakamura T, Funahashi T, Iwahashi H, Shimomura I, Miyagawa J, Yamagata K. Impaired early insulin secretion in Japanese type 2 diabetes with metabolic syndrome. *Diabetes Res Clin Pract* 2008; **79**: 482-489 [PMID: 18006169 DOI: 10.1016/j.diabres.2007.10.003]

35   **Kamada Y**, Nakamura T, Funahashi T, Ryo M, Nishizawa H, Okauchi Y, Fukushima J, Yoshida Y, Kiso S, Shimomura I, Hayashi N. Visceral obesity and hypoadiponectinemia are significant determinants of hepatic dysfunction: An epidemiologic study of 3827 Japanese subjects. *J Clin Gastroenterol* 2009; **43**: 995-1000 [PMID: 19407661 DOI: 10.1097/MCG.0b013e3181962de8]

36   **Tamba S**, Nakatsuji H, Kishida K, Noguchi M, Ogawa T, Okauchi Y, Nishizawa H, Imagawa A, Nakamura T, Matsuzawa Y, Funahashi T, Shimomura I. Relationship between visceral fat accumulation and urinary albumin-creatinine ratio in middle-aged Japanese men. *Atherosclerosis* 2010; **211**: 601-605 [PMID: 20363472 DOI: 10.1016/j.atherosclerosis.2010.02.037]

37   **Nakatsuji H**, Kishida K, Funahashi T, Noguchi M, Ogawa T, Okauchi Y, Nishizawa H, Nakamura T, Matsuzawa Y, Shimomura I. One-year reductions in body weight and blood pressure, but not in visceral fat accumulation and adiponec-

tin, improve urinary albumin-to-creatinine ratio in middle-aged Japanese men. *Diabetes Care* 2010; **33**: e110-e111 [PMID: 20668146 DOI: 10.2337/dc10-0739]

38   **Okauchi Y**, Kishida K, Funahashi T, Noguchi M, Ogawa T, Ryo M, Okita K, Iwahashi H, Imagawa A, Nakamura T, Matsuzawa Y, Shimomura I. Absolute value of bioelectrical impedance analysis-measured visceral fat area with obesity-related cardiovascular risk factors in Japanese workers. *J Atheroscler Thromb* 2010; **17**: 1237-1245 [PMID: 20834192 DOI: 10.5551/jat.5694]

39   **Okauchi Y**, Kishida K, Funahashi T, Noguchi M, Morita S, Ogawa T, Imagawa A, Nakamura T, Matsuzawa Y, Shimomura I. 4-year follow-up of cardiovascular events and changes in visceral fat accumulation after health promotion program in the Amagasaki Visceral Fat Study. *Atherosclerosis* 2010; **212**: 698-700 [PMID: 20627199 DOI: 10.1016/j.atherosclerosis.2010.06.011]

40   **Akita EF**, Iwahashi H, Okauchi Y, Okita K, Noguchi M, Ogawa T, Ryo M, Kishida K, Funahashi T, Nakamura T, Matsuzawa Y, Imagawa A, Shimomura I. Predictors of deterioration of glucose tolerance and effects of lifestyle intervention aimed at reducing visceral fat in normal glucose tolerance subjects with abdominal obesity. *J Diabetes Invest* 2011; **2**: 218-224 [DOI: 10.1111/j.2040-1124.2010.00080.x]

41   **Friedman JM**, Halaas JL. Leptin and the regulation of body weight in mammals. *Nature* 1998; **395**: 763-770 [PMID: 9796811 DOI: 10.1038/27376]

42   **Hotamisligil GS**, Arner P, Caro JF, Atkinson RL, Spiegelman BM. Increased adipose tissue expression of tumor necrosis factor-alpha in human obesity and insulin resistance. *J Clin Invest* 1995; **95**: 2409-2415 [PMID: 7738205 DOI: 10.1172/JCI117936]

43   **Shimomura I**, Funahashi T, Takahashi M, Maeda K, Kotani K, Nakamura T, Yamashita S, Miura M, Fukuda Y, Takemura K, Tokunaga K, Matsuzawa Y. Enhanced expression of PAI-1 in visceral fat: possible contributor to vascular disease in obesity. *Nat Med* 1996; **2**: 800-803 [PMID: 8673927 DOI: 10.1038/nm0796-800]

44   **Ryo M**, Nakamura T, Kihara S, Kumada M, Shibazaki S, Takahashi M, Nagai M, Matsuzawa Y, Funahashi T. Adiponectin as a biomarker of the metabolic syndrome. *Circ J* 2004; **68**: 975-981 [PMID: 15502375 DOI: 10.1253/circj.68.975]

TOPIC HIGHLIGHT

Clinical significance of computed tomography assessment for third molar surgery

Kenji Nakamori, Kei Tomihara, Makoto Noguchi

Kenji Nakamori, Kei Tomihara, Makoto Noguchi, Department of Oral and Maxillofacial Surgery, Graduate School of Medicine and Pharmaceutical Sciences for Research, University of Toyama, Toyama 930-0194, Japan
Author contributions: Nakamori K reviewed the relevant literature and wrote the manuscript; Tomihara K and Noguchi M organized the research and edited and revised the manuscript.
Correspondence to: Kenji Nakamori, DDS, PhD, Department of Oral and Maxillofacial Surgery, Graduate School of Medicine and Pharmaceutical Sciences for Research, University of Toyama, 2630 Sugitani, Toyama 930-0194, Japan. nakamori@med.u-toyama.ac.jp
Telephone: +81-76-434-5041   Fax: +81-76-434-5041
Received: December 24, 2013   Revised: March 27, 2014
Accepted: May 28, 2014
Published online: July 28, 2014

Abstract

Surgical extraction of the third molar is the most commonly performed surgical procedure in the clinical practice of oral surgery. Third molar surgery is warranted when there is inadequate space for eruption, malpositioning, or risk for cyst or odontogenic tumor formation. Preoperative assessment should include a detailed morphologic analysis of the third molar and its relationship to adjacent structures and surrounding tissues. Due to developments in medical engineering technology, computed tomography (CT) now plays a critical role in providing the clear images required for adequate assessment prior to third molar surgery. Removal of the maxillary third molar is associated with a risk for maxillary sinus perforation, whereas removal of the mandibular third molar can put patients at risk for a neurosensory deficit from damage to the lingual nerve or inferior alveolar nerve. Multiple factors, including demographic, anatomic, and treatment-related factors, influence the incidence of nerve injury during or following removal of the third molar. CT assessment of the third molar prior to surgery can identify some of these risk factors, such as the absence of cortication between the mandibular third molar and the inferior alveolar canal, prior to surgery to reduce the risk for nerve damage. This topic highlight presents an overview of the clinical significance of CT assessment in third molar surgery.

Core tip: Surgical extraction of the third molar is the most commonly performed procedure in oral surgery. Careful preoperative examinations, including the use of computed tomography (CT) assessment, assist in the planning of in predicting the risks related to surgical interventions. The clinical significance of CT assessment in relation to third molar surgery is therefore reviewed and discussed.

Nakamori K, Tomihara K, Noguchi M. Clinical significance of computed tomography assessment for third molar surgery. *World J Radiol* 2014; 6(7): 417-423 Available from: URL: http://www.wjgnet.com/1949-8470/full/v6/i7/417.htm DOI: http://dx.doi.org/10.4329/wjr.v6.i7.417

INTRODUCTION

Surgical extraction of the third molar is the most common procedure performed by oral surgeons. Appropriate surgical procedures should be determined based on findings from the preoperative examinations that critically assess the morphology of the third molar, and its relationships with adjacent structures [particularly the inferior alveolar canal (IAC)] and surrounding tissues.

Preoperative imaging assessments have typically included conventional intraoral radiography or orthopantomography (OPG). Following more recent developments in medical engineering technology, computed tomography (CT)
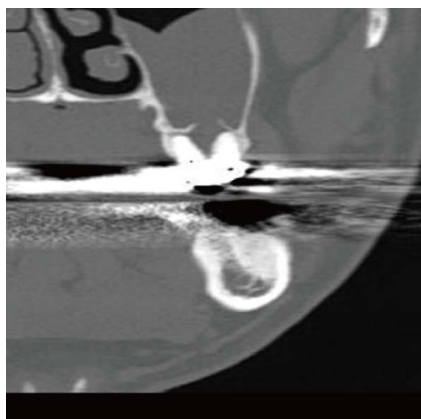
Figure 1 Coronal view of the maxillary molar with multi-detector computed tomography. The absence of cortication between the root apex and maxillary sinus can be observed.

now serves as an integral method to provide clear images for use in clinical practice. Multi-detector CT (MDCT) and cone-beam CT (CBCT) imaging of oral and maxillofacial regions serve as essential methods for diagnosis and treatment planning. Recently, the clinical importance of preoperative CT assessments in third molar surgery has been reported[1-3]. In this article, the general problems related to third molar surgery are reviewed. In addition, current topics associated with the clinical significance of CT assessment for third molar surgery are discussed.

WHY SHOULD THE THIRD MOLAR BE EXTRACTED?

Third molars should be extracted when there is inadequate space for eruption in the retromolar region, between the second molar and the mandibular ramus. This can lead to a disturbed eruption of the third molar, which may create a flap of gingival tissue around the partially erupted tooth, or a pericoronal pocket, which can potentially develop into pericoronitis. In addition, Rahman *et al*[4] recently reported that asymptomatic pericoronal tissue associated with impacted teeth showed a high rate of squamous metaplasia and proliferative activity. Although impacted teeth with pericoronal tissue can lead to cyst formation or odontogenic tumors, the prophylactic removal of disease-free third molars is still controversial[5,6]. Extraction is also warranted when there is mesioangular or "horizontal" malpositioning of the third molar. Such malpositioning can lead to difficulties in plaque control between the second and third molars and may occasionally lead to second molar dental caries. Furthermore, this form of malpositioning may also affect the dental arch shape and result in tooth crowding.

COMPLICATIONS OF THIRD MOLAR SURGERY

Careful preoperative evaluation of the relationship be-tween the maxillary third molar (UM3) and the maxillary sinus is critical in order to prevent perforation of this sinus. For example, a patient is at risk for perforation in the absence of cortication between the UM3 and the maxillary sinus. It is important to note that excessive curettage at the base of the root apex region should be avoided (Figure 1). Removal of the mandibular third molar (LM3) can put patients at risk for serious neurosensory deficits, particularly due to injury of the lingual nerve (LN) and the inferior alveolar nerve (IAN). Lastly, if the third molar is fully or partially impacted in the alveolar bone, bone removal and tooth sectioning are required. Such surgically invasive procedures may cause postoperative pain, edema, and limited opening or mobility of the mouth due to muscle spasms.

RISK FACTORS ASSOCIATED WITH NERVE INJURIES

LN and IAN nerve injuries are thought to be due to mechanical irritations from surgical intervention and are influenced by several demographic, anatomic, and treatment-related factors[7,8]. Risk for injury is increased with the age of the patient because of technical difficulties during surgery, decreased bone elasticity, or increased incidence of tooth hypercementosis. In addition, age may contribute to a reduced capacity for damaged nerve fiber recovery. Furthermore, elderly patients with evidence of sclerotic change are at a considerably higher risk for pathologic osteomyelitis around the impacted tooth[9]. Nakagawa *et al*[10] reported that female patients are at a higher risk for IAN injuries due to decreased buccolingual thickness of the mandible. The risk for damage is increased with a thinner mandible as there is less space between the IAC and LM3. Additional anatomic risk factors for injury from surgery include tooth angulation, the presence of a distal overhang, and the degree of impaction, which are integrally related to the need for surgical intervention. Treatment-related risk factors include injection of local anesthesia, mucoperiosteal incision and elevation of the mucoperiosteal flap, bur usage during alveolar bone removal and tooth sectioning, stretching of the nerve during surgery, and accidental fractures of the lingual cortical bone of the mandible[11]. These treatment-related risk factors are associated with the surgeon's level of experience[12,13].

The lingual split technique for third molar extraction is highly associated with a risk for LN deficit, though the associated risk for LN morbidity remains controversial[11,12]. Therefore, the most widely used technique in clinical practice to decrease the risk of LN injury is the buccal approach. Preoperative imaging assessments can also be employed to limit nerve injury occurrence. Ultrasonography should be used to detect the LN, since the location of the nerve in the mandible prohibits detection by CT imaging[14]. As the IAN is located within the IAC, it can be indirectly evaluated through radiographic assessment of the IAC. Importantly, preoperative radiographic
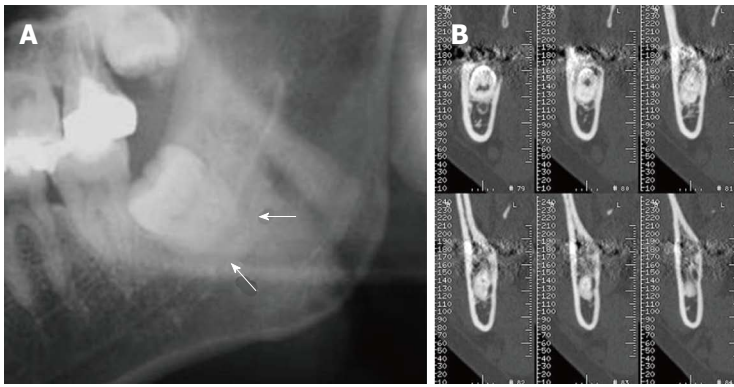
Figure 2 Root darkening and inferior alveolar canal shape.
A: Darkening of the root is observed in this orthopantomography image. A black band is visible (white arrows) at the root apex site; B: A cross-sectional multi-detector computed tomography image indicates alterations (dumbbell shape) to the inferior alveolar canal shape and a loss of the lingual cortex of the mandibular bone.

Table 1 Specificity and sensitivity for predicting inferior alveolar nerve injury with third molar surgery

Imaging procedure	Sensitivity	Specificity
Orthopantomography[22-26]		
Darkening of the root	32%-71%	73%-96%
Interruption of the canal	22%-80%	47%-97%
Diversion of the canal	3%-50%	82%-100%
CT/Cone-beam CT[1,38,41,42]		
Cortication	66%-100%	46%-86%

CT: Electronic computer X-ray tomography technique.

assessment provides increased information on the relationship between the LM3 and the IAC and can be used to identify whether risk factors for IAN injury are present prior to LM3 extraction. In cases where preoperative examination has identified a high-risk factor, surgeons may consider the use of special surgical approaches, including coronectomy[15,16], multistep extraction[17,18], or orthodontic extraction techniques[19-21] to decrease the risk for IAN injuries.

RADIOLOGICAL IMAGING

There are several different radiology procedures that can be used prior to third molar surgery. Conventional intraoral radiography provides surgeons with detailed information regarding structures at the exposed site. If two structures are superimposed, a parallax technique can be applied to determine the buccolingual relationship. However, it is sometimes difficult to position films or an imaging plate at an ideal position, as the LM3 is predominantly located posterior to the mandible.

OPG

OPG is widely used during treatment planning for third molar surgery because it enables assessment of the two-dimensional relationship between the tooth and the IAC. Rood and Shebab have outlined seven important findings that can be obtained from OPG images: darkening of the root, deflected roots, narrowing of the root, dark and bifid roots, interruption of the white line(s), and diversion and narrowing of the IAC[22]. These authors concluded

that the diversion of IAC, darkening of the root and interruption of the white line were significantly related to IAN injuries. There have been several OPG assessment studies which support the usefulness of these seven findings[3,23-25]. According to a meta-analysis study, three signs-darkening of the root or increased radiolucency, interruption of radiopaque borders of the mandibular canal, and diversion of the mandibular canal-have been implicated as the most significant predictive factors of a close relationship between the IAN and the LM3[26]. It should be noted, though, that the statistical results from these analyses had various levels of specificity and sensitivity (Table 1).

Recent research indicated that high-risk signs identified by OPG are significantly associated with absence of the cortication between LM3 and IAC[27,28]. In particular, darkening of the root is closely related to cortical bone loss and/or grooving of the root[27,29-31] (Figure 2). Furthermore, interruption of radiopaque borders has been attributed to loss of cortical structure of the canal. A sign for diversion of the mandibular canal is classified by a nerve running between the roots or the interposition between the root and the mandibular cortical bone.

CT

CT and/or CBCT examinations enable easy assessment of three-dimensional anatomic relationships between the third molar and adjacent structures and surrounding tissues, as well as for detection of the mental foramen and bifid mandibular canal[32-34]. Furthermore, if the third molar becomes dislocated during surgery, the CT image is a useful tool for detecting the dislocated tooth (Figure 3).

The accuracy of measurement by CT was evaluated by a comparative study of the skull, showing that medical CT (single-detector CT or MDCT) or CBCT is sufficient if preoperative CTs have been taken[35,36]. Accurate assessment of the IAC position is important in the field of oral surgery, and several studies have reported the clinical significance of the position of the IAC with respect to LM3[10,32,37]. When the IAN is positioned at the lingual site of the LM3, and sandwiched between the LM3 and the lingual cortex, it may become compressed during LM3 extraction. Several studies have reported that the predictive value of CT assessment for IAN injuries was
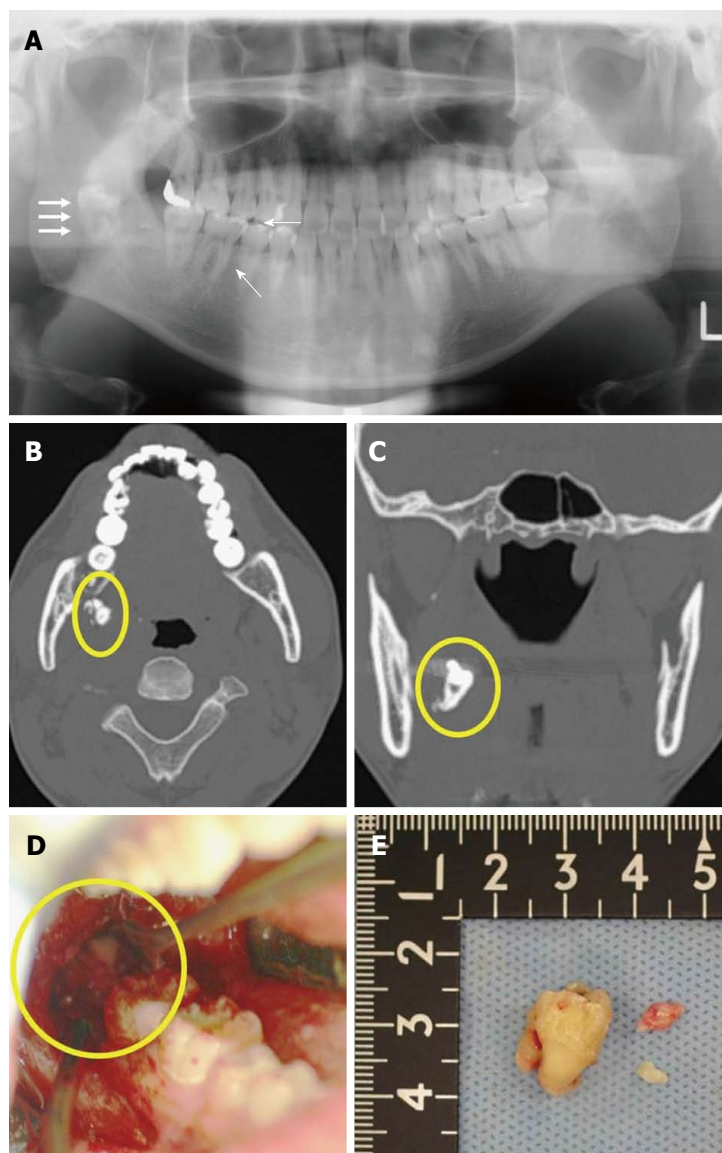
Figure 3 Imaging and surgical removal of a dislocated third mandibular molar (LM3). A: Orthopantomography showing a dislocated LM3 during surgical removal. The dislocated LM3 is superimposed over the middle part of the mandibular ramus (white arrows); B: Axial multi-detector computed tomography (MDCT) image and C: coronal MDCT image of the dislocated LM3 deviating into the pterygomandibular space (yellow circle); D: Surgical extraction; E: Extracted LM3.
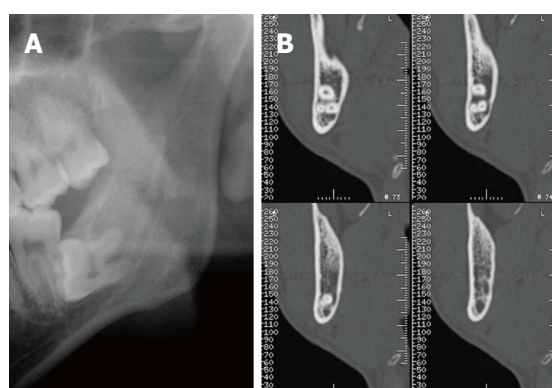
Figure 4 Radiolucency is not observed with orthopantomography. A: No significant radiolucency is observed in the roots of the third mandibular molar with orthopantomography; B: A cross-sectional multi-detector computed tomography image shows the dumbbell shape of the inferior alveolar canal and loss of the lingual cortex of the mandibular bone.

approximately 20%-30%[1,37-39], and 30% when the nerve-vascular bundle was observed[40].

CT images of reconstructed cross-sectional (or coronal) views have been used for assessment of the cortical status around the IAC. Two studies have suggested a predictive value for cortication status in IAN injuries[2,41], which currently appears to be the gold standard finding for predicting signs of IAN injuries. In our own retrospective and prospective studies, the absence of cortication between LM3 and the IAC was a requirement for IAN injuries[38,42,43]. In addition, Susarla *et al*[39] reported that the estimated cortical defect size, computed by counting the number of consecutive slice images with interruptions in the white line around the IAC, was closely related to IAN injury. If reconstruction software is unavailable, a reformatted coronal view can be obtained through reconstruction of the perpendicular image of the IAC, which is based on the axial and sagittal vertical planes[38].

The shape of the IAC has become a significant new finding for estimating the proximity between the IAC and LM3[38,42,44]. Although high-risk signs from OPG findings
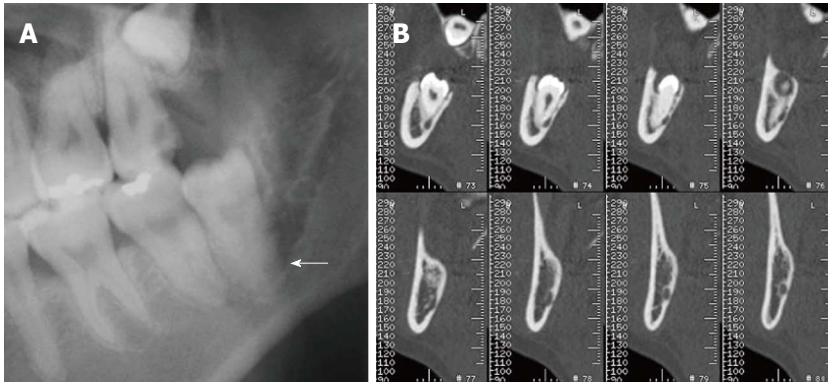
Figure 5 Root darkening and altered third mandibular molar (LM3) root. A: Darkening of the root observed by orthopantomography. A black band is visible (white arrow) at the root apex site; B: Alteration of the LM3 root (grooved) and loss of the lingual cortex of mandibular bone can be observed on cross-sectional multi-detector computed tomography images.

indicated a relationship with lost cortication, some alterations have been recognized in the IAC without the OPG finding (Figure 4). All IAC shapes are initially round/oval near the mandibular foramen, although some canals change shape toward the anterior aspect of the mandible[42]. Alteration of canals is observed most often at the section closest to LM3 (Figure 4B). The altered canal shapes are described as "teardrop-shaped", "dumbbell-shaped"[42], or as an invagination[44]. Collectively, the alteration indicates the degree of proximity between the IAC and LM3.

The number and shape of the LM3 roots can also be assessed by CT examination and should be recommended to surgeons seeking important clinical information. For instance, if the LM3 has three roots, a root-sectioning technique may be needed. However, the number of LM3 roots does not correlate with the incidence of IAN injury. A grooved root shape is intimated due to the close relationship between the root and IAC (Figure 5).

CONCLUSION

Preoperative CT examination is now considered an important assessment tool for third molar surgery. Despite this, standard eligibility criteria have not yet been established to necessitate the use of CT examination[45,46]. Furthermore, standardized significant findings have not been put in place for third molar surgery. This may be due to the low incidence of complications during third molar surgery. To resolve these issues, multi-institutional studies and development of a uniform protocol are needed.

REFERENCES

1   **Susarla SM**, Dodson TB. Preoperative computed tomography imaging in the management of impacted mandibular third molars. *J Oral Maxillofac Surg* 2007; **65**: 83-88 [PMID: 17174769 DOI: 10.1016/j.joms.2005.10.052]
2   **Palma-Carrió C**, García-Mira B, Larrazabal-Morón C, Peñarrocha-Diago M. Radiographic signs associated with inferior alveolar nerve damage following lower third molar extraction. *Med Oral Patol Oral Cir Bucal* 2010; **15**: e886-e890 [PMID: 20526245 DOI: 10.4317/medoral.15.e886]
3   **Monaco G**, Montevecchi M, Bonetti GA, Gatto MR, Checchi L. Reliability of panoramic radiography in evaluating the topographic relationship between the mandibular canal and impacted third molars. *J Am Dent Assoc* 2004; **135**: 312-318 [PMID: 15058618 DOI: 10.14219/jada.archive.2004.0179]
4   **Rahman F**, Bhargava A, Tippu SR, Kalra M, Bhargava N, Kaur I, Srivastava S. Analysis of the immunoexpression of Ki-67 and Bcl-2 in the pericoronal tissues of impacted teeth, dentigerous cysts and gingiva using software image analysis. *Dent Res J* (Isfahan) 2013; **10**: 31-37 [PMID: 23878561 DOI: 10.4103/1735-3327.111764]
5   **Leone SA**, Edenfield MJ, Cohen ME. Correlation of acute pericoronitis and the position of the mandibular third molar. *Oral Surg Oral Med Oral Pathol* 1986; **62**: 245-250 [PMID: 3462627 DOI: 10.1016/0030-4220(86)90001-0]
6   **Weir S**, Lopes V, Malden N. Influence of SIGN guidelines on removal of third molars in The Lothians, Scotland, a clinical audit. *Oral Surg* 2010; **3**: 57-60 [DOI: 10.1111/j.1752-248X.2010.01081.x]
7   **Leung YY**, Cheung LK. Risk factors of neurosensory deficits in lower third molar surgery: an literature review of prospective studies. *Int J Oral Maxillofac Surg* 2011; **40**: 1-10 [PMID: 21035310 DOI: 10.1016/j.ijom.2010.09.005]
8   **Renton T**, Yilmaz Z, Gaballah K. Evaluation of trigeminal nerve injuries in relation to third molar surgery in a prospective patient cohort. Recommendations for prevention. *Int J Oral Maxillofac Surg* 2012; **41**: 1509-1518 [PMID: 23017786 DOI: 10.1016/j.ijom.2012.06.025]
9   **Miyamoto I**, Ishikawa A, Morimoto Y, Takahashi T. Potential risk of asymptomatic osteomyelitis around mandibular third molar tooth for aged people: a computed tomography and histopathologic study. *PLoS One* 2013; **8**: e73897 [PMID: 24040109 DOI: 10.1371/journal.pone.0073897]
10   **Nakagawa Y**, Ishii H, Nomura Y, Watanabe NY, Hoshiba D, Kobayashi K, Ishibashi K. Third molar position: reliability of panoramic radiography. *J Oral Maxillofac Surg* 2007; **65**: 1303-1308 [PMID: 17577493 DOI: 10.1016/j.joms.2006.10.028]
11   **Boffano P**, Roccia F, Gallesio C. Lingual nerve deficit following mandibular third molar removal: review of the literature and medicolegal considerations. *Oral Surg Oral Med Oral Pathol Oral Radiol* 2012; **113**: e10-e18 [PMID: 22669152 DOI: 10.1016/j.tripleo.2011.06.034]
12   **Cheung LK**, Leung YY, Chow LK, Wong MC, Chan EK, Fok YH. Incidence of neurosensory deficits and recovery after lower third molar surgery: a prospective clinical study of 4338 cases. *Int J Oral Maxillofac Surg* 2010; **39**: 320-326 [PMID: 20061121 DOI: 10.1016/j.ijom.2009.11.010]
13   **Jerjes W**, Upile T, Shah P, Nhembe F, Gudka D, Kafas P, McCarthy E, Abbas S, Patel S, Hamdoon Z, Abiola J, Vourvachis M, Kalkani M, Al-Khawalde M, Leeson R, Banu B, Rob J, El-Maaytah M, Hopper C. Risk factors associated with injury to the inferior alveolar and lingual nerves following third molar surgery-revisited. *Oral Surg Oral Med Oral Pathol Oral Radiol Endod* 2010; **109**: 335-345 [PMID: 20097103 DOI: 10.1016/j.tripleo.2009.10.010]
14   **Benninger B**, Kloenne J, Horn JL. Clinical anatomy of the

lingual nerve and identification with ultrasonography. *Br J Oral Maxillofac Surg* 2013; **51**: 541-544 [PMID: 23182453 DOI: 10.1016/j.bjoms.2012.10.014]

15   **Frafjord R**, Renton T. A review of coronectomy. *Oral Surg* 2010; **3**: 1-7

16   **Renton T**. Update on coronectomy. A safer way to remove high risk mandibular third molars. *Dent Update* 2013; **40**: 362-364, 362-364 [PMID: 23909229]

17   **Landi L**, Manicone PF, Piccinelli S, Raia A, Raia R. Staged removal of horizontally impacted third molars to reduce risk of inferior alveolar nerve injury. *J Oral Maxillofac Surg* 2010; **68**: 442-446 [PMID: 20116720 DOI: 10.1016/j.joms.2009.07.038]

18   **Landi L**, Manicone PF, Piccinelli S, Raia A, Raia R. A novel surgical approach to impacted mandibular third molars to reduce the risk of paresthesia: a case series. *J Oral Maxillofac Surg* 2010; **68**: 969-974 [PMID: 20156664 DOI: 10.1016/j.joms.2009.09.097]

19   **Park W**, Park JS, Kim YM, Yu HS, Kim KD. Orthodontic extrusion of the lower third molar with an orthodontic mini implant. *Oral Surg Oral Med Oral Pathol Oral Radiol Endod* 2010; **110**: e1-e6 [PMID: 20674416 DOI: 10.1016/j.tripleo.2010.04.031]

20   **Wang Y**, He D, Yang C, Wang B, Qian W. An easy way to apply orthodontic extraction for impacted lower third molar compressing to the inferior alveolar nerve. *J Craniomaxillofac Surg* 2012; **40**: 234-237 [PMID: 21641229 DOI: 10.1016/j.jcms.2011.05.001]

21   **Ma ZG**, Xie QY, Yang C, Xu GZ, Cai XY, Li JY. An orthodontic technique for minimally invasive extraction of impacted lower third molar. *J Oral Maxillofac Surg* 2013; **71**: 1309-1317 [PMID: 23763903 DOI: 10.1016/j.joms.2013.03.025]

22   **Rood JP**, Shehab BA. The radiological prediction of inferior alveolar nerve injury during third molar surgery. *Br J Oral Maxillofac Surg* 1990; **28**: 20-25 [PMID: 2322523]

23   **Blaeser BF**, August MA, Donoff RB, Kaban LB, Dodson TB. Panoramic radiographic risk factors for inferior alveolar nerve injury after third molar extraction. *J Oral Maxillofac Surg* 2003; **61**: 417-421 [PMID: 12684956 DOI: 10.1053/joms.2003.50088]

24   **Kim JW**, Cha IH, Kim SJ, Kim MR. Which risk factors are associated with neurosensory deficits of inferior alveolar nerve after mandibular third molar extraction? *J Oral Maxillofac Surg* 2012; **70**: 2508-2514 [PMID: 22901857 DOI: 10.1016/j.joms.2012.06.004]

25   **Szalma J**, Lempel E, Jeges S, Szabó G, Olasz L. The prognostic value of panoramic radiography of inferior alveolar nerve damage after mandibular third molar removal: retrospective study of 400 cases. *Oral Surg Oral Med Oral Pathol Oral Radiol Endod* 2010; **109**: 294-302 [PMID: 19846324 DOI: 10.1016/j.tripleo.2009.09.023]

26   **Atieh MA**. Diagnostic accuracy of panoramic radiography in determining relationship between inferior alveolar nerve and mandibular third molar. *J Oral Maxillofac Surg* 2010; **68**: 74-82 [PMID: 20006158 DOI: 10.1016/j.joms.2009.04.074]

27   **Umar G**, Bryant C, Obisesan O, Rood JP. Correlation of the radiological predictive factors of inferior alveolar nerve injury with cone beam computed tomography findings. *Oral Surg* 2010; **3**: 72-82 [DOI: 10.1111/j.1752-248X.2010.01088.x]

28   **Shahidi S**, Zamiri B, Bronoosh P. Comparison of panoramic radiography with cone beam CT in predicting the relationship of the mandibular third molar roots to the alveolar canal. *Imaging Sci Dent* 2013; **43**: 105-109 [PMID: 23807934 DOI: 10.5624/isd.2013.43.2.105]

29   **Tantanapornkul W**, Okochi K, Bhakdinaronk A, Ohbayashi N, Kurabayashi T. Correlation of darkening of impacted mandibular third molar root on digital panoramic images with cone beam computed tomography findings. *Dentomaxillofac Radiol* 2009; **38**: 11-16 [PMID: 19114418 DOI: 10.1259/dmfr/83819416]

30   **Szalma J**, Vajta L, Lempel E, Jeges S, Olasz L. Darkening of third molar roots on panoramic radiographs: is it really predominantly thinning of the lingual cortex? *Int J Oral Maxillofac Surg* 2013; **42**: 483-488 [PMID: 22835682 DOI: 10.1016/j.ijom.2012.06.018]

31   **Harada N**, Vasudeva SB, Joshi R, Seki K, Araki K, Matsuda Y, Okano T. Correlation between panoramic radiographic signs and high risk anatomical factors for impacted mandibular third molars. *Oral Surg* 2013; **6**: 129-136 [DOI: 10.1111/ors.12025]

32   **Yamada T**, Ishihama K, Yasuda K, Hasumi-Nakayama Y, Ito K, Yamaoka M, Furusawa K. Inferior alveolar nerve canal and branches detected with dental cone beam computed tomography in lower third molar region. *J Oral Maxillofac Surg* 2011; **69**: 1278-1282 [PMID: 21256640 DOI: 10.1016/j.joms.2010.07.010]

33   **Naitoh M**, Hiraiwa Y, Aimiya H, Gotoh K, Ariji E. Accessory mental foramen assessment using cone-beam computed tomography. *Oral Surg Oral Med Oral Pathol Oral Radiol Endod* 2009; **107**: 289-294 [PMID: 19071039 DOI: 10.1016/j.tripleo.2008.09.010]

34   **Neves FS,** Nascimento MC, Oliveira ML, Almeida SM, Bóscolo FN. Comparative analysis of mandibular anatomical variations between panoramic radiography and cone beam computed tomography. *Oral Maxillofac Surg* 2013 Aug 24; Epub ahead of print [PMID: 23975215]

35   **Williams FL**, Richtsmeier JT. Comparison of mandibular landmarks from computed tomography and 3D digitizer data. *Clin Anat* 2003; **16**: 494-500 [PMID: 14566895 DOI: 10.1002/ca.10095]

36   **Ludlow JB**, Laster WS, See M, Bailey LJ, Hershey HG. Accuracy of measurements of mandibular anatomy in cone beam computed tomography images. *Oral Surg Oral Med Oral Pathol Oral Radiol Endod* 2007; **103**: 534-542 [PMID: 17395068 DOI: 10.1016/j.tripleo.2006.04.008]

37   **Xu GZ**, Yang C, Fan XD, Yu CQ, Cai XY, Wang Y, He D. Anatomic relationship between impacted third mandibular molar and the mandibular canal as the risk factor of inferior alveolar nerve injury. *Br J Oral Maxillofac Surg* 2013; **51**: e215-e219 [PMID: 23411471 DOI: 10.1016/j.bjoms.2013.01.011]

38   **Shiratori K**, Nakamori K, Ueda M, Sonoda T, Dehari H. Assessment of the shape of the inferior alveolar canal as a marker for increased risk of injury to the inferior alveolar nerve at third molar surgery: a prospective study. *J Oral Maxillofac Surg* 2013; **71**: 2012-2019 [PMID: 24045186 DOI: 10.1016/j.joms.2013.07.030]

39   **Susarla SM**, Sidhu HK, Avery LL, Dodson TB. Does computed tomographic assessment of inferior alveolar canal cortical integrity predict nerve exposure during third molar surgery? *J Oral Maxillofac Surg* 2010; **68**: 1296-1303 [PMID: 20356665 DOI: 10.1016/j.joms.2010.01.021]

40   **Tay AB**, Go WS. Effect of exposed inferior alveolar neurovascular bundle during surgical removal of impacted lower third molars. *J Oral Maxillofac Surg* 2004; **62**: 592-600 [PMID: 15122566 DOI: 10.1016/j.joms.2003.08.033]

41   **Nakayama K**, Nonoyama M, Takaki Y, Kagawa T, Yuasa K, Izumi K, Ozeki S, Ikebe T. Assessment of the relationship between impacted mandibular third molars and inferior alveolar nerve with dental 3-dimensional computed tomography. *J Oral Maxillofac Surg* 2009; **67**: 2587-2591 [PMID: 19925976 DOI: 10.1016/j.joms.2009.07.017]

42   **Ueda M**, Nakamori K, Shiratori K, Igarashi T, Sasaki T, Anbo N, Kaneko T, Suzuki N, Dehari H, Sonoda T, Hiratsuka H. Clinical significance of computed tomographic assessment and anatomic features of the inferior alveolar canal as risk factors for injury of the inferior alveolar nerve at third molar surgery. *J Oral Maxillofac Surg* 2012; **70**: 514-520 [PMID: 22079065 DOI: 10.1016/j.joms.2011.08.021]

43   **Nakamori K**, Fujiwara K, Miyazaki A, Tomihara K, Tsuji M, Nakai M, Michifuri Y, Suzuki R, Komai K, Shimanishi M, Hiratsuka H. Clinical assessment of the relationship

between the third molar and the inferior alveolar canal using panoramic images and computed tomography. *J Oral Maxillofac Surg* 2008; **66**: 2308-2313 [PMID: 18940497 DOI: 10.1016/j.joms.2008.06.042]

44   **Selvi F**, Dodson TB, Nattestad A, Robertson K, Tolstunov L. Factors that are associated with injury to the inferior alveolar nerve in high-risk patients after removal of third molars. *Br J Oral Maxillofac Surg* 2013; **51**: 868-873 [PMID: 24012054 DOI: 10.1016/j.bjoms.2013.08.007]

45   **Lübbers HT**, Matthews F, Damerau G, Kruse AL, Obwege-ser JA, Grätz KW, Eyrich GK. Anatomy of impacted lower third molars evaluated by computerized tomography: is there an indication for 3-dimensional imaging? *Oral Surg Oral Med Oral Pathol Oral Radiol Endod* 2011; **111**: 547-550 [PMID: 20952229 DOI: 10.1016/j.tripleo.2010.06.010]

46   **Roeder F**, Wachtlin D, Schulze R. Necessity of 3D visualization for the removal of lower wisdom teeth: required sample size to prove non-inferiority of panoramic radiography compared to CBCT. *Clin Oral Investig* 2012; **16**: 699-706 [PMID: 21519882 DOI: 10.1007/s00784-011-0553-8]

TOPIC HIGHLIGHT

WJR 6ᵗʰ Anniversary Special Issues (8): fMRI

Magnetic resonance cholangiography in the assessment and management of biliary complications after OLT

Rossano Girometti, Lorenzo Cereser, Massimo Bazzocchi, Chiara Zuiani

Rossano Girometti, Lorenzo Cereser, Massimo Bazzocchi, Chiara Zuiani, Institute of Diagnostic Radiology, Department of Medical and Biological Sciences, University of Udine, 33100 Udine, Italy
Author contributions: Girometti R and Cereser L wrote the paper; Girometti R, Cereser L, Bazzocchi M and Zuiani C designed the paper; Cereser L, Bazzocchi M and Zuiani C performed literature research; all the authors selected and supervised the editing of study images and tables
Correspondence to: Rossano Girometti, MD, Research Assistant Professor of Radiology, Institute of Diagnostic Radiology, Department of Medical and Biological Sciences, University of Udine, via Colugna n. 50, 33100 Udine, Italy. rgirometti@sirm.org
Telephone: +39-04-32559266 Fax: +39-04-32559867
Received: January 17, 2014 Revised: March 5, 2014
Accepted: May 28, 2014
Published online: July 28, 2014

Abstract

Despite advances in patient and graft management, biliary complications (BC) still represent a challenge both in the early and delayed period after orthotopic liver transplantation (OLT). Because of unspecific clinical presentation, imaging is often mandatory in order to diagnose BC. Among imaging modalities, magnetic resonance cholangiography (MRC) has gained widespread acceptance as a tool to represent the reconstructed biliary tree noninvasively, using both the conventional technique (based on heavily T2-weighted sequences) and contrast-enhanced MRC (based on the acquisition of T1-weighted sequences after the administration of hepatobiliary contrast agents). On this basis, MRC is generally indicated to: (1) avoid unnecessary procedures of direct cholangiography in patients with a negative examination and/or identify alternative complications; and (2) provide a road map for interventional procedures or surgery. As illustrated in the review, MRC is accurate in the diagnosis of different types of biliary complications, including anastomotic strictures, non-anastomotic strictures, leakage and stones.

© 2014 Baishideng Publishing Group Inc. All rights reserved.

Key words: Orthotopic liver transplantation; Orthotopic liver transplantation complications; Magnetic resonance imaging cholangiopancreatography; Endoscopic retrograde cholangiography; Bile ducts obstruction

Core tip: The review is focused on three main topics, in order to emphasize why magnetic resonance cholangiography (MRC) is the preferred imaging modality to noninvasively assess the biliary system after orthotopic liver transplantation. First, the authors describe the different techniques that can be used, namely conventional MRC and contrast-enhanced MRC. Second, exemplificative imaging findings are illustrated in order to show the diagnostic reliability of the technique. Third, the Authors discuss the state-of-the-art role for MRC in assessing biliary complications as emerging from updated literature review.

Girometti R, Cereser L, Bazzocchi M, Zuiani C. Magnetic resonance cholangiography in the assessment and management of biliary complications after OLT. *World J Radiol* 2014; 6(7): 424-436 Available from: URL: http://www.wjgnet.com/1949-8470/full/v6/i7/424.htm DOI: http://dx.doi.org/10.4329/wjr.v6.i7.424

INTRODUCTION

Despite improvements in organ preservation, surgical technique, immunosuppression and postoperative management, biliary complications (BC) still represent the "Achille's heel" of orthotopic liver transplantation (OLT),
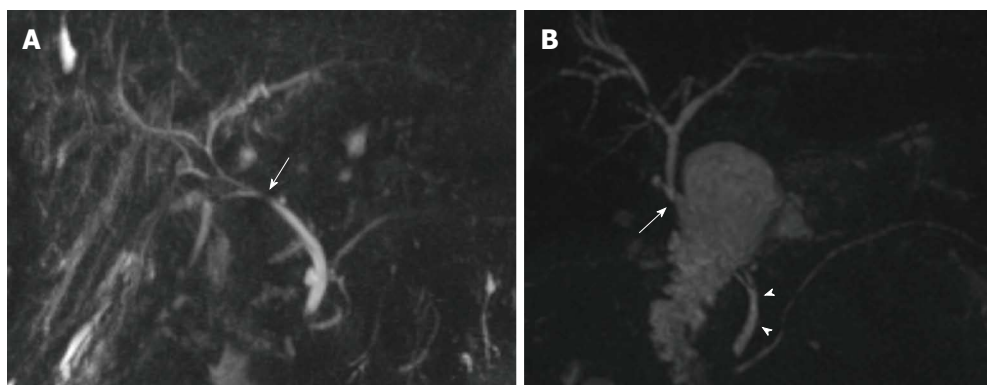
Figure 1 Biliary reconstructions variants after orthotopic liver transplantation illustrated by coronal maximum intensity projection reconstruction from 3D magnetic resonance cholangiography. A: Choledocho-choledochostomy with mild donor-to-recipient discrepancy in ductal calibers giving prominence to the anastomotic site (arrow); B: Bilioenteric anastomosis (arrow) between donor's common bile duct and a jejuneal loop. Note the recipient common bile duct remnant (arrowheads).

occurring in 10%-34% of graft recipients[1,2]. BC are associated with a significant morbidity and mortality rate (2%-7%)[3,4], representing the second leading cause of graft dysfunction and loss after rejection[1]. Prompt recognition or exclusion of BC is crucial in order to address patient to proper treatment. However, differentiating BC from other post-OLT complications can be difficult based solely on clinical presentation and biochemical findings, thus making imaging essential in the diagnostic process[5].

Among different imaging modalities, magnetic resonance cholangiography (MRC) plays a key role in evaluating BC after OLT. Due to the technical advances occurred over the last decades, MRC can be performed on magnetic resonance (MR) systems equipped with highly performing gradients, multichannel phased-array coils and dedicated sequences in order to produce panoramic and detailed representation of the biliary tree without significant motion-related artefacts[2]. Although it is questionable whether MRC can be viewed as the new standard of reference in biliary imaging[6], this technique has gained acceptance as the most reliable alternative to direct cholangiography in depicting the biliary system. In the setting of liver transplant, MRC is useful both in the pre- and post-operative period, e.g. in assessing the biliary anatomy of living donors[7,8]. Moreover, MRC is safe, repeatable and reproducible[7].

In this review, we: (1) describe different technical approaches to MRC; (2) discuss the evidence-based role of MRC in assessing BC after adult OLT; and (3) illustrate imaging findings of main BC. Although split-liver transplantation and LDTL are not directly discussed in this work, the paper statements on the use of MRC can be extended to these variants of transplantation.

CLINICAL OVERVIEW

Classification of biliary complications

BC can be classified according to the clinical phenotype, localization, timing of occurrence and etiology[5]. A useful classification for radiologists is based on the temporary onset from OLT, which is of help in identifying the most probable complication occurring at the time of image interpretation. Complications occurring within 3 mo after OLT are defined as "early", and are typically represented by bile leakage and nonanastomotic strictures (NAS) related to hepatic artery thrombosis (HAT)[5]. "Late" complications occur a few months to several years later, and mainly consist in strictures. Anastomotic strictures (AS) show a tendency to develop earlier (within 4-5 mo) compared to non-HAT related NAS[5,9]. Overall, the large majority of BC (up to 80%) present within 6 mo from OLT[9], with annual incidence less than 4% after the first post-transplant year[10].

The characteristics of main BC are shown in Table 1, including the time of onset and main risk factors. Notably, split-liver transplant and LDLT have been associated with a moderate increase in BC, *e.g.*, because of cut-surface leakage originating both in donors and recipients[11].

Biliary reconstruction

Prior to the examination, type of transplant (*e.g.*, left/right split-liver transplant or living donor liver transplantation) and surgical technique should be evaluated in order to correctly interpret patient anatomy and MRC findings. Nowadays, biliary reconstruction during OLT is performed according to two main options[5] (Figure 1): (1) choledocho-choledochostomy, consisting in an end-to-end anastomosis between donor and recipient choledochal ducts (duct-to-duct technique); and (2) bilioenteric anastomosis, consisting in an end-to-side anastomosis between the donor hepatic duct and a recipient jejuneal loop (Roux-en-Y hepaticojejunostomy). Compared to bilioenteric anastomosis, duct-to-duct anastomosis is technically simpler and preserves the sphincter of Oddi as a barrier against bacterial colonization of the biliary tract[12]. This is why choledocho-choledochostomy is the preferred technique of biliary reconstruction. Bilioenteric anastomosis is usually reserved for cases of primary sclerosing cholangitis (PSC) as the indication to OLT, surgi-

Table 1 Overview of main biliary complications occurring after liver transplantation

Type of complication	Prevalence in adult OLT patients	Risk factors	Time of onset from OLT	Clinical features	Treatment
Bile leak	7.8% OLT 9.5% LDLT	T-tube displacement or removal (T-tube leak) technical failure during surgery (anastomotic leak) HAT (nonanastomotic leak) Ischemic-related injury, immunologically-related injury, cytotoxic injury induced by bile salts (nonanastomotic leak in pts. without HAT)	1-3 mo	Fever, abdominal complaint, signs of cholestasis and or cholangitis	Leaving the T-tube open (T-Tube leaks) ERC with Sphincterotomy and stent placement Percutaneous drainage
Anastomotic stricture	13% OLT 19% LDLT	Older donor age Roux-en-Y choledochojejunostomy Technical factors (earlier manifestation) Ischemia of the donor bile duct (earlier manifestation) Previous anastomotic leakage (late manifestation)	within 6 mo-1 yr, occasionally later	Biliary obstruction	Surgical revision (repair or conversion to bilio-enteric anastomosis) ERC with balloon dilatation and stent placement (usually repeated procedures) Surgical revision (conversion to bilio-enteric anastomosis)
NAS	5%-25%	HAT Microangiopathic injury (prolonged warm or cold ischemia times of the graft) (ITBL) Immunogenic injury (AB0 incompatibility between donor and recipient, chronic ductopenic rejection, primitive sclerosing cholangitis) (ITBL) Cytotoxic injury by bile salts (ITBL)	Within 6 mo (HAT-associated NAS) After 6 mo (ITBL)	Cholestasis with recurrent cholangitis	Biliary toilette, dilatation ± stent placement *via* ERC/PTC Medical therapy (ursodeoxycholic acid and antibiotics if recurrent cholangitis)
Stones, casts and sludge	5.70%	Anastomotic and nonanastomotic biliary strictures Presence of T-tube or stent Hepaticojejunostomy Ischemia Infectious alteration in bile composition	Within 1 yr (casts and sludge) After 1 yr (stones)	Biliary obstruction	Conversion to hepaticojejunostomy (rarely) Retransplantation Bile ducts toilette using ERC/PTC Medical therapy with ursodeoxycholic acid Retransplantation
Sphincter of Oddi dysfunction and papillary stenosis	2%-7%	Denervation of the recipient common bile duct leading to sphincter of Oddi spasm Inflammation and/or scarring of the sphincter of Oddi	6 mo to 1 yr	Increased cholestatic enzymes	Endoscopic sphincterotomy

Data from[5,11]. OLT: Orthotopic liver transplantation; NAS: Nonanastomotic strictures; ITBL: Ischemic-type biliary lesions; HAT: Hepatic artery thrombosis.
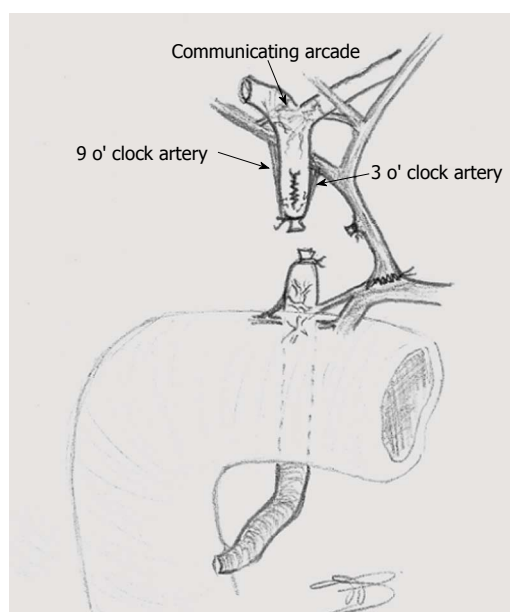
Figure 2 Arterial supply to the biliary tree in liver-transplanted patients.

cal salvage after BC or re-transplantation[12].

The vascular supply of the biliary tract

Contrary to liver parenchyma, the biliary tree is nourished by arterial vessels only, which can be divided in two interconnected systems (Figure 2). The first one supplies the common bile duct and consist of the ascending axial branches originating from the gastroduodenal artery, which run on medial ("3 o'clock") and lateral ("9 o'clock") aspects of the common bile duct and communicate (usually) with the right hepatic artery. The second system is the peribiliary vascular plexus, which supplies the hepatic confluence and intrahepatic bile ducts. It consists of a complex arterial network originating from terminal arterial branches, being supported mainly through a "communicating arcade" running between hilar branches of the hepatic artery, with substantial anatomic variability[5,13].

Although surgical technique is aimed to preserve as much as possible biliary vascularization both in the donor and recipient, surgical sacrifice of arterial branches during

the transplant make the bile ducts sensitive to "disconnection" from the hepatic artery and/or recipient gastroduodenal artery, as occurs during organ preservation or HAT. Hypoperfusion from HAT translates into ischemic cholangitis ("macroangiopathic" injury), with extensive bile epithelium necrosis, intraductal casts formation, bile leakage and evolution to scarring and multiple strictures, typically involving the hepatic confluence and intrahepatic bile ducts[9]. Surgical preservation of adequate perfusion at biliary ends and periductal tissue is also essential in reducing the risk of anastomotic stenosis[5]. Furthermore, hypoperfusion may result from a variety of transplant-related or immunologically-mediated causes (Table 1), causing "microangiopathic" ischemic damage of the peribiliary plexus. Such a damage translates into a macroscopic MRC pattern similar to that of macroangiopathic injury[5], as illustrated below.

Diagnostic approach to biliary complications

Clinical and laboratory diagnosis of BC is challenging, since manifestations such as fever, increase in bilirubin and altered liver function tests significantly overlap with other post-OLT entities, including rejection[9]. Of note, BC may co-exist with different types of complications or being a consequence of HAT, thus making differential diagnosis even more difficult. However, prompt recognition of primary or secondary biliary involvement is mandatory to allow proper treatment.

Ultrasound with color Doppler examination and/or contrast-enhanced ultrasound (CEUS) represent the first-line tool in excluding HAT as the primary source of BC and in assessing fluid collections suspicious for bilomas[14]. Despite the high negative predictive value (NPV) reported by some authors[15], US shows well known limitations in clinical practice, especially in the case of biliary obstruction. US lacks panoramicity and is often impaired by reduced patients' compliance and presence of bowel gas and surgical dressing material. Additionally, the presence of epithelial casts filling the bile ducts in the postoperative period may further limit sonographic visibility[16]. As a consequence, it is difficult to establish the type and the site of the obstructive cause with US. Although biliary dilatation is a reliable indirect sign of biliary obstruction, biliary dilatation develops slowly and disproportionally with regard to the severity of the stricture[17], being undetectable in more than 60% with anastomotic stenosis[18]. In summary, normal US examination should not preclude further investigations in case of clinical suspicion.

According to Zoepf *et al*[16], Computed Tomography (CT) is able to show biliary dilatation in up to 40% and 83% of anastomotic and nonanastomotic strictures, respectively. However, because of limited contrast resolution and relative inability to show the anastomotic site, CT correctly identifies the site of biliary obstruction in 10% of patients only[2,16]. The main role for CT is then to assess HAT[19] and/or detect intra- and extra-hepatic hypoattenuating collections when a suspicious biloma has been raised by US.

The use of T-tube after OLT is still a matter for debate[5]. When available, T-tube cholangiography under fluoroscopic or CT guidance is a rapid and accurate tool to demonstrate the presence of bile leak during the limited period of time in which direct access to bile ducts is present (1-3 mo). According to Singh *et al*[20], T-tube cholangiography should be preferred over MRC because the distension of the bile ducts with contrast medium permits better stricture analysis and functional assessment. Therefore, once the T-tube is removed, alternative imaging methods must be used.

Because of the above limitations of US, CT and T-tube cholangiography, ERC and PTC are still considered the standard of reference in imaging patients with duct-to-duct anastomosis and bilioenteric anastomosis, respectively. The advantage of ERC and PTC is to allow interventional procedures such as sphincterotomy, ballooning or stenting, which are the first-line treatment of biliary obstruction. On the other hand, morbidity and mortality rates associated with direct cholangiography procedures have encouraged the use of MRC as the preferred, panoramic tool to assess BC, limiting ERC and PTC to interventional rather than diagnostic purpose[5,21]. We further discuss the role for ERC/PTC and MRC in the dedicated paragraph below, together with the advantages and disadvantages of these techniques.

Further investigations such as hepatobiliary scintigraphy provided controversial results, gaining no routine use[5]. On the contrary, liver biopsy is frequently necessary to establish final diagnosis underlying graft dysfunction[22], especially if microangiopathic biliary injury is suspected.

MRC TECHNIQUE

The goal of MRC is to provide a panoramic representation of hyperintense biliary tree against a low signal intensity background. Currently, two techniques are used to obtain images with such an elevated contrast, namely conventional MRC (C-MRC) and contrast-enhanced MRC (CE-MRC) (Figure 3). The difference between these techniques relies on the type of sequence, use of *iv* contrast agent, timing of acquisition and clinical indication.

Regardless of the technique, MRC is rarely used as a standing-alone examination. MRI scanning protocols in post-OLT patients should always include non cholangiographic sequences in order to evaluate liver parenchyma and/or extrabiliary manifestations of BC such as bilomas and perihepatic free fluid[2].

Conventional MRC

In C-MRC, image contrast is the result of heavily T2-weighted sequences with a long TE. This emphasizes differences in transverse relaxation times between "slow motion" fluids such as the bile (long T2) and background tissues with intermediate to short T2[21]. In our Institution, we administer oral 1:10 mL water solution of a
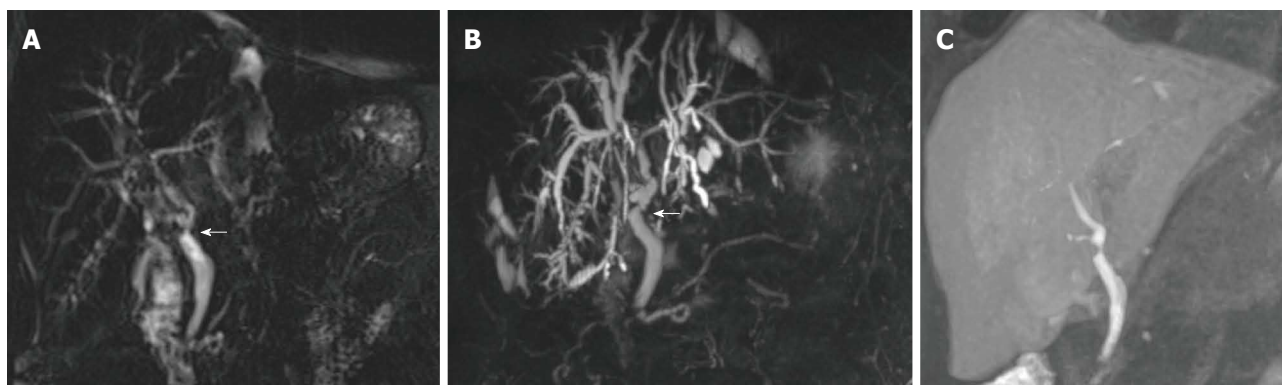
Figure 3 Technical variants of magnetic resonance cholangiography, as shown in coronal images of a 66-year-old male patient transplanted for alcoholic cirrhosis. A: Conventional, T2-weighted 2D MRC; B: MIP reconstruction from conventional, T2-weighted 3D MRC; C: Thick MIP reconstruction from T1-weighted, contrast-enhanced MRC. Both the degree and functional significance of the mild anastomotic stricture indicated by arrows are better showed by contrast passage in (C). MRC: Magnetic resonance cholangiography; MIP: Maximum intensity projection.

gadolinium chelate contrast agent just before the acquisition of MRC in order to suppress overlapping fluid signal from the stomach and/or duodenum with paramagnetic effects on the T2 relaxation time[23]. However, because of the risk to mask the vaterian region of the common bile duct as a possible site of BC, the use of oral negative contrast agent is a matter of expertise and institutional preferences. Based on the inherent high contrast of C-MRC, no *i.v.* administration of gadolinium-based contrast agents is needed, which is of relevance in patients with renal function impairment at risk of developing Nephrogenic Systemic Fibrosis (NSF)[24].

C-MRC can be performed with the 3D and/or 2D approach choosing among a variety of well-established MRC sequences (Figure 3). The 3D technique is usually based on respiratory-triggered or navigator-gated volumetric Turbo/Fast Spin Echo sequences acquired during normal patient respiration, and provides numerous thin slices with higher signal-to-noise ratio and spatial resolution as a base for multiplanar reformations ad maximum intensity projection (MIP) reconstructions[25]. Compared to the 2D variant, 3D C-MRC has the advantage of higher longitudinal spatial resolution, with the capability of achieving isotropic imaging and assessing more subtle anatomic and pathological details, such as small calculi[25]. On the other hand, 3D C-MRC can be significantly affected by motion artifacts in non-collaborating patients. The 2D technique is acquired more rapidly, during few and short breath-holds using thick slices, thus reducing the effects of respiratory artefacts on image quality[26]. Different sequences are currently available to perform 2D C-MRC, including RARE (rapid acquisition with relaxation enhancement), HASTE (half-Fourier acquisition single-shot turbo spic echo) and SS-F/TSE (single-shot fast/turbo spin echo)[26].

To our knowledge, only a few studies by Kinner *et al*[26,27] compared the 2D and 3D techniques in assessing BC after OLT. According to these Authors, overall image quality and accuracy are comparable in patients with biliary obstruction, regardless of the C-MRC sequence.

However, the 3D technique shows slight better diagnostic performance in assessing BC, especially in the case of patients with choledocho-choledochostomy and biliary strictures[27]. Although the use of the 2D or 3D technique depends on institutional preferences, both approaches should be used in the standard examination, in order to exploit the advantages and counterbalance the drawbacks of each technique.

Contrast-enhanced MRC

Over the last years, there has been an increasing interest in the use of CE-MRC in the post-surgical assessment of the biliary tree[28]. This technique is based on *i.v.* administration of hepatospecific contrast agents such as gadoxetic acid (Gd-EOB-DTPA), gadobenate dimeglumine (Gd-BOPTA)[29] or mangafodipir trisodium[30], that are excreted into the bile after hepatocellular uptake, thus complementing morphological C-MRC with information on the bile flow. In our experience, the most suitable contrast agent in this setting is gadoxetic acid, because of larger hepatocellular uptake (50% of the administered dose) and the relatively short time to achieve the hepatobiliary phase, *i.e.*, 10 to 20 min after contrast administration in patients with preserved liver function[31]. As T2-shortening effects might mask the biliary tree on T2-weighted images, it is mandatory to perform CE-MRC after C-MRC, using a volumetric, high-resolution T1-weighted 3D fat-satured sequence)[31]. The use of larger flip angles (*e.g.*, 35°) is recommended in order to increase the conspicuity of the biliary tree over the background[32].

Despite the increasing use of CE-MRC, there is a paucity of literature-based evidence in the setting of OLT, mainly focused on the preoperative evaluation of liver donors[33,34]. However, studies on patients with BC after hepatobiliary surgery, including OLT subjects, suggest that CE-MRC improves the accuracy of C-MRC in evaluating bile leakage showing the site of the leak and direct contrast extravasation into perihepatic/peribiliary fluid collections[35]. Moreover, CE-MRC is indicated to "functionally" assess the degree of biliary obstruction
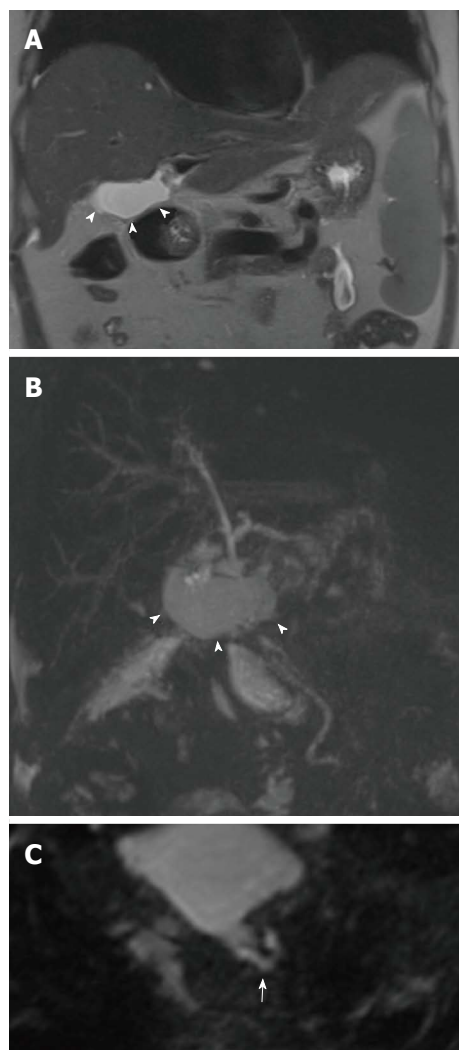
Figure 4 Bile leakage in a 54-year-old male subject transplanted for hepatitis C virus-related cirrhosis. Perihilar biloma shown by arrowheads on coronal T2-weighted HASTE image (A) and paracoronal MIP reconstruction from 3D MRC (B). Thin communication between the anastomotic site and fluid collection is visible on the axially-reformatted 3D source image (arrow in C). MRC: Magnetic resonance cholangiography; MIP: Maximum intensity projection.

according to the presence or absence of the contrast medium downstream in the bile duct (Figure 3). This is of importance in patients with bilioenteric anastomosis, since the diagnosis of anastomotic stricture can be difficult even in the presence of biliary dilatation[31]. In our experience, the degree of contrast flow is helpful (1) in the distinction between "normal" scarring of the anastomotic site and obstructive anastomotic stenosis in patients with choledocho-coledochostomy; or (2) in the assessment of diffuse bile ducts damage in the case of bile casts syndrome.

Hepatocellular uptake of gadoxetic acid is mediated by the same anionic transporter of bilirubin. As a consequence, biliary excretion of gadoxetic acid is limited or delayed by impaired liver function[35]. Although impaired biliary excretion can be used as an indirect sign of biliary obstruction[31,35], this translates into reduced visualization of the bile ducts or the need to perform delayed image acquisitions up to 90-180 min after contrast administra-

tion[31]. In our opinion, the costs inherent to contrast agents imply that CE-MRC should be used to complement C-MRC when "functional" information is needed, after careful evaluation of patients liver function. In our Institution, we avoid CE-MRC when bilirubin level is higher than 5 mg/dL.

MRC FINDINGS

Normal findings after OLT

Normal post-OLT Imaging findings mirror some "physiologic" effects of the surgical procedure. Not surprisingly, then, it is frequent to observe small amounts of free fluid or small fluid collections in the perihepatic region, intersegmental fissure and subhepatic space, as well as along the resection margin after split liver-OLT and LDLT[56]. Clinical and biochemical correlation is helpful in order not to misinterpret these findings as bilomas. Collections tend to resolve spontaneously after few weeks from the intervention[20].

Mild anastomotic narrowing with minimal concentric wall thickening of the common bile duct is a frequent MRC finding[2] that should be interpreted as normal, unless biliary dilatation upstream and symptoms of biliary origin are present[37]. In most cases, anastomotic narrowing is the effect of surrounding edema, resolving during the first weeks after OLT[11]. In our experience, narrowing or kinking of the common bile duct at the anastomotic site are common findings, especially in the case of redundancy or disproportion between the donor and recipient common bile ducts[3]. These conditions are useful in identifying the site of anastomosis in the case of choledochocholedochostomy, and should not be assessed as a complication unless biliary obstruction is associated (Figure 1).

Bile leakage

Leakage represents the most common early biliary complication. In up to 80% of patients with leakage[9], leaks manifest at the insertion of the T-tube, usually as a consequence of dislocation or after the removal of the device[38]. Other sites include: (1) the biliary anastomosis or cystic duct remnant, as an effect of technical failure[11]; (2) the cut-surface after split-liver OLT or LDLT, possibly in relation to patent or aberrant bile ducts and necrosis of liver tissue[5]; and (3) wherever along the biliary tree (intrahepatic and/or extrahepatic bile leakage) because of bile ducts ischemia after HAT (see above).

On T2-weighted C-MRC, biliary leakage manifests indirectly as bilomas, *i.e.*, a well-delineated fluid collections lying in the perihilar or subhepatic space, as well as along the resection margin in LDLT or split-liver OLT. A variable amount of free bile can be associated around the perihepatic space or intersegmental fissure. These findings can be indistinguishable from normal postoperative free fluid or collections. Bilomas can be suspected when a thin, hyperintense direct communication between a fluid collection and the T-tube entry site and/or biliary anastomosis is shown[11] (Figure 4). When leakage is suspected, CE-MRC is an effective complement to C-MRC
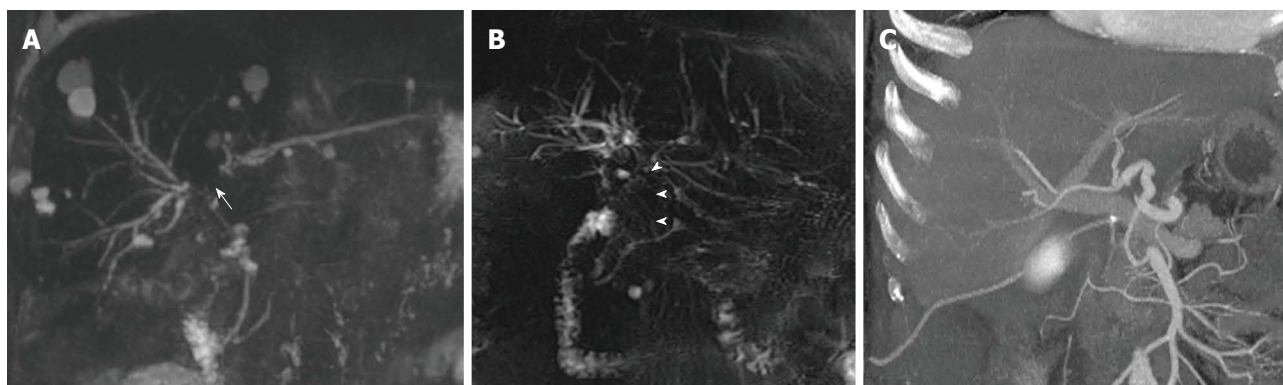
Figure 5 Nonanastomotic strictures in two different transplanted patients. A: MIP reconstruction shows early effects of HAT in a 58-year-old subject with hepatitis B virus infection, consisting in a stricture of the hepatic confluence (arrow) and multiple intrahepatic bilomas; B: ITBL in a 68 male patient transplanted for alcoholic cirrhosis. 2D MRC image shows a stricture of the hepatic confluence extended to the donor common hepatic duct (arrowheads); C: CT angiography found patent hepatic artery in this patient. MRC: Magnetic resonance cholangiography; MIP: Maximum intensity projection; ITBL: Ischemic-type biliary lesions.

in order to demonstrate both the site of contrast extravasation and contrast transit into the biloma or free fluid, with sensitivity for combined C-MRC and CE-MRC of 84%[35]. Confirmation of diagnosis is usually obtained during therapeutic ERC.

Strictures

Strictures can be classified into anastomotic strictures (AS) or nonanastomotic strictures (NAS) according to the site of manifestation, which reflects different pathological mechanisms of origin (Table 1). NAS are further differentiated into forms associated with HAT (macroangiopathic damage) and forms occurring during later from OLT, in the presence of patent hepatic artery (microangiopathic damage). Non-HAT associated NAS are overall categorized as Ischemic-type biliary lesions (ITBL)[5,9,11].

Anastomotic strictures

In patients with choledocho-choledochostomy, luminal narrowing manifests as a focal tract of decreased or absent bile signal intensity of the reconstructed common bile duct, lying between donor and recipient remnants of the cystic duct. A variable degree of common bile duct angulation can be associated[11]. AS can be classified as mild, moderate or severe. Of note, MIP reconstructions from 3D C-MRC tend to overestimate the degree of luminal narrowing compared to ERC[39,40]. Consequently, 3D source data and/or 2D MRC should always be evaluated when assessing strictures, although functional effects on the bile flow are easily inferred by the degree (1) of the associated suprastenotic biliary dilatation; and (2) contrast passage downward when using CE-MRC.

In the case of bilioenteric AS, luminal narrowing appears as a focal absence of biliary signal in the segment immediately above the jejuneal loop, corresponding to low-signal thickening of the common bile duct on axial or axially-reformatted 3D images[2,41]. However, the accuracy of C-MRC in evaluating AS is lower in patients with bilioenteric anastomoses compared to those with choledocho-choledochostomy, regardless of the use of 2D

or 3D technique[27]. This difference has been explained by the difficulty in correctly identifying the anastomotic site, which is partially masked by the hyperintense fluid content of the anastomotic bowel tract. Furthermore, mild duct dilatation is frequently present in patients with patent bilioenteric anastomosis due to physiological changes in caliber as the bile duct enters the bowel wall[26] or temporary folding of the anastomotic site caused by the anastomotic loop motility[41]. CE-MRC with delayed imaging has the potential to clearly define the presence of biliary obstruction, thus avoiding false-positive results. Based on the degree of contrast transit at 30 min from contrast injection, the degree of bile duct obstruction can be classified as[31]: (1) complete (absence of contrast filling in the proximal part of the stricture); (2) near-complete (significantly delayed contrast agent filling only in the proximal part of the stricture); and (3) partial (passage of contrast agent beyond the stricture).

Nonanastomotic strictures

Regardless of the timing of onset and different pathogenic mechanism (Table 1), NAS related to HAT and ITBL manifest with a similar pattern of extensive biliary injury, consisting in irregularly marginated bile ducts with multiple focal stenoses typically involving the hepatic confluence (with the hepatic duct) and/or intrahepatic bile ducts (Figure 5). Bile ducts segments above or between strictures show a variable degree of biliary dilatation upstream[11]. The involvement of intrahepatic ducts equal or larger than the second-order should be clearly identified, because this findings is associated with worst response to therapy[42]. The involvement of small peripheral ducts (third-order or larger) is typical of microangiopathic forms of NAS, frequently evolving to ducts rarefaction over time[5]. Potential disadvantages of MRC are the difficulty in establishing the degree and length of dominant strictures[43], as well as the identification of subtle alterations of peripheral bile ducts[27]. Additionally findings of NAS include (Figure 6): (1) intrahepatic or extrahepatic bilomas in HAT-related forms, as a conse-
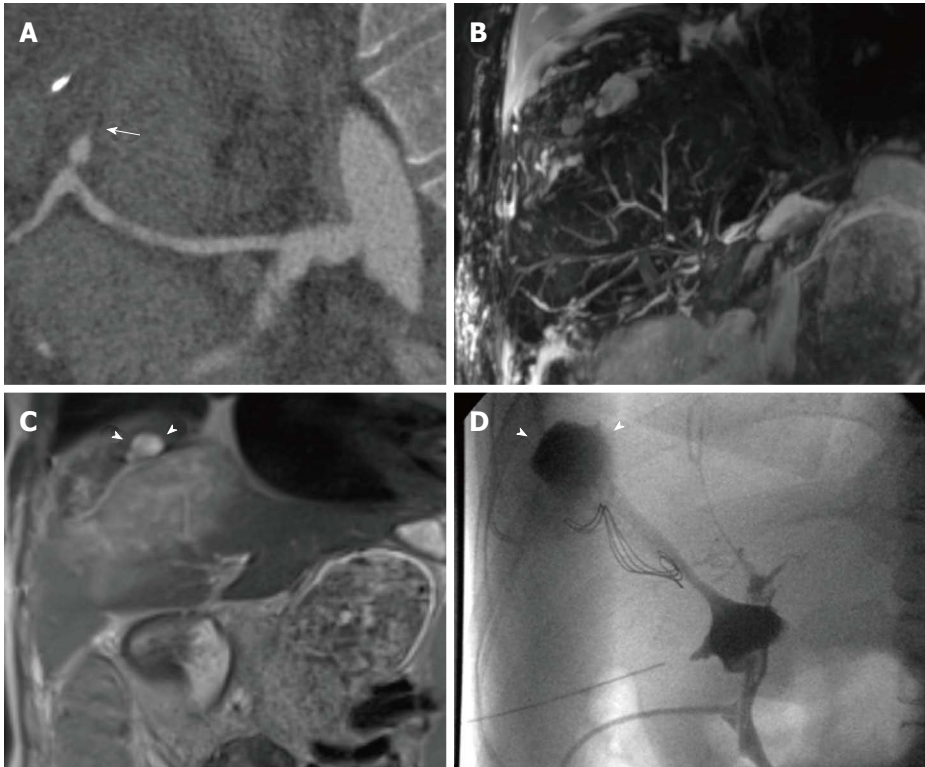
Figure 6 Multiple findings in a 28-year-old female patient transplanted for primary sclerosing cholangitis. Because of the hepatic artery thrombosis shown on curved-reformatted CT image (arrow in A), the biliary tree appears as fragmented and anatomically ill-defined on a panoramic maximum intensity projection view (B). Coronal T2-weighted HASTE image (C) shows extensive, hyperintense ischemic damage of liver parenchyma, together with intrahepatic fluid collections (arrowheads) confirmed to be the effect of bile leakage on T-tube cholangiography (arrowheads in D).

quence of the necrosis of bile duct walls[11]; (2) ischemic damage of liver parenchyma; and (3) casts and sludge filling bile ducts, originated by the aggregation between bile products and desquamated epithelial cells[5].

Recurrent PSC and biliary involvement secondary to chronic rejection may mimic NAS. In particular, chronic rejection has been associated with diffuse "vanishing bile duct" appearance involving more peripheral intrahepatic branches, thus showing some aspects in common with late NAS[11]. Timing of presentation, clinical history and results of liver biopsy are helpful in performing differential diagnosis.

Other complications
Sludge, casts and stones: Sludge, casts and stones are usually a concomitant manifestation of AS and NAS, showing a common appearance of an intense filling defects surrounded by a thin rim of bile signal. Typical locations include larger intrahepatic ducts[2] or the common bile duct immediately above a stricture. Usually, stones form later than sludge and casts, showing more rounded shape and smooth margins (Figure 7)[11]. Casts can be extensively distributed along biliary branches, obscuring the visibility of the hyperintense bile on C-MRC images. The only indirect sign of casts can be intermediate signal on T1- and T2-weighted noncholangiographic images with portal distribution, with periportal enhancement on postcontrast images due inflammation of the peribili-

ary space[44]. Notably, cast can accumulate extensively in the so-called "biliary-cast syndrome" (BCS), in which hardened, lithogenic material occupies the biliary ductal system shaping on the bile ducts, regardless of ischemic injury[45]. Since diagnosis of BCS and smaller filling defects is challenging on C-MRC, the use of CE-MRC has been advocated as a useful tool to improve diagnostic accuracy[46].

Differential diagnosis with stones, sludge and casts mainly includes aerobilia. Aerobilia is frequent after ERC or in patients with bilioenteric anastomosis. Air bubbles usually form an air-fluid level on axial images[11] (Figure 8) and can be associated with characteristic magnetic susceptibility artefact on noncholangiographic images obtained with GRE T1-weighted or Diffusion-weighted sequences (Figure 9).

Sphincter of Oddi dysfunction and papillary stricture: Distal obstruction of the common bile ducts usually translates into significant biliary dilatation of the recipient portion of the extrahepatic bile duct, although dilatation can rarely extends to intrahepatic bile ducts. In our experience, serial acquisition of "cinematic" 2D MRC images are useful in establishing the diagnosis, showing persistent lack of visualization of the vaterian sphincter tract of the common bile duct, suggesting spasm or stenosis (Figure 10). Final diagnosis is usually obtained with ERC or manometry of the sphincter of Oddi[11].
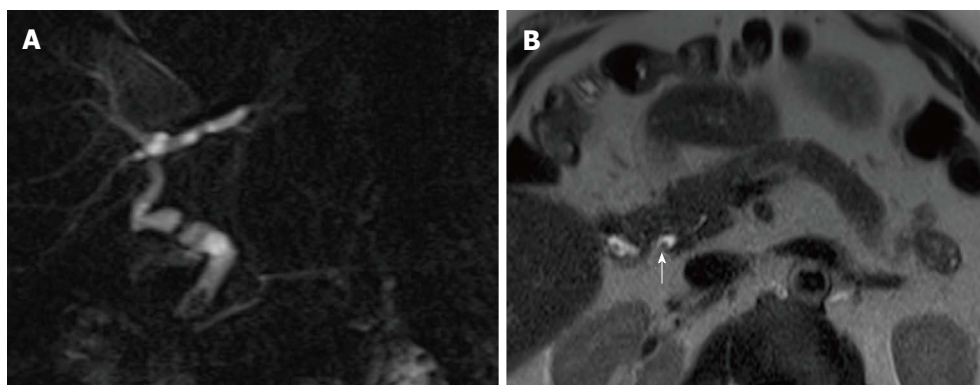
Figure 7 Calculi in a 62-year-old male subject who underwent orthotopic liver transplantation for hepatitis C virus-infection and hepatocellular carcinoma. A: The patient shows chronic kinking and moderate anastomotic stricture without biliary obstruction; B: Filling defect visible in the distal common bile duct were confirmed on axial HASTE image (arrow) and proven to be small calculi on ERC.
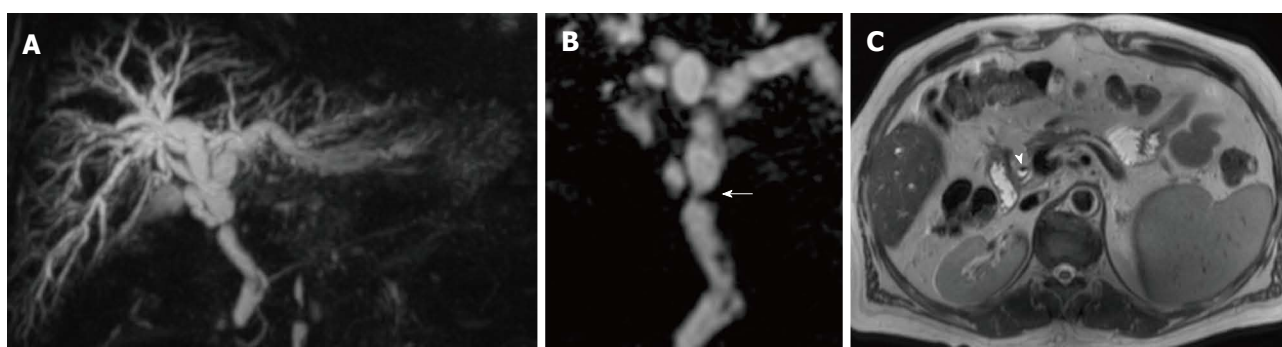
Figure 8 Anastomotic stricture in a 54-year-old male patient who underwent orthotopic liver transplantation for alcoholic cirrhosis. A: Coronal MIP reconstruction shows the stricture at the middle third of the extrahepatic bile duct, with biliary dilatation upstream; B: The degree of the stricture is better delineated on the paracoronally-reformatted thin 3D image (arrow); C: Filling defects visible on MRC images correspond to pneumobilia, appearing as air-fluid levels (arrowhead) on the axial T2-weighted HASTE sequence. MRC: Magnetic resonance cholangiography; MIP: Maximum intensity projection.
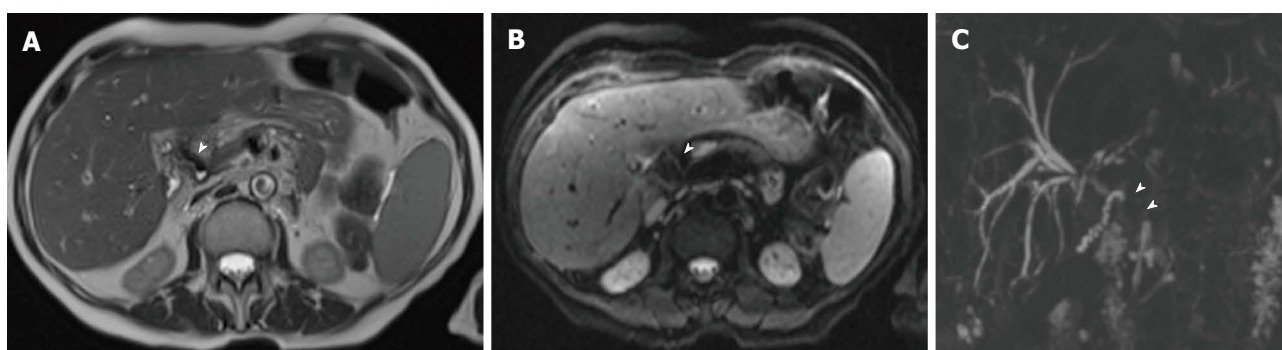
Figure 9 Aerobilia in a 62-year-old female patient transplanted for alcoholic cirrhosis. Anintense filling defect in the common bile duct on T2-weighted axial HASTE image (arrowhead in A) is associated to distortion artifact on axial Diffusion-weighted sequence (arrowhead in B). The effect of pneumobilia was to extensively mask the common bile duct on 3D magnetic resonance cholangiography (arrowheads in C).

ROLE FOR MRC IN PATIENT'S MANAGEMENT

ERC still represents the standard of reference for biliary obstruction complicating OLT[1]. One might conclude that patients with suspicious BC should undergo ERC after preliminary US and/or CT evaluation. On the other hand, ERC is associated with a significant risk of pancreatitis, bleeding, infection, perforation and sedation-related complications, with morbidity and mortality rates of 10% and 0.5%, respectively[1]. The risk of complications is even higher when using PTC. Thus, the risk profile for diagnostic procedures of direct cholangiography seems not justifiable given the high diagnostic accuracy of MRC, which shows 97% sensitivity and 98% specificity for biliary obstruction according to a recent metanalysis[47]. Unfortunately, there is a relative paucity of studies[3,21,43,48-53] investigating the role for MRC in the specific setting of
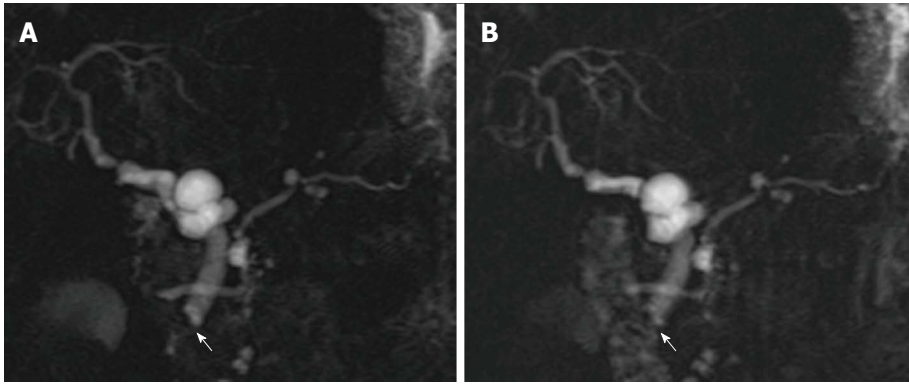
Figure 10 Sphincter of Oddi dysfunction in a liver-transplanted female patient with cholestasis and abdominal complaint years after orthotopic liver transplantation. Serial 2D cinematic magnetic resonance cholangiography images (A) and (B) acquired after few seconds show redundancy of the reconstructed common bile duct, which appear slightly dilated in the recipient tract, and persistent lack of visualization of the vaterian sphincter complex, with typical "meniscus sign" (arrow) suggesting spasm.

Table 2 Results of previous systematic reviews on the role for magnetic resonance cholangiography in assessing biliary complications after orthotopic liver transplantation

Goal	Jorgensen *et al*[1] Biliary obstruction	Xu *et al*[55] All biliary complications	Subset of strictures
Pooled sensitivity	96.0% (0.92%-0.98%)	0.95% (0.92%-0.97%)	0.94% (0.88%-0.98%)
Pooled specificity	0.94% (0.90%-0.97%)	0.92% (0.89%-0.94%)	0.95% (0.88%-0.99%)
AUC	0.99	0.97	0.97
Pooled PLR	17.00 (9.4-29.6)	10.23 (6.21-16.84)	9.96 (2.52-39.36)
Pooled NLR	0.04 (0.02-0.08)	0.08 (0.06-0.12)	0.09 (0.04-0.17)

Number between parentheses represent the 95%CI. Analysis by Xu *et al* is stratified for the whole of complications and the subset of strictures. AUC: Area under the curve at Summary Receiving Operating Characteristic (SROC) curve; PLR: Positive likelihood ratio; NLR: Negative likelihood ratio.

post-OLT BC, leading to difficulties in generalizing results from general population to transplant recipients[1]. For instance, some authors[47] have hypothesized that reduced biliary dilatation following post-OLT strictures might limit the accuracy of MRC. Detractors of MRC also argue that, although MRC correlates well with direct cholangiography procedures ($P = 0.01$)[54], the examination delays the diagnosis when interventional ERC or PTC are finally needed. This is why the use of MRC still depends on local preferences based on availability, expertise and costs.

Based on the above premises, one might ask which evidence-based task can be reasonably attributed to MRC in patients management. Table 2 shows the results of the two systematic reviews[1,55] focusing on this topic. Interestingly, Jorgensen *et al*[1] provide indirect information on the role for MRC by hypothesizing clinical scenarios with pre-test probability of BC of 25% and 50%, respectively. In the case of positive MRC, the post-test probability of BC reaches 80% and 94%, respectively, whereas in the case of negative MRC, the post-test probability reduces to 1% and 4%, respectively. These estimates emphasize

the results of previous direct comparison between MRC, ERC and PTC[54], suggesting that the strength of MRC is represented by the large negative predictive value (94.4%), which is of help in excluding BC and avoiding unnecessary invasive procedures in patients with clinical low-to-moderate risk of BC[54]. Unfortunately, several methodological flaws affect the studies included in the above systematic reviews, including small sample size, uncertainty in clinical criteria defining the suspicion for BC, verification bias given the heterogeneity in the standard of reference tools and absence of a standardized MRC technique[1,55]. This is why the increasing (and reasonable) practice of using MRC as a screening tool for BC should be more adequately supported by: (1) prospective, large studies performed on patients initially assessed as having low-to-moderate risk for BC; (2) studies of cost-effectiveness on the systematic use of MRC in this category of patients.

On the other hand, it should be emphasized that a positive MRC examination cannot be simply considered as a cause of diagnostic delay. Differently from ERC and PTC, C-MRC depicts the bile ducts: (1) in their normal state, rather than artificially dilated by contrast injection pressure; and (2) below and above obstruction sites[54], thus making visible the whole biliary tract, regardless of impaired contrast passage. CE-MRC can complement this panoramic information as illustrated above. As a consequence, a positive MRC examination provides a road-map useful to plan better interventional or surgical approach, thus potentially contributing to reduce morbidity related to invasive procedures.

CONCLUSION

MRC has gained widespread acceptance as a tool to panoramically and reliably represent the biliary tree in post-OLT patients with suspected BC. Conventional technique, based on 2D or 3D heavily T2-weighted sequences, can be now complemented by CE-MRC using hepatospecific contrast agents, thus adding functional information to the morphological depiction of bile ducts.

Although a consensus on the best study protocol is still lacking, a combination of the available technique is reasonably the best choice to enhance the diagnostic capabilities of MRC.

Because of the inherent high contrast of bile ducts, MRC has the capability to reliably identify most relevant BC, including bile leakage, AS, NAS and a variety of further disorders including calculi or sphincter of Oddi dysfunction. However, concerns still exist regarding the cost-effectiveness of this imaging modality in the everyday clinical practice, since positive MRC examinations often lead to ERC and PTC, which are still considered as the standard of reference for final diagnosis. A review of the literature suggests that, despite the absence of large multicentric trials on proper target populations, the high negative predictive of MRC is of value in excluding BC in patients with low-to-moderate risk, thus avoiding unnecessary invasive procedures. On the other hand, positive MRC provides a detailed road-map for interventional procedures or surgery, thus further contributing to reduce morbidity.

In summary, MRC is gaining an increasing role in the diagnosis and management of BC after OLT, and should be performed confidently in patients with low-to-intermediate risk of disease.

ACKNOWLEDGMENTS

REFERENCES

1   **Jorgensen JE**, Waljee AK, Volk ML, Sonnenday CJ, Elta GH, Al-Hawary MM, Singal AG, Taylor JR, Elmunzer BJ. Is MRCP equivalent to ERCP for diagnosing biliary obstruction in orthotopic liver transplant recipients? A meta-analysis. *Gastrointest Endosc* 2011; **73**: 955-962 [PMID: 21316670 DOI: 10.1016/j.gie.2010.12.014]

2   **Pecchi A**, De Santis M, Di Benedetto F, Gibertini M, Gerunda G, Torricelli P. Role of magnetic resonance cholangiography in biliary complications of orthotopic liver transplantation. *Radiol Med* 2010; **115**: 1065-1079 [PMID: 20680501 DOI: 10.1007/s11547-010-0563-7]

3   **Valls C**, Alba E, Cruz M, Figueras J, Andía E, Sanchez A, Lladó L, Serrano T. Biliary complications after liver transplantation: diagnosis with MR cholangiopancreatography. *AJR Am J Roentgenol* 2005; **184**: 812-820 [PMID: 15728602 DOI: 10.2214/ajr.184.3.01840812]

4   **Boraschi P**, Donati F. Complications of orthotopic liver transplantation: imaging findings. *Abdom Imaging* 2004; **29**: 189-202 [PMID: 15290945]

5   **Seehofer D**, Eurich D, Veltzke-Schlieker W, Neuhaus P. Biliary complications after liver transplantation: old problems and new challenges. *Am J Transplant* 2013; **13**: 253-265 [PMID: 23331505 DOI: 10.1111/ajt.12034]

6   **Shanmugam V**, Beattie GC, Yule SR, Reid W, Loudon MA. Is magnetic resonance cholangiopancreatography the new gold standard in biliary imaging? *Br J Radiol* 2005; **78**: 888-893 [PMID: 16177010 DOI: 10.1259/bjr/51075444]

7   **Sirvanci M**, Duran C, Ozturk E, Balci D, Dayangaç M, Onat L, Yüzer Y, Tokat Y, Killi R. The value of magnetic resonance cholangiography in the preoperative assessment of

8   **An SK**, Lee JM, Suh KS, Lee NJ, Kim SH, Kim YJ, Han JK, Choi BI. Gadobenate dimeglumine-enhanced liver MRI as the sole preoperative imaging technique: a prospective study of living liver donors. *AJR Am J Roentgenol* 2006; **187**: 1223-1233 [PMID: 17056909 DOI: 10.2214/AJR.05.0584]

9   **Verdonk RC**, Buis CI, Porte RJ, Haagsma EB. Biliary complications after liver transplantation: a review. *Scand J Gastroenterol Suppl* 2006; **(243)**: 89-101 [PMID: 16782628]

10   **Brown RS**, Russo MW, Lai M, Shiffman ML, Richardson MC, Everhart JE, Hoofnagle JH. A survey of liver transplantation from living adult donors in the United States. *N Engl J Med* 2003; **348**: 818-825 [PMID: 12606737 DOI: 10.1056/NEJMsa021345]

11   **Girometti R**, Cereser L, Como G, Zuiani C, Bazzocchi M. Biliary complications after orthotopic liver transplantation: MRCP findings. *Abdom Imaging* 2008; **33**: 542-554 [PMID: 17851711 DOI: 10.1007/s00261-007-9316-z]

12   **García-Criado A**, Gilabert R, Bargalló X, Brú C. Radiology in liver transplantation. *Semin Ultrasound CT MR* 2002; **23**: 114-129 [PMID: 11866218]

13   **Gunji H**, Cho A, Tohma T, Okazumi S, Makino H, Shuto K, Mochizuki R, Matsubara K, Hayano K, Mori C, Murakami G, Ochiai T. The blood supply of the hilar bile duct and its relationship to the communicating arcade located between the right and left hepatic arteries. *Am J Surg* 2006; **192**: 276-280 [PMID: 16920417 DOI: 10.1016/j.amjsurg.2006.01.046]

14   **Claudon M**, Dietrich CF, Choi BI, Cosgrove DO, Kudo M, Nolsøe CP, Piscaglia F, Wilson SR, Barr RG, Chammas MC, Chaubal NG, Chen MH, Clevert DA, Correas JM, Ding H, Forsberg F, Fowlkes JB, Gibson RN, Goldberg BB, Lassau N, Leen EL, Mattrey RF, Moriyasu F, Solbiati L, Weskott HP, Xu HX. Guidelines and good clinical practice recommendations for Contrast Enhanced Ultrasound (CEUS) in the liver - update 2012: A WFUMB-EFSUMB initiative in cooperation with representatives of AFSUMB, AIUM, ASUM, FLAUS and ICUS. *Ultrasound Med Biol* 2013; **39**: 187-210 [PMID: 23137926]

15   **Hussaini SH**, Sheridan MB, Davies M. The predictive value of transabdominal ultrasonography in the diagnosis of biliary tract complications after orthotopic liver transplantation. *Gut* 1999; **45**: 900-903 [PMID: 10562590 DOI: 10.1136/gut.45.6.900]

16   **Zoepf T**, Maldonado-Lopez EJ, Hilgard P, Dechêne A, Malago M, Broelsch CE, Schlaak J, Gerken G. Diagnosis of biliary strictures after liver transplantation: which is the best tool? *World J Gastroenterol* 2005; **11**: 2945-2948 [PMID: 15902733]

17   **Girometti R**, Molinari C, Del Pin M, Toniutto P, Bitetto D, Como G, Zuiani C, Bazzocchi M. Degree of bile-duct dilatation in liver-transplanted patients with biliary stricture: a magnetic resonance cholangiography-based study. *Radiol Med* 2012; **117**: 1097-1111 [PMID: 22438111 DOI: 10.1007/s11547-012-0805-1]

18   **Zemel G**, Zajko AB, Skolnick ML, Bron KM, Campbell WL. The role of sonography and transhepatic cholangiography in the diagnosis of biliary complications after liver transplantation. *AJR Am J Roentgenol* 1988; **151**: 943-946 [PMID: 3051961 DOI: 10.2214/ajr.151.5.943]

19   **Katyal S**, Oliver JH, Buck DG, Federle MP. Detection of vascular complications after liver transplantation: early experience in multislice CT angiography with volume rendering. *AJR Am J Roentgenol* 2000; **175**: 1735-1739 [PMID: 11090412 DOI: 10.2214/ajr.175.6.1751735]

20   **Singh AK**, Nachiappan AC, Verma HA, Uppot RN, Blake MA, Saini S, Boland GW. Postoperative imaging in liver transplantation: what radiologists should know. *Radiographics* 2010; **30**: 339-351 [PMID: 20228321 DOI: 10.1148/rg.302095124]

21   **Fulcher AS**, Turner MA. Orthotopic liver transplantation:

evaluation with MR cholangiography. *Radiology* 1999; **211**: 715-722 [PMID: 10352596]

22 **Desai M**, Neuberger J. Chronic liver allograft dysfunction. *Transplant Proc* 2009; **41**: 773-776 [PMID: 19328977 DOI: 10.1016/j.transproceed.2009.01.038]

23 **Chan JH**, Tsui EY, Yuen MK, Szeto ML, Luk SH, Wong KP, Wong NO. Gadopentetate dimeglumine as an oral negative gastrointestinal contrast agent for MRCP. *Abdom Imaging* 2000; **25**: 405-408 [PMID: 10926195]

24 **Chow DS**, Bahrami S, Raman SS, Rotchel S, Sayre JW, Busuttil RW, Lu DS. Risk of nephrogenic systemic fibrosis in liver transplantation patients. *AJR Am J Roentgenol* 2011; **197**: 658-662 [PMID: 21862808 DOI: 10.2214/AJR.10.5976]

25 **Nandalur KR**, Hussain HK, Weadock WJ, Wamsteker EJ, Johnson TD, Khan AS, D'Amico AR, Ford MK, Nandalur SR, Chenevert TL. Possible biliary disease: diagnostic performance of high-spatial-resolution isotropic 3D T2-weighted MRCP. *Radiology* 2008; **249**: 883-890 [PMID: 18941164 DOI: 10.1148/radiol.2493080389]

26 **Kinner S**, Dechêne A, Ladd SC, Zöpf T, de Dechêne EM, Gerken G, Lauenstein TC. Comparison of different MRCP techniques for the depiction of biliary complications after liver transplantation. *Eur Radiol* 2010; **20**: 1749-1756 [PMID: 20157816 DOI: 10.1007/s00330-010-1714-x]

27 **Kinner S**, Dechêne A, Paul A, Umutlu L, Ladd SC, de Dechêne EM, Zöpf T, Gerken G, Lauenstein TC. Detection of biliary stenoses in patients after liver transplantation: is there a different diagnostic accuracy of MRCP depending on the type of biliary anastomosis? *Eur J Radiol* 2011; **80**: e20-e28 [PMID: 20580506 DOI: 10.1016/j.ejrad.2010.06.003]

28 **Salvolini L**, Urbinati C, Valeri G, Ferrara C, Giovagnoni A. Contrast-enhanced MR cholangiography (MRCP) with GD-EOB-DTPA in evaluating biliary complications after surgery. *Radiol Med* 2012; **117**: 354-368 [PMID: 22020424 DOI: 10.1007/s11547-011-0731-4]

29 **Ergen FB**, Akata D, Sarikaya B, Kerimoglu U, Hayran M, Akhan O, Hussain HK. Visualization of the biliary tract using gadobenate dimeglumine: preliminary findings. *J Comput Assist Tomogr* 2008; **32**: 54-60 [PMID: 18303288 DOI: 10.1097/RCT.0b013e3180616b87]

30 **Fayad LM**, Holland GA, Bergin D, Iqbal N, Parker L, Curcillo PG, Kowalski TE, Park P, Intenzo C, Mitchell DG. Functional magnetic resonance cholangiography (fMRC) of the gallbladder and biliary tree with contrast-enhanced magnetic resonance cholangiography. *J Magn Reson Imaging* 2003; **18**: 449-460 [PMID: 14508782 DOI: 10.1002/jmri.10369]

31 **Boraschi P**, Donati F. Biliary-enteric anastomoses: spectrum of findings on Gd-EOB-DTPA-enhanced MR cholangiography. *Abdom Imaging* 2013; **38**: 1351-1359 [PMID: 23820693 DOI: 10.1007/s00261-013-0007-7]

32 **Stelter L**, Grieser C, Fernándes CM, Rothe JH, Streitparth F, Seehofer D, Hamm B, Denecke T. Flip angle modulations in late phase Gd-EOB-DTPA MRI improve the identification of the biliary system. *Eur J Radiol* 2012; **81**: e991-e995 [PMID: 22884706 DOI: 10.1016/j.ejrad.2012.07.015]

33 **Mangold S**, Bretschneider C, Fenchel M, Seeger A, Kramer U, Klumpp B, Nadalin S, Königsrainer A, Claussen CD, Miller S. MRI for evaluation of potential living liver donors: a new approach including contrast-enhanced magnetic resonance cholangiography. *Abdom Imaging* 2012; **37**: 244-251 [PMID: 21479607 DOI: 10.1007/s00261-011-9736-7]

34 **Lee MS**, Lee JY, Kim SH, Park HS, Kim SH, Lee JM, Han JK, Choi BI. Gadoxetic acid disodium-enhanced magnetic resonance imaging for biliary and vascular evaluations in preoperative living liver donors: comparison with gadobenate dimeglumine-enhanced MRI. *J Magn Reson Imaging* 2011; **33**: 149-159 [PMID: 21182133 DOI: 10.1002/jmri.22429]

35 **Kantarc₁ M**, Pirimoglu B, Karabulut N, Bayraktutan U, Ogul H, Ozturk G, Aydinli B, Kizrak Y, Eren S, Yilmaz S. Non-invasive detection of biliary leaks using Gd-EOB-DTPA-enhanced MR cholangiography: comparison with T2-weighted MR cholangiography. *Eur Radiol* 2013; **23**: 2713-2722 [PMID: 23695221 DOI: 10.1007/s00330-013-2880-4]

36 **Ito K**, Siegelman ES, Stolpen AH, Mitchell DG. MR imaging of complications after liver transplantation. *AJR Am J Roentgenol* 2000; **175**: 1145-1149 [PMID: 11000180 DOI: 10.2214/ajr.175.4.1751145]

37 **Campbell WL**, Foster RG, Miller WJ, Lecky JW, Zajko AB, Lee KY. Changes in extrahepatic bile duct caliber in liver transplant recipients without evidence of biliary obstruction. *AJR Am J Roentgenol* 1992; **158**: 997-1000 [PMID: 1566706 DOI: 10.2214/ajr.158.5.1566706]

38 **Holt AP**, Thorburn D, Mirza D, Gunson B, Wong T, Haydon G. A prospective study of standardized nonsurgical therapy in the management of biliary anastomotic strictures complicating liver transplantation. *Transplantation* 2007; **84**: 857-863 [PMID: 17984838]

39 **Pavone P**, Laghi A, Catalano C, Broglia L, Panebianco V, Messina A, Salvatori FM, Passariello R. MR cholangiography in the examination of patients with biliary-enteric anastomoses. *AJR Am J Roentgenol* 1997; **169**: 807-811 [PMID: 9275901 DOI: 10.2214/ajr.169.3.9275901]

40 **Tang Y**, Yamashita Y, Arakawa A, Namimoto T, Mitsuzaki K, Abe Y, Katahira K, Takahashi M. Pancreaticobiliary ductal system: value of half-Fourier rapid acquisition with relaxation enhancement MR cholangiopancreatography for postoperative evaluation. *Radiology* 2000; **215**: 81-88 [PMID: 10751471 DOI: 10.1148/radiology.215.1.r00ap0281]

41 **Pecchi A**, De Santis M, Gibertini MC, Tarantino G, Gerunda GE, Torricelli P, Di Benedetto F. Role of magnetic resonance imaging in the detection of anastomotic biliary strictures after liver transplantation. *Transplant Proc* 2011; **43**: 1132-1135 [PMID: 21620070 DOI: 10.1016/j.transproceed.2011.03.016]

42 **Buis CI**, Verdonk RC, Van der Jagt EJ, van der Hilst CS, Slooff MJ, Haagsma EB, Porte RJ. Nonanastomotic biliary strictures after liver transplantation, part 1: Radiological features and risk factors for early vs. late presentation. *Liver Transpl* 2007; **13**: 708-718 [PMID: 17457932 DOI: 10.1002/lt.21166]

43 **Boraschi P**, Braccini G, Gigoni R, Sartoni G, Neri E, Filipponi F, Mosca F, Bartolozzi C. Detection of biliary complications after orthotopic liver transplantation with MR cholangiography. *Magn Reson Imaging* 2001; **19**: 1097-1105 [PMID: 11711234]

44 **Shaikh F**, Elazzazi M, Ryan A, Semelka RC. Debris-filled biliary system: a difficult diagnosis on MRI and MRCP. *Clin Imaging* 2012; **36**: 153-155 [PMID: 22370138 DOI: 10.1016/j.clinimag.2011.08.009]

45 **Gor NV**, Levy RM, Ahn J, Kogan D, Dodson SF, Cohen SM. Biliary cast syndrome following liver transplantation: Predictive factors and clinical outcomes. *Liver Transpl* 2008; **14**: 1466-1472 [PMID: 18825683 DOI: 10.1002/lt.21492]

46 **Kim YK**, Kim CS, Lee JM, Ko SW, Chung GH, Lee SO, Han YM, Lee SY. Value of adding T1-weighted image to MR cholangiopancreatography for detecting intrahepatic biliary stones. *AJR Am J Roentgenol* 2006; **187**: W267-W274 [PMID: 16928904 DOI: 10.2214/AJR.05.0266]

47 **Romagnuolo J**, Bardou M, Rahme E, Joseph L, Reinhold C, Barkun AN. Magnetic resonance cholangiopancreatography: a meta-analysis of test performance in suspected biliary disease. *Ann Intern Med* 2003; **139**: 547-557 [PMID: 14530225]

48 **Boraschi P**, Donati F, Gigoni R, Salemi S, Urbani L, Filipponi F, Falaschi F, Bartolozzi C. Complications after liver transplantation: evaluation with magnetic resonance imaging, magnetic resonance cholangiography, and 3-dimensional contrast-enhanced magnetic resonance angiography in a single session. *Can Assoc Radiol J* 2008; **59**: 259-263 [PMID: 19385153]

49 **Laghi A**, Pavone P, Catalano C, Rossi M, Panebianco V, Alfani D, Passariello R. MR cholangiography of late biliary

complications after liver transplantation. *AJR Am J Roentgenol* 1999; **172**: 1541-1546 [PMID: 10350286 DOI: 10.2214/ajr.172.6.10350286]

50   **Cereser L**, Girometti R, Como G, Molinari C, Toniutto P, Bitetto D, Zuiani C, Bazzocchi M. Impact of magnetic resonance cholangiography in managing liver-transplanted patients: preliminary results of a clinical decision-making study. *Radiol Med* 2011; **116**: 1250-1266 [PMID: 21744253 DOI: 10.1007/s11547-011-0707-4]

51   **Kitazono MT**, Qayyum A, Yeh BM, Chard PS, Ostroff JW, Coakley FV. Magnetic resonance cholangiography of biliary strictures after liver transplantation: a prospective double-blind study. *J Magn Reson Imaging* 2007; **25**: 1168-1173 [PMID: 17520726 DOI: 10.1002/jmri.20927]

52   **Meersschaut V**, Mortelé KJ, Troisi R, Van Vlierberghe H, De Vos M, Defreyne L, de Hemptinne B, Kunnen M. Value of MR cholangiography in the evaluation of postoperative biliary complications following orthotopic liver transplantation. *Eur Radiol* 2000; **10**: 1576-1581 [PMID: 11044927]

53   **Beltrán MM**, Marugán RB, Oton E, Blesa C, Nuño J. Accuracy of magnetic resonance cholangiography in the evaluation of late biliary complications after orthotopic liver transplantation. *Transplant Proc* 2005; **37**: 3924-3925 [PMID: 16386586 DOI: 10.1016/j.transproceed.2005.10.044]

54   **Katz LH**, Benjaminov O, Belinki A, Geler A, Braun M, Knizhnik M, Aizner S, Shaharabani E, Sulkes J, Shabtai E, Pappo O, Atar E, Tur-Kaspa R, Mor E, Ben-Ari Z. Magnetic resonance cholangiopancreatography for the accurate diagnosis of biliary complications after liver transplantation: comparison with endoscopic retrograde cholangiography and percutaneous transhepatic cholangiography - long-term follow-up. *Clin Transplant* 2010; **24**: E163-E169 [PMID: 21039885 DOI: 10.1111/j.1399-0012.2010.01300.x]

55   **Xu YB**, Min ZG, Jiang HX, Qin SY, Hu BL. Diagnostic value of magnetic resonance cholangiopancreatography for biliary complications in orthotopic liver transplantation: a meta-analysis. *Transplant Proc* 2013; **45**: 2341-2346 [PMID: 23953547 DOI: 10.1016/j.transproceed.2013.03.031]

TOPIC HIGHLIGHT

WJR 6th Anniversary Special Issues (8): fMRI

Recent developments in optimal experimental designs for functional magnetic resonance imaging

Ming-Hung Kao, M'hamed Temkit, Weng Kee Wong

Ming-Hung Kao, M'hamed Temkit, School of Mathematical and Statistical Sciences, Arizona State University, Tempe, AZ 85287, United States
Weng Kee Wong, Department of Biostatistics, University of California at Los Angeles, Los Angeles, CA 90095, United States
Author contributions: Kao MH wrote the paper; Temkit M and Wong WK revised it critically for important intellectual content.
Correspondence to: Ming-Hung Kao, Assistant Professor of Statistics, School of Mathematical and Statistical Sciences, Arizona State University, PO Box 871804, Tempe, AZ 85287, United States. mkao3@asu.edu
Telephone: +1-480-9653951   Fax: +1-480-9658119
Received: December 31, 2013   Revised: April 30, 2014
Accepted: May 28, 2014
Published online: July 28, 2014

Abstract

Functional magnetic resonance imaging (fMRI) is one of the leading brain mapping technologies for studying brain activity in response to mental stimuli. For neuroimaging studies utilizing this pioneering technology, there is a great demand of high-quality experimental designs that help to collect informative data to make precise and valid inference about brain functions. This paper provides a survey on recent developments in experimental designs for fMRI studies. We briefly introduce some analytical and computational tools for obtaining good designs based on a specified design selection criterion. Research results about some commonly considered designs such as blocked designs, and m-sequences are also discussed. Moreover, we present a recently proposed new type of fMRI designs that can be constructed using a certain type of Hadamard matrices. Under certain assumptions, these designs can be shown to be statistically optimal. Some future research directions in design of fMRI experiments are also discussed.

Core tip: This paper provides an overview on recent developments in the design of functional magnetic resonance imaging experiments (fMRI). We discuss both analytical results and computational approaches that are currently available for selecting high-quality fMRI designs.

Kao MH, Temkit M, Wong WK. Recent developments in optimal experimental designs for functional magnetic resonance imaging . *World J Radiol* 2014; 6(7): 437-445 Available from: URL: http://www.wjgnet.com/1949-8470/full/v6/i7/437.htm DOI: http://dx.doi.org/10.4329/wjr.v6.i7.437

INTRODUCTION

Recent years have seen an upsurge of functional brain imaging experiments for a better understanding of how humans learn, remember and make decisions. Such experiments are also widely conducted by researchers to help provide paths to treat/prevent some terrifying brain disorders such as Alzheimer's disease, and are thus very valuable. As in many scientific investigations, designing a high-quality experiment is an important first step for successful functional brain imaging studies. A carefully designed experiment allows experimenters to collect informative data to make precise inference on the goals/hypotheses at minimal cost. On the other extreme, data collected from a poorly designed experiment may fail to provide valid answers to the research questions of interest, resulting in a waste of resource. The importance of the use of a carefully selected experimental design (or

data collection plan) cannot be overemphasized.

This paper provides a survey on some recent developments in experimental designs for functional magnetic resonance imaging (fMRI) experiments. Functional MRI is one of the most common functional brain mapping technologies. This pioneering, noninvasive technology helps to study experimental subjects' brain activity when they are cognitively engaging with mental stimuli such as viewing pictures, tapping fingers, solving problems, recalling events, or making decisions. It is used in various research areas including psychology, economics, and cognitive neuroscience[1], and has great clinical potentials as highlighted in a special issue on clinical applications of fMRI in Neuropsychology Review, Vol. 7, No. 2, 2007. However, fMRI experiments are usually expensive, and the collected data is notoriously noisy, making it difficult to draw precise statistical inference on brain functions. We thus would like a high-quality experimental design to help us make the best use of the limited resources to collect informative fMRI data.

An fMRI design is a sequence of mental stimuli to be presented to an experimental subject in an fMRI experiment. While the subject is performing the tasks determined by the selected stimulus sequence, an MRI scanner repeatedly scans his/her brain to acquire fMRI data for making statistical inference about the brain activity. The quality of the collected data depends on the selected design. However, due to the complexity of fMRI, obtaining the "best" fMRI design suited to the goal(s) of the experiment is a challenging task. We usually need to consider not only the statistical efficiency in achieving one or more (competing) study objectives, but also some unwanted psychological effects that can contaminate the data. In addition, we may want the obtained design to fulfill some practical constraints. The large diversity of the fMRI experimental settings and protocols also contributes to the difficulty of design selection. In almost all cases, we deal with a very challenging combinatorial problem.

There are some advances in the selection of fMRI designs, but much more work is needed to move this new emerging research area forward. The purpose of this article is to provide a brief overview of stochastic and deterministic computational tools for designing efficient fMRI studies as well as recent insights obtained for such studies using analytical methods. We begin in the next section with background information on fMRI studies, and introduce terminology and notation used in this article. We then present the general linear models widely used for the design and analysis of fMRI studies and popular design criteria in this area. Some recently obtained results and guidelines for selecting fMRI designs are discussed. We close the article with a summary and discussion.

BACKGROUND

Terminology and notation

In a typical fMRI experiment, a sequence of mental stimuli (*e.g.*, pictures) of one or more types interlaced with periods of rest or, say, visual fixation is presented to each experimental subject. These stimuli give rise to neuronal activity at some brain regions that triggers an increased inflow of oxygenated blood, leading to a decrease in the concentration of deoxygenated blood. This change in the ratio of oxy- to deoxy-blood can influence the strength of the magnetic field, and results in a rise and fall in the intensity of signals collected by the MRI scanner. Specifically, the MRI scanner collects MRI measurements by repeatedly scanning each of the, say, $64 \times 64 \times 30$ brain voxels, which are volumetric image elements that cover (part of) the subject's brain. Some voxels may fall outside the brain; see also Subsection 2.1.1 of Lazar[2]. At each voxel, MRI measurements are collected every τ_{TR} (*e.g.*, 2) seconds to form a blood oxygenation level dependent fMRI time series. The pre-specified time τ_{TR} is called the time to repetition. These time series serve as surrogate measurements of the underlying neuronal activity, and are analyzed to make inference about how the brain reacts to the stimuli; see also Lazar[2].

The inference on brain activity is mainly based on some characteristics of the hemodynamic impulse response function (HRF). The HRF is a function of time describing the rise and fall of the noise-free MRI measurements following a brief neuronal firing that occurs at a voxel. Previous studies suggest that the HRF may increase from baseline in about two seconds after the onset of a brief stimulus, reach the peak in five to eight seconds, and possibly fall down below baseline before its complete return to baseline[1,3]. This process may take about 30 s, counting from the onset of the brief stimulus to the HRF's complete return to baseline. If there are other neuronal firings (*e.g.*, due to the onset of other stimuli) before the cessation of the previous HRF, the evoked HRFs overlap and their heights accumulate. Since fMRI time series is typically very noisy, identifying the characteristics of the HRF by visual inspections is difficult, if not impossible. Statistical methods are thus needed to help extract useful information from the data. As an integral part of the statistical process, we would like to select a "good" fMRI design that helps to make valid inference.

An fMRI design is a sequence of mental stimuli of one or more types. When the sequence is presented to an experimental subject, each stimulus may last as brief as several milliseconds or as long as, say, a minute. Stimuli with extended presentation duration, *e.g.*, 10-60 s, are used in traditional blocked designs, which are also termed as boxcar designs. In such a design, the stimulus of the same type can appear at multiple time points during the experiment, but each long stimulus is immediately followed by a long stimulus of another type or by a period of control (*e.g.*, rest). It also is not uncommon to replace each long stimulus by a short sequence of separate but brief stimuli of the the same type. The resulting designs are still called blocked designs. For experiments with Q stimulus types, a typical blocked design may be the repetitions of $\{A_1 A_2 \ldots A_Q A_0\}$, where, for q =1, ...,

Q, A_q represents a presentation of a long stimulus (or a sequence of brief stimuli) of the qth type, and A_0 is a period of control. At a brain voxel responding to the qth-type stimulus, neuronal firings can be expected throughout the time span of each "on-period" A_q. This leads to an accumulation of overlapping HRFs. With a long on-period of the stimulus, the MRI signal intensity increases to a high level, and may reach a plateau before dropping down to baseline following the cessation of the stimulus. The large contrast between the elevated signal intensity and baseline facilitates the detection of brain voxels (or regions) that respond to the stimulus. Blocked designs are thus often recommended for detecting brain voxels that are activated by the stimuli; see the Results on Design Selection section for a further discussion.

Moving away from blocked designs, some studies showed that an individual stimulus that is as brief as several tens of milliseconds can evoke a detectable change in the MRI measurements; see Rosen *et al*[3] and references therein. In addition, the heights of overlapping HRFs following multiple brief stimuli tend to be (roughly) additive when the time between stimulus onsets is not overly short (*e.g.*, at least 2 s); see also Friston *et al*[4]. These observations make it possible to consider event-related (ER-) fMRI designs that consist of brief stimuli whose order may be randomized. An ER-fMRI design of Q stimulus types is often written as a finite sequence of elements 0, 1, ..., Q, and may look like d = (1012021…1). A positive integer q in d represents an onset of a qth-type stimulus, and 0 means no stimulus onset. Specifically, when the ith element of d is $d_i = q$ (> 0), a qth-type stimulus appears briefly at time $(i-1)\tau_{ISI}$ for a pre-determined τ_{ISI}; time 0 may be synchronized to the first valid MRI scan. For example, when $d_3 = 1$ and $\tau_{ISI} = 4$ s, a stimulus of the first type (*e.g.*, a picture of a familiar face) will occur briefly at the $(3-1)\tau_{ISI} = 8^{th}$ second after the first valid MRI scan. With $d_4 = 2$, a stimulus of the second type (*e.g.*, a picture of an unfamiliar face) will appear at the 12th second after the first valid MRI scan. When $d_i = 0$, there is no stimulus onset at time $(i-1)\tau_{ISI}$. With these 0's in the design, time between stimulus onsets may be "jittered"[5], and thus, may not be fixed to τ_{ISI}. Typically, the control (*e.g.*, a visual fixation or rest period) fills in the time between the offset of a brief stimulus to the onset of the next stimulus. Due to its flexibility, ER-fMRI designs have gained much popularity[6]. However, a typical design can easily contain tens or hundreds of elements, making it very challenging for selecting good designs. In this paper, we discuss some recently developed approaches for finding high-quality fMRI designs, including both blocked and ER-fMRI designs. Most of these approaches are built upon the popular general linear model framework. This framework is described below.

The general linear model framework

The fMRI time series, $\{y(t): t \geq 0\}$, of a brain voxel is typically modeled as the sum of (1) the convolution of the stimulus function and the HRF, (2) a nuisance term allowing for a trend or drift of y(t); and (3) noise[7,8]. We consider the foxllowing continuous-time model:

$$y(t) = \sum_{q=1}^{Q} \int_0^t x_q(t-\tau)h_q(\tau; \beta_q)d\tau + s(t; \gamma) + e(t) \qquad (1)$$

where $x_q(t)$ is the stimulus function for the stimuli of the qth type, $h_q(\tau; \beta_q)$ is the HRF evoked by the qth-type stimulus, β_q is an unknown parameter vector, q = 1, ..., Q, $s(t; \gamma)$ is a nuisance term approximating the drift/trend of the time series, γ is the corresponding unknown parameter vector, and e(t) is noise. The stimulus function $x_q(t)$ indicates the appearances of the qth-type stimuli, and may be a sum of boxcar functions or a sum of (shifted) Dirac delta functions; see also Henson and Friston[9]. Boxcar functions are often employed in experiments with blocked designs. In this case, $x_q(t)$ takes a positive value during the "on-periods" of the qth-type stimulus of a block design, and is 0, otherwise. The resulting model is sometimes referred to as the epoch model[10]. In an event-related model, the $x_q(t)$ is a sum of (shifted) Dirac delta functions that indicates the onset times of the brief stimuli of the qth type.

The most commonly used fMRI data analysis method is probably the general linear model approach[1]. Partly due to this popularity, existing studies on fMRI designs mainly focus on linear models such as models (2) and (3) that are extensions of (1), and are linear in the parameters β_q's and γ. In the fMRI literature[11,12], dual models are commonly considered for two popular study objectives, namely the detection of brain activations (or detection) and the estimation of the HRF (or estimation). The main difference between the two models is that they used different sets of basis functions to describe $h_q(\tau; \beta_q)$ of model (1); see also Friston *et al*[4].

For detection, the HRF $h_q(\tau; \beta_q)$ is typically approximated by $\theta_q h^*(\tau)$, where $h^*(\tau)$ is an assumed shape of the HRF, and θ_q is the unknown amplitude (or maximum height) of the HRF. Thus, β_q contains only one parameter θ_q that signals the strength of brain activation due to the qth-type stimulus. Since the MRI measurements y(t) is collected every τ_{TR} seconds, we consider the following discrete-time model:

$$y = \sum_{q=1}^{Q} z_q\theta_q + S\gamma + e. \qquad (2)$$

Here, $\mathbf{y} = (y_1, ..., y_T)'$ with $y_t = y((t-1)\tau_{TR})$. The vector $\mathbf{z}_q$ is obtained by subsampling the convolution of $x_q(t)$ and $h^*(\tau)$ with a sampling rate of τ_{TR} seconds. $S\gamma$ corresponds to $s(t; \gamma)$ of (1) with S being a specified matrix. For example, the tth element of $S\gamma$ might be $\gamma_0 + \gamma_1 t + \gamma_2 t^2$. The vector e in model (2) represents the noise. The focus of model (2) is typically on $C_1\theta$ for a given matrix C_1 whose rows contain coefficients of linear combinations of $\theta_1, ..., \theta_Q$; here, $\theta = (\theta_1, ..., \theta_Q)'$. When $C_1 = I_Q$ is the identity matrix of order Q, the focus is on the strength of brain activation due to each stimulus type. It is also common to study $(\theta_p - \theta_q)$ for $p \neq q$. In such a case, the rows of C_1 contain the coefficients of the pairwise comparisons between the HRF amplitudes.

The estimation of the HRF is a study objective that has gained much popularity with the advent of ER-fMRI.

A widely used model for this objective is:

$$y = \sum_{q=1}^{Q} X_q h_q + S\gamma + e. \tag{3}$$

Here, $h_q = (h_{1q}, ..., h_{Kq})$' is an unknown parameter vector representing the heights of the HRF that contribute to y. Specifically, $h_{kq} = h_q((k-1)\Delta T; \beta_q)$ is the HRF height at $(k-1)\Delta T$ seconds after the onset of a qth-type stimulus, where ΔT is the greatest real value making $(\tau_{ISI}/\Delta T)$ and $(\tau_{TR}/\Delta T)$ integers; k=1, ...,K. The value of K is selected so that $h_q((k-1)\Delta T; \beta_q)$ becomes negligible when $\tau > (K-1)\Delta T$. For a commonly considered 32-second HRF, $K = [32/\Delta T]$ with [a] being the integer part of a. The consideration of h_q is equivalent to modeling $h_q((k-1)\Delta T; \beta_q)$ of (1) by a linear combination of K shifted Kronecker delta functions; *i.e.*, $h_q((k-1)\Delta T; \beta_q) = \sum_{k=1}^{K} h_{kq}\delta_k(\tau)$, where $\delta_k(\tau) = 1$ when $\tau = (k-1)\Delta T$, and $\delta_k(\tau) = 0$, otherwise; β_q thus contain all the K coefficients (HRF heights) $h_{1q}, ..., h_{Kq}$. $X_q = [x_{1q}, ..., x_{Kq}]$ in model (3) is the 0-1 design matrix of size T-by-K for the qth-type stimuli. The tth element of x_{kq} is 1 when h_{kq} contributes to y_t. The remaining terms in (3) are as in (2). In contrast to model (2) for detection, model (3) does not assume a known shape for the HRF. The goal is to estimate all the unknown HRF heights h_{kq} or to study some linear combinations C_2h of these heights with h = (h_1', ..., h_Q')' and a given linear combination coefficient matrix C_2.

Design selection criteria

With models (2) and (3) respectively for detection and estimation, the main design goal is to select an fMRI design that yields the most precise parameter estimates of the parametric functions of interest. Some statistically meaningful optimality criteria have been proposed for evaluating the goodness of competing designs. Two popular criteria in the fMRI literature are A- and D-optimality criteria. For detection problems with model (2), the A-optimality criterion can be defined as the following 'larger-the better' criterion:

$$\varphi_\theta^A (d) = r_1/\text{trace} \{C_1[Z'V'(I_T-\omega\{VS\}VZ)]-C_1'\} = r_1/\text{trace} \{C_1[M_1(d)]-C_1'\}' \tag{4}$$

Here, r_1 is the number of rows of C_1, and Z = [z_1, ..., z_Q]. V is a whitening matrix such that cov(Ve) = σ^2 VRV' = $\sigma^2 I_T$, where σ^2 is the error variance, and R = corr(e) is the correlation matrix of errors. The matrix $\omega\{A\}$ = A (A'A)$^-$A' is the orthogonal projection matrix onto the column space of A. A$^-$ is a generalized inverse of A, and $M_1(d) = Z'V'(I_T - \omega\{VS\}VZ$ is the information matrix of θ. We note that V may be obtained by, *e.g.*, the Cholesky decomposition of R^{-1}, and, depending on the assumptions made at the design stage, it may or may not contain unknown parameters; see also the Results on Design Selection section and Maus *et al*[13]. The criterion in (4) depends on the selected design d through the design matrix Z, and is inversely proportional to the average variance of the least-squares estimates of the parametric functions defined by $C_1\theta$. For estimating the HRF with model (3), the A-optimality criterion can be written as:

$$\varphi_h^A (d) = r_2/\text{trace} \{C_2[X'V'(I_T-\omega\{VS\}VX)]-C_2'\} = r_2/\text{trace}$$

$$\{C_2[M_2(d)]-C_2'\}' \tag{5}$$

where r_2 is the number of rows of C_2, X=[X_1, ..., X_Q] is the design matrix depending on the selected design d, $M_2(d)$ is the information matrix for h, and all the remaining terms are as in (4).

The D-optimality criterion seeks to minimize the volume of the (asymptotic) confidence ellipsoid of C_2h. For the detection of brain activation with model (2) and the estimation of the HRF with model (3), D-optimal designs are found by maximizing the following two criteria, respectively:

$$\varphi_\theta^D (d) = \det\{C_1[M_1(d)]-C_1'\}^{-1/r_1} \tag{6}$$

$$\varphi_h^D (d) = \det\{C_2[M_2(d)]-C_2'\}^{-1/r_2} \tag{7}$$

All the terms in (6) and (7) are as in (4) and (5), respectively. For the D-optimality criteria, the coefficient matrices C_1 and C_2 are required to be full row rank. The selection between the A- and D-optimality criteria depends on the need and preference of the experimenter. As indicated in Maus *et al*[14], while early works on fMRI designs mainly focused on the A-optimality criterion, there is no obvious reason to generally prefer one criterion over the other. In the subsequent sections, we discuss some results on fMRI design selection. Most of these results are based on the A- or D-optimality criterion.

RESULTS ON DESIGN SELECTION

Blocked designs for detecting brain activations

There is some guidance on selecting blocked designs for detecting brain activations in the literature. For example, Henson[15] advocated the use of blocked designs having a 15-s-on-15-s-off pattern. For such a blocked design formed by {$A_1A_2...A_QA_0$}, the duration of each A_q is fixed to 15 s. This suggestion is based on the Fourier transformations of the convolution in (1) by assuming that the HRF has the form of the double-gamma function:

$$g^*(\tau) = \tau^s e^{-\tau}/S! - 1/6 \times \tau^{1s}e^{-\tau}/1S! \tag{8}$$

The double-gamma function is widely used as the HRF shape, and is built in a software package, called SPM (http://www.fil.ion.ucl.ac.uk/spm/), for fMRI data analysis. In the frequency domain, this HRF acts as a low-pass filter that `passes' low-frequency signals and reduces the amplitude of high-frequency signals. As demonstrated in Henson[15], after the Fourier transformation, a large proportion of the signal energy of a 15-s-on-15-s-off blocked design is retained by the selected HRF shape. In addition, the use of an on-period A_q that is longer than 50 seconds is not recommended. This is because the signal energy of the resulting blocked designs may be lost after accounting for the low-frequency nuisance signals such as heartbeats or respirations which is modeled by s(t; γ) in (1).

Setting the block length (or duration of A_q) to 15 s may not be optimal for an HRF shape that is different from (8). For example, Liu *et al*[16] considered cases with one stimulus type (Q = 1), and evaluated the performance of designs with the A-optimality criterion. They

observed that the blocked design with a block length of 64 s tends to have a high statistical efficiency in detection when a single gamma density function is used to model the HRF shape. This latter HRF shape is also not uncommon, especially for cases where the HRF does not fall below baseline when returning from its peak. In addition, Liu *et al*[16] suggested that the selection of block length also depends on s(t; γ). In particular, they demonstrated that the blocked design with a 64-s block length can yield a smaller φ_θ^A-value than designs with a shorter (*e.g.*, 32 s) blocked length when the statistical model also allows for a second- or third-order Legendre polynomial drift.

To provide additional information on design selection, Maus *et al*[14] studied blocked designs of two stimulus types (Q = 2) with selected block lengths (10, 15, 20, 30 or 60 s), and patterns (repetitions of $\{A_1A_2\}$, $\{A_1A_2A_0\}$, or $\{A_1A_0A_2A_0\}$). Each block A_q is formed by a sequence of 1-second stimuli of the qth type; q = 1, 2, and the time between the onsets of consecutive stimuli in the same block is τ_{ISI} = 1, 2, or 3 s. They compare the statistical efficiencies of these blocked designs in detecting brain activations *via* model (2). In their model, the nuisance term Sγ corresponds to a linear trend, and the HRF shape used to construct z_q is set to the double-gamma function of (8). The errors are assumed to have one of the three possible structures, including uncorrelated errors, first order autoregressive (AR1) process, and an AR1 process plus a measurement error (AR1+ME).

Considering both φ_θ^A (d) and φ_θ^D (d), Maus *et al*[14] suggested to keep τ_{ISI} as short as possible. In addition, they recommended to use the design pattern $\{A_1A_2A_0\}$ for studying the HRF amplitudes θ_1 and θ_2. When the focus is on comparing the amplitudes (*i.e.*, $\theta_1 - \theta_2$), blocked designs formed by $\{A_1A_2\}$ are recommended. The results of Maus *et al*[14] also indicate that the selection of block length may hinge on the assumed error correlation. When the focus is on θ_q's, a block length of 15 s is recommended for both uncorrelated and AR1 errors. As for AR1 + ME errors, a block length of 10 s is the best among the selected blocked lengths. For studying the contrast between the HRF amplitudes, the suggested block lengths are 20 s and 15 s for uncorrelated errors and correlated errors (AR1 or AR1 + ME), respectively.

These previous studies provide some guidelines on selecting blocked designs for detecting brain activations. It can also be seen that the selection of blocked designs depend on a few factors. These factors include the parametric function $C_1\theta$ of interest, the selected HRF shape, the model for capturing the drift/trend of the fMRI time series, and the error correlation structure. For cases that are not covered by these guidelines, we may obtain a good design for detection by using a computer algorithm. Some algorithms have already been proposed in the fMRI literature. Most of these computational approaches can be employed for cases considering the detection of brain activations, the estimation of the HRF, or when both detection and estimation are of interest. Some practical constraints may also be imposed when using these com-

putational tools. In what follows, we first describe some guidelines for selecting ER-fMRI designs for estimating the HRF. We then discuss computer algorithms for obtaining good fMRI designs.

ER-fMRI designs for estimating the HRF

The estimation of the HRF helps to make inference about some characteristics of the underlying neuronal activity as also described in Lindquist *et al*[17]. For this objective, model (3) may be considered, and the goal is to obtain a design yielding the most precise parameter estimates of C_2h for a given C_2. By considering the A-optimality criterion of (5), Dale[18] suggested to allow for variable time intervals between onsets of consecutive stimuli, and the average of these time intervals should be kept small. This suggestion can also be applied to the D-optimality criterion of (7). However, one should take caution that if the time between stimulus onsets is overly short (*e.g.*, < 2 s), the accumulated heights of the overlapping HRFs may saturate at a certain level. Consequently, the assumption of the additivity of the HRF heights can be violated. For such a case, the nonadditive HRF heights should be taken into account when evaluating the goodness of designs; see also, Wager *et al*[19] and Wager *et al*[20]. However, current methods for accounting for the nonadditive HRF heights tend to be ad hoc, and additional investigations are needed.

While rendering useful information, Dale[18] did not provide a systematic way for design construction. Buračas and Boynton[21] worked on the same design issue, and advocated the use of maximum length shift-register sequences (or m-sequences). Such a design can be generated by a primitive polynomial over a Galois field GF(Q+1) consisting of Q+1 elements, where Q+1 is a prime power. To construct an m-sequence, one may select a primitive polynomial $f(x) = x^r - \sum_{i=1}^{r} \alpha_i x^{r-i}$ from, *e.g.*, Table 3.5, 3.6 or 3.7 of Golomb and Gong[22]. The m-sequence d = $(d_1, ..., d_N)$ is then determined by the relation, $d_{n+r} = \sum_{i=1}^{r} \alpha_i d_{n+r-j}$ (mod Q+1) with a nonzero initial r-tuple $(d_1, ..., d_r)$; see also Lidl and Niederreiter[23], and MacWilliams and Sloane[24]. Such a design can also be obtained *via* an MATLAB program developed by Liu[11]. For an m-sequence of length $N = (Q+1)^r - 1$, every nonzero r-tuple appears exactly once in the set $\{(d_1, ..., d_r), (d_2, ..., d_{r+1}), ..., (d_N, d_1 ..., d_{r-1})\}$.

Buračas *et al*[21] and Liu[11] reported the high performance of m-sequences in terms of the φ_h^A-value when $C_2 = I_{QK}$ is the QK-by-QK identity matrix. However, when Q > 1, the frequency of the appearance of each stimulus type of an m-sequence can be different from the optimal stimulus frequency approximated by Liu *et al*[12] for A-optimality. In particular, Liu and Frank[12] indicated that the optimal stimulus frequency of an A-optimal design for estimating the HRF h is about $1/(Q + \sqrt{Q})$ for each of the Q stimulus types. The optimal number of 0 is thus approximately $N/(1 + \sqrt{Q})$. Since the stimulus frequency of m-sequences is about $1/(Q+1)$, these designs may not be A-optimal; see also Kao *et al*[25]. For φ_h^D with $C_2 = I_{QK}$,

the optimal stimulus frequency approximated by Maus *et al*[13] is 1/(Q+1), and is close to that of m-sequences. Maus *et al*[13] thus suggested that the optimality of m-sequences may depend on the selected criterion.

However, attaining the (approximated) optimal stimulus frequency does not guarantee an optimal design. To derive additional insightful results, Kao[26] also studied model (3) with the following assumption: Assumption 1. (a) The number of MRI scans T equals the length N of the design d and $\tau_{TR} = \tau_{ISI}$; (b) S = j_T is the T-by-1 vector of ones, and cov(e) proportional I_T; and (c) the last K - 1 elements of design d are also presented to the subject before the first valid MRI scan.

Assumptions 1(a) and 1(c) are mild, and can often be controlled by the experimenters. Assumption 1(b) is mainly for mathematical simplicity, and is also considered in some previous studies such as Liu *et al*[16] and Maus *et al*[27]. Following an argument in Kushner[28], for the results to be discussed in the remaining of this subsection, Assumption 1(b) can be relaxed to include cases with cov(e) = $\alpha I_T + \lambda j_T' + j_T \lambda'$, where α is a constant and λ is a vector of constants. The results thus hold for a compound symmetric covariance matrix with cov(e) = $\alpha I_T + \lambda J_T$, where λ is a constant, and J_T is the T-by-T matrix of ones. For estimating the K-by-1 HRF parameter vector h_1 with one stimulus type (Q = 1), Kao[26] showed that a design of length N having $n_1 = N/2$ and $n_r^{(11)} = (n_1)^2/N$ for all r = 1, ..., K - 1 is universally optimal. Here, n_q is the frequency of the qth-type stimuli in the design d, and $n_r^{(pq)}$ is the number of times $(d_{n-r}, d_n) = (q,p)$ for *n* = 1, ..., N; $d_{n-r} = d_{N+n-r}$ when n ⩽ r. We also note that an universally optimal design can be shown to be optimal in a large class of optimality criteria, including A- and D-optimality[29]. For Q > 1, a similar sufficient condition for an ER-fMRI design to be D-optimal can also be found in Kao[26]. In particular, if all the symbols 0, 1, ..., Q appear equally often in a design **d** of length N, and that $n_r^{(pq)} = n_p n_q/N$ for all p, q = 1, ..., Q and r = 1, ..., K - 1, then the design d maximizes φ_h^D of (7) under Assumption 1 and $C_2 = I_{QK}$.

As described in Kao[26], designs satisfying the previously mentioned sufficient conditions can be constructed by inserting an additional 0 to any (K - 1)-tuple of zeros in an m-sequence of length $(Q+1)^K - 1$. The resulting design is a de Bruijn sequence[22,30]. Aguirre *et al*[30] proposed to use de Bruijn sequences for estimating the HRF. The results of Kao[26] help to establish the optimality of such designs.

Clearly, m-sequences do not satisfy the sufficient conditions provided by Kao[26]. Additional results are thus needed for establishing the optimality of these popular designs. Kao[31] worked on this direction, and proved that a binary m-sequence of length N ⩾ 2K - 3 is D-optimal for estimating the HRF h_1 under Assumption 1 with Q = 1. He also proposed a new type of ER-fMRI designs for estimating the HRF. This new type of designs, which are termed as Hadamard sequences, can be constructed by a normalized Hadamard matrix, H, having a circulant core. Specifically, the elements of the first row and column of

H are 1 and all the other entries are +1 or -1 with HH' proportional I. After deleting the first row and column of H, we have a circulant matrix called the circulant core. As described in Kao[31], a D-optimal design can be achieved by replacing +1 and -1 in any column of the circulant core by 0 and 1, respectively. It is noteworthy that binary m-sequences can also be generated using this same method and are thus special cases of Hadamard sequences. Nevertheless, Hadamard sequences exist in many different lengths for which a binary m-sequence is unavailable. These newly proposed designs are thus much more flexible than m-sequences and the previously mentioned de Bruijn sequences in terms of design length.

Kao[31] also conducted some case studies on the performance of Hadamard sequences when Assumptions 1(b) and 1(c) are violated. Based on empirical results, Hadamard sequences tend to remain efficient when the nuisance term $S\gamma$ in model (3) corresponds to a second-order polynomial drift, the noise follows an AR1 process, and/or no stimulus is presented before the first valid MRI scan. This result is especially true when the autocorrelation coefficient of the AR1 noise is not as high as ϱ = 0.5 or when the design is not too short (*e.g.*, N < 100). We also note that a violation of Assumption 1(a) can have a great impact on the performance of Hadamard sequences. For cases with $\tau_{TR} \neq \tau_{ISI}$, we may consider efficient computational methods for obtaining good designs. Some computational approaches are introduced in the next subsection. These approaches are also applicable when both estimation and detection are of interest.

Computational tools for obtaining fMRI designs

In the fMRI literature, some computer algorithms are proposed for finding an ER-fMRI design of the form d = $(d_1, ..., d_N)$ with d_n belong to {0, 1, ..., Q} that optimizes a specific single- or multi-objective optimality criterion. To efficiently search over the enormous space of ER-fMRI designs for good designs, Wager and Nichols[19] advocated the use of the genetic algorithm (GA) technique. Due to their versatility, GAs can accommodate various experimental settings to find designs suited to individual fMRI experiments. Following Wager and Nichols[19], Kao *et al*[25] put forward an efficient GA that takes advantage of knowledge on the performance of some ER-fMRI designs to improve the efficiency of the GA search. Some well-known designs such as m-sequences, blocked designs, and their combinations are employed in the algorithm of Kao *et al*[25] to increase the diversity of the designs being explored, and to maintain a supply of good traits (or building blocks) that help to form good designs during the GA search. As demonstrated in Kao *et al*[25], this strategy is very effective.

With the previously mentioned GAs, one can find a (near-)optimal design for user-specified number of stimulus types Q, design length N, τ_{ISI}, τ_{TR}, and model assumptions, including the model for drift/trend of the time series, error correlation structure, and, if model (2) is considered, the HRF shape. Depending on the study

objective(s), the optimality criterion for evaluating the quality of designs may be φ^A_θ, φ^A_h, φ^D_θ, φ^D_h or a weighted sum of some of these criteria; weights are user-selected to reflect the relative importance of detection and estimation. In a weighted sum criterion, one may also include other individual criteria to account for quantifiable constraints/requirements of the study. For example, Wager *et al*[19] included a counterbalancing criterion for avoiding psychological confounds such as anticipation and habituation. By optimizing this criterion, the order of the stimuli in the resulting design cannot be easily predicted by the experimental subject. Moreover, we may include an additional individual criterion to measure the departure from a target frequency of appearances of each stimulus type; see also, Kao *et al*[25]. Such a customized requirement on the stimulus frequency may help to increase the subject's engagement in the presented mental tasks[32].

The GA of Kao *et al*[25] has been applied for studying several fMRI design issues. For example, this algorithm was used to obtain designs for cases where both individual stimulus effects (h and θ) and pairwise comparisons (h_p - h_q and θ_p - θ_q for $p \neq q$) are of interest. Maus *et al*[13] used the GA to work on cases where the autocorrelation coefficient ρ of the AR1 noise is uncertain. The GA is also adapted in Kao *et al*[33,34] for finding designs suited to experiments with multiple scanning sessions.

In addition, Maus *et al*[35] and Kao *et al*[36] utilized the GA to tackle the design problem concerning an uncertain HRF shape. The need for considering the uncertainty of the HRF shape is manifested in some previous studies[37,38]. These studies pointed out that the HRF shape may vary across brain voxels, and that specifying a wrong HRF shape in, say, model (2) for detection may lead to an incorrect conclusion. To accommodate different HRF shapes, Kao[39] considered at the design stage the following nonlinear model:

$$y = \sum_{q=1}^{Q} X_q h(u)\theta_q + s\gamma + e \qquad (9)$$

where h(u) is a K-by-1 vector representing the shape of the HRF, u is an unknown parameter vector that needs to be estimated from data, and all the remaining terms are as in (2) and (3). The vector h(u) may be determined by the double-gamma function of (8) with free parameters for accounting for the variability in the HRF shape; see also Wager et al[20]. In particular, the kth element of h(u) is g((k - 1) ΔT; u)/$\max_s$ g(s; u) with u = (u_1, u_2)' and

$$g(\tau; u) = [(\tau-u_2)^{u_1-1}e^{-(\tau-u_2)}]/\Gamma(u_1) - 1/6 \times [(\tau-u_2)^{1S-1}e^{-(\tau-u_2)}]/15!$$
$$(\tau \geqslant u) \text{ or } 0 \text{ (otherwise)} \qquad (10)$$

Here, u_1 is the time-to-peak parameter, which mainly determines the time for the HRF to reach the peak, counting from its onset time. The time-to-onset parameter u_2 determines the time when the HRF starts to increase from baseline, counting from the onset of a stimulus. As indicated by Wager *et al*[20], these two parameters are the most influential, although some additional free parameters may also be included in (10). For example, one may use a free parameter to replace the coefficient 1/6 in the second term of the non-zero part of (10). The function $\Gamma(u) = \int_0^\infty t^{u-1}e^{-1}dt = (u-1) \Gamma(u - 1)$ in (10) is the gamma

function. We note that the function $g^*(\tau)$ in (8) is a special case of (10) with u = (6, 0)'. Specifically, the HRF shape $h^*(\tau)$ in model (2) depends on $g^*(\tau)$, and is fixed. By contrast, the HRF shape in model (9) is determined by g(τ; u), and involves unknown parameters to be estimated from the data. The latter model is thus more flexible.

When making inference about θq for detecting brain activations, model (9) allows for an uncertain HRF shape. However, obtaining a good design for such a flexible model is quite challenging. Again, we would like a design optimizing some function (*e.g.*, the A- or D-optimality criterion) of the information matrix of θ. For model (9), this information matrix, denoted by M(d; θ, u), can be approximated by first-order Taylor approximation. In contrast to M1(d) and M2(d) in (4)-(7), M(d; θ, u) depends not only on the design d, but also on the unknown model parameters θ and u; see Kao[39] and Kao *et al*[36] for details. By treating θ and u as random variables, and assuming the availability of a (prior) distribution of θ and u, Kao[39] targeted a (pseudo-)Bayesian design that maximizes E{ϕ(M(d; θ, u))} for a larger-the-better criterion ϕ, where the expectation E{.} is taken over the (prior) distribution of the parameters.

When a prior distribution of the parameters is unavailable, it is common to consider to maximize the minimum of ϕ(M(d; θ, u)), where the minimum is taken over the possible values of θ and u. It also is popular to maximize the the minimum of the relative efficiency, which is defined as

min (θ ∈ u, u ∈ U) ϕ[M(d; θ, u)]/ϕ[M($d^*_{\theta,u}$; θ, u)]

Here, Θ and U contain the possible values for θ and u, respectively; and $d^*_{\theta, u}$ is a locally optimal design that maximizes ϕ(M(d; θ, u)) for given θ and u. Designs maximizing the former criterion are termed as maximin designs, whereas those optimizing the latter criterion are maximin-efficient designs. Both criteria are popular in the literature; see also Kao *et al*[36] and references therein. However, obtaining maximin-type designs is computationally very expensive. Kao *et al*[36] proposed an efficient shortcut. Building on some analytical results, they showed that the size of the parameter space of Θ can be greatly reduced when obtaining maximin-type designs. Specifically, when Q=1, we may find a very efficient maximin (or maximin-efficient) design by focusing on θ_1 = 1 (or θ_1 belong to {0,1}). For Q > 1, instead of setting Θ to the entire Q-dimensional space, we may focus on a subspace consisting of (1/Q!) of the surface of the Q-dimensional unit hemisphere centered at the origin when obtaining a maximin design; the origin needs to be included in the subspace for finding a maximin-efficient design. To further reduce computing time, Kao *et al*[36] focused on a restricted class, Ξ_0, of designs when using a search algorithm to find maximin-type designs. Specifically, each design of length N in Ξ_0 is formed by a short design of length [N/Q], where [a] is the smallest integer greater than or equal to a. For any short design, a full-length design is constructed by cyclically permuting the labels of the Q stimulus types with 0's staying intact, and then leav-

ing out the excess elements, if any. The stimulus frequencies in the resulting design are thus (nearly) equal across stimulus types. Kao *et al*[36] showed that their approach is quite efficient and effective when obtaining maximin-type designs when the HRF shape is uncertain.

In addition to the GA technique, a deterministic optimization algorithm for obtaining optimal fMRI designs has recently been proposed and studied by Kao and Mittelmann[40]. Without stochastic explorations, this latter approach has been demonstrated to be efficient for some cases for which the GA requires much CPU time in finding a good design. The main idea is to combine a greedy hill-climbing algorithm with the previously mentioned cyclic permutation method for constructing designs of Ξ_0. In particular, the algorithm first systematically perturbs a small fraction (*e.g.*, the first four elements) of a short design d_s of length $[N/Q]$ to create some neighboring short designs that are close to d_s in terms of Hamming distance. The search then moves to the neighboring short design d_s that yields the best full-length design *via* the cyclic permutation method. After this movement, the algorithm continues to work on perturbing another small fraction (*e.g.*, the fifth to eighth elements) of d_s. This process is repeated until no improvement can be achieved. Based on our experience, this approach tends to lead to very efficient designs with greatly reduced CPU time, although the obtained design might not be optimal. Kao and Mittelmann[40] demonstrated the usefulness of their algorithm by finding maximin designs that are robust to mis-specified error autocorrelation coefficients when stationary AR2 errors are assumed. For this case, the GA approach can be very challenging in terms of CPU time.

The algorithms described so far are used to optimize a single objective function. For experiments with two or more study objectives, these previous studies mainly considered weighted-sum criteria that are convex combinations of all the individual criteria of interest. However, selecting appropriate weights for such a weighted-sum criterion might be challenging for some cases, and the assigned weights may not guarantee a satisfactory design. For example, assigning equal weights does not always lead to a design with equal relative efficiency across all the study objectives of interest. To address this fMRI design issue, Kao *et al*[41] proposed a multi-objective optimization algorithm by modifying the nondominated sorting GA Ⅱ (NSGA Ⅱ) of Deb *et al*[42]. With a single run of the algorithm, the experimenter can obtain not one, but a class of diverse designs for approximating the Pareto frontier; a Pareto frontier is formed by the best possible solutions in a multi-objective optimization problem. A design best suited to the needs of the experiment can then be selected from the obtained design class. The algorithm can also be used to find fMRI designs when there is a constraint such as a required stimulus frequency. This algorithm is recommended when weights on the multiple study objectives are hard to determine.

CONCLUSION

Design of fMRI experiments is an exciting research area. Several analytical and computational approaches have been proposed for obtaining designs that attain high efficiencies in terms of certain practically meaningful design selection criterion. As demonstrated in Jansma *et al*[43], among others, fMRI designs with theoretically superior performance are often very useful in real-world experiments. The designs obtained in the previous studies are thus valuable. However, much work remains to be done in this area. As indicated by Lindquist[1] in his recent survey on statistical methods for fMRI studies, "as research hypotheses ultimately become more complicated, the need for more advanced experimental designs will only increase further."

One possible direction of future research is on developing designs for cases with compound stimuli, each containing two or more components; *e.g.*, each stimulus is formed by a cue followed by a task. To our knowledge, there is no systematic study on this important design issue. In addition, fMRI is also widely considered for studying the functional connectivity between brain regions. High-quality experimental designs for this type of studies are also in a great demand. Moreover, developing powerful computational approaches, and insightful analytical results for optimal fMRI designs should always be helpful. For example, the analytical results described in the Results on Design Selection section are mainly for cases where Assumption 1 holds and $C_2 = I_{QK}$. It is also useful to consider the case where C_2 is not the identity matrix when contrasts between the HRFs are of interest. Developing novel, insightful analytical results by relaxing Assumption 1 can also help to move this new research field forward.

REFERENCES

1   **Lindquist M.** The statistical analysis of fMRI data. *Stat Sci* 2008; **23**: 439-464 [DOI: 10.1214/09-STS282]
2   **Lazar N.** The Statistical Analysis of Functional MRI Data. New York: Springer, 2008 [DOI: 10.1007/978-0-387-78191-4]
3   **Rosen BR**, Buckner RL, Dale AM. Event-related functional MRI: past, present, and future. *Proc Natl Acad Sci USA* 1998; **95**: 773-780 [PMID: 9448240 DOI: 10.1073/pnas.95.3.773]
4   **Friston KJ**, Zarahn E, Josephs O, Henson RN, Dale AM. Stochastic designs in event-related fMRI. *Neuroimage* 1999; **10**: 607-619 [PMID: 10547338 DOI: 10.1006/nimg.1999.0498]
5   **Serences JT**. A comparison of methods for characterizing the event-related BOLD timeseries in rapid fMRI. *Neuroimage* 2004; **21**: 1690-1700 [PMID: 15050591 DOI: 10.1016/j.neuroimage.2003.12.021]
6   **Huettel SA**. Event-related fMRI in cognition. *Neuroimage* 2012; **62**: 1152-1156 [PMID: 21963919 DOI: 10.1016/j.neuroimage.2011.08.113]
7   **Martin PI**, Naeser MA, Doron KW, Bogdan A, Baker EH, Kurland J, Renshaw P, Yurgelun-Todd D. Overt naming in aphasia studied with a functional MRI hemodynamic delay design. *Neuroimage* 2005; **28**: 194-204 [PMID: 16009568 DOI: 10.1002/hbm.460010207]
8   **Worsley KJ**, Liao CH, Aston J, Petre V, Duncan GH, Morales F, Evans AC. A general statistical analysis for fMRI data. *Neuroimage* 2002; **15**: 1-15 [PMID: 11771969 DOI: 10.1006/nimg.2001.0933]

9   **Henson R,** Friston K. Convolution models for fMRI. In: Friston K, Ashburner J, Kiebel S, Nichols T, Penny W. Statistical parametric mapping: the analysis of functional brain images. London: Academic, 2007: 178-192

10   **Mechelli A**, Henson RN, Price CJ, Friston KJ. Comparing event-related and epoch analysis in blocked design fMRI. *Neuroimage* 2003; **18**: 806-810 [PMID: 12667857 DOI: 10.1016/S1053-8119(02)00027-7]

11   **Liu TT**. Efficiency, power, and entropy in event-related fMRI with multiple trial types. Part II: design of experiments. *Neuroimage* 2004; **21**: 401-413 [PMID: 14741677 DOI: 10.1016/j.neuroimage.2003.09.031]

12   **Liu TT**, Frank LR. Efficiency, power, and entropy in event-related FMRI with multiple trial types. Part I: theory. *Neuroimage* 2004; **21**: 387-400 [PMID: 14741676 DOI: 10.1016/j.neuroimage.2003.09.030]

13   **Maus B**, van Breukelen GJ, Goebel R, Berger MP. Robustness of optimal design of fMRI experiments with application of a genetic algorithm. *Neuroimage* 2010; **49**: 2433-2443 [PMID: 19833212 DOI: 10.1016/j.neuroimage.2009.10.004]

14   **Maus B,** van Breukelen G, Goebel R, Berger M. Optimization of blocked designs in fMRI studies. *Psychometrika* 2010; **75**: 373-390 [DOI: 10.1007/S11336-010-9159-3]

15   **Henson R**. Efficient experimental design for fMRI. In: Friston K, Ashburner J, Kiebel S, Nichols T, Penny W. Statistical parametric mapping: the analysis of functional brain images. London: Academic, 2007: 193-210

16   **Liu TT**, Frank LR, Wong EC, Buxton RB. Detection power, estimation efficiency, and predictability in event-related fMRI. *Neuroimage* 2001; **13**: 759-773 [PMID: 11305903 DOI: 10.1006/nimg.2000.0728]

17   **Lindquist MA**, Meng Loh J, Atlas LY, Wager TD. Modeling the hemodynamic response function in fMRI: efficiency, bias and mis-modeling. *Neuroimage* 2009; **45**: S187-S198 [PMID: 19084070 DOI: 10.1016/j.neuroimage.2008.10.065]

18   **Dale AM**. Optimal experimental design for event-related fMRI. *Hum Brain Mapp* 1999; **8**: 109-114 [PMID: 10524601]

19   **Wager TD**, Nichols TE. Optimization of experimental design in fMRI: a general framework using a genetic algorithm. *Neuroimage* 2003; **18**: 293-309 [PMID: 12595184 DOI: 10.1016/S1053-8119(02)00046-0]

20   **Wager TD**, Vazquez A, Hernandez L, Noll DC. Accounting for nonlinear BOLD effects in fMRI: parameter estimates and a model for prediction in rapid event-related studies. *Neuroimage* 2005; **25**: 206-218 [PMID: 15734356 DOI: 10.1016/j.neuroimage.2004.11.008]

21   **Buracas GT**, Boynton GM. Efficient design of event-related fMRI experiments using M-sequences. *Neuroimage* 2002; **16**: 801-813 [PMID: 12169264 DOI: 10.1006/nimg.2002.1116]

22   **Golomb S,** Gong G. Signal design for good correlation for wireless communication, cryptography, and radar. New York: Cambridge University Press, 2005

23   **Lidl R**, Niederreiter H. Introduction to finite fields and their applications. New York: Cambridge University Press, 1994

24   **MacWilliams F,** Sloane N. The theory of error correcting codes. Amsterdam: Elsevier/North-Holland, 1977

25   **Kao MH**, Mandal A, Lazar N, Stufken J. Multi-objective optimal experimental designs for event-related fMRI studies. *Neuroimage* 2009; **44**: 849-856 [PMID: 18948212 DOI: 10.1016/j.neuroimage.2008.09.025]

26   **Kao MH.** On the optimality of extended maximal length linear feedback shift register sequences. *Stat Probabil Lett* 2013; **83**: 1479-1483 [DOI: 10.1016/j.spl.2013.02.012]

27   **Maus B**, van Breukelen GJ, Goebel R, Berger MP. Optimal design of multi-subject blocked fMRI experiments. *Neuroimage* 2011; **56**: 1338-1352 [PMID: 21406234 DOI: 10.1016/j.neuroimage.2011.03.019]

28   **Kushner H.** Optimal repeated measurements designs: The linear optimality equations. *Ann Stat* 1997; **25**: 2328-2344 [DOI: 10.1214/aos/1030741075]

29   **Kiefer J.** Construction and optimality of generalized youden designs. In: Srivastava J. A survey of statistical designs and linear models. Amsterdam: North-Holland, 1975: 333-353

30   **Aguirre GK**, Mattar MG, Magis-Weinberg L. de Bruijn cycles for neural decoding. *Neuroimage* 2011; **56**: 1293-1300 [PMID: 21315160 DOI: 10.1016/j.neuroimage.2011.02.005]

31   **Kao MH.** A new type of experimental designs for event-related fMRI via Hadamard matrices. *Stat Probabil Lett* 2014; **84**: 108-112 [DOI: 10.1016/j.spl.2013.09.024]

32   **Brendel B**, Hertrich I, Erb M, Lindner A, Riecker A, Grodd W, Ackermann H. The contribution of mesiofrontal cortex to the preparation and execution of repetitive syllable production: an fMRI study. *Neuroimage* 2010; **50**: 1219-1230 [PMID: 20080191 DOI: 10.1016/j.neuroimage.2010.01.039]

33   **Kao MH,** Mandal A, Stufken J. Optimal design for event-related functional magnetic resonance imaging considering both individual stimulus effects and pairwise contrasts. *Stat Appl* 2008; **6**: 225-241

34   **Kao MH,** Mandal A, Stufken J. Efficient designs for event-related functional magnetic resonance imaging with multiple scanning sessions. *Commun Stat-Theory Methods* 2009; **38**: 3170-3182 [DOI: 10.1080/03610920902947626]

35   **Maus B**, van Breukelen GJ, Goebel R, Berger MP. Optimal design for nonlinear estimation of the hemodynamic response function. *Hum Brain Mapp* 2012; **33**: 1253-1267 [PMID: 21567658 DOI: 10.1002/hbm.21289]

36   **Kao MH,** Majumdar D, Mandal A, Stufken J. Maximin and maximin-efficient event-related fMRI designs under a nonlinear model. *Ann Appl Stat* 2013; **7**: 1940-1959 [DOI: 10.1214/13-AOAS658]

37   **Handwerker DA**, Ollinger JM, D'Esposito M. Variation of BOLD hemodynamic responses across subjects and brain regions and their effects on statistical analyses. *Neuroimage* 2004; **21**: 1639-1651 [PMID: 15050587 DOI: 10.1016/j.neuroimage.2003.11.029]

38   **Lindquist MA**, Wager TD. Validity and power in hemodynamic response modeling: a comparison study and a new approach. *Hum Brain Mapp* 2007; **28**: 764-784 [PMID: 17094118 DOI: 10.1002/hbm.20310]

39   **Kao MH.** Optimal experimental designs for event-related functional magnetic resonance imaging. PhD thesis: University of Georgia, 2009

40   **Kao MH,** Mittelmann H. A fast algorithm for constructing efficient event-related functional magnetic resonance imaging designs. *J Stat Comput Simul* 2014; to appear [DOI: 10.1080/00949655.2013.804524]

41   **Kao MH,** Mandal A, Stufken J. Constrained multi-objective designs for functional MRI experiments via a modified nondominated sorting genetic algorithm. *J Roy Stat Soc C-App* 2012; **61**: 515-534 [DOI: 10.1111/j.1467-9876.2011.01036.x]

42   **Deb K**, Pratap A, Agarwal S, Meyarivan T. A fast and elitist multiobjective genetic algorithm: NSGA-II. IEEE T Evolut Comput 2002; **6**: 182-197 [DOI: 10.1109/4235.996017]

43   **Jansma JM**, de Zwart JA, van Gelderen P, Duyn JH, Drevets WC, Furey ML. In vivo evaluation of the effect of stimulus distribution on FIR statistical efficiency in event-related fMRI. *J Neurosci Methods* 2013; **215**: 190-195 [PMID: 23473798 DOI: 10.1016/j.jneumeth.2013.02.017]

Nuclear medicine and the failed joint replacement: Past, present, and future

Christopher J Palestro

Christopher J Palestro, Division of Nuclear Medicine, Molecular Imaging Long Island Jewish Medical Center, New York, NY 11040, United States
Author contributions: Palestro CJ solely contributed to this paper.
Correspondence to: Christopher J Palestro, MD, Division of Nuclear Medicine, Molecular Imaging Long Island Jewish Medical Center, 270-05 76th Avenue New Hyde Park, New York, NY 11040, United States. palestro@lij.edu
Telephone: +1-718-4707081   Fax: +1-718-8311147
Received: December 4, 2013   Revised: February 26, 2014
Accepted: May 28, 2014
Published online: July 28, 2014

Abstract

Soon after the introduction of the modern prosthetic joint, it was recognized that radionuclide imaging provides useful information about these devices. The bone scan was used extensively to identify causes of prosthetic joint failure. It became apparent, however, that although sensitive, regardless of how the images were analyzed or how it was performed, the test was not specific and could not distinguish among the causes of prosthetic failure. Advances in anatomic imaging, notably cross sectional modalities, have facilitated the diagnosis of many, if not most, causes of prosthetic failure, with the important exception of infection. This has led to a shift in the diagnostic paradigm, in which nuclear medicine investigations increasingly have focused on diagnosing infection. The recognition that bone scintigraphy could not reliably diagnose infection led to the development of combined studies, first bone/gallium and subsequently leukocyte/bone and leukocyte/marrow imaging. Labeled leukocyte imaging, combined with bone marrow imaging is the most accurate (about 90%) imaging test for diagnosing joint arthroplasty infection. Its value not withstanding, there are significant disadvantages to this test. *In-vivo* techniques for labeling leukocytes, using antigranulocyte antibodies have been explored, but have their own limitations and the results have been inconsistent. Fluorodeoxyglucose (FDG)-positron emission tomography (FDG-PET) has been extensively investigated for more than a decade but its role in diagnosing the infected prosthesis has yet to be established. Antimicrobial peptides bind to bacterial cell membranes and are infection specific. Data suggest that these agents may be useful for diagnosing prosthetic joint infection, but large scale studies have yet to be undertaken. Although for many years nuclear medicine has focused on diagnosing prosthetic joint infection, the advent of hybrid imaging with single-photon emission computed tomography (SPECT)/electronic computer X-ray tomography technique (CT) and the availability of fluorine-18 fluoride PET suggests that the diagnostic paradigm may be shifting again. By providing the anatomic information lacking in conventional radionuclide studies, there is renewed interest in bone scintigraphy, performed as a SPECT/CT procedure, for detecting joint instability, mechanical loosening and component malpositioning. Fluoride-PET may provide new insights into periprosthetic bone metabolism. The objective of this manuscript is to provide a comprehensive review of the evolution of nuclear medicine imaging of joint replacements.

Core tip: Advances in anatomic imaging, notably cross sectional modalities, have facilitated the diagnosis of many, if not most, causes of prosthetic failure, with the important exception of infection. This has led to a shift in the diagnostic paradigm, in which nuclear medicine investigations increasingly have focused on diagnosing infection. This article is a comprehensive review of

the evolution of nuclear medicine imaging of joint replacements. In addition to conventional planar imaging studies such as bone, gallium, and labeled leukocyte imaging, single-photon emission computed tomography/electronic computer X-ray tomography technique and positron emission tomography imaging with ^{18}F-fluorodeoxyglucose and ^{18}F (NaI) are covered.

INTRODUCTION

Contemporary joint arthroplasty procedures began less than 75 years ago, when the predecessor of the modern day hip replacement was introduced. A total hip arthroplasty includes both femoral and acetabular components; a hemiarthroplasty consists of only the femoral component. These prostheses are anchored to bone by various methods including polymethylmethacrylate and osseous ingrowth into the device's surface. Some devices are coated with hydroxyapatite which induces new bone formation and attaches to newly produced periprosthetic osseous tissue. The acetabular component can be forced into the acetabulum or secured by screws[1].

The predecessor of the contemporary knee prosthesis, developed about 40 years ago, consisted of a metallic femoral component, together with plastic patellar and tibial components. Today's devices provide improved range of motion and greater durability of the components[1].

The vast majority of lower extremity joint replacement surgeries are successful; complications like infection, fracture, dislocation, and heterotopic ossification are uncommon. At the present time the most common cause of prosthetic failure is aseptic loosening, which develops in more than a quarter of these devices and frequently results from an inflammatory reaction instigated by prosthetic components[2,3]. The debris created by component breakdown activates and draws surrounding leukocytes, triggering secretion of cytokines and enzymes damaging osseous tissues and leading to prosthetic loosening. The cellular response is characterized by an influx of various types of leukocytes. Neutrophils, however, rarely are present[4-6]. Most cases of aseptic loosening are treated with one surgery, the single stage exchange arthroplasty.

Infection, which occurs in up to 2% of primary implants, and up to 5% of revision implants is an uncommon complication of prosthetic joint surgery. Risk factors for infection include operative suite characteristics, surgical complexity, condition of the osseous tissue surrounding the prosthesis, and immune status of the patient.

Bacteria bind to most joint replacement components and once attached they secrete a protective biofilm[3]. Or-

ganisms commonly encountered in infected joint replacements include *Staphylococcus epidermidis* and *Staphylococcus aureus*. *Streptococcus viridans*, *Escherichia coli*, *Enterococcus faecalis*, and *group-B Streptococcus* are occasionally identified[4]. Early prosthetic joint infections occur by three months after implantation, while delayed infections develop within three months to one year after implantation. Late infections are defined as infections that occur more than one year after surgery. Early and delayed infections are thought to be due to organisms introduced at surgery; late infections are more likely to be due to hematogenous spread[7].

The infected joint replacement is accompanied by an inflammatory reaction characterized by a neutrophilic response, often intense[6]. Management of the infected joint replacement consists of removal of the device, a lengthy course (weeks to months) of antibiotic treatment, and eventually a reimplantation procedure[8].

The correct therapeutic approach often depends on the accurate differentiation of aseptic loosening and infection. This differentiation is not always obvious. Signs and symptoms, except for pain, frequently are lacking. Laboratory tests may be suggestive, but are not diagnostic, of infection. Joint aspiration with culture, the definitive preoperative test is specific, but sensitivity is variable[9,10]. Plain radiographs are not specific and prosthesis related artifacts limit, to some degree, cross sectional imaging studies.

Nuclear medicine procedures have, for many years, contributed useful information about the painful joint replacement. This manuscript is a comprehensive review of the evolution of nuclear medicine imaging of joint replacements.

LITERATURE SEARCH

An electronic search with no language restrictions was conducted in the bibliographic database PubMed using the terms infection, osteomyelitis, arthroplasty, joint replacement, prosthetic joint, bone scintigraphy, bone marrow scintigraphy, gallium, labeled leukocytes, besilesomab, sulesomab, sulfur colloid, antimicrobial peptides, positron emission tomography, positron emission tomography (PET), fluorodeoxyglucose (FDG), fluoride and ^{18}F. The list of articles generated was augmented by crosschecking the reference lists of the retrieved papers. This was designed as a comprehensive review, not a meta analysis, of the failed joint replacement and therefore neither specific inclusion criteria nor any evidence based quality assessment tools were used to select the included articles.

RADIONUCLIDE IMAGING

Bone scintigraphy

The first, and undoubtedly the most extensively investigated, radionuclide procedure used for imaging joint arthroplasties was bone scintigraphy. Technetium-99m (^{99m}Tc) labeled diphosphonates, usually methylene di-
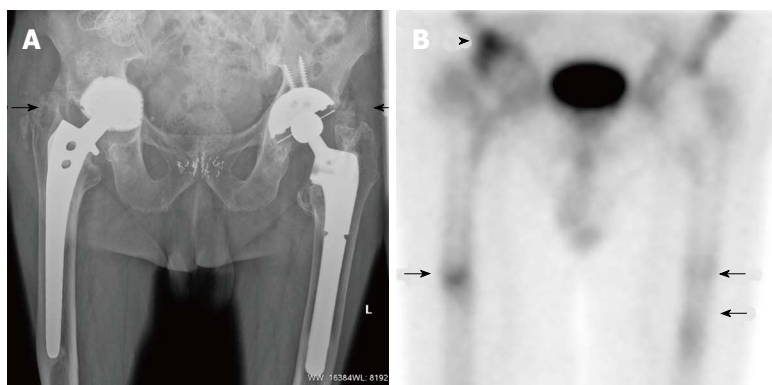
Figure 1 Aseptically loosened right hip arthroplasty. A: X-ray reveals medial protrusion of the acetabular component of a painful 15 year old hip replacement. There is heterotopic ossification around both greater trochanters (arrows); B: On the ⁹⁹ᵐTc-methylene diphosphonate bone scan, there is focally increased radiopharmaceutical accumulation at the distal tip of the femoral component (arrow) of the right hip replacement and lateral to the femoral neck (arrowhead) corresponding to the heterotopic bone seen on the X-ray. An aseptically loosened prosthesis was revised. Focally increased radiopharmaceutical accumulation is present at the tip of the femoral component of the asymptomatic left hip arthroplasty (double arrows) which also was 15 years old.
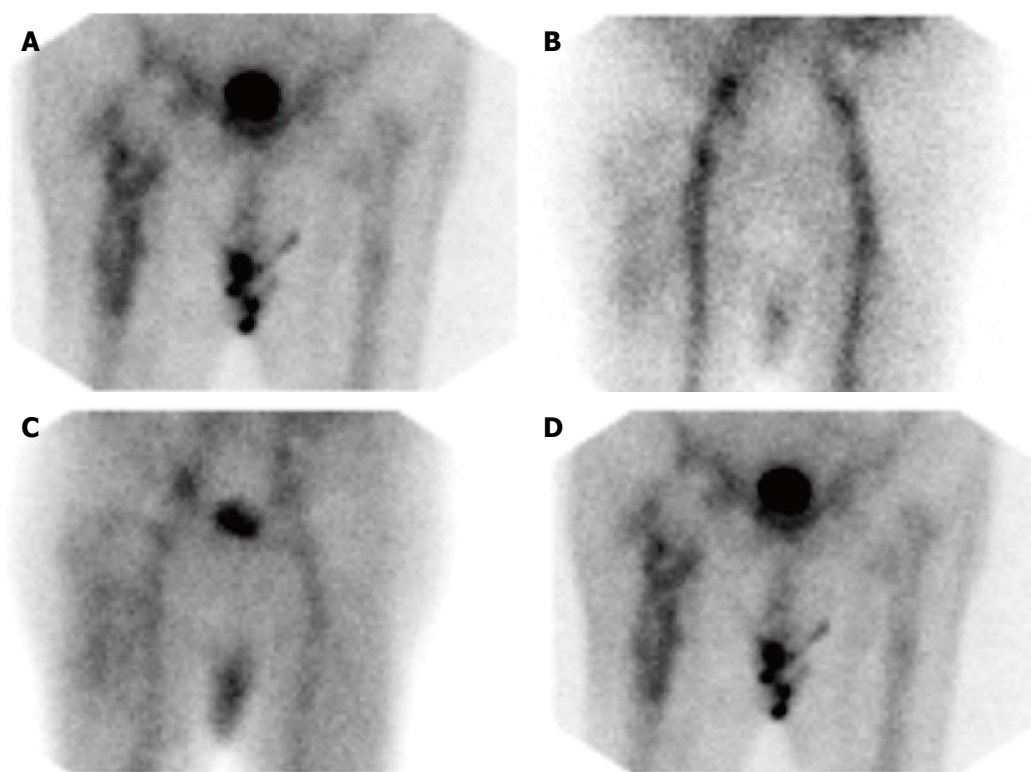
Figure 2 Infected right hip arthroplasty. A: On the ⁹⁹ᵐTc-methylene diphosphonate bone scan, there is irregularly increased radiopharmaceutical accumulation around the entire femoral component of the 2 years old cementless (revision) prosthesis, a pattern which some investigators have reported as specific for infection; B-D: On the ⁹⁹ᵐTc-MDP bone scan, there is diffuse hyperperfusion, and hyperemia around the prosthesis on the flow and blood pool images, and diffusely increased periprosthetic radiopharmaceutical on the delayed, bone image (same patient illustrated in Figure 2A); B: Flow; C: Blood pool; D: Bone.

phosphonate (MDP), are used for this study. Radiopharmaceutical incorporation into the bone depends on perfusion and rate of new bone formation. Imaging usually is performed two to fours after injection. The procedure also can be performed as a three phase bone scan: the flow or perfusion phase, acquired immediately after radiopharmaceutical injection, followed immediately by the soft tissue or blood pool phase. The third, or bone, phase is performed between two and four hours later.

Gelman et al[10] reported that bone scintigraphy was 85% accurate for prosthetic hip loosening. Weiss et al[11] reported that bone scintigraphy accurately identified prostheses requiring surgical intervention. Another group of investigators, however, observed that bone scintigraphy cannot determine the cause of the failure, information critical to patient management[12].

In an effort to enhance its specificity, investigators have studied periprosthetic uptake patterns on bone scans. Williamson et al[13] suggested that focal periprosthetic uptake indicated loosening and diffuse uptake indicated infection (Figures 1, 2A). Williams et al[14] reported that diffuse periprosthetic uptake was sensitive (100%), but not specific (54%) for infection. Another group of investigators came to the opposite conclusion: diffuse periprosthetic uptake was specific, but not sensitive, for infection[15]. Aliabadi et al[16] reported that bone scintigraphy did not differentiate septic from aseptic loosening (Figure 3A).

Further confounding the analysis of periprosthetic uptake is the numerous uptake patterns present around
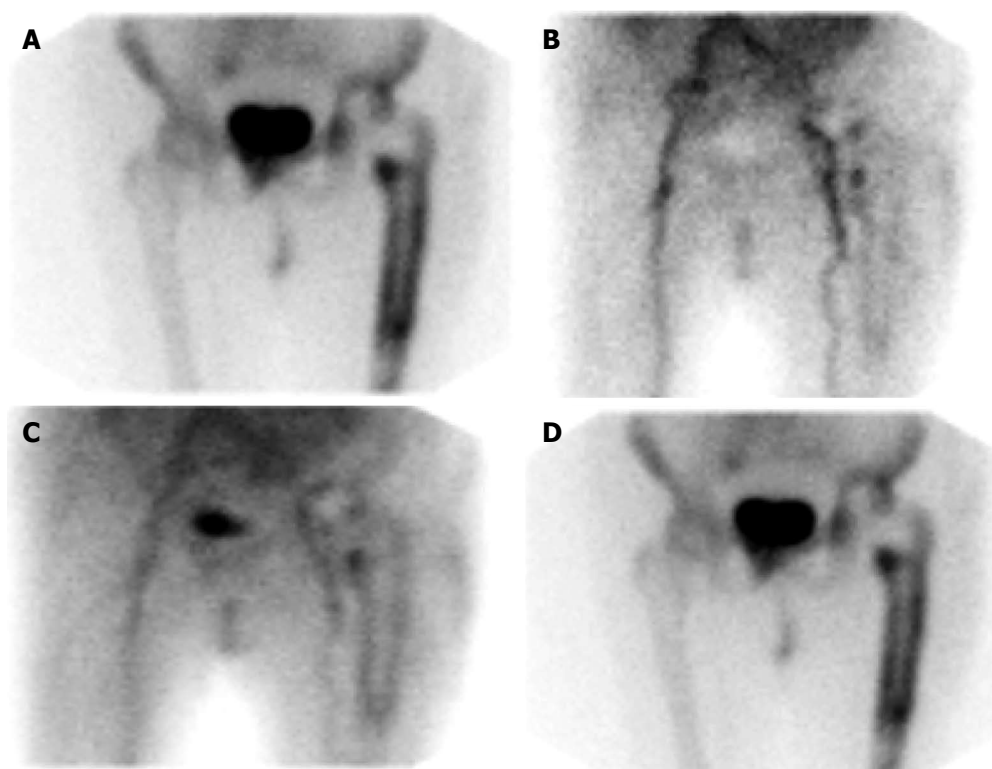
Figure 3 Aseptically loosened left hip replacement. A: On the ⁹⁹ᵐTc-MDP bone scan, there is diffusely increased radiopharmaceutical accumulation around the femoral component of the cemented 2 years old prosthesis. Compare with Figure 2A; B-D: On the ⁹⁹ᵐTc-MDP bone scan, there is diffuse hyperperfusion, and hyperemia around the prosthesis on the flow and blood pool images, and diffusely increased periprosthetic radiopharmaceutical on the delayed, bone image (same patient illustrated in Figure 3A), B: Flow; C: Blood pool; D: Delayed. The scan appearance is nearly identical to that of the infected prosthesis in Figure 2B.
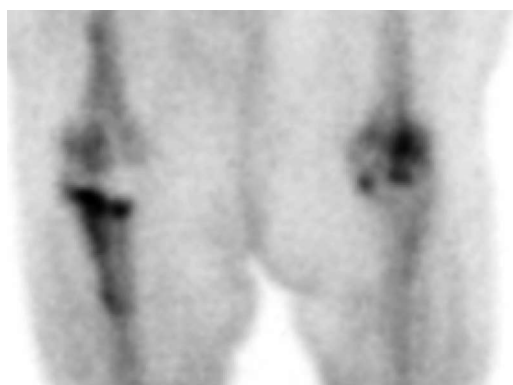
Figure 4 Asymptomatic right knee arthroplasty. On the ⁹⁹ᵐTc-MDP bone scan, there is irregular, intense radiopharmaceutical accumulation around the long stemmed tibial component of a three year old right knee replacement. The femoral component is unremarkable. The patient had a history of breast carcinoma and bone scintigraphy was performed as part of a routine evaluation for metastatic disease.

asymptomatic devices. For up to 12 m after insertion of a hip prosthesis, periprosthetic uptake is very variable; after this time ten percent of asymptomatic cemented hip prostheses still demonstrate uptake[17]. Increased periprosthetic uptake is even more frequent in cementless devices[18-20].

Gallo *et al*[21] studied 27 hydroxyapatite coated hip replacements, observing that while a normal study excluded aseptic loosening with a high degree of certainty, a posi-

tive study was not reliable for diagnosing either loosening or infection. Complicating matters further is the paucity of data on radionuclide bone imaging of hybrid and bipolar prostheses.

Assessment of knee replacements also is challenging. In one investigation periprosthetic activity was seen around more than sixty percent of femoral components and nearly 90% of tibial components of asymptomatic devices for up to several years[22] (Figure 4). In an investigation of asymptomatic knee replacements with serial bone scans periprosthetic activity generally diminished over time after implantation. There was considerable variation among patients. The authors stated, in order to determine the significance of periprosthetic activity, serial scans need to be performed[23] (Figure 5A). Another group of investigators reported that bone scintigraphy does not accurately diagnose the infected knee arthroplasty[24].

Performing radionuclide bone imaging as a three-phase study has been advocated to enhance its specificity[25]. Nagoya *et al*[26] reported that the test was 88% sensitive and 90% specific for hip replacement infection. Most other investigations, however, have reported low sensitivity, low specificity, or both[24,27-30] (Figures 2B and 3B).

Regardless of how bone scintigraphy is performed, its accuracy for diagnosing complications of lower extremity joint prostheses is about 50%-70%. At the present time this test is used primarily for screening purposes. A nor-
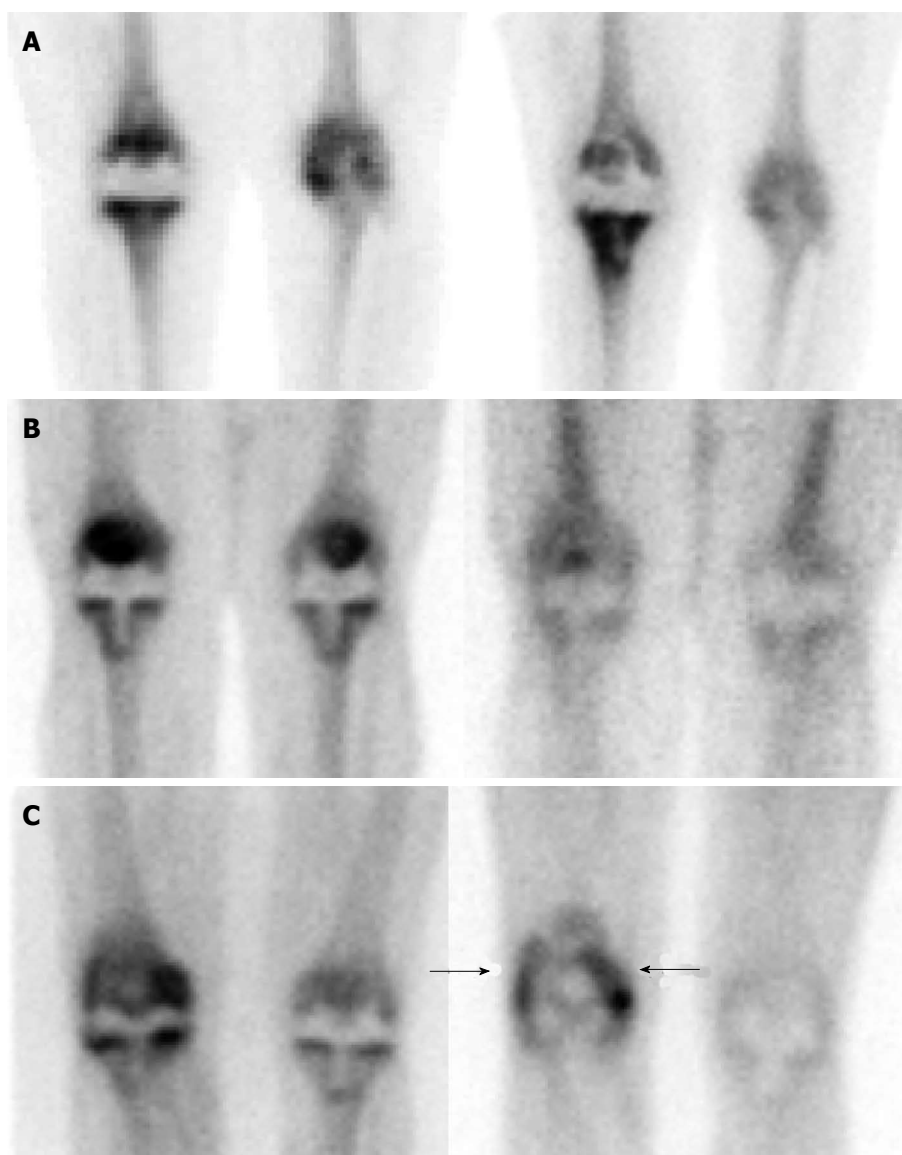
Figure 5 Aseptically loosened right knee arthroplasty. A: On the ^{99m}Tc-methylene diphosphonate (MDP) bone scan, performed about 6 mo after implantation (left), shows mildly increased radiopharmaceutical accumulation around the femoral and tibial components. On the repeat study, performed 9 mo later (15 mo after implantation), there is intensely increased radiopharmaceutical accumulation around the tibial component, while activity around the femoral component has resolved. An aseptically loosened tibial component was revised; B: On the ^{99m}Tc-MDP bone scan (left) there is increased radiopharmaceutical accumulation around the tibial component of both the symptomatic right and asymptomatic left knee prostheses. There is normal periprosthetic distribution around both prostheses on the gallium-67 image (right), and the combined study is negative for infection; C: On the ^{99m}Tc-MDP bone scan (left) there is increased radiopharmaceutical accumulation around the tibial component of the symptomatic right and faintly increased accumulation around the tibial component of the asymptomatic left knee prosthesis. On the gallium-67 image (right), in contrast to the bone scan, there is increased radiopharmaceutical accumulation around the femoral component (arrows) of the right knee replacement, while activity around the tibial component is normal. There is normal periprosthetic gallium activity around the asymptomatic left prosthesis. The distribution of activity around the right knee prosthesis on the bone and gallium studies is spatially incongruent and the combined study is (false) positive for infection. Aseptic loosening of joint replacements often is accompanied by an intense inflammatory response and gallium cannot reliably differentiate infection from inflammation.

Figure 6 Normal ^{99m}Tc-methylene diphosphonate bone scans of bilateral hip (left) and right knee (right) prostheses. A normal bone scan is defined as a scan in which periprosthetic activity is indistinguishable from adjacent, non-articular bone. The bone scan has a high negative predictive value and therefore a normal study makes it very unlikely that the patient's symptoms are related to the prosthesis.

mal study makes it very unlikely that the patient's symptoms are related to the prosthesis (Figure 6).

Gallium scintigraphy

Over the years various techniques designed to overcome the limitations inherent in bone scintigraphy have been investigated. One of the earliest was gallium-67 citrate (gallium) imaging. Gallium uptake in infection likely is due to several factors including increased blood flow and vascular membrane permeability at inflammatory sites, lactoferrin binding and siderophore and bacterial uptake of gallium. Some gallium may be transported by leukocytes. Imaging typically is performed two to three days after injection[31].

Reing *et al*[32] observed that bone scintigraphy was sensitive (100%), but not specific (15%), while gallium was sensitive (95%) and specific (100%). Other investigators have reported similar results[15,33,34]. Aliabadi *et al*[16], in contrast, found, for the infected hip replacement, gallium scintigraphy was specific (100%) but insensitive (37%).

While some investigators have evaluated gallium imaging alone, other investigators have interpreted bone and gallium imaging together. Standardized criteria for interpretation of the combined study have been developed. The test is positive for osteomyelitis when distribution of the two tracers is different or, when their distribution is the same and the relative intensity of gallium uptake exceeds that of the bone agent. The test is equivocal for osteomyelitis when the distribution of the two radiotracers is the same, both spatially and in intensity. The test is negative for osteomyelitis when the gallium images are normal, regardless of the bone scan findings, or, when the distribution of the two tracers is the same and the relative intensity of gallium uptake is less than that of the bone agent (Figure 5B and 5C)[1].

Tehranzadeh *et al*[35] reported that bone/gallium imaging was 95% accurate for prosthetic joint infection. In most other series the test has been less successful. In 30 patients the test identified only 50% of the infected joint replacements[14]. Gómez-Luzuriaga *et al*[36] found that bone/gallium imaging was 80% accurate for prosthetic joint infection. Kraemer *et al*[37] reported that the combined test was 38% sensitive, and 100% specific for hip replacement infection. Merkel *at al*[38,39] evaluated bone/gallium imaging in an animal investigation and in patients and reported similar results.

Over the years the use of gallium for joint replacement infection has declined, and it has been replaced in most circumstances by labeled leukocyte imaging.

Labeled leukocyte scintigraphy

The accumulation of *in-vitro* labeled white cells at a site of infection depends on chemotaxis, the quantity and sorts of leukocytes labeled, and the primary cellular response in a particular situation. Neutrophils usually comprise the majority of leukocytes labeled and consequently sensitivity of WBC imaging is highest for neutrophil-mediated inflammatory processes[40]. When indium-111 is the radiolabel, images are acquired 18-30 h after administration. When technetium-99m is the radiolabel, imaging usually is performed four to six and repeated 18 to 30 h after administration.

One would anticipate that, because neutrophils invariably are present labeled leukocyte (WBC) imaging would accurately diagnose prosthetic joint infection. Interestingly, for quite some time, the value of the test was a subject of controversy.

In a canine study, Merkel *et al*[38] reported that WBC imaging was 94% sensitive and 86% specific for prosthetic infection. Pring *at al*[41] found that WBC imaging was 100% sensitive and 89.5% specific for the infected prosthetic joint. In another investigation, Pring *et al*[42]

observed that WBC activity around infected prostheses was always significant. Rand *et al*[43] found that sensitivity and specificity for prosthetic knee infection was 83% and 85% when moderately to markedly increased periprosthetic activity was present. Magnuson *et al*[27], in an investigation of 98 patients reported sensitivity and specificity for WBC imaging of 88% and 73% respectively, for lower extremity joint replacement infection.

In some studies, WBC imaging was specific, but not sensitive for prosthetic joint infection, while in others the test was sensitive but not specific[15,34,44,45].

Poor sensitivity has been ascribed to the chronicity of the process; *i.e.*, presumably the neutrophilic response had ceased, or at least waned, by the time the patient underwent imaging. Neutrophils, however, almost always are present in the infected joint replacement, regardless of the duration of symptoms, so chronicity does not explain low sensitivity.

Poor specificity often has been attributed to nonspecific inflammation. It was thought that false positive results were secondary to labeled leukocyte accumulation in aseptic inflammation. Although aseptic inflammation around a prosthetic joint replacement is often accompanied by an intense leukocyte response, neutrophils rarely are present. In most situations, primarily neutrophils are labeled and the sensitivity of WBC imaging is greatest for detecting infections characterized by a neutrophilic response. The test is not at all sensitive, however, for detecting inflammation that is not neutrophil mediated[40]. Given the lack of a neutrophilic response in the aseptically inflamed prosthesis, inflammation cannot be the sole explanation for poor specificity.

What is the reason for the variable and often contradictory observations? WBC images usually are interpreted by comparing intensity of periprosthetic uptake to intensity of uptake in some predefined reference point, typically an area of presumably normal bone marrow. Studies in which intensity of labeled leukocyte activity in the area of interest exceeds intensity of activity in the reference point are classified as positive for infection; otherwise the study is negative. The likelihood of infection, however, is not related to intensity of periprosthetic activity (Figures 7A and 8A). In one investigation[46] the accuracy of the test varied with the manner in which the studies were interpreted. The mere presence of periprosthetic activity, regardless of intensity, was 100% sensitive and 23% specific. Using periprosthetic activity exceeding activity in the contralateral extremity as the criterion for infection, sensitivity was 65%, specificity was 61%[46].

There is another problem inherent in the interpretation of WBC images. Leukocytes, labeled or otherwise, accumulate in bone marrow, the normal distribution of which can be variable. Generalized, as well as localized, marrow expansion alter the "normal" distribution of marrow making it difficult to differentiate labeled leukocyte uptake in unusually located, but normal, marrow from uptake in infection[47].

In a manner analogous to bone/gallium imaging, it
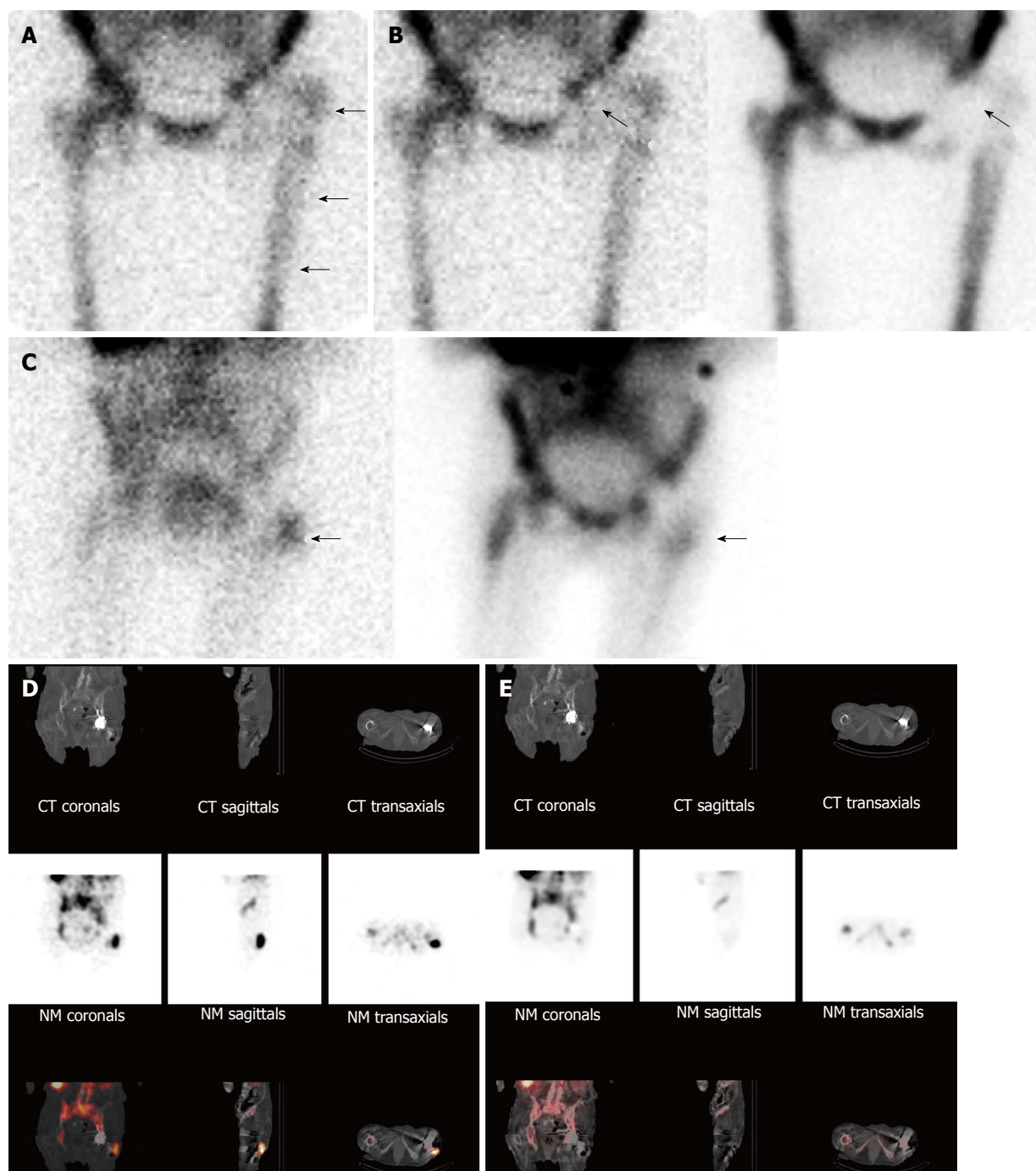
Figure 7 Infected left hip arthroplasty. A: On this anterior image from an indium-111 labeled leukocyte study, periprosthetic activity (arrows) is similar in intensity to activity in the contralateral lower extremity and less intense than pelvic activity, areas typically used as reference points when interpreting these studies. Because studies in which the intensity of labeled leukocyte activity in the region of interest does not exceed intensity of activity in the reference point, this study could be erroneously interpreted as negative for infection; B: The distribution of periprosthetic activity on the labeled leukocyte (left, ^{111}In-WBC) and sulfur colloid bone marrow (right, ^{99m}Tc-SC) images is spatially incongruent (arrows), *i.e.*, there is activity in the left hip joint on the labeled leukocyte image, but not on the bone marrow image. The combined study is positive for infection. (Same patient illustrated in Figure 7A); Although the planar combined indium labeled leukocyte/bone marrow study (C, left, ^{111}In-WBC; right, ^{99m}Tc-SC) is positive for infection (arrows), precise information about the location and extent of infection is lacking. On the fused images (bottom row) from the labeled leukocyte SPECT/CT (D) the location of the abnormal labeled leukocyte accumulation (arrows) can clearly be seen adjacent and extending to the prosthesis at the level of the greater trochanter. Note also the adjacent hypodense area in the soft tissues, consistent with abscess. Bone marrow SPECT/CT images (E) acquired simultaneously with the labeled leukocyte images in 16a confirm that the activity on the labeled leukocyte component of the examination is due to infection. Whether or not the bone marrow component of the SPECT/CT study contributes additional information beyond what planar imaging provides remains to be determined.

has been suggested that interpreting WBC images together with bone scans improves results. In one study, WBC imaging alone was 45% specific for prosthetic joint in-

fection, but improved to 85% with the addition of bone imaging[44]. Johnson *et al*[45] observed that the combined test was more specific and only slightly less sensitive than
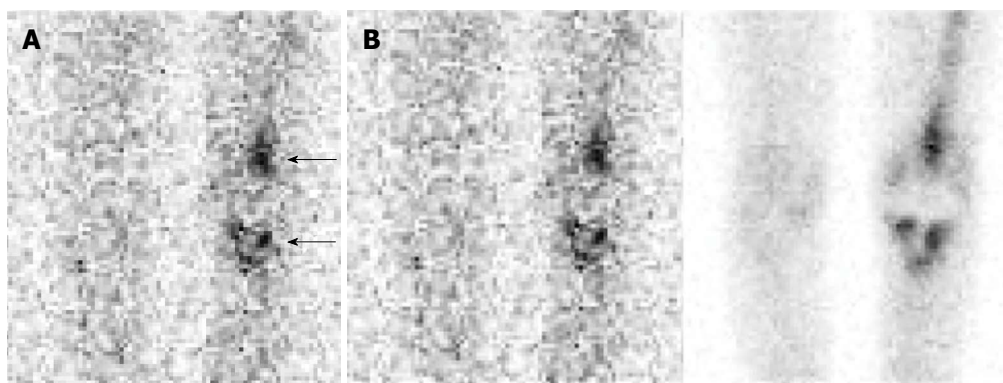
Figure 8 Aseptically loosened left knee arthroplasty. A: On this anterior image from an indium-111 labeled leukocyte study, there is intense periprosthetic activity around both the tibial and femoral components (arrows), while there is no activity around the contralateral knee. The study could be interpreted erroneously as positive for infection. Compare the intensity of activity around this prosthesis with the intensity of activity around the infected hip arthroplasty in Figure 7A. As these two cases illustrate, the intensity of labeled leukocyte activity around a prosthetic joint is not a reliable criterion for determining the presence or absence of infection; B: The distribution of periprosthetic activity on the labeled leukocyte (left, ^{111}In-WBC) and sulfur colloid bone marrow (right, ^{99m}Tc-SC) images is virtually identical (spatially congruent) and the combined study is negative for infection. The periprosthetic activity on the labeled leukocyte image is due to marrow, not to infection. Performing complementary bone marrow imaging eliminates the two major difficulties inherent in the interpretation of labeled leukocyte images: variable intensity of periprosthetic activity and differentiating bone marrow activity from infection. Same patient illustrated in Figure 8A.

WBC imaging for hip replacement infection.

Palestro *et al*[24] observed that the addition of bone imaging did not increase the accuracy of WBC imaging for knee arthroplasty infection. In another investigation, the accuracy of the combined test for lower extremity joint replacement infection was only 76%[48]. In an investigation of patients with asymptomatic cementless hip replacements, using standard interpretive criteria, WBC/bone imaging would have been classified as positive for infection 15% of the time[18].

Another approach to WBC imaging of the prosthetic joint is to combine the test with bone marrow imaging, which usually is performed with ^{99m}Tc sulfur colloid. Both radiopharmaceuticals accumulate in the reticuloendothelial cells of the bone marrow. The distribution of marrow activity on WBC and bone marrow images parallel one another in most situations. The one exception is osteomyelitis, in which the distribution of these two agents differs, *i.e.*, the images are spatially incongruent (Figures 7B and 8B)[47].

Mulamba *et al*[49] reported 92% sensitivity and 100% specificity for prosthetic hip infection. Palestro *et al*[24,46] reported similar results for infected hip and knee arthroplasties. Love *et al*[50] studied 59 lower extremity joint prostheses and reported that WBC/marrow imaging was 95% accurate for infection. El Espera *et al*[51] reported 91% accuracy for lower extremity prosthetic joint infection.

Virtually all of the investigations published to date indicate that WBC/marrow imaging is specific for joint replacement infection. In most of the investigations the test has proved to be sensitive as well. Joseph *et al*[52] however, reported that although test was 100% specific, the test was only 66% sensitive. Pill *et al*[53] reported similar results. It is unfortunate indeed that no illustrations of false negative studies, the salient point of these investigations, were provided in either publication.

There are some data that indicate performing WBC imaging at more than one time point could obviate the need for marrow imaging. The hypothesis is that images acquired shortly after injection represent marrow while images acquired later represent infection. Difference in uptake patterns over time is indicative of infection. The accuracy of the test improved from about 75% when images were interpreted visually, to about 95% when semiquantitative analysis was performed[54].

There are, unfortunately, disadvantages to WBC/marrow imaging. The leukocyte labeling procedure is demanding, not routinely available, and involves contact with blood products. Labeling enough leukocytes to produce diagnostically useful studies can be difficult in immunocompromised individuals. Image quality, especially when using indium-111, is not ideal. The need to perform marrow imaging is another disadvantage. Radiolabeled antigranulocyte antibodies and antibody fragments have been explored as alternatives.

Besilesomab is a murine monoclonal G1 immunoglobulin that binds to Normal Cross-reactive Antigen-95 on leukocytes[55]. Using visual image analysis the sensitivity and specificity for joint replacement infection range from 67%-91% and 57%-75%, respectively. By performing complementary bone imaging or semiquantitative analysis, sensitivity ranged from 67% to 100%; specificity ranged from 84% to 100%[56-59].

Sulesomab is a fragment antigen binding (Fab') portion of a murine monoclonal G1 immunoglobulin that binds to Nonspecific Cross-reactive Antigen-90 on leukocytes[55]. Reported sensitivity and specificity for prosthetic joint infection have ranged from 75% to 93% and 65% to 86%, respectively[60-62]. Dual time point imaging and time activity curve analysis may improve test accuracy[63-65].

Somewhat surprisingly, even though *in-vivo* labeled leukocytes accumulate in the marrow, in much the same way that *in-vitro* labeled leukocytes do, scant attention has

been paid to combining these studies with bone marrow imaging. In one of the few investigations in which complementary bone marrow imaging was performed, Sousa et al[66] reported that the specificity of ^{99m}Tc-sulesomab increased from 20% to 100%, when complementary marrow imaging was performed.

Using in-vivo labeled leukocytes overcomes the limitations of the in-vitro labeling procedure. Based on published data however, an additional study, either bone or marrow imaging probably still needs to be performed. Furthermore, besilesomab, which is a murine antibody, incites a human antimurine antibody (HAMA) response in up to 30% of patients[57]. Patients should be screened for HAMA and a positive result is a contraindication to the procedure. Because of immunogenicity concerns, patients should not undergo repeat studies with this agent. Not surprisingly, in-vivo labeled WBC imaging, using antigranulocyte antibodies, has not gained wide acceptance in the diagnostic workup of the painful joint replacement.

[18]F-fluorodeoxyglucose

[18]F-fluorodeoxyglucose (FDG) is transported into cells via glucose transporters and phosphorylated to [18]F-2'-FDG-6 phosphate but is not metabolized. FDG uptake depends on cellular metabolic rate and the number of glucose transporters. Activated leukocytes demonstrate increased expression of these transporters with increased affinity for FDG in the presence of cytokines and growth factors. There are several advantages to FDG. The procedure is completed within two hours after injection. Target to background ratio is high. Images obtained with positron emission tomography (PET) have much higher resolution than those obtained with conventional agents[67].

Several investigators have studied the role of FDG-PET for evaluating painful lower extremity joint prostheses. Zhuang et al[68] evaluated 74 lower extremity joint prostheses and reported that increased activity along the bone prosthesis interface was 89.5% and 77.8 % for diagnosing infection of hip and knee arthroplasties, respectively. Accuracy depended on location, not intensity, of FDG uptake. Using similar criteria Chacko et al[69] reported that the test was 92% sensitive and 97% specific for hip replacement infection. Infection could not be differentiated from aseptic loosening based on intensity of periprosthetic uptake.

Reinartz et al[29] studied 92 hip prostheses with three phase bone scintigraphy and FDG-PET. Sensitivity, specificity and accuracy of three phase bone scintigraphy were 68%, 76% and 74% vs 94%, 95%, and 95%, respectively, for FDG-PET. Activity around the acetabular component and proximal aspect of the femoral component on FDG-PET images was not associated with infection. Pattern, but not intensity, of periprosthetic uptake was useful for differentiating infection from aseptic loosening. Cremerius et al[70] reported that FDG was 89% accurate for hip replacement infection. Gravius et al[71] reported similar results. Pill et al[53] studied 92 painful hip prostheses, including 21 infected devices, and reported that FDG

was 95% sensitive and 93% specific for diagnosing infection. Fifty one of the prostheses, including ten infected devices, also were studied with WBC/marrow imaging. The sensitivity and specificity of WBC/marrow imaging in this subgroup were 50% and 95.1%, respectively.

Manthey et al[72] reported that FDG was 96% accurate for prosthetic joint infection. They also reported that activity around the femoral head and neck indicated synovitis plus infection, observations that contradict those of previous investigations[68,69].

Stumpe et al[30] observed that, in patients with painful hip replacements, intense bone prosthesis interface activity was reasonably specific (81% for reader 1 and 85% for reader 2), but not sensitive (33% for reader 1, 56% for reader 2) for diagnosing infection (33% for reader 1, 56% for reader 2). The accuracy of the test, for both readers, was 69%. Bone scintigraphy was more accurate than FDG-PET (80% vs 69%) in this investigation.

Van Acker et al[73] studied 21 patients with suspected prosthetic knee infection. FDG-PET was 100% sensitive and 73% specific. Sensitivity and specificity of WBC/bone imaging was 100% and 93%, respectively. Vanquickenborne et al[74] reported similar results.

García-Barrecheguren et al[75] studied 24 hip replacements. FDG-PET was neither sensitive (64%) nor specific (67%) for infection. Delank et al[76] studied 27 patients with failed hip and knee replacements and concluded that FDG-PET could not reliably differentiate between infection and aseptic inflammation.

Love et al[50] evaluated 59 failed lower extremity joint prostheses with FDG-PET and WBC/marrow imaging. Among the criteria used for image interpretation, bone prosthesis interface activity, with a target to background ratio greater than 3.6 for hip replacements and 3.1 for knee replacements was the most accurate (71%) for diagnosing infection. The accuracy of WBC/marrow imaging, in contrast, was 95%.

In a met analysis sensitivity and specificity of FDG-PET for prosthetic joint infection were 82% and 87% respectively[77]. In view of the large number of inconsistent and contradictory results that have been reported to date, the place of FDG-PET in the assessment of the prosthetic joint remains to be determined.

Infection-specific tracers

Given the dramatic differences in the management of aseptic loosening and infection of prostheses, the importance of accurately differentiating between these two conditions cannot be overstated. The development of an infection specific imaging agent would be a welcome improvement over the current procedures.

The potential of radiolabeled antibiotics as "infection-specific" radiopharmaceuticals has been explored. The hypothesis is that the radiolabeled antibiotic enters, and is metabolized by, bacteria and could be used to accurately localize infection. Although the results of initial studies were encouraging, subsequent investigations raised significant doubts about the validity of this concept and

enthusiasm for radiolabeled antibiotics has faded[78-81].

Antimicrobial peptides bind to the bacterial cell membrane. Their expression may be constant or induced on contact with microbes. They also can be transported *via* leukocytes[82]. ^{99m}Tc-UBI 29-41, a radiolabeled synthetic fragment of the naturally occurring human antimicrobial peptide ubiquicidin, appears to be able to differentiate between infection and sterile inflammation[83]. Recent data suggest that this agent is both sensitive and specific for prosthetic joint infection[84,85].

FUTURE

Initial data suggest that single-photon emission computed tomography (SPECT)/electronic computer X-ray tomography technique (CT) may contribute useful information to the evaluation of the failed joint arthroplasty. For example, nuclear arthrography often is performed as a dual isotope procedure, in which the bone scan provides "anatomic detail" and another radiopharmaceutical, often an indium-111 labeled complex, is used for the arthrographic component. A potential alternative to the dual isotope technique is SPECT/CT arthrography, in which the CT component provides the anatomic landmarks necessary for radiopharmaceutical localization. In one investigation SPECT/CT was significantly better than planar imaging for the acetabular cup of hip prostheses[86]. For knee arthroplasties, SPECT/CT offered a significant improvement over planar imaging for detecting femoral component loosening. SPECT/CT also was better than planar imaging for detecting tibial component loosening but statistical significance was not reached.

Hirschmann *et al*[87] reported that SPECT/CT could detect mechanical loosening, joint instability, component malposition, and patellofemoral problems in patients with knee arthroplasties. In another investigation of knee arthroplasties, SPECT/CT significantly altered the working diagnosis and proposed treatment, and changed the initial intention to revise or treat the patients non-surgically. The diagnosis made with SPECT/CT was correct in all patients who underwent surgery[88].

Graute *et al*[89] evaluated the contribution of SPECT/CT as an adjunct to planar scintigraphy with ^{99m}Tc-besilesomab for diagnosing and localizing low-grade prosthetic joint infection. Planar imaging was 66% sensitive, and 60% specific for infection. Combining planar imaging with SPECT/CT, sensitivity and specificity improved to 89% and 73%, respectively.

The potential impact of SPECT/CT extends well beyond diagnosing infection. In patients with a positive study, for example, the examination could provide information about the extent of infection as well as other abnormalities involving the native bone and the prosthesis (Figure 7C-E); joint aspiration and culture could be performed at the same time. In patients with negative studies the CT component could provide information about other causes of prosthetic failure. In such a scenario patients would be spared the need to undergo multiple imaging tests at different times and possibly different locations, and a diagnosis could be made more expeditiously.

Flourine18-fluoride-PET (fluoride-PET) bone imaging shows great promise in the evaluation of joint arthroplasties. Some investigators have used this test in a manner analogous to that of conventional bone scintigraphy. Sterner *et al*[90] compared the results of fluoride-PET bone scans to plain radiographs in 14 patients with painful knee arthroplasties. Sensitivity, specificity, and accuracy of the fluoride PET study for detecting aseptic loosening were 100%, 56%, and 71%, respectively. Sensitivity, specificity, and accuracy of plain radiographs were 43%, 86%, and 64%, respectively.

Other investigators have explored the potential of fluoride-PET for studying bone metabolism. An important concern in patients undergoing hip resurfacing arthroplasty is the viability of the remaining femoral head, and the risk of postoperative fracture or avascular necrosis. Conventional radiographs are of limited utility, because the femoral head is obscured by the overlying metallic components of the device. Ullmark *et al*[91] reported that fluoride PET correctly identified aseptic necrosis in three of fourteen patients with a hip resurfacing arthroplasty. Radiographs were negative in all cases. These investigators concluded that fluoride-PET is useful for evaluating bone metabolism at resurfacing arthroplasty. In another investigation, Ullmark *et al*[92] studied bone mineralization around the femoral component of cementless hip arthroplasties. They concluded that fluoride-PET is a valuable tool for analysis of bone mineralization patterns around uncemented femoral stems and together with the modified Polar Map system could be useful to study metabolic bone responses to prosthetic implants.

There are recent data that suggest that Fluoride-PET is a valuable tool to analyse bone formation and secondary stabilization of a press-fit acetabular cup in patients undergoing total hip arthroplasty[93].

CONCLUSION

At the moment, nuclear medicine is most valuable for determining whether or not a painful joint prosthesis is infected. WBC/marrow imaging, currently, is the best available imaging test for this purpose. Preliminary data suggest that SPECT/CT, in addition to providing information about the presence and extent of infection, may be able to provide additional information about other conditions that cause joint replacements to fail. Fluoride-PET also may provide hitherto unknown insight into periprosthetic bone metabolism.

REFERENCES

1   **Love C**, Marwin SE, Palestro CJ. Nuclear medicine and the infected joint replacement. *Semin Nucl Med* 2009; **39**: 66-78 [PMID: 19038601 DOI: 10.1053/j.semnuclmed.2008.08.007]
2   **Wooley PH**, Nasser S, Fitzgerald RH. The immune response to implant materials in humans. *Clin Orthop Relat Res* 1996; **(326)**: 63-70 [PMID: 8620660]

3   **Toumbis CA**, Kronick JL, Wooley PH, Nasser S. Total joint arthroplasty and the immune response. *Semin Arthritis Rheum* 1997; **27**: 44-47 [PMID: 9287389 DOI: 10.1016/S0049-0172(97)80036-4]

4   **Spector M**, Shortkroff S, Hsu HP, Lane N, Sledge CB, Thornhill TS. Tissue changes around loose prostheses. A canine model to investigate the effects of an antiinflammatory agent. *Clin Orthop Relat Res* 1990; **(261)**: 140-152 [PMID: 2245540]

5   **Pandey R**, Drakoulakis E, Athanasou NA. An assessment of the histological criteria used to diagnose infection in hip revision arthroplasty tissues. *J Clin Pathol* 1999; **52**: 118-123 [PMID: 10396239 DOI: 10.1136/jcp.52.2.118]

6   **Del Arco A**, Bertrand ML. The diagnosis of periprosthetic infection. *Open Orthop J* 2013; **7**: 178-183 [PMID: 23898349 DOI: 10.2174/1874325001307010178]

7   **Hanssen AD**, Rand JA. Evaluation and treatment of infection at the site of a total hip or knee arthroplasty. *Instr Course Lect* 1999; **48**: 111-122 [PMID: 10098033]

8   **Palestro CJ**, Love C, Miller TT. Infection and musculoskeletal conditions: Imaging of musculoskeletal infections. *Best Pract Res Clin Rheumatol* 2006; **20**: 1197-1218 [PMID: 17127204 DOI: 10.1016/j.berh.2006.08.009]

9   **Tomas X**, Bori G, Garcia S, Garcia-Diez AI, Pomes J, Soriano A, Ríos J, Almela M, Mensa J, Gallart X, Martinez JC, Riba J. Accuracy of CT-guided joint aspiration in patients with suspected infection status post-total hip arthroplasty. *Skeletal Radiol* 2011; **40**: 57-64 [PMID: 20449586 DOI: 10.1007/s00256-010-0940-2]

10   **Gelman MI**, Coleman RE, Stevens PM, Davey BW. Radiography, radionuclide imaging, and arthrography in the evaluation of total hip and knee replacement. *Radiology* 1978; **128**: 677-682 [PMID: 674636]

11   **Weiss PE**, Mall JC, Hoffer PB, Murray WR, Rodrigo JJ, Genant HK. 99mTc-methylene diphosphonate bone imaging in the evaluation of total hip prostheses. *Radiology* 1979; **133**: 727-729 [PMID: 504654]

12   **McInerney DP**, Hyde ID. Technetium 99Tcm pyrophosphate scanning in the assessment of the painful hip prosthesis. *Clin Radiol* 1978; **29**: 513-517 [PMID: 710036 DOI: 10.1016/S0009-9260(78)80039-7]

13   **Williamson BR**, McLaughlin RE, Wang GW, Miller CW, Teates CD, Bray ST. Radionuclide bone imaging as a means of differentiating loosening and infection in patients with a painful total hip prosthesis. *Radiology* 1979; **133**: 723-725 [PMID: 504653]

14   **Williams F**, McCall IW, Park WM, O'Connor BT, Morris V. Gallium-67 scanning in the painful total hip replacement. *Clin Radiol* 1981; **32**: 431-439 [PMID: 7249522 DOI: 10.1016/S0009-9260(81)80292-9]

15   **Mountford PJ**, Hall FM, Wells CP, Coakley AJ. 99Tcm-MDP, 67Ga-citrate and 111In-leucocytes for detecting prosthetic hip infection. *Nucl Med Commun* 1986; **7**: 113-120 [PMID: 3459112]

16   **Aliabadi P**, Tumeh SS, Weissman BN, McNeil BJ. Cemented total hip prosthesis: radiographic and scintigraphic evaluation. *Radiology* 1989; **173**: 203-206 [PMID: 2675184]

17   **Utz JA**, Lull RJ, Galvin EG. Asymptomatic total hip prosthesis: natural history determined using Tc-99m MDP bone scans. *Radiology* 1986; **161**: 509-512 [PMID: 3763923]

18   **Oswald SG**, Van Nostrand D, Savory CG, Callaghan JJ. Three-phase bone scan and indium white blood cell scintigraphy following porous coated hip arthroplasty: a prospective study of the prosthetic tip. *J Nucl Med* 1989; **30**: 1321-1331 [PMID: 2502609]

19   **Oswald SG**, Van Nostrand D, Savory CG, Anderson JH, Callaghan JJ. The acetabulum: a prospective study of three-phase bone and indium white blood cell scintigraphy following porous-coated hip arthroplasty. *J Nucl Med* 1990; **31**: 274-280 [PMID: 2307997]

20   **Ashbrooke AB**, Calvert PT. Bone scan appearances after uncemented hip replacement. *J R Soc Med* 1990; **83**: 768-769 [PMID: 2269959]

21   **Gallo J**, Kamínek M, Myslivecek M, Zapletalová J, Spicka J. [Validity of bone scintigraphy for the diagnosis of periprosthetic complications in hydroxyapatite-coated total hip arthroplasty]. *Acta Chir Orthop Traumatol Cech* 2004; **71**: 345-351 [PMID: 15686635]

22   **Rosenthall L**, Lepanto L, Raymond F. Radiophosphate uptake in asymptomatic knee arthroplasty. *J Nucl Med* 1987; **28**: 1546-1549 [PMID: 3655908]

23   **Hofmann AA**, Wyatt RW, Daniels AU, Armstrong L, Alazraki N, Taylor A. Bone scans after total knee arthroplasty in asymptomatic patients. Cemented versus cementless. *Clin Orthop Relat Res* 1990; **(251)**: 183-188 [PMID: 2295172]

24   **Palestro CJ**, Swyer AJ, Kim CK, Goldsmith SJ. Infected knee prosthesis: diagnosis with In-111 leukocyte, Tc-99m sulfur colloid, and Tc-99m MDP imaging. *Radiology* 1991; **179**: 645-648 [PMID: 2027967]

25   **Schauwecker DS**. The scintigraphic diagnosis of osteomyelitis. *AJR Am J Roentgenol* 1992; **158**: 9-18 [PMID: 1727365 DOI: 10.2214/ajr.158.1.1727365]

26   **Nagoya S**, Kaya M, Sasaki M, Tateda K, Yamashita T. Diagnosis of peri-prosthetic infection at the hip using triple-phase bone scintigraphy. *J Bone Joint Surg Br* 2008; **90**: 140-144 [PMID: 18256077]

27   **Magnuson JE**, Brown ML, Hauser MF, Berquist TH, Fitzgerald RH, Klee GG. In-111-labeled leukocyte scintigraphy in suspected orthopedic prosthesis infection: comparison with other imaging modalities. *Radiology* 1988; **168**: 235-239 [PMID: 3380966]

28   **Levitsky KA**, Hozack WJ, Balderston RA, Rothman RH, Gluckman SJ, Maslack MM, Booth RE. Evaluation of the painful prosthetic joint. Relative value of bone scan, sedimentation rate, and joint aspiration. *J Arthroplasty* 1991; **6**: 237-244 [PMID: 1940929 DOI: 10.1016/S0883-5403(06)80170-1]

29   **Reinartz P**, Mumme T, Hermanns B, Cremerius U, Wirtz DC, Schaefer WM, Niethard F-, Buell U. Radionuclide imaging of the painful hip arthroplasty: positron-emission tomography versus triple-phase bone scanning. *J Bone Joint Surg Br* 2005; **87**: 465-470 [PMID: 15795194 DOI: 10.1302/0301-620X.87B4.14954]

30   **Stumpe KD**, Nötzli HP, Zanetti M, Kamel EM, Hany TF, Görres GW, von Schulthess GK, Hodler J. FDG PET for differentiation of infection and aseptic loosening in total hip replacements: comparison with conventional radiography and three-phase bone scintigraphy. *Radiology* 2004; **231**: 333-341 [PMID: 15044748 DOI: 10.1148/radiol.2312021596]

31   **Palestro CJ.** Scintigraphic diagnosis of inflammation and infection. In: Brant WE, Helms CA, editors. Fundamentals of Diagnostic Radiology. 4th ed. Philadelphia: Lippincott, Williams and Wilkins, 2012: 1339-1352

32   **Reing CM**, Richin PF, Kenmore PI. Differential bone-scanning in the evaluation of a painful total joint replacement. *J Bone Joint Surg Am* 1979; **61**: 933-936 [PMID: 479243]

33   **Rushton N**, Coakley AJ, Tudor J, Wraight EP. The value of technetium and gallium scanning in assessing pain after total hip replacement. *J Bone Joint Surg Br* 1982; **64**: 313-318 [PMID: 6212587]

34   **McKillop JH**, McKay I, Cuthbert GF, Fogelman I, Gray HW, Sturrock RD. Scintigraphic evaluation of the painful prosthetic joint: a comparison of gallium-67 citrate and indium-111 labelled leucocyte imaging. *Clin Radiol* 1984; **35**: 239-241 [PMID: 6425000 DOI: 10.1016/S0009-9260(84)80148-8]

35   **Tehranzadeh J**, Gubernick I, Blaha D. Prospective study of sequential technetium-99m phosphate and gallium imaging in painful hip prostheses (comparison of diagnostic modalities). *Clin Nucl Med* 1988; **13**: 229-236 [PMID: 3163533]

36   **Gómez-Luzuriaga MA**, Galán V, Villar JM. Scintigraphy with Tc, Ga and In in painful total hip prostheses. *Int Orthop* 1988; **12**: 163-167 [PMID: 3410621 DOI: 10.1007/BF00266983]

37   **Kraemer WJ**, Saplys R, Waddell JP, Morton J. Bone scan,

gallium scan, and hip aspiration in the diagnosis of infected total hip arthroplasty. *J Arthroplasty* 1993; **8**: 611-616 [PMID: 8301279 DOI: 10.1016/0883-5403(93)90008-R]

38 **Merkel KD**, Fitzgerald RH, Brown ML. Scintigraphic examination of total hip arthroplasty: comparison of indium with technetium-gallium in the loose and infected canine arthroplasty. *Hip* 1984: 163-192 [PMID: 6597183]

39 **Merkel KD**, Brown ML, Fitzgerald RH. Sequential technetium-99m HMDP-gallium-67 citrate imaging for the evaluation of infection in the painful prosthesis. *J Nucl Med* 1986; **27**: 1413-1417 [PMID: 3462352]

40 **Palestro CJ**, Love C, Bhargava KK. Labeled leukocyte imaging: current status and future directions. *Q J Nucl Med Mol Imaging* 2009; **53**: 105-123 [PMID: 19182734]

41 **Pring DJ**, Henderson RG, Keshavarzian A, Rivett AG, Krausz T, Coombs RR, Lavender JP. Indium-granulocyte scanning in the painful prosthetic joint. *AJR Am J Roentgenol* 1986; **147**: 167-172 [PMID: 3487209]

42 **Pring DJ**, Henderson RG, Rivett AG, Krausz T, Coombs RR, Lavender JP. Autologous granulocyte scanning of painful prosthetic joints. *J Bone Joint Surg Br* 1986; **68**: 647-652 [PMID: 3733846]

43 **Rand JA**, Brown ML. The value of indium 111 leukocyte scanning in the evaluation of painful or infected total knee arthroplasties. *Clin Orthop Relat Res* 1990; **(259)**: 179-182 [PMID: 2208853]

44 **Wukich DK**, Abreu SH, Callaghan JJ, Van Nostrand D, Savory CG, Eggli DF, Garcia JE, Berrey BH. Diagnosis of infection by preoperative scintigraphy with indium-labeled white blood cells. *J Bone Joint Surg Am* 1987; **69**: 1353-1360 [PMID: 3126189]

45 **Johnson JA**, Christie MJ, Sandler MP, Parks PF, Homra L, Kaye JJ. Detection of occult infection following total joint arthroplasty using sequential technetium-99m HDP bone scintigraphy and indium-111 WBC imaging. *J Nucl Med* 1988; **29**: 1347-1353 [PMID: 3404252]

46 **Palestro CJ**, Kim CK, Swyer AJ, Capozzi JD, Solomon RW, Goldsmith SJ. Total-hip arthroplasty: periprosthetic indium-111-labeled leukocyte activity and complementary technetium-99m-sulfur colloid imaging in suspected infection. *J Nucl Med* 1990; **31**: 1950-1955 [PMID: 2266391]

47 **Palestro CJ**, Love C, Tronco GG, Tomas MB, Rini JN. Combined labeled leukocyte and technetium 99m sulfur colloid bone marrow imaging for diagnosing musculoskeletal infection. *Radiographics* 2006; **26**: 859-870 [PMID: 16702459 DOI: 10.1148/rg.263055139]

48 **Teller RE**, Christie MJ, Martin W, Nance EP, Haas DW. Sequential indium-labeled leukocyte and bone scans to diagnose prosthetic joint infection. *Clin Orthop Relat Res* 2000; **(373)**: 241-247 [PMID: 10810483]

49 **Mulamba L**, Ferrant A, Leners N, de Nayer P, Rombouts JJ, Vincent A. Indium-111 leucocyte scanning in the evaluation of painful hip arthroplasty. *Acta Orthop Scand* 1983; **54**: 695-697 [PMID: 6670484 DOI: 10.3109/17453678308996613]

50 **Love C**, Marwin SE, Tomas MB, Krauss ES, Tronco GG, Bhargava KK, Nichols KJ, Palestro CJ. Diagnosing infection in the failed joint replacement: a comparison of coincidence detection 18F-FDG and 111In-labeled leukocyte/99mTc-sulfur colloid marrow imaging. *J Nucl Med* 2004; **45**: 1864-1871 [PMID: 15534056]

51 **El Espera I**, Blondet C, Moullart V, Saïdi L, Havet E, Mertl P, Canarelli B, Schmit JL, Meyer ME. The usefulness of 99mTc sulfur colloid bone marrow scintigraphy combined with 111In leucocyte scintigraphy in prosthetic joint infection. *Nucl Med Commun* 2004; **25**: 171-175 [PMID: 15154708]

52 **Joseph TN**, Mujtaba M, Chen AL, Maurer SL, Zuckerman JD, Maldjian C, Di Cesare PE. Efficacy of combined technetium-99m sulfur colloid/indium-111 leukocyte scans to detect infected total hip and knee arthroplasties. *J Arthroplasty* 2001; **16**: 753-758 [PMID: 11547374 DOI: 10.1054/arth.2001.24446]

53 **Pill SG**, Parvizi J, Tang PH, Garino JP, Nelson C, Zhuang H, Alavi A. Comparison of fluorodeoxyglucose positron emission tomography and (111)indium-white blood cell imaging in the diagnosis of periprosthetic infection of the hip. *J Arthroplasty* 2006; **21**: 91-97 [PMID: 16950069 DOI: 10.1016/j.arth.2006.05.021]

54 **Pelosi E**, Baiocco C, Pennone M, Migliaretti G, Varetto T, Maiello A, Bellò M, Bisi G. 99mTc-HMPAO-leukocyte scintigraphy in patients with symptomatic total hip or knee arthroplasty: improved diagnostic accuracy by means of semiquantitative evaluation. *J Nucl Med* 2004; **45**: 438-444 [PMID: 15001684]

55 **Love C**, Palestro CJ. 99mTc-fanolesomab Palatin Technologies. *IDrugs* 2003; **6**: 1079-1085 [PMID: 14600841]

56 **Boubaker A**, Delaloye AB, Blanc CH, Dutoit M, Leyvraz PF, Delaloye B. Immunoscintigraphy with antigranulocyte monoclonal antibodies for the diagnosis of septic loosening of hip prostheses. *Eur J Nucl Med* 1995; **22**: 139-147 [PMID: 7758501 DOI: 10.1007/BF00838944]

57 **Gratz S**, Höffken H, Kaiser JW, Behr TM, Strosche H, Reize P. [Nuclear medical imaging in case of painful knee arthroplasty]. *Radiologe* 2009; **49**: 59-67 [PMID: 18597065 DOI: 10.1007/s00117-008-1703-0]

58 **Klett R**, Steiner D, Puille M, Khalisi A, Matter HP, Stürz H, Bauer R. [Antigranulocyte scintigraphy of septic loosening of hip endoprosthesis: effect of different methods of analysis]. *Nuklearmedizin* 2001; **40**: 75-79 [PMID: 11475076]

59 **Klett R**, Kordelle J, Stahl U, Khalisi A, Puille M, Steiner D, Bauer R. Immunoscintigraphy of septic loosening of knee endoprosthesis: a retrospective evaluation of the antigranulocyte antibody BW 250/183. *Eur J Nucl Med Mol Imaging* 2003; **30**: 1463-1466 [PMID: 14579084 DOI: 10.1007/s00259-003-1275-1]

60 **von Rothenburg T**, Schoellhammer M, Schaffstein J, Koester O, Schmid G. Imaging of infected total arthroplasty with Tc-99m-labeled antigranulocyte antibody Fab'fragments. *Clin Nucl Med* 2004; **29**: 548-551 [PMID: 15311121]

61 **Iyengar KP**, Vinjamuri S. Role of 99mTc Sulesomab in the diagnosis of prosthetic joint infections. *Nucl Med Commun* 2005; **26**: 489-496 [PMID: 15891591]

62 **Pakos EE**, Fotopoulos AD, Stafilas KS, Gavriilidis I, Al Boukarali G, Tsiouris S, Xenakis TA. Use of (99m)Tc-sulesomab for the diagnosis of prosthesis infection after total joint arthroplasty. *J Int Med Res* 2007; **35**: 474-481 [PMID: 17697524 DOI: 10.1177/147323000703500406]

63 **Rubello D**, Casara D, Maran A, Avogaro A, Tiengo A, Muzzio PC. Role of anti-granulocyte Fab' fragment antibody scintigraphy (LeukoScan) in evaluating bone infection: acquisition protocol, interpretation criteria and clinical results. *Nucl Med Commun* 2004; **25**: 39-47 [PMID: 15061263]

64 **Rubello D**, Rampin L, Banti E, Massaro A, Cittadin S, Cattelan AM, Al-Nahhas A. Diagnosis of infected total knee arthroplasty with anti-granulocyte scintigraphy: the importance of a dual-time acquisition protocol. *Nucl Med Commun* 2008; **29**: 331-335 [PMID: 18317296]

65 **Gratz S**, Behr TM, Reize P, Pfestroff A, Kampen WU, Höffken H. (99m)Tc-Fab' fragments (sulesomab) for imaging septically loosened total knee arthroplasty. *J Int Med Res* 2009; **37**: 54-67 [PMID: 19215674 DOI: 10.1177/147323000903700107]

66 **Sousa R**, Massada M, Pereira A, Fontes F, Amorim I, Oliveira A. Diagnostic accuracy of combined 99mTc-sulesomab and 99mTc-nanocolloid bone marrow imaging in detecting prosthetic joint infection. *Nucl Med Commun* 2011; **32**: 834-839 [PMID: 21799370]

67 **Love C**, Tomas MB, Tronco GG, Palestro CJ. FDG PET of infection and inflammation. *Radiographics* 2005; **25**: 1357-1368 [PMID: 16160116 DOI: 10.1148/rg.255045122]

68 **Zhuang H**, Duarte PS, Pourdehnad M, Maes A, Van Acker F, Shnier D, Garino JP, Fitzgerald RH, Alavi A. The promising role of 18F-FDG PET in detecting infected lower limb prosthesis implants. *J Nucl Med* 2001; **42**: 44-48 [PMID: 11197979]

69 **Chacko TK**, Zhuang H, Stevenson K, Moussavian B, Alavi

A. The importance of the location of fluorodeoxyglucose uptake in periprosthetic infection in painful hip prostheses. *Nucl Med Commun* 2002; **23**: 851-855 [PMID: 12195089]

70   **Cremerius U**, Mumme T, Reinartz P, Wirtz D, Niethard FU, Büll U. [Analysis of (18)F-FDG uptake patterns in PET for diagnosis of septic and aseptic loosening after total hip arthroplasty]. *Nuklearmedizin* 2003; **42**: 234-239 [PMID: 14668955]

71   **Gravius S**, Gebhard M, Ackermann D, Büll U, Hermanns-Sachweh B, Mumme T. [Analysis of 18F-FDG uptake pattern in PET for diagnosis of aseptic loosening versus prosthesis infection after total knee arthroplasty. A prospective pilot study]. *Nuklearmedizin* 2010; **49**: 115-123 [PMID: 20407734 DOI: 10.3413/nukmed-0278]

72   **Manthey N**, Reinhard P, Moog F, Knesewitsch P, Hahn K, Tatsch K. The use of [18 F]fluorodeoxyglucose positron emission tomography to differentiate between synovitis, loosening and infection of hip and knee prostheses. *Nucl Med Commun* 2002; **23**: 645-653 [PMID: 12089487]

73   **Van Acker F**, Nuyts J, Maes A, Vanquickenborne B, Stuyck J, Bellemans J, Vleugels S, Bormans G, Mortelmans L. FDG-PET, 99mtc-HMPAO white blood cell SPET and bone scintigraphy in the evaluation of painful total knee arthroplasties. *Eur J Nucl Med* 2001; **28**: 1496-1504 [PMID: 11685492 DOI: 10.1007/s002590100603]

74   **Vanquickenborne B**, Maes A, Nuyts J, Van Acker F, Stuyck J, Mulier M, Verbruggen A, Mortelmans L. The value of (18)FDG-PET for the detection of infected hip prosthesis. *Eur J Nucl Med Mol Imaging* 2003; **30**: 705-715 [PMID: 12616322 DOI: 10.1007/s00259-002-1109-6]

75   **García-Barrecheguren E**, Rodríguez Fraile M, Toledo Santana G, Valentí Nín JR, Richter Echevarría JA. [FDG-PET: a new diagnostic approach in hip prosthetic replacement]. *Rev Esp Med Nucl* 2007; **26**: 208-220 [PMID: 17662187 DOI: 10.1157/13107972]

76   **Delank KS**, Schmidt M, Michael JW, Dietlein M, Schicha H, Eysel P. The implications of 18F-FDG PET for the diagnosis of endoprosthetic loosening and infection in hip and knee arthroplasty: results from a prospective, blinded study. *BMC Musculoskelet Disord* 2006; **7**: 20 [PMID: 16512924 DOI: 10.1186/1471-2474-7-20]

77   **Kwee TC**, Kwee RM, Alavi A. FDG-PET for diagnosing prosthetic joint infection: systematic review and metaanalysis. *Eur J Nucl Med Mol Imaging* 2008; **35**: 2122-2132 [PMID: 18704405 DOI: 10.1007/s00259-008-0887-x]

78   **Britton KE**, Wareham DW, Das SS, Solanki KK, Amaral H, Bhatnagar A, Katamihardja AH, Malamitsi J, Moustafa HM, Soroa VE, Sundram FX, Padhy AK. Imaging bacterial infection with (99m)Tc-ciprofloxacin (Infecton). *J Clin Pathol* 2002; **55**: 817-823 [PMID: 12401818 DOI: 10.1136/jcp.55.11.817]

79   **Sonmezoglu K**, Sonmezoglu M, Halac M, Akgün I, Türkmen C, Onsel C, Kanmaz B, Solanki K, Britton KE, Uslu I. Usefulness of 99mTc-ciprofloxacin (infecton) scan in diagnosis of chronic orthopedic infections: comparative study with 99mTc-HMPAO leukocyte scintigraphy. *J Nucl Med* 2001; **42**: 567-574 [PMID: 11337543]

80   **Sarda L**, Crémieux AC, Lebellec Y, Meulemans A, Lebtahi R, Hayem G, Génin R, Delahaye N, Huten D, Le Guludec D. Inability of 99mTc-ciprofloxacin scintigraphy to discriminate between septic and sterile osteoarticular diseases. *J Nucl Med* 2003; **44**: 920-926 [PMID: 12791820]

81   **Siaens RH**, Rennen HJ, Boerman OC, Dierckx R, Slegers G. Synthesis and comparison of 99mTc-enrofloxacin and 99mTc-ciprofloxacin. *J Nucl Med* 2004; **45**: 2088-2094 [PMID: 15585486]

82   **Lupetti A**, Pauwels EK, Nibbering PH, Welling MM. 99mTc-antimicrobial peptides: promising candidates for infection imaging. *Q J Nucl Med* 2003; **47**: 238-245 [PMID: 14973416]

83   **Lupetti A**, Welling MM, Mazzi U, Nibbering PH, Pauwels EK. Technetium-99m labelled fluconazole and antimicrobial peptides for imaging of Candida albicans and Aspergillus fumigatus infections. *Eur J Nucl Med Mol Imaging* 2002; **29**: 674-679 [PMID: 11976807 DOI: 10.1007/s00259-001-0760-7]

84   **Sarda-Mantel L**, Saleh-Mghir A, Welling MM, Meulemans A, Vrigneaud JM, Raguin O, Hervatin F, Martet G, Chau F, Lebtahi R, Le Guludec D. Evaluation of 99mTc-UBI 29-41 scintigraphy for specific detection of experimental Staphylococcus aureus prosthetic joint infections. *Eur J Nucl Med Mol Imaging* 2007; **34**: 1302-1309 [PMID: 17334764 DOI: 10.1007/s00259-007-0368-7]

85   **Arteaga de Murphy C**, Gemmel F, Balter J. Clinical trial of specific imaging of infections. *Nucl Med Commun* 2010; **31**: 726-733 [PMID: 20526222]

86   **Chew CG**, Lewis P, Middleton F, van den Wijngaard R, Deshaies A. Radionuclide arthrogram with SPECT/CT for the evaluation of mechanical loosening of hip and knee prostheses. *Ann Nucl Med* 2010; **24**: 735-743 [PMID: 20976575 DOI: 10.1007/s12149-010-0419-1]

87   **Hirschmann MT**, Iranpour F, Konala P, Kerner A, Rasch H, Cobb JP, Friederich NF. A novel standardized algorithm for evaluating patients with painful total knee arthroplasty using combined single photon emission tomography and conventional computerized tomography. *Knee Surg Sports Traumatol Arthrosc* 2010; **18**: 939-944 [PMID: 20148324 DOI: 10.1007/s00167-010-1070-z]

88   **Hirschmann MT**, Konala P, Iranpour F, Kerner A, Rasch H, Friederich NF. Clinical value of SPECT/CT for evaluation of patients with painful knees after total knee arthroplasty--a new dimension of diagnostics? *BMC Musculoskelet Disord* 2011; **12**: 36 [PMID: 21294878 DOI: 10.1186/1471-2474-12-36]

89   **Graute V**, Feist M, Lehner S, Haug A, Müller PE, Bartenstein P, Hacker M. Detection of low-grade prosthetic joint infections using 99mTc-antigranulocyte SPECT/CT: initial clinical results. *Eur J Nucl Med Mol Imaging* 2010; **37**: 1751-1759 [PMID: 20309680 DOI: 10.1007/s00259-010-1431-3]

90   **Sterner T**, Pink R, Freudenberg L, Jentzen T, Quitmann H, Bockisch A, Löer F. The role of [18F]fluoride positron emission tomography in the early detection of aseptic loosening of total knee arthroplasty. *Int J Surg* 2007; **5**: 99-104 [PMID: 17448973 DOI: 10.1016/j.ijsu.2006.05.002]

91   **Ullmark G**, Sundgren K, Milbrink J, Nilsson O, Sörensen J. Osteonecrosis following resurfacing arthroplasty. *Acta Orthop* 2009; **80**: 670-674 [PMID: 19995317 DOI: 10.3109/17453670903278258]

92   **Ullmark G**, Nilsson O, Maripuu E, Sörensen J. Analysis of bone mineralization on uncemented femoral stems by [18F]-fluoride-PET: a randomized clinical study of 16 hips in 8 patients. *Acta Orthop* 2013; **84**: 138-144 [PMID: 23506163 DOI: 10.3109/17453674.2013.786632]

93   **Ullmark G**, Sörensen J, Nilsson O. Analysis of bone formation on porous and calcium phosphate-coated acetabular cups: a randomised clinical [18F]fluoride PET study. *Hip Int* 2012; **22**: 172-178 [PMID: 22547382 DOI: 10.5301/HIP.2012.9233]

REVIEW

Echographic imaging of tumoral cells through novel nanosystems for image diagnosis

Marco Di Paola, Fernanda Chiriacò, Giulia Soloperto, Francesco Conversano, Sergio Casciaro

Marco Di Paola, Fernanda Chiriacò, Giulia Soloperto, Francesco Conversano, Sergio Casciaro, Nanoimaging LAB and Bioengineering Division of the National Research Council, Institute of Clinical Physiology, 73100 Lecce, Italy

Sergio Casciaro, Consiglio Nazionale delle Ricerche, Istituto di Fisiologia Clinica (CNR-IFC) c/o Campus Ecotekne, 73100 Lecce, Italy

Correspondence to: Dr. Sergio Casciaro, Consiglionale delle Ricerche, Istituto di Fisiologia Clinica (CNR-IFC) c/o Campus Ecotekne, via per Monteroni, 73100 Lecce, Italy. sergio.casciaro@cnr.it
Telephone: +39-0832-422310 Fax: +39-0832-422341

Abstract

Since the recognition of disease molecular basis, it has become clear that the keystone moments of medical practice, namely early diagnosis, appropriate therapeutic treatment and patient follow-up, must be approached at a molecular level. These objectives will be in the near future more effectively achievable thanks to the impressive developments in nanotechnologies and their applications to the biomedical field, starting-up the nanomedicine era. The continuous advances in the development of biocompatible smart nanomaterials, in particular, will be crucial in several aspects of medicine. In fact, the possibility of manufacturing nanoparticle contrast agents that can be selectively targeted to specific pathological cells has extended molecular imaging applications to non-ionizing techniques and, at the same time, has made reachable the perspective of combining highly accurate diagnoses and personalized therapies in a single theranostic intervention. Main developing applications of nanosized theranostic agents include targeted molecular imaging, controlled drug release, therapeutic monitoring, guidance of radiation-based treatments and surgical interventions. Here we will review the most recent findings in nanoparticles contrast agents and their applications in the field of cancer molecular imaging employing non-ionizing techniques and disease-specific contrast agents, with special focus on recent findings on those nanomaterials particularly promising for ultrasound molecular imaging and simultaneous treatment of cancer.

Core tip: The development of novel nanomaterials specifically targeting diseased cells has made possible their employment as nanosized contrast agents also for non-ionizing molecular imaging techniques namely, magnetic resonance, ultrasound and optical imaging. Among them, ultrasound imaging might represent the best choice because of its low cost, ease of use and wide availability in clinical practice. Unfortunately, their actual employment in molecular imaging is limited due to their low tissue contrast discrimination. Hence, the described development of novel ultrasound targeted contrast agent may play a crucial role for their use in clinical molecular imaging.

Di Paola M, Chiriacò F, Soloperto G, Conversano F, Casciaro S. Echographic imaging of tumoral cells through novel nano-

INTRODUCTION

One of the hottest research topic of the last decade in the medical field is related to nanomedicine, a new open field of modern medicine relying on advanced nanotechnology applied to medicine. In fact, the latest advances in nanotechnology and their application to the biomedical environment are dramatically changing the overall disease management process, starting from first diagnosis to the evaluation of treatment effects, leading to the concept of personalized medicine, characterized by very early, even pre-symptomatic, diagnosis accompanied by highly-effective targeted therapies[1-4]. At this regard, the introduction of novel nanotechnology-based techniques in medical imaging and drug delivery allows to define personalized diagnoses and therapies, employing minimally invasive approaches based on non-ionizing imaging techniques for early detection of diseases[5]. From these recent advances arises the concept of molecular imaging, which is gaining an increasingly important role in both pathology understanding and specific choice of treatment[6]. Rather than morphological or functional characteristics, molecular imaging techniques are specifically aimed at identifying the molecular causes of disease[7], with consequent ability to detect molecular and cellular processes in living organisms and to allow an early and careful identification and differentiation between healthy and pathological tissues. The basic aspect of molecular imaging is the use of smart contrast agents able to selectively identify specific molecular targets or cellular processes, highlighting them on the corresponding images. The rationale for the development of these new methods is that many diseases have a molecular basis, whose visualization may result in a number of advantages like early diagnosis, precise staging, real-time monitoring of therapeutic treatment, and better prognostic evaluation. The quality of the final result depends on two key-factors: (1) actual ability of contrast agents to reach their specific biological target and binding to it (targeting); and (2) performance of the detection system in terms of sensitivity and contrast enhancement.

Chemical manipulation of drugs and other nanomaterials may allow a controlled modification of some of their properties and bioactivity such as solubility, blood pool retention times, controlled release, highly specific site-targeted delivery. Concerning this particular aspect, surface functionalization with synthetic polymers and/or specific ligands can target nanosized carriers to specific cells and organs within the body after intravenous or subcutaneous injection[8-16]. These approaches may thus be used to enhance detection sensitivity in medical imaging and to improve therapeutic effectiveness with concomitant decrease of side effects. In addition, some of the

carriers can be engineered in such a way to be activated by changes in the environmental pH, chemical stimuli, by the application of a rapidly oscillating magnetic field or by the application of an external heat source[9,17-19]. Furthermore, nanoparticles for specific diagnostic purposes can be designed to act as multifunctional agents capable, for example, to simultaneously produce signals that are detectable by more than one imaging techniques, like ultrasound (US) and magnetic resonance imaging (MRI)[20,21].

Although different pathological conditions like atherosclerotic plaques, inflammation, angiogenesis and thrombus formation have been identified as possible targets of these innovative methodologies, the most promising applications of nanomedicine are those related to the new approaches to cancer diagnosis and therapy at cellular and molecular level[5,22-24]. Cancer is widely considered to be one the main cause of death in modern society, characterized by a high mortality rate often due to a late diagnosis available with conventional techniques. Current therapeutic strategies for cancer treatment, which include surgery, chemotherapy and radiotherapy, are largely invasive and exhibit significant toxicities together with a variety of side effects that worsen the quality of life of patients. It is then conceivable that the specific targeting of therapeutic agents (drugs or genes) to tumor tissues may result in a great improvement of treatment effectiveness and decrease of systemic toxicity. For these reasons nanoparticle-mediated drug targeting has been widely explored in recent years, by incorporating anticancer agents into suitable nanocapsules or by attaching therapeutic molecules to nanoparticle surface, and it actually exhibits several advantages like reduced drug dosage, increased pharmaceutical effectiveness, minimal side effects, drug protection against degradation and enhanced drug stability[10,25,26]. Anyway, one of the aspects of absolute novelty introduced by nanovector drug delivery is represented by the possibility of assessing therapy response, by directly monitoring the localization of targeted nanoparticles through non ionizing imaging techniques. Apart from these advantages, however, the possible toxicity related to nanoparticles themselves is an aspect that requires attention. The assessment of the biocompatibility of nanomaterials and their safety profile is in fact of crucial importance not only for patients treated, which can retain these materials for long period of time, but also for the production, management and disposal processes, which should be strictly regulated.

MOLECULAR IMAGING OF TUMORS

Imaging is a tool of fundamental importance in medical practice in general, and in cancer research in particular. Despite the impressive amount of imaging technologies and their applications available today, early and detailed cancer diagnosis is made possible only by using molecular imaging systems[27]. Among these, positron emission tomography (PET) is currently the only diagnostic technique

Table 1 Nanoparticles contrast agents for molecular imaging applications

Nanomaterials	Properties	Applications	Ref.
Liposomes	Lipid spherical membranes	*In vivo* ultrasound and MRI molecular imaging	[37,38]
Emulsions	Oil-in-water-type mixtures	Ultrasound and MRI	[39-41]
Polymers	Single or multiple molecular components	Molecular imaging, drug delivery	[33]
Iron particles	Paramagnetism, superparamagnetism	MRI	[42]
Gold nanoshells	Infrared absorption	MRI, photonics imaging, *in vivo* photo-thermal therapy	[43-45]
Carbon nanotubes	Fluorescence	*In vitro* optical imaging	[46-49]
Quantum dots	Fluorescence	Optical imaging	[50-53]

MRI: Magnetic resonance imaging.

in clinical use that provides imaging of tumours at molecular level. PET systems can in fact detect abnormal cellular activity well before any anatomical change is visible and structural anomalies detectable by other macroscopic imaging techniques like ultrasound, magnetic resonance (MRI), X-rays or computed tomography (CT). Nevertheless, since the high cost and the involvement of highly ionizing radiation, with consequent risks for patients, operators and environment, PET examinations cannot be routinely used for patient follow-up or for population screening purposes.

However, the recent advances in the development of smart nanoparticle contrast agents (NPCAs) opened new perspectives for diagnostic imaging techniques, allowing on one hand the extension of molecular imaging applications to non-ionizing techniques[28], like MRI[29], ultrasound[23,30] and optical imaging[31,32], and, on the other hand, introducing the possibility of combining highly detailed diagnoses and personalized therapies in single theranostic interventions[5].

A short overview of the most interesting properties of novel NPCAs and a summary of the most significant approaches to early molecular cancer diagnosis by employing non-ionizing techniques in combination with NPCAs will be illustrated in the next subparagraphs.

NPCAS

In recent years, many efforts have been made to synthesize new NPCAs suitable for cellular and molecular imaging through non-ionizing diagnostic techniques. To obtain an effective diagnostic imaging, NPCA must be designed to have the following basic characteristics: long circulating half-life, high vascular endothelium permeability, selective binding to the cellular/molecular target of interest, significant contrast-to-noise ratio enhancement, absence of toxicity, ease of clinical use, and compatibility with standard commercially available imaging systems[22,33].

The very crucial point is the effective interaction of NPCAs with their molecular targets, which is strongly dependent on nanoparticle size. In normal conditions, 50 nm can be considered as the upper size threshold to cross the vascular endothelium and directly target extravascular cells, larger diameters allowing only the recognition of intravascular targets. However, since the consistent difference between normal and tumor vessels, effective targeting of cancer cells beyond the capillary endothelium can occur also with bigger NPCAs. In fact, due to the aberrant angiogenesis, tumor vasculature is more leaky than normal one and exhibits the so-called EPR (enhanced permeability and retention) effect, which results in enhanced permeability and retention of particles that are smaller than the pore diameter of tumor endothelium (typically between 380 and 780 nm)[34-36].

One of the most common strategies to selectively target specific cellular receptors is functionalization, which is the conjugation of NPCA surface with specific ligands. Sometimes, a polymeric coating of particles may be necessary not only to improve particle stability and to modulate their intravascular half-life, but also to increase biocompatibility and to avoid immediate sequestration by the reticulo-endothelial system (RES).

Hitherto, the variety of nanomaterials synthesized that can be used as contrast agents for molecular imaging is very wide. Table 1 provides a list of different nanosized materials, with their chemical-physical properties, applications and the main literature-reported studies, their detailed description being beyond the goal of this review.

NON-IONIZING TECHNIQUES FOR MOLECULAR IMAGING

Magnetic resonance imaging

Owing to its high resolution and elevated anatomical contrast, MRI is widely and successfully adopted in clinical routine. However, while standard MRI protocols are effective in detecting global properties of a tissue (*e.g.*, relaxation times T1, T2, *etc.*), the low sensitivity of these techniques in normal conditions hampers their direct employment for molecular imaging purposes[6].

Nevertheless, the relatively low MRI contrast might be enhanced by using novel nanotechnologies[22]. Indeed, paramagnetic nanoparticles functionalized with several copies of Gd chelates were successfully exploited in both MRI molecular imaging and targeted therapy of atherosclerotic plaques[22,41].

Other clinical applications of MRI molecular imaging, ranging from liver disease to several type of cancers[27], have also been reported by using FeO nanoparticles coated with PEG (polyethylene glycol) or other polymers[54,55].

To further improve MRI sensitivity and image contrast, alternative strategies are currently under evaluation, based mainly on the synthesis of superparamagnetic nanoparticles made of metal alloys with specific chemical and physical properties (*e.g.*, $2CoFe_4O$, $2MnFe_4O$, $2NiFe_4O$, $FePt-FeO$)[56, 57].

Other methodological approaches are aimed at synthesizing multifunctional nanoparticles, detectable by high resolution MRI as well as by less expensive techniques like ultrasound or fluorescence imaging, so taking advantages of different diagnostic techniques with a single contrast agent. At this regard, "*in vitro*" experiments with dual mode silica nanospheres covered by an outer shell of superparamagnetic nanoparticles (in order to combine MRI and ultrasonography)[21] and with core-shell iron oxide/fluorescent silica nanoparticles (for MRI/fluorescence imaging applications)[58] have been successfully carried out.

Ultrasound imaging

Ultrasound imaging is a cheap and widely available technique offering all the previously mentioned exciting perspectives even if some limitations do apply, which are mostly related to the physical needs for wave transmission pathway: some anatomical sites remain not easily reachable because of boundary bone structures like brain, bone marrow, pelvic organs, *etc.* Furthermore, some technological limitations for 3D and multi-planar imaging acquisitions still remain, which make echographic examinations the first level diagnostic approach and not the ideal candidate for in depth more accurate investigations.

Some of the above described limitations, however, can be overcome by employing ultrasound contrast agents, commercially available for clinical use like microbubbles, and other novel nanosized targeted contrast agents under research development.

All contrast agents approved for routinely use in clinical ultrasound imaging are in the form of aqueous solutions of shell-stabilized gas-filled microbubbles[59]. Under an ultrasonic beam, microbubbles undergo volumetric oscillations with consequent emission of detectable ultrasound signals that can be exploited to enhance image contrast.

Upon controlled structural modifications, microbubbles can acquire targeting specificity, becoming then suitable also for molecular imaging purposes[23]. Based on the strategy adopted[60], microbubble targeting can be passive, in which the intrinsic properties of the shell promote cell adhesion[61,62], or active, in which the shell is functionalized with specific ligands toward target cells or tissues[63-66].

However, since microbubbles diameter ranges in the micrometer scale, they cannot cross endothelium wall, with consequent important limitations in their use to target extravascular cells. As a further limitation, half-lives of circulating microbubbles are in the order of just a few minutes, because of both sequestrations by reticuloendothelial system (RES) and gas diffusion phenomena[6].

As discussed before, mainly due to their lower size NPCAs show significant intrinsic advantages with respect to microbubbles. In fact, nanoparticles can easily reach extravascular targets through endothelium crossing, and elude RES capturing. Moreover, the variety of specific surface modifications available for nanosized particles is particularly wide, with consequent effective targeting of a wide range of selected pathologies. In the last years most of the experimental work aimed at developing novel NPCAs for ultrasound molecular imaging has focused mainly on testing few type of nanoparticles, namely liposomes, perfluorocarbon nanoemulsions and nanobubbles[67-69].

Recent studies have demonstrated, however, that the use of solid nanoparticles as NPCAs may be even more effective[21,70,71]. With respect to liquid nanoparticles, solid nanomaterials exhibit in fact higher contrast enhancements, since of their higher acoustic impedance with respect to surrounding tissues, and, at the same time, are much more stable than nanobubbles, whose circulating half-life is quite limited by the aforementioned gas diffusion phenomena.

First experiments performed on solid nanoparticles as contrast agents for ultrasound imaging were carried out by using echographic probes working at very high frequencies (30-40 MHz)[72,73], whose clinical usefulness is closely restricted to intravascular or dermatological applications. More recent studies, instead, have demonstrated that silica nanospheres can be effectively detected on conventional echographic images acquired at diagnostic frequencies (7.5-10 MHz). In addition, the coating of silica nanospheres with a shell of smaller superparamagnetic nanoparticles has made possible to obtain dual-mode NCPAs, detectable by both ultrasound and MRI[21].

On the basis of these and other literature findings, the development of silica nanoparticles-based NPCAs for ultrasound molecular imaging seems to be particularly promising since of their well-documented biocompatibility[74-76], ease of functionalization[75] as well as synthesis procedures[76], potential employment as nanovectors for controlled release of drugs[77] or genes[78].

Optical and optoacoustic imaging

Since of their high sensitivity and non-invasiveness, optical imaging techniques have recently attracted the interest of researchers working on the development of novel molecular imaging protocols[6]. Optical imaging is actually mainly limited to cell biology and other non-clinical applications, due to the very low penetration of visible wavelengths into anatomical tissues. Interestingly, the use of NPCAs also in optical imaging may enhance its potential suitability in clinical applications like molecular detection of tumours. In fact, optically detectable quantum dots targeting cancer cells have been effectively visualized in both "*in vitro*" and "*in vivo*" studies[79,80]. Gold nanoshells have been used for optical coherence tomography imaging in a mouse model of colon cancer[81]. Detectable fluorescence has been observed in carbon nanotubes excited at visible wavelengths after uptake by breast cancer cells[82].
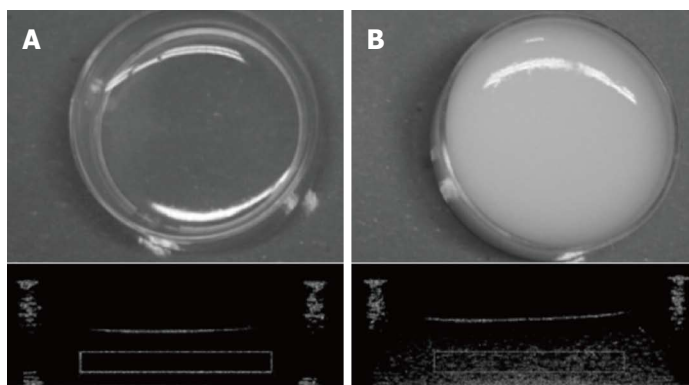
Figure 1 Echographic detection of silica nanoparticles. Sample pictures and corresponding echographic images of pure agarose gel (A) and 330 nm nanoparticle-containing gel (B).

Optoacoustic imaging is an emerging technique that combines high sensitivity and elevated contrast of optical imaging with spatial resolutions and penetration depths typical of ultrasound-based techniques[83]. Essentially, when irradiated with near-infrared short laser pulses, tissues emit acoustic waves (photoacoustic effect) that can be detected by ultrasound probes and used for imaging purposes[84]. As an example, the optical absorption of hemoglobin has allowed the optoacoustic visualization of breast tumor microvasculature[85].

Many efforts are in progress to extend the optoacoustic techniques to molecular imaging applications. Particularly promising seem to be, at this regard, noble metal nanoparticles which, as a consequence of surface Plasmon resonance, strongly absorb laser energy with subsequent generation of ultrasound signals. Although several plasmonic nanoparticles have been recently tested as potential NPCAs for optoacoustic imaging[86,87], the metal of choice seems to be gold[86,88-90] because of its high stability, facile chemistry, easy bioconjugation and very low toxicity[87,91-96]. Among the various type of gold nanoparticles, the most studied for molecular optoacoustic imaging applications are nanorods[87,97-103], which are of particular interest since of their high tendency to accumulate in tumors[24] and their potential for simultaneous photothermal therapy[104].

LATEST DEVELOPMENTS OF NPCAs FOR ULTRASOUND MOLECULAR IMAGING

Silica nanoparticles for ultrasound imaging at clinical diagnostic frequencies

As mentioned before, solid nanoparticles exhibit both higher ultrasound signal enhancement and longer stability as compared to liquid and gaseous particles of the same size. Nevertheless, ultrasound experiments carried out so far on solid nanoparticles at very high frequencies (30-40 MHz)[72,73] have limited clinical usefulness.

We have recently demonstrated that silica nanospheres are effective ultrasound contrast agents already at common diagnostic frequencies, and quantified the contrast enhancement observed as a function of particle concentration and diameter, in a range of clinical usefulness for tumor targeting purposes[70].

Diagnostic power of silica nanospheres of three different diameters (160 nm, 330 nm and 660 nm) was evaluated by measuring ultrasound backscatter in agarose phantoms containing nanoparticles at concentrations ranging from 10^{10} to 10^{13} part/mL. Imaging was performed with a digital echograph equipped with a linear transducer operating at 7.5 MHz and linked to a prototype platform for acquisition of unprocessed radiofrequency (RF) data.

Quantitative off-line analyses showed that while amplitude of nanoparticle-backscattered signals did increase as a linear function of particle concentration, image brightness did not because of saturation effects. However, when nanoparticle diameter, instead of concentration, was increased both backscatter amplitude and image brightness showed significant increments. Taking into account the previously discussed particle size characteristics for effective endothelial crossing and tumor targeting, the best combination was found to be the sample containing 330 nm silica nanospheres at a concentration of about 1 to 2×10^{11} part/mL[70]. Figure 1 shows a typical picture, with the corresponding echographic image, of agarose sample containing 330 nm silica nanoparticles at 2×10^{11} part/mL concentration.

PEG-coating and targeting of silica nanoparticles

Among the characteristics considered basic for any NPCA to be suitable for clinical molecular imaging, their biocompatibility and effective target recognition are without doubt of major importance. In a recent paper[105] we have evaluated the cytotoxicity of silica nanospheres of different diameters (160 nm, 240 nm and 330 nm) on two different tumor cell lines, namely MCF-7 cells (breast cancer) and HeLa cells (cervical cancer). Moreover, since sometimes polymeric coating of nanoparticle surface may affect significantly their biocompatibility as well as other parameters, we have synthesized and tested both uncoated and Methoxy (polyethyleneoxy) propyltrimethoxysilane (PEG)-coated silica nanospheres. Acoustic behavior of coated and uncoated particles was also investigated. The results obtained, summarized in Figure 2, showed that the incubation of MCF-7 cells with increasing concentration (up to 5 mg/mL) of uncoated silica nanospheres over 72 h caused a remarkable cytotoxicity,
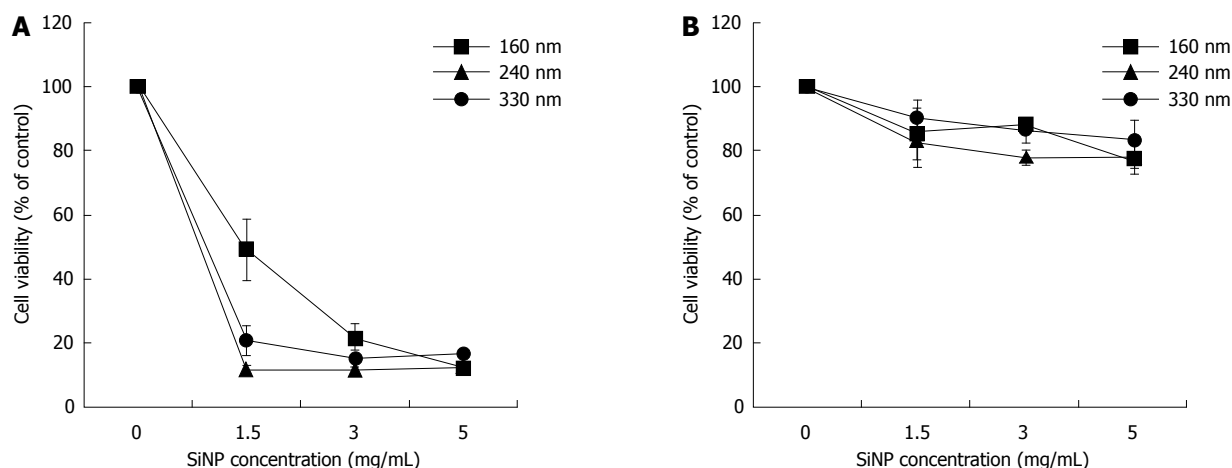
Figure 2 Effect of polyethylene glycol coating on silica nanoparticle biocompatibility. MCF-7 cells were incubated for 72 h in the presence of indicated concentrations of uncoated (A) or polyethylene glycol-coated (B) silica nanoparticles (SiNP).

which was dependent on nanoparticle diameter, concentration and incubation time, reaching percentages of cell mortality close to 80%. Conversely, in the experiments carried out using PEG-coated silica nanospheres cell viability was only slightly affected, with percentage of cell mortality lower than 30% (considered as threshold value of cytotoxicity by ISO 10993-5 international guide) at any time and at any particle concentration and diameter. Comparable results were obtained when HeLa, instead of MCF-7, cells were assayed.

Acoustic behavior of these nanoparticles was characterized exactly as described above and gave results in good agreement with those already obtained. Interestingly, at the same concentrations, 240 nm nanospheres exhibited ultrasound backscattered signals even slightly stronger than 330 nm nanoparticles, this ensuring a good contrast enhancement together with a more effective targeting potential since of their lower diameter.

Work is in progress in our laboratory aimed at functionalizing 240 nm silica nanoparticles incorporating a fluorescent probe for "*in vitro*" molecular imaging of hepatocellular carcinoma (HCC), with both ultrasound and laser-scanning confocal microscopy. HCC is the most common among all liver cancer cases (around 75%)[106], and is characterized by the particular feature to express on its cell surface Glypican-3 protein (GPC-3) which, therefore, is a good candidate for specific targeting of HCC cells[107]. On the basis of recent findings by Lee *et al*[108] demonstrating that a seven amino acid peptide exhibit high affinity in GPC-3 recognizing and binding, we have synthesized GPC-3 peptide-functionalized 240 nm fluorescent silica nanoparticles and tested them on HepG2 cells, a GPC-3 positive human hepatocarcinoma cell line. Interestingly, preliminary results show that, at concentration useful for ultrasound detection, GPC-3-targeted silica nanoparticles exhibit only negligible cytotoxic effects and seem to effectively bind to HepG2 cell plasmamembrane, as revealed by confocal microscopy and transmission electron microscopy. These results,

which however require be further substantiating by parallel experiments on GPC-3 negative cells and, more importantly, confirming also "*in vivo*", indicate that 240 nm silica nanoparticles might be a very promising theranostic agents since of their high biocompatibility, targeting effectiveness and acoustic behavior.

SILICA-BASED NANOCOMPOSITES FOR DUAL-MODE MOLECULAR IMAGING

As mentioned in previous paragraphs, our interest in exploring the employability of silica nanoparticles as effective NPCAs was extended to the possibility of designing novel silica-based hybrid nanocomposites for dual-mode molecular imaging, combining MRI and ultrasounds. At this regard, we have developed a simple and efficient synthesis protocol for multi-component nanoparticles having a spherical silica core (160 nm, 330 nm or 660 nm in diameter) coated with an outer shell of smaller superparamagnetic nanoparticles, represented by either 15-nm FeO or 17-nm FePt-FeO nanocrystals[21,109].

To evaluate the potential of these nanocomposites as MRI contrast agents, proton relaxivity measurements were performed at three radio frequency (RF) frequencies: 12.5, 23 and 60 MHz. Both the transversal relaxivity r_2 and the longitudinal relaxivity r_1 values were calculated for the different silica host nanospheres covered by IO or FePt-IO nanoparticles. As the ratio r_2/r_1 was greater than 2, all the synthesized systems were classified as good T2-relaxing systems. In particular, for each employed RF frequency and SiNP-core diameter, the r_2/r_1 ratios of FePt-IO coated SiNPs were higher than those of IO coated SiNPs, indicating that FePt-IO-coated SiNPs are more efficient as MRI negative contrast agents with respect to IO coated SiNPs[110].

Ultrasound measurements were carried out on silica nanospheres dispersed in agarose gel samples, with the employment of a 10-MHz incident ultrasound frequency. As shown in Figure 3, all the nanoparticle-containing phan-
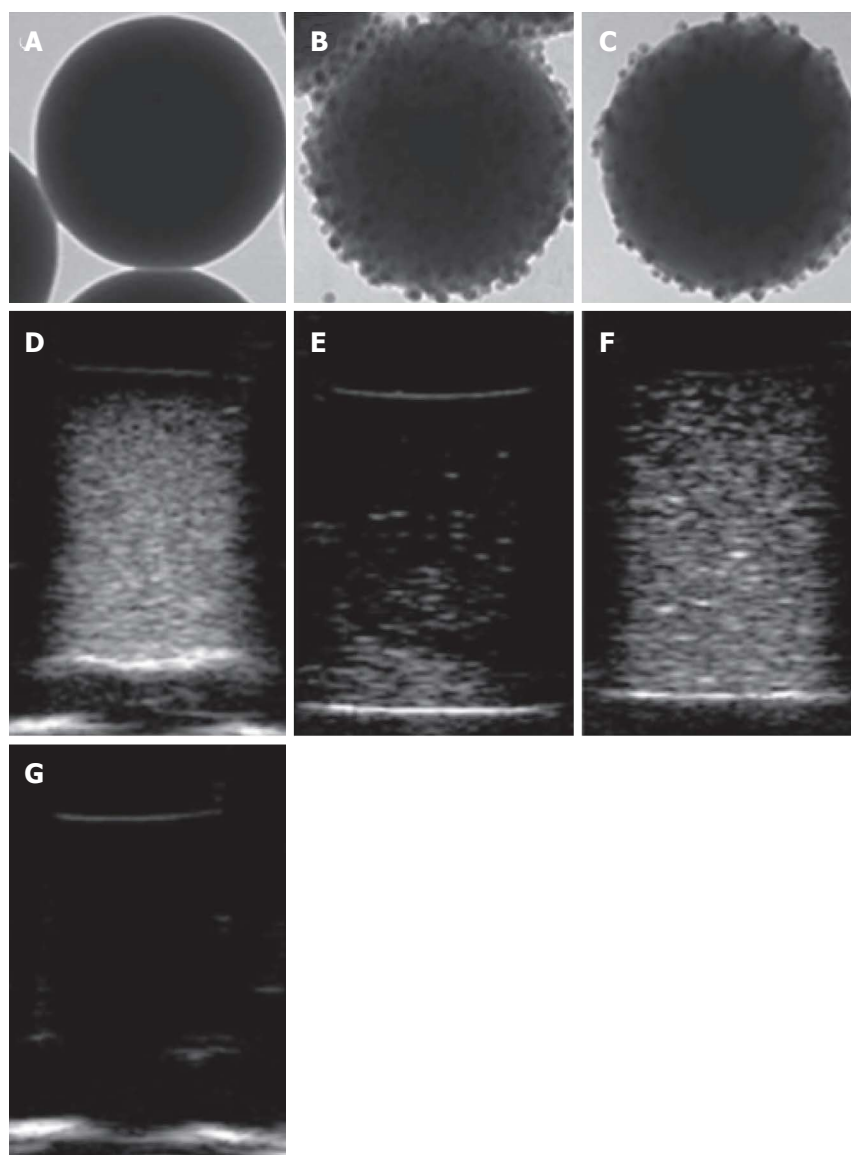
Figure 3 Morphological and echographic characterization of dual mode silica nanoparticles. A-C: Transmission electron microscopy and (D-F) corresponding ultrasound images of uncoated (A, D), IO-coated (B, E) and FePt-IO-coated (C, F) 330 nm silica nanoparticles; G: Image of pure agarose gel (negative control).

toms exhibited a clear image enhancement with respect to the pure agarose gel, that was almost completely transparent to ultrasound. Among the three nanoparticle type tested, uncoated silica nanospheres provided the highest image brightness for each considered size, as compared to IO-coated silica nanospheres, whereas FePt-IO nanocrystals showed image enhancements qualitatively analogous to those of pure silica but with a slightly less uniform brightness.

Therefore, the acoustic and magnetic characterization of coated SiNSs shows that FePt-IO, rather than IO, seems to be the best magnetic coating for realizing NPCAs suitable for dual mode molecular imaging through US and MRI techniques.

HALLOYSITE CLAY NANOTUBES FOR ECHOGRAPHIC IMAGING AT CONVENTIONAL DIAGNOSTIC FREQUENCIES

Nanostructured aluminosilicates are other new materials of particular interest for their potential medical applications. In particular, halloysite clay is a double-layered aluminosilicate spontaneously forming empty tubular structures in the submicrometer range. They size 1 ± 0.5 μm in length, 50 to 70 nm in external diameter and around 15 nm diameter lumen, and are capable of entrapping a wide variety of active agents in the inner lumen, followed by their retention and slow release[111-119]. Moreover, owing to their easy surface functionalization[120] as well as high level of biocompatibility[121], halloysite clay nanotubes (HNTs) present an ideal profile for cell targeting and drug delivery purposes. In fact, HNTs have been recently demonstrated to be successful in intracellular delivery of antisense oligonucleotides[122]. Furthermore, Resveratrol-loaded HNTs have been shown to effectively promote apoptotic cell death in MCF-7 breast cancer cell line[112]. It is then conceivable that therapeutic protocols involving HNTs may take enormous advantage from the possibility of monitoring them through non-invasive imaging techniques. On the basis of these considerations, we have recently explored the feasibility of using HNTs as ultra-
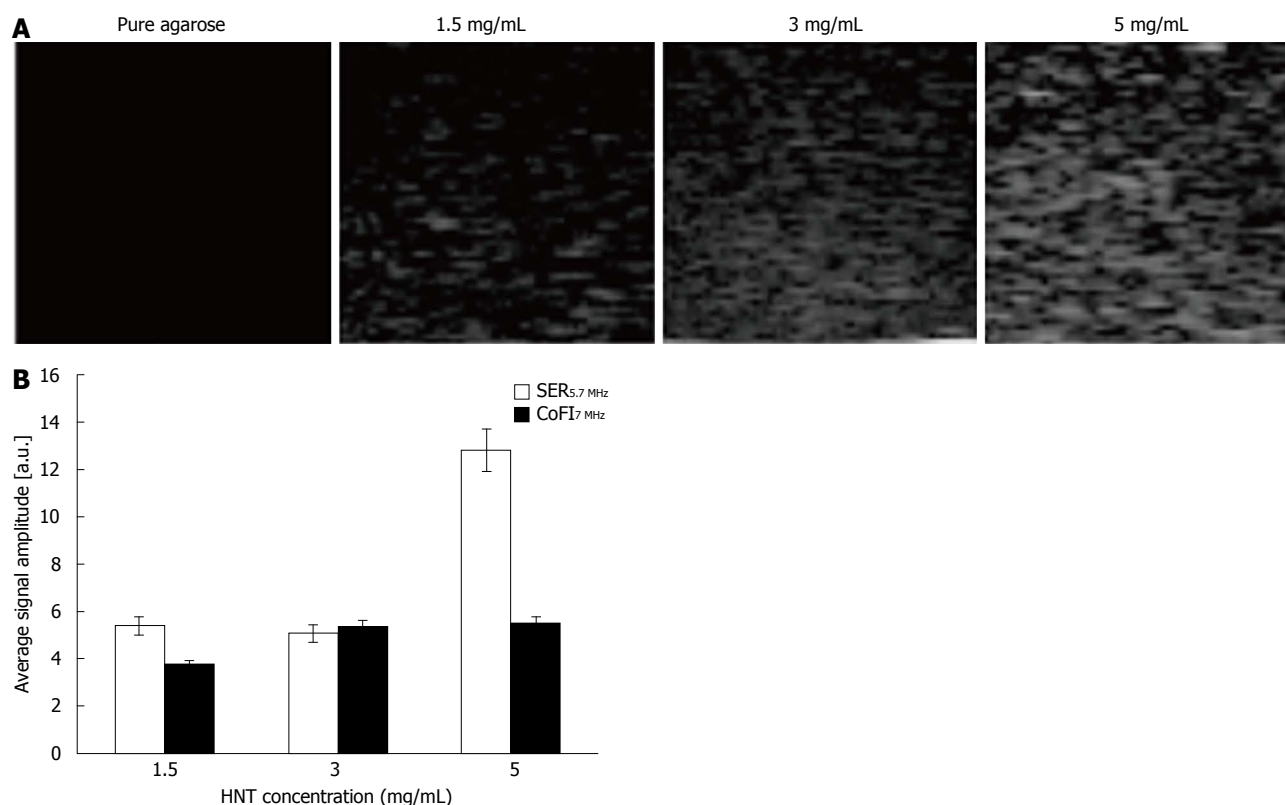
Figure 4 Ultrasound detection of halloysite clay nanotube. A: Gel sample echographic images of pure and agarose containing halloysite clay nanotube (HNT) at the indicated concentrations; B: Quantitative analysis of backscattered signal as a function of ultrasonic frequency and HNT concentration. SER: Signal enhancement ratio; CoFI: Contribution of frequency increment.

sound contrast agents for clinical echographic imaging.

HNT at different concentrations (1.5, 3 and 5 mg/mL) were dispersed in agarose gel and imaged through a commercially available echographic system, employing conventional ultrasonic frequencies (5.7-7 MHz) at an intermediate level of power (50%) of the signal emitted by clinical equipment (Figure 4A).

Acquired data were processed through a dedicated prototypal platform for ultrasonic signal amplitude extraction. The signal enhancement ratio (SER) was calculated between different values of HNT concentration at the considered echographic frequency; additionally, the contribution of frequency increment (CoFI) to the image backscatter was also quantified (Figure 4B). The average contribution of frequency increment from 5.7 to 7 MHz was found to be 4.86 ± 0.80 (corresponding to about 20%), indicating that the increasing HNT concentration determined a nonlinear increment of absolute SER. Hence, it might be useful to study a wider range of HNT concentration in order to achieve safe and effective dose optimization in future clinical application.

CONCLUSION

Recent progresses in the field of nanotechnology applied to medical diagnostic imaging are overcoming most of the constraints offered by classical clinical approaches: molecular imaging without using ionizing techniques, ear-

ly diagnosis of major social diseases, targeted tissue local therapies instead of systemic approaches, *etc*. Echography and ultrasonography provided so far, in the research arena, one of the most promising result by supporting very interesting future clinical perspectives for both diagnosis and therapies still presenting the above mentioned limitations.

Several research applications unveiled many classes of novel nanosystems as effective "theranostic" agents based on both organic and inorganic components. For ultrasound cellular applications the latter certainly offer a wide range of advantages in terms of contrast enhancement, drug loading capabilities, highly effective cell targeting even making possible gene therapy approaches at very low costs.

Nevertheless, many challenges need to be faced in order to translate in clinics those research findings, mainly related to classical difficulties faced by all new drug development steps prior to reach the human clinical trials with additional incognita for the new physical features of novel nano-materials and their eventual toxicity.

Nowadays, our society is experiencing a rapid evolution in terms of population aging, social dynamic modifications accompanied by significant cost reductions in government spending. The real challenge for modern medicine is offering higher medical standards at reduced costs: this ideal objective is not reachable relying on actual classical approaches, but that can be done only pushing

medical research toward the new frontiers made feasible by nanotheranostics and nanomedicines, whose main potentialities and challenges still remain unexpressed and unexplored.

REFERENCES

1   Liu Y, Miyoshi H, Nakamura M. Nanomedicine for drug delivery and imaging: a promising avenue for cancer therapy and diagnosis using targeted functional nanoparticles. *Int J Cancer* 2007; **120**: 2527-2537 [PMID: 17390371 DOI: 10.1002/ijc.22709]

2   Moghimi SM, Hunter AC, Murray JC. Nanomedicine: current status and future prospects. *FASEB J* 2005; **19**: 311-330 [PMID: 15746175 DOI: 10.1096/fj.04-2747rev]

3   Gewin V. Big opportunities in a small world. *Nature* 2009; **460**: 540-541 [DOI: 10.1038/nj7254-540a]

4   Caruthers SD, Wickline SA, Lanza GM. Nanotechnological applications in medicine. *Curr Opin Biotechnol* 2007; **18**: 26-30 [PMID: 17254762 DOI: 10.1016/j.copbio.2007.01.006]

5   Casciaro S. Theranostic applications: Non-ionizing cellular and molecular imaging through innovative nanosystems for early diagnosis and therapy. *World J Radiol* 2011; **3**: 249-255 [PMID: 22229079 DOI: 10.4329/wjr.v3.i10.49]

6   Pascali G, Conversano F, Casciaro S, Salvadori PA. [Translational perspectives in molecular imaging: methodological evolution and nanostructured materials]. *Recenti Prog Med* 2012; **103**: 142-153 [PMID: 22561993]

7   Weissleder R, Mahmood U. Molecular imaging. *Radiology* 2001; **219**: 316-333 [PMID: 11323453 DOI: 10.1148/radiology.219.2.r01ma19316]

8   Allen TM, Cullis PR. Drug delivery systems: entering the mainstream. *Science* 2004; **303**: 1818-1822 [PMID: 15031496 DOI: 10.1126/science.1095833]

9   Moghimi SM, Hunter AC, Murray JC. Long-circulating and target-specific nanoparticles: theory to practice. *Pharmacol Rev* 2001; **53**: 283-318 [PMID: 11356986]

10   Sahoo SK, Labhasetwar V. Nanotech approaches to drug delivery and imaging. *Drug Discovery Today* 2003; **8**: 1112-1120 [DOI: 10.1016/S1359-6446(03)02903-9]

11   Krämer M, Stumbé JF, Grimm G, Kaufmann B, Krüger U, Weber M, Haag R. Dendritic polyamines: simple access to new materials with defined treelike structures for application in nonviral gene delivery. *Chembiochem* 2004; **5**: 1081-1087 [PMID: 15300831 DOI: 10.1002/cbic.200300905]

12   Raja KS, Wang Q, Gonzalez MJ, Manchester M, Johnson JE, Finn MG. Hybrid virus-polymer materials. 1. Synthesis and properties of PEG-decorated cowpea mosaic virus. *Biomacromolecules* 2003; **4**: 472-476 [PMID: 12741758 DOI: 10.1021/bm025740]

13   Fenske DB, MacLachlan I, Cullis PR. Long-circulating vectors for the systemic delivery of genes. *Curr Opin Mol Ther* 2001; **3**: 153-158 [PMID: 11338928]

14   Allen TM. Ligand-targeted therapeutics in anticancer therapy. *Nat Rev Cancer* 2002; **2**: 750-763 [PMID: 12360278 DOI: 10.1038/nrc903]

15   Sudimack J, Lee RJ. Targeted drug delivery via the folate receptor. *Advanced Drug Delivery Reviews* 2000; **41**: 147-162 [DOI: 10.1016/S0169-409X(99)00062-9]

16   Torchilin VP, Lukyanov AN, Gao Z, Papahadjopoulos-Sternberg B. Immunomicelles: targeted pharmaceutical carriers for poorly soluble drugs. *Proc Natl Acad Sci USA* 2003; **100**: 6039-6044 [PMID: 12716967 DOI: 10.1073/pnas.0931428100]

17   Drummond DC, Zignani M, Leroux JC. Current status of pH-sensitive liposomes in drug delivery. *Progress in Lipid Research* 2000; **39**: 409-460 [DOI: 10.1016/S0163-7827(00)00011-4]

18   Panyam J, Zhou WZ, Prabha S, Sahoo SK, Labhasetwar V. Rapid endo-lysosomal escape of poly(DL-lactide-co-glycolide) nanoparticles: implications for drug and gene delivery. *FASEB J* 2002; **16**: 1217-1226 [PMID: 12153989 DOI: 10.1096/fj.02-0088com]

19   Clark HA, Hoyer M, Philbert MA, Kopelman R. Optical nanosensors for chemical analysis inside single living cells. 1. Fabrication, characterization, and methods for intracellular delivery of PEBBLE sensors. *Anal Chem* 1999; **71**: 4831-4836 [PMID: 10565274 DOI: 10.1021/ac990629o]

20   Wickline SA, Neubauer AM, Winter P, Caruthers S, Lanza G. Applications of nanotechnology to atherosclerosis, thrombosis, and vascular biology. *Arterioscler Thromb Vasc Biol* 2006; **26**: 435-441 [PMID: 16373609 DOI: 10.1161/01.ATV.0000201069.47550.8b]

21   Malvindi MA, Greco A, Conversano F, Figuerola A, Corti M, Bonora M, Lascialfari A, Doumari HA, Moscardini M, Cingolani R, Gigli G, Casciaro S, Pellegrino T, Ragusa A. Magnetic/silica nanocomposites as dual-mode contrast agents for combined magnetic resonance imaging and ultrasonography. *Advanced Functional Materials* 2011; **21**: 2548-2555 [DOI: 10.1002/adfm.201100031]

22   Wickline SA, Neubauer AM, Winter PM, Caruthers SD, Lanza GM. Molecular imaging and therapy of atherosclerosis with targeted nanoparticles. *J Magn Reson Imaging* 2007; **25**: 667-680 [PMID: 17347992 DOI: 10.1002/jmri.20866]

23   Conversano F, Casciaro S. Last advances in ultrasound molecular imaging. In: Casciaro S, Gersak B, editors. New technology frontiers in minimally invasive therapies. Lecce (Italy): Lupiensis Biomedical Publications, 2007: 161-171

24   Puvanakrishnan P, Park J, Chatterjee D, Krishnan S, Tunnell JW. In vivo tumor targeting of gold nanoparticles: effect of particle type and dosing strategy. *Int J Nanomedicine* 2012; **7**: 1251-1258 [PMID: 22419872 DOI: 10.2147/IJN.S29147]

25   Fahmy TM, Samstein RM, Harness CC, Mark Saltzman W. Surface modification of biodegradable polyesters with fatty acid conjugates for improved drug targeting. *Biomaterials* 2005; **26**: 5727-5736 [PMID: 15878378 DOI: 10.1016/j.biomaterials.2005.02.025]

26   Couvreur P, Barratt G, Fattal E, Legrand P, Vauthier C. Nanocapsule technology: a review. *Crit Rev Ther Drug Carrier Syst* 2002; **19**: 99-134 [PMID: 12197610 DOI: 10.1615/CritRevTherDrugCarrierSyst.v19.i2.10]

27   Weissleder R, Pittet MJ. Imaging in the era of molecular oncology. *Nature* 2008; **452**: 580-589 [PMID: 18385732 DOI: 10.1038/nature06917]

28   Hahn MA, Singh AK, Sharma P, Brown SC, Moudgil BM. Nanoparticles as contrast agents for in-vivo bioimaging: current status and future perspectives. *Anal Bioanal Chem* 2011; **399**: 3-27 [PMID: 20924568 DOI: 10.1007/s00216-010-4207-5]

29   Wickline SA, Lanza GM. Nanotechnology for molecular imaging and targeted therapy. *Circulation* 2003; **107**: 1092-1095 [PMID: 12615782 DOI: 10.1161/01.CIR.0000059651.17045.77]

30   Lanza GM, Wickline SA. Targeted ultrasonic contrast agents for molecular imaging and therapy. *Curr Probl Cardiol* 2003; **28**: 625-653 [PMID: 14691443 DOI: 10.1016/j.cpcardiol.2003.11.001]

31   Tsien RY. Imagining imaging's future. *Nat Rev Mol Cell Biol* 2003; **Suppl**: SS16-SS21 [PMID: 14587522]

32   Herschman HR. Molecular imaging: looking at problems, seeing solutions. *Science* 2003; **302**: 605-608 [PMID: 14576425 DOI: 10.1126/science.1090585]

33   Hawker CJ, Wooley KL. The convergence of synthetic organic and polymer chemistries. *Science* 2005; **309**: 1200-1205 [PMID: 16109874 DOI: 10.1126/science.1109778]

34   Pasqualini R, Arap W, McDonald DM. Probing the structural and molecular diversity of tumor vasculature. *Trends in Molecular Medicine* 2002; **8**: 563-571 [DOI: 10.1016/S1471-4914(02)02429-2]

35   Hobbs SK, Monsky WL, Yuan F, Roberts WG, Griffith L, Torchilin VP, Jain RK. Regulation of transport pathways in tumor vessels: role of tumor type and microenvironment.

Proc Natl Acad Sci USA 1998; **95**: 4607-4612 [PMID: 9539785 DOI: 10.1073/pnas.95.8.4607]

36   **Iyer AK**, Khaled G, Fang J, Maeda H. Exploiting the enhanced permeability and retention effect for tumor targeting. *Drug Discov Today* 2006; **11**: 812-818 [PMID: 16935749 DOI: 10.1016/j.drudis.2006.07.005]

37   **Demos SM,** Alkan-Onyuksel H, Kane BJ, Ramani K, Nagaraj A, Greene R, Klegerman M, McPherson DD. In vivo targeting of acoustically reflective liposomes for intravascular and transvascular ultrasonic enhancement. *JACC* 1999; **33**: 867-875 [DOI: 10.1016/S0735-1097(98)00607-X]

38   **Sipkins DA**, Cheresh DA, Kazemi MR, Nevin LM, Bednarski MD, Li KC. Detection of tumor angiogenesis in vivo by alphaVbeta3-targeted magnetic resonance imaging. *Nat Med* 1998; **4**: 623-626 [PMID: 9585240 DOI: 10.1038/nm0598-623]

39   **Marsh JN**, Partlow KC, Abendschein DR, Scott MJ, Lanza GM, Wickline SA. Molecular imaging with targeted perfluorocarbon nanoparticles: quantification of the concentration dependence of contrast enhancement for binding to sparse cellular epitopes. *Ultrasound Med Biol* 2007; **33**: 950-958 [PMID: 17434667 DOI: 10.1016/j.ultrasmedbio.2006.12.007]

40   **Lanza GM**, Winter P, Caruthers S, Schmeider A, Crowder K, Morawski A, Zhang H, Scott MJ, Wickline SA. Novel paramagnetic contrast agents for molecular imaging and targeted drug delivery. *Curr Pharm Biotechnol* 2004; **5**: 495-507 [PMID: 15579039 DOI: 10.2174/1389201043376544]

41   **Flacke S,** Fischer S, Scott MJ, Fuhrhop RJ, Allen JS, McLean M, Winter P, Sicard GA, Gaffney PJ, Wickline SA, Lanza GM. Novel MRI contrast agent for molecular imaging of fibrin: implications for detecting vulnerable plaques. *Circulation* 2001; **104**: 1280-1285 [DOI: 10.1161/hc3601.094303]

42   **Schmitz SA**, Coupland SE, Gust R, Winterhalter S, Wagner S, Kresse M, Semmler W, Wolf KJ. Superparamagnetic iron oxide-enhanced MRI of atherosclerotic plaques in Watanabe hereditable hyperlipidemic rabbits. *Invest Radiol* 2000; **35**: 460-471 [PMID: 10946973 DOI: 10.1097/00004424-200008000-00002]

43   **Hirsch LR**, Stafford RJ, Bankson JA, Sershen SR, Rivera B, Price RE, Hazle JD, Halas NJ, West JL. Nanoshell-mediated near-infrared thermal therapy of tumors under magnetic resonance guidance. *Proc Natl Acad Sci USA* 2003; **100**: 13549-13554 [PMID: 14597719 DOI: 10.1073/pnas.2232479100]

44   **Loo C**, Lin A, Hirsch L, Lee MH, Barton J, Halas N, West J, Drezek R. Nanoshell-enabled photonics-based imaging and therapy of cancer. *Technol Cancer Res Treat* 2004; **3**: 33-40 [PMID: 14750891]

45   **O'Neal DP**, Hirsch LR, Halas NJ, Payne JD, West JL. Photothermal tumor ablation in mice using near infrared-absorbing nanoparticles. *Cancer Lett* 2004; **209**: 171-176 [PMID: 15159019 DOI: 10.1016/j.canlet.2004.02.004]

46   **Cherukuri P**, Bachilo SM, Litovsky SH, Weisman RB. Near-infrared fluorescence microscopy of single-walled carbon nanotubes in phagocytic cells. *J Am Chem Soc* 2004; **126**: 15638-15639 [PMID: 15571374 DOI: 10.1021/ja0466311]

47   **Tsyboulski DA**, Bachilo SM, Weisman RB. Versatile visualization of individual single-walled carbon nanotubes with near-infrared fluorescence microscopy. *Nano Lett* 2005; **5**: 975-979 [PMID: 15884905 DOI: 10.1021/nl050366f]

48   **Barone PW**, Baik S, Heller DA, Strano MS. Near-infrared optical sensors based on single-walled carbon nanotubes. *Nat Mater* 2005; **4**: 86-92 [PMID: 15592477 DOI: 10.1038/nmat1276]

49   **Hertel T**, Hagen A, Talalaev V, Arnold K, Hennrich F, Kappes M, Rosenthal S, McBride J, Ulbricht H, Flahaut E. Spectroscopy of single- and double-wall carbon nanotubes in different environments. *Nano Lett* 2005; **5**: 511-514 [PMID: 15755104 DOI: 10.1021/nl050069a]

50   **Akerman ME**, Chan WC, Laakkonen P, Bhatia SN, Ruoslahti E. Nanocrystal targeting in vivo. *Proc Natl Acad Sci USA* 2002; **99**: 12617-12621 [PMID: 12235356 DOI: 10.1073/pnas.152463399]

51   **Chen L**, Zurita AJ, Ardelt PU, Giordano RJ, Arap W, Pasqualini R. Design and validation of a bifunctional ligand display system for receptor targeting. *Chem Biol* 2004; **11**: 1081-1091 [PMID: 15324809 DOI: 10.1016/j.chembiol.2004.05.019]

52   **Gao X**, Nie S. Quantum dot-encoded beads. *Meth Mol Biol* 2005; **303**: 61-71

53   **Michalet X**, Pinaud FF, Bentolila LA, Tsay JM, Doose S, Li JJ, Sundaresan G, Wu AM, Gambhir SS, Weiss S. Quantum dots for live cells, in vivo imaging, and diagnostics. *Science* 2005; **307**: 538-544 [PMID: 15681376 DOI: 10.1126/science.1104274]

54   **Corot C**, Robert P, Idée JM, Port M. Recent advances in iron oxide nanocrystal technology for medical imaging. *Adv Drug Deliv Rev* 2006; **58**: 1471-1504 [PMID: 17116343 DOI: 10.1016/j.addr.2006.09.013]

55   **Semelka RC**, Helmberger TK. Contrast agents for MR imaging of the liver. *Radiology* 2001; **218**: 27-38 [PMID: 11152776 DOI: 10.1148/radiology.218.1.r01ja2427]

56   **Alric C**, Taleb J, Le Duc G, Mandon C, Billotey C, Le Meur-Herland A, Brochard T, Vocanson F, Janier M, Perriat P, Roux S, Tillement O. Gadolinium chelate coated gold nanoparticles as contrast agents for both X-ray computed tomography and magnetic resonance imaging. *J Am Chem Soc* 2008; **130**: 5908-5915 [PMID: 18407638 DOI: 10.1021/ja078176p]

57   **Figuerola A**, Fiore A, Di Corato R, Falqui A, Giannini C, Micotti E, Lascialfari A, Corti M, Cingolani R, Pellegrino T, Cozzoli PD, Manna L. One-pot synthesis and characterization of size-controlled bimagnetic FePt-iron oxide heterodimer nanocrystals. *J Am Chem Soc* 2008; **130**: 1477-1487 [PMID: 18181628 DOI: 10.1021/ja078034v]

58   **Yang H**, Zhao F, Li Y, Xu M, Li L, Wu C, Miyoshi H, Liu Y. VCAM-1-targeted core/shell nanoparticles for selective adhesion and delivery to endothelial cells with lipopolysaccharide-induced inflammation under shear flow and cellular magnetic resonance imaging in vitro. *Int J Nanomedicine* 2013; **8**: 1897-1906 [PMID: 23696701]

59   Molecular Imaging and Contrast Agent Database (MICAD) [Internet]. Bethesda (MD): National Center for Biotechnology Information (US); 2004-2012. Available from: URL: http://www.ncbi.nlm.nih.gov/books/NBK5330/

60   **Kaufmann BA**, Lindner JR. Molecular imaging with targeted contrast ultrasound. *Curr Opin Biotechnol* 2007; **18**: 11-16 [PMID: 17241779 DOI: 10.1016/j.copbio.2007.01.004]

61   **Kindberg GM**, Tolleshaug H, Roos N, Skotland T. Hepatic clearance of Sonazoid perfluorobutane microbubbles by Kupffer cells does not reduce the ability of liver to phagocytose or degrade albumin microspheres. *Cell Tissue Res* 2003; **312**: 49-54 [PMID: 12712317]

62   **Bryant TH**, Blomley MJ, Albrecht T, Sidhu PS, Leen EL, Basilico R, Pilcher JM, Bushby LH, Hoffmann CW, Harvey CJ, Lynch M, MacQuarrie J, Paul D, Cosgrove DO. Improved characterization of liver lesions with liver-phase uptake of liver-specific microbubbles: prospective multicenter study. *Radiology* 2004; **232**: 799-809 [PMID: 15284434 DOI: 10.1148/radiol.2323030596]

63   **Willmann JK**, Lutz AM, Paulmurugan R, Patel MR, Chu P, Rosenberg J, Gambhir SS. Dual-targeted contrast agent for US assessment of tumor angiogenesis in vivo. *Radiology* 2008; **248**: 936-944 [PMID: 18710985]

64   **Palmowski M**, Huppert J, Ladewig G, Hauff P, Reinhardt M, Mueller MM, Woenne EC, Jenne JW, Maurer M, Kauffmann GW, Semmler W, Kiessling F. Molecular profiling of angiogenesis with targeted ultrasound imaging: early assessment of antiangiogenic therapy effects. *Mol Cancer Ther* 2008; **7**: 101-109 [PMID: 18202013 DOI: 10.1158/1535-7163.MCT-07-0409]

65   **Palmowski M**, Peschke P, Huppert J, Hauff P, Reinhardt

M, Maurer M, Karger CP, Scholz M, Semmler W, Huber PE, Kiessling FM. Molecular ultrasound imaging of early vascular response in prostate tumors irradiated with carbon ions. *Neoplasia* 2009; **11**: 856-863 [PMID: 19724679]

66 **Lutz AM**, Bachawal SV, Drescher CW, Pysz MA, Willmann JK, Gambhir SS. Ultrasound molecular imaging in a human CD276 expression-modulated murine ovarian cancer model. *Clin Cancer Res* 2014; **20**: 1313-1322 [PMID: 24389327]

67 **Negishi Y**, Hamano N, Tsunoda Y, Oda Y, Choijamts B, Endo-Takahashi Y, Omata D, Suzuki R, Maruyama K, Nomizu M, Emoto M, Aramaki Y. AG73-modified Bubble liposomes for targeted ultrasound imaging of tumor neovasculature. *Biomaterials* 2013; **34**: 501-507 [PMID: 23088840 DOI: 10.1016/j.biomaterials.2012.09.056]

68 **Díaz-López R**, Tsapis N, Fattal E. Liquid perfluorocarbons as contrast agents for ultrasonography and (19)F-MRI. *Pharm Res* 2010; **27**: 1-16 [PMID: 19902338 DOI: 10.1007/s11095-009-0001-5]

69 **Yin T**, Wang P, Zheng R, Zheng B, Cheng D, Zhang X, Shuai X. Nanobubbles for enhanced ultrasound imaging of tumors. *Int J Nanomedicine* 2012; **7**: 895-904 [PMID: 22393289 DOI: 10.2147/IJN.S28830]

70 **Casciaro S**, Conversano F, Ragusa A, Malvindi MA, Franchini R, Greco A, Pellegrino T, Gigli G. Optimal enhancement configuration of silica nanoparticles for ultrasound imaging and automatic detection at conventional diagnostic frequencies. *Invest Radiol* 2010; **45**: 715-724 [PMID: 20562708 DOI: 10.1097/RLI.0b013e3181e6f42f]

71 **Conversano F,** Greco A, Casciaro E, Ragusa A, Lay-Ekuakille A, Casciaro S. Harmonic ultrasound imaging of nanosized contrast agents for multimodal molecular diagnoses. *IEEE Trans Instrum Meas* 2012; **61**: 1848-1856 [DOI: 10.1109/TIM.2012.2192354]

72 **Liu J**, Levine AL, Mattoon JS, Yamaguchi M, Lee RJ, Pan X, Rosol TJ. Nanoparticles as image enhancing agents for ultrasonography. *Phys Med Biol* 2006; **51**: 2179-2189 [PMID: 16625034 DOI: 10.1088/0031-9155/51/9/004]

73 **Liu J**, Li J, Rosol TJ, Pan X, Voorhees JL. Biodegradable nanoparticles for targeted ultrasound imaging of breast cancer cells in vitro. *Phys Med Biol* 2007; **52**: 4739-4747 [PMID: 17671332 DOI: 10.1088/0031-9155/52/16/002]

74 **Jin Y**, Kannan S, Wu M, Zhao JX. Toxicity of luminescent silica nanoparticles to living cells. *Chem Res Toxicol* 2007; **20**: 1126-1133 [PMID: 17630705 DOI: 10.1021/tx7001959]

75 **Barbé C**, Bartlett J, Kong L, Finnie K, Lin HQ, Larkin M, Calleja S, Bush A, Calleja G. Silica particles: a novel drug-delivery system. *Adv Funct Mater* 2004; **16**: 1959-1966 [DOI: 10.1002/adma.200400771]

76 **Piao Y**, Burns A, Kim J, Wiesner U, Hyeon, T. Designed fabrication of silica-based nanostructured particle systems for nanomedicine applications. *Adv Funct Mater* 2008; **18**: 3745-3758 [DOI: 10.1002/adfm.200800731]

77 **Moulari B**, Pertuit D, Pellequer Y, Lamprecht A. The targeting of surface modified silica nanoparticles to inflamed tissue in experimental colitis. *Biomaterials* 2008; **29**: 4554-4560 [PMID: 18790531 DOI: 10.1016/j.biomaterials.2008.08.009]

78 **Roy I**, Ohulchanskyy TY, Bharali DJ, Pudavar HE, Mistretta RA, Kaur N, Prasad PN. Optical tracking of organically modified silica nanoparticles as DNA carriers: a nonviral, nanomedicine approach for gene delivery. *Proc Natl Acad Sci USA* 2005; **102**: 279-284 [PMID: 15630089 DOI: 10.1073/pnas.0408039101]

79 **Liu L**, Yong KT, Roy I, Law WC, Ye L, Liu J, Liu J, Kumar R, Zhang X, Prasad PN. Bioconjugated pluronic triblock-copolymer micelle-encapsulated quantum dots for targeted imaging of cancer: in vitro and in vivo studies. *Theranostics* 2012; **2**: 705-713 [PMID: 22896772 DOI: 10.7150/thno.3456]

80 **Poulose AC**, Veeranarayanan S, Mohamed MS, Raveendran S, Nagaoka Y, Yoshida Y, Maekawa T, Kumar DS. PEG coated biocompatible cadmium chalcogenide quantum dots for

targeted imaging of cancer cells. *J Fluoresc* 2012; **22**: 931-944 [PMID: 22227700 DOI: 10.1007/s10895-011-1032-y]

81 **Winkler AM**, Rice PF, Drezek RA, Barton JK. Quantitative tool for rapid disease mapping using optical coherence tomography images of azoxymethane-treated mouse colon. *J Biomed Opt* 2010; **15**: 041512 [PMID: 20799790 DOI: 10.1117/1.3446674]

82 **Avti PK**, Sitharaman B. Luminescent single-walled carbon nanotube-sensitized europium nanoprobes for cellular imaging. *Int J Nanomedicine* 2012; **7**: 1953-1964 [PMID: 22619533 DOI: 10.2147/IJN.S29545]

83 **Wang LV.** Multiscale photoacoustic microscopy and computed tomography. *Nat Photonics* 2009; **3**: 503-509 [PMID: 20161535 DOI: 10.1038/nphoton.2009.157]

84 **Oraevsky AA,** Karabutov AA. Optoacoustic tomography. In: Vo-Dinh T, editor. Biomedical Photonics Handbook. Boca Raton: CRC Press/Francis and Taylor Group, 2003

85 **Ermilov SA**, Khamapirad T, Conjusteau A, Leonard MH, Lacewell R, Mehta K, Miller T, Oraevsky AA. Laser optoacoustic imaging system for detection of breast cancer. *J Biomed Opt* 2009; **14**: 024007 [PMID: 19405737 DOI: 10.1117/1.3086616]

86 **Lu W**, Huang Q, Ku G, Wen X, Zhou M, Guzatov D, Brecht P, Su R, Oraevsky A, Wang LV, Li C. Photoacoustic imaging of living mouse brain vasculature using hollow gold nanospheres. *Biomaterials* 2010; **31**: 2617-2626 [PMID: 20036000 DOI: 10.1016/j.biomaterials.2009.12.007]

87 **Song KH**, Kim C, Maslov K, Wang LV. Noninvasive in vivo spectroscopic nanorod-contrast photoacoustic mapping of sentinel lymph nodes. *Eur J Radiol* 2009; **70**: 227-231 [PMID: 19269762 DOI: 10.1016/j.ejrad.2009.01.045]

88 **Mallidi S**, Larson T, Tam J, Joshi PP, Karpiouk A, Sokolov K, Emelianov S. Multiwavelength photoacoustic imaging and plasmon resonance coupling of gold nanoparticles for selective detection of cancer. *Nano Lett* 2009; **9**: 2825-2831 [PMID: 19572747 DOI: 10.1021/nl802929u]

89 **Li ML**, Wang JC, Schwartz JA, Gill-Sharp KL, Stoica G, Wang LV. In-vivo photoacoustic microscopy of nanoshell extravasation from solid tumor vasculature. *J Biomed Opt* 2009; **14**: 010507 [PMID: 19256687 DOI: 10.1117/1.3081556]

90 **Kim C**, Cho EC, Chen J, Song KH, Au L, Favazza C, Zhang Q, Cobley CM, Gao F, Xia Y, Wang LV. In vivo molecular photoacoustic tomography of melanomas targeted by bioconjugated gold nanocages. *ACS Nano* 2010; **4**: 4559-4564 [PMID: 20731439 DOI: 10.1021/nn100736c]

91 **Jain PK,** El-Sayed IH, El-Sayed MA. Au nanoparticles target cancer. *Nano Today* 2007; **2**: 18-29 [DOI: 10.1016/S1748-0132(07)70016-6]

92 **Pan D,** Pramanik M, Senpan A, Wickline SA, Wang LV, Lanza GM. A facile synthesis of novel self-assembled gold nanorods designed for near-infrared imaging. *JNN* 2010; **10**: 8118-8123 [DOI: 10.1166/jnn.2010.3034]

93 **Boisselier E**, Astruc D. Gold nanoparticles in nanomedicine: preparations, imaging, diagnostics, therapies and toxicity. *Chem Soc Rev* 2009; **38**: 1759-1782 [PMID: 19587967 DOI: 10.1039/b806051g]

94 **Connor EE**, Mwamuka J, Gole A, Murphy CJ, Wyatt MD. Gold nanoparticles are taken up by human cells but do not cause acute cytotoxicity. *Small* 2005; **1**: 325-327 [PMID: 17193451 DOI: 10.1002/smll.200400093]

95 **Cai QY**, Kim SH, Choi KS, Kim SY, Byun SJ, Kim KW, Park SH, Juhng SK, Yoon KH. Colloidal gold nanoparticles as a blood-pool contrast agent for X-ray computed tomography in mice. *Invest Radiol* 2007; **42**: 797-806 [PMID: 18007151 DOI: 10.1097/RLI.0b013e31811ecdcd]

96 **Chen YS,** Hung YC, Liau I, Huang GS. Assessment of the In Vivo Toxicity of Gold Nanoparticles. *Nanoscale Res Lett* 2009; **4**: 858-864 [PMID: 20596373 DOI: 10.1007/s11671-009-9334-6]

97 **Eghtedari M**, Oraevsky A, Copland JA, Kotov NA, Conjusteau A, Motamedi M. High sensitivity of in vivo detection of

gold nanorods using a laser optoacoustic imaging system. *Nano Lett* 2007; **7**: 1914-1918 [PMID: 17570730 DOI: 10.1021/nl070557d]

98   **Ha S**, Carson A, Agarwal A, Kotov NA, Kim K. Detection and monitoring of the multiple inflammatory responses by photoacoustic molecular imaging using selectively targeted gold nanorods. *Biomed Opt Express* 2011; **2**: 645-657 [PMID: 21412469 DOI: 10.1364/BOE.2.000645]

99   **Agarwal A,** Huang SW, O'Donnel M, Day KC, Day M, Kotov N, Ashkenazi S. Targeted gold nanorod contrast agent for prostate cancer detection by photoacoustic imaging. *J Appl Phys* 2007; **102**: 064701 [DOI: 10.1063/1.2777127]

100   **Li PC,** Wei CW, Liao CK, Chen CD, Pao KC, Wang CRC, Wu TN, Shieh DB. Photoacoustic imaging of multiple targets using gold nanorods. *IEEE Trans Ultrason Ferroelectr Freq Control* 2007; **54**: 1642-1647 [DOI: 10.1109/TUFFC.2007.435]

101   **Kim K,** Huang SW, Ashkenazi S, O'Donnell M, Agarwal A, Kotov NA, Denny MF, Kaplan MJ. Photoacoustic imaging of early inflammatory response using gold nanorods. *Applied Physics Letters* 2007; **90**: 223901-223903 [DOI: 10.1063/1.2743752]

102   **Li PC**, Wang CR, Shieh DB, Wei CW, Liao CK, Poe C, Jhan S, Ding AA, Wu YN. In vivo photoacoustic molecular imaging with simultaneous multiple selective targeting using antibody-conjugated gold nanorods. *Opt Express* 2008; **16**: 18605-18615 [PMID: 19581946 DOI: 10.1364/OE.16.018605]

103   **Conversano F**, Soloperto G, Greco A, Ragusa A, Casciaro E, Chiriacò F, Demitri C, Gigli G, Maffezzoli A, Casciaro S. Echographic detectability of optoacoustic signals from low-concentration PEG-coated gold nanorods. *Int J Nanomedicine* 2012; **7**: 4373-4389 [PMID: 22927756]

104   **Samim M**, Prashant CK, Dinda AK, Maitra AN, Arora I. Synthesis and characterization of gold nanorods and their application for photothermal cell damage. *Int J Nanomedicine* 2011; **6**: 1825-1831 [PMID: 22114472 DOI: 10.2147/IJN.S11600]

105   **Chiriacò F,** Conversano F, Soloperto G, Casciaro E, Ragusa A, Sbenaglia EA, Dipaola L, Casciaro S. Epithelial cells biocompatibility of silica nanospheres for contrast-enhanced ultrasound molecular imaging. *J Nanopart Research* 2013; **15**: 1779-1792 [DOI: 10.1007/s11051-013-1779-y]

106   **Ahn BC**, Ronald JA, Kim YI, Katzenberg R, Singh A, Paulmurugan R, Ray S, Hofmann LV, Gambhir SS. Potent, tumor-specific gene expression in an orthotopic hepatoma rat model using a Survivin-targeted, amplifiable adenoviral vector. *Gene Ther* 2011; **18**: 606-612 [PMID: 21307888 DOI: 10.1038/gt.2011.5]

107   **Ho M**, Kim H. Glypican-3: a new target for cancer immunotherapy. *Eur J Cancer* 2011; **47**: 333-338 [PMID: 21112773 DOI: 10.1016/j.ejca.2010.10.024]

108   **Lee YL**, Ahn BC, Lee Y, Lee SW, Cho JY, Lee J. Targeting of hepatocellular carcinoma with glypican-3-targeting peptide ligand. *J Pept Sci* 2011; **17**: 763-769 [PMID: 21976137 DOI: 10.1002/psc.1400]

109   **Casciaro S,** Soloperto G, Greco A, Casciaro E, Franchini R, Conversano F. Effectiveness of functionalized nanosystems for multimodal molecular sensing and imaging in medicine. *IEEE Sens J* 2013; **13**: 2305-2312 [DOI: 10.1109/JSEN.2013.2252164]

110   **Chiriacò F**, Soloperto G, Greco A, Conversano F, Ragusa A, Menichetti L, Casciaro S. Magnetically-coated silica nanospheres for dual-mode imaging at low ultrasound frequency. *World J Radiol* 2013; **5**: 411-420 [PMID: 24349645]

111   **Price RR**, Gaber BP, Lvov Y. In-vitro release characteristics of tetracycline HCl, khellin and nicotinamide adenine dineculeotide from halloysite; a cylindrical mineral. *J Microencapsul* 2001; **18**: 713-722 [PMID: 11695636 DOI: 10.1080/02652040010019532]

112   **Vergaro V**, Lvov YM, Leporatti S. Halloysite clay nanotubes for resveratrol delivery to cancer cells. *Macromol Biosci* 2012; **12**: 1265-1271 [PMID: 22887783 DOI: 10.1002/mabi.201200121]

113   **Kelly HM**, Deasy PB, Ziaka E, Claffey N. Formulation and preliminary in vivo dog studies of a novel drug delivery system for the treatment of periodontitis. *Int J Pharm* 2004; **274**: 167-183 [PMID: 15072793 DOI: 10.1016/j.ijpharm.2004.01.019]

114   **Veerabadran NG,** Price RR, Lvov YM. Clay nanotubes for encapsulation and sustained release of drugs. *Nano* 2007; **2**: 115-120 [DOI: 10.1142/S1793292007000441]

115   **Lvov YM**, Shchukin DG, Möhwald H, Price RR. Halloysite clay nanotubes for controlled release of protective agents. *ACS Nano* 2008; **2**: 814-820 [PMID: 19206476 DOI: 10.1021/nn800259q]

116   **Veerabadran NG**, Mongayt D, Torchilin V, Price RR, Lvov YM. Organized shells on clay nanotubes for controlled release of macromolecules. *Macromol Rapid Commun* 2009; **30**: 99-103 [PMID: 21706582 DOI: 10.1002/marc.200800510]

117   **Kommireddy D,** Ichinose I, Lvov Y, Mills D. Nanoparticle multilayer: surface modification for cell attachment and growth. *J Biomed Nanotechnol* 2005; **1**: 286-290 [DOI: 10.1166/jbn.2005.046]

118   **Viseras MT**, Aguzzi C, Cerezo P, Cultrone G, Viseras C. Supramolecular structure of 5-aminosalicylic acid/halloysite composites. *J Microencapsul* 2009; **26**: 279-286 [PMID: 18686141 DOI: 10.1080/02652040802312499]

119   **Soloperto G,** Conversano F, Greco A, Casciaro E, Ragusa A, Leporatti S, Lay-Ekuakille A, Casciaro S. Multiparametric evaluation of the acoustic behaviour of halloysite nanotubes for medical echographic image enhancement. *IEEE Trans Instrum Meas* 2014, In press

120   **Duartel AH,** Lourenco MP, Heine T, Guimares L. Clay mineral nanotubes: stability, structure and properties. In: Stoichiometry, Material Sciences-When Numbers Matter, A Innocenti, N Kamarulzaman, editors. Vukovar, Croatia: InTech, 2012

121   **Vergaro V**, Abdullayev E, Lvov YM, Zeitoun A, Cingolani R, Rinaldi R, Leporatti S. Cytocompatibility and uptake of halloysite clay nanotubes. *Biomacromolecules* 2010; **11**: 820-826 [PMID: 20170093 DOI: 10.1021/bm9014446]

122   **Shi YF**, Tian Z, Zhang Y, Shen HB, Jia NQ. Functionalized halloysite nanotube-based carrier for intracellular delivery of antisense oligonucleotides. *Nanoscale Res Lett* 2011; **6**: 608 [PMID: 22122822 DOI: 10.1186/1556-276X-6-608]

MINIREVIEWS

Neural mechanisms of mindfulness and meditation: Evidence from neuroimaging studies

William R Marchand

William R Marchand, Mental Health Service, George E Wahlen Veterans Affairs Medical Center, Salt Lake City, UT 84148, United States
William R Marchand, Department of Psychiatry, University of Utah, Salt Lake City, UT 84112, United States
Author contributions: Marchand WR reviewed the literature and wrote the manuscript.
Correspondence to: William R Marchand, MD, Mental Health Service, George E Wahlen Veterans Affairs Medical Center, 500 Foothill Drive, Salt Lake City, UT 84148, United States. wmarchand@me.com
Telephone: +1-801-5578950   Fax: +1-801-9983818

Abstract

Mindfulness is the dispassionate, moment-by-moment awareness of sensations, emotions and thoughts. Mindfulness-based interventions are being increasingly used for stress, psychological well being, coping with chronic illness as well as adjunctive treatments for psychiatric disorders. However, the neural mechanisms associated with mindfulness have not been well characterized. Recent functional and structural neuroimaging studies are beginning to provide insights into neural processes associated with the practice of mindfulness. A review of this literature revealed compelling evidence that mindfulness impacts the function of the medial cortex and associated default mode network as well as insula and amygdala. Additionally, mindfulness practice appears to effect lateral frontal regions and basal ganglia, at least in some cases. Structural imaging studies are consistent with these findings and also indicate changes in the hippocampus. While many questions remain unanswered, the current literature provides evidence of brain regions and networks relevant for understanding neural processes associated with mindfulness.

Core tip: Mindfulness training is used for stress and as an adjunctive treatment for psychiatric disorders. Functional neuroimaging studies are beginning to provide insights into neural processes associated with the practice of mindfulness. These studies clearly indicate that the practice of mindfulness changes brain function in areas including the medial cortex, default mode network, insula, amygdala, lateral frontal regions and basal ganglia.

INTRODUCTION

Mindfulness has been described as dispassionate, non-evaluative, and continuous moment-by-moment awareness of, sensations, perceptions, emotions and thoughts[1]. A similar definition explains mindfulness as "the awareness that emerges through paying attention on purpose, in the present moment, and non-judgmentally to the unfolding of experience moment by moment[2]."

Mindfulness training involves meditation. Mindfulness meditation practice is the framework used to develop the state, or skill, of mindfulness. The word "meditation" stems from the Latin *meditari,* which means to participate in contemplation or deliberation. Meditation includes a variety of practices aimed at focusing attention and awareness. Two general forms of meditation exist. These are focused attention and open monitoring[3]. Initially a

practitioner will often utilize focused attention practice to enhance attentional skills[4]. Then, it will be possible to engage in open monitoring, which involves moment-by-moment awareness of whatever occurs in one's awareness[4].

Mindfulness originated in Buddhist spiritual practices. However, secular, group therapy approaches utilizing manuals and standardized methods have been developed for clinical use. Two of these are Mindfulness-Based Stress Reduction (MBSR) and Mindfulness-Based Cognitive Therapy (MBCT). As reviewed elsewhere[5], there has been increased interest in mindfulness and meditation in recent years. In particular, there has been increased use of the secular mindfulness-based interventions for stress, coping with physical illness and as adjunctive treatments for psychiatric disorders[5].

This manuscript reviews recent neuroimaging studies that enhance our understanding of the neural mechanisms of mindfulness.

SEARCH

Several PubMed searches were conducted with terms mindfulness and neuroimaging, mindfulness and fMRI, mindfulness and MRI and mindfulness and mechanisms, meditation and neuroimaging, meditation and fMRI and mediation and MRI. These initial searches resulted in the review of 248 abstracts. Those most relevant for understanding neural mechanisms of mindfulness are included herein.

STUDIES OF NEUROBIOLOGICAL MECHANISMS OF MINDFULNESS AND MEDITATION

A relatively large number of functional neuroimaging studies now enhance our understanding of the neural processes associated with mindfulness. A smaller number of structural imaging studies have been conducted as well.

FUNCTIONAL IMAGING STUDIES

The review focused on recent functional imaging studies that enhance our understanding of neural processes associated with the practice of mindfulness meditation. Results are summarized in detail in Table 1.

Many investigations studied individuals who had completed mindfulness training[6-19]. A relatively large number studied experienced meditators[20-33]. Additionally, some studies focused on brief mindfulness training[34,35], state[36] and trait[37-39] mindfulness. One study compared expert and novice meditators[40]. Finally some investigation focused on using mindfulness interventions for social anxiety disorder (SAD)[8,13,15], generalized anxiety disorder (GAD)[16] and bipolar disorder[17].

STRUCTURAL IMAGING STUDIES

A growing body of literature indicates that mindfulness is associated with changes in brain structure. While this review focused on functional imaging a number of structural imaging studies were reviewed as well. These findings are summarized in Table 2. Studies reviewed used magnetic resonance imaging (MRI) to investigate brain morphometry[19,41-50] as well as fractional anisotropy (FA)[51,52] and gyrification[53].

DISCUSSION

Though many questions remain unanswered, there is now a body of literature that provides important insights into the neural mechanisms associated with mindfulness. This evidence indicates brain regions that may be generally associated with mindfulness. More importantly, it is now possible to begin to understand neural processes that underlie the cognitive and emotional benefits of a mindfulness practice.

BRAIN REGIONS ASSOCIATED WITH MECHANISMS OF MINDFULNESS

The functional imaging studies reviewed herein indicate that mindfulness is associated with neural mechanisms involving multiple brain regions (Table 3). It is difficult to draw firm conclusions given the variability of methods utilized and diversity of the populations studied. Nonetheless, there is convincing evidence that mindfulness is associated with brain activation and/or connectivity of several regions as outlined in Table 3. Multiple studies implicate mechanisms involving frontal regions[6,10,11,14,16-18,20,25,28,32-36,39]. A few studies implicate lateral regions[11,16,25] including ventrolateral prefrontal cortex (VLPFC)[16] and dorsolateral prefrontal cortex (DLPFC)[11]. However, the strongest evidence is for medial frontal regions[6,10,13,14,17,18,20,25,27,28,33,36] including anterior cingulate cortex (ACC)[10,18,20,25,36]. Posterior medial regions are also involved[13,22,29-31,33,36,37] primarily in the area of the posterior cingulate cortex (PCC) and precuneus[13,22,30,31,33,36,37]. Thus, there is very strong evidence that anterior and posterior cortical midline structures (CMS) play a key role in the mechanisms of mindfulness[6,10,13,14,17,18,20,25,27-33,36,37]. Since the CMS are key components of the default mode network (DMN), this circuitry is clearly implicated and a number of investigations have specifically focused on the role of the DMN[21,24,26,30,33,37]. In addition, there is strong evidence for involvement of the insula[6,10,14,18,23,25,32,35,38] and amygdala[8,12,16,24,32,35,39]. A few studies also suggest involvement of the basal ganglia[22,28] and thalamus[10].

Structural imaging investigations (Table 2) provide strong evidence of mindfulness-related changes in the hippocampus[19,41,45-49]. Other results are consistent with functional imaging studies and implicate CMS/DMN[42,48,51], insula[49,53], amygdala[43-45], basal ganglia[44,45,50] and thalamus[45].

Table 1 Functional imaging studies of mindfulness and meditation

Ref.	Mindfulness intervention or condition	Result
Allen et al[11]	Mindfulness	Diminished Stroop conflict and greater DLPFC responses during executive processing.
Baerentsen et al[22]	Meditators	At onset of meditation, activations occurred bilaterally in putamen and supplementary motor cortex with deactivations in the precuneus, the posterior cingulate cortex and the parieto-temporal area. With sustained meditation, activations were found in the caudate and deactivations were in right hemisphere white matter.
Brefczynski-Lewis et al[40]	Experienced meditators	Activation during sustained attention showed an inverted curve. Expert meditators (average 19000 h) of practice had more activation than novices but experts (average 44000 h) had less activation. In response to distracter sounds, expert meditators had less brain activation in areas associated with discursive thoughts and emotions but more activation in regions related to response inhibition and attention compared to novices.
Creswell et al[39]	Dispositional mindfulness	Dispositional mindfulness was associated with widespread prefrontal cortical activation, and decreased bilateral amygdala activity during affect labeling. Negative associations were found between prefrontal cortex and right amygdala responses in participants high in mindfulness.
Desbordes et al[12]	Mindfulness training	Decreased right amygdala activation in response to positive images.
Dickenson et al[34]	Brief mindfulness induction	Focused breathing activated a parietal and prefrontal attention network and trait-level mindfulness correlated with parietal activation.
Farb et al[6]	MBSR	Interoceptive attention predicted greater activity in anterior insula but decreased recruitment of the DMPFC as well as altered functional connectivity between the DMPFC and the insula.
Farb et al[7]	Mindfulness training	Experiential focus resulted in reductions in cortical midline regions associated with narrative focus in novices. In trained participants, experiential focus was associated with reductions in the mPFC and increased engagement the lateral PFC, insula and somatosensory area. Analyses of functional connectivity revealed coupling between the insula and the mPFC in novices that was uncoupled in the mindfulness group.
Farb et al[14]	Mindfulness training	Participants had right-lateralized recruitment, including visceral and somatosensory areas associated with body sensation.
Gard et al[25]	Healthy meditators	Mindfulness practitioners experienced reduced unpleasantness of pain, which was associated with decreased activation in the lateral PFC and increased activation in the right insula. Anticipation of pain was associated with increased anterior cingulate cortex activation.
Garrison et al[30]	Healthy meditators	"Undistracted awareness" was associated with PCC deactivation. In contrast, "distracted awareness" corresponded with PCC activation.
Garrison et al[31]	Healthy meditators	Volitional decrease of the feedback graph was associated with deactivation of the PCC.
Goldin et al[8]	MBSR for social anxiety disorder	MBSR yielded greater reductions in negative emotion and increased activation in attention-related parietal cortex compared to aerobic exercise.
Goldin et al[13]	MBSR for social anxiety disorder	MBSR led to increased activation in the PCC during negative self-view condition. DMPFC activation increases during negative self-view were associated with decreased disability and enhanced mindfulness.
Goldin et al[15]	MBSR for social anxiety disorder	MBSR associated with decreased anxiety and depression symptoms and improved self-esteem. Breath-focused attention task associated with decreased negative emotion and reduced amygdala activation.
Hasenkamp et al[26]	Healthy meditators	Brain activation in DMN during mind wandering, and in salience network regions during awareness of mind wandering.
Hasenkamp et al[27]	Healthy meditators	Meditation experience was associated with increased connectivity within attention networks and between regions involved with attention and medial frontal cortex.
Hölzel et al[16]	MBSR for GAD	Amygdala activation in response to neutral faces decreased, VLPFC activation increased and functional connectivity between amygdala and PFC increased. Changes in VLPFC activation and amygdala-PFC connectivity correlated with changes in Beck Anxiety Inventory scores.
Hölzel et al[20]	Vipassana meditators	Meditation associated with increased activation in ACC and dorsal medial prefrontal cortex.
Ives-Deliperi et al[17]	MBCT for bipolar disorder	Activation increased in the medial PFC and posterior parietal lobe, in response to a mindfulness task. There was a correlation between activation changes in medial PFC and increased mindfulness.
Ives-Deliperi et al[36]	State mindfulness	Decreased activation in anterior insula, ACC, medial prefrontal cortex and bilateral precuneus during mindfulness meditation.
Kilpatrick et al[9]	MBSR	Increased functional connectivity of auditory and visual networks as well as between auditory cortex and areas associated with attention and self-referential processes. Enhanced anticorrelation between auditory and visual cortex as well as between visual cortex and attention and self-referential processing areas.
Kirk et al[23]	Experienced meditators	During the Ultimatum Game, controls recruit the anterior insula during unfair offers. In contrast, meditators display attenuated activity in high-level emotional representations of the anterior insula and increased activity in the low-level interoceptive representations of the posterior insula.
Kozasa et al[28]	Healthy meditators	Meditators had decreased activity relative to non-meditators in medial frontal, temporal, precentral, postcentral and basal ganglia regions during the incongruent conditions of the Stroop task.

Lutz et al[32]	Healthy subjects	Mindfulness increased activations in prefrontal regions during expectation of negative pictures. During perception of negative stimuli, reduced activation was found in amygdala and parahippocampal regions. Prefrontal and insular activations when expecting negative pictures correlated negatively with trait mindfulness.
Lutz et al[35]	Experienced meditators	Enhanced activity in the anterior insula and the mid-cingulate was associated with decreased pain-related unpleasantness.
Pagnoni et al[21]	Experienced meditators	vPMC activity was lower in meditators and was correlated with performance on a test for sustained attention. Functional connectivity analysis with a vPMC seed revealed attention performance was associated with the degree of temporal correlation between vPMC and the temporoparietal junction.
Pagnoni et al[29]	Zen meditators	Practitioners displayed reduced duration of the neural response linked to conceptual processing in regions of the DMN.
Paul et al[38]	Healthy subjects	Non-reactivity was inversely correlated with insula activation during inhibition to negative stimuli.
Shaurya Prakash et al[37]	Mindfulness disposition	Mindfulness disposition was associated with greater connectivity of the DMN, particularly in the PCC and the precuneus.
Taylor et al[24]	Experienced and beginning meditators	Experienced meditators had weaker functional connectivity between DMN regions.
Taylor et al[33]	Experienced and beginning meditators	Mindfulness attenuated emotional intensity. For experienced meditators, mindfulness induced a deactivation of DMN areas. For beginners, mindfulness induced a down-regulation of the left amygdala.
Wells et al[19]	MBSR	Increased functional connectivity between the PCC and medial prefrontal cortex and left hippocampus.
Baerentsen et al[22]	Mindfulness training	Reduced smoking craving associated with reduced activation of ACC. Mindful attention reduced functional connectivity between ACC and other craving-related regions.
Zeidan et al[10]	Mindfulness training	Anxiety relief associated with activation of the PFC and insula.
Zeidan et al[18]	Mindfulness training	Meditation decreased pain-associated activation of the contralateral somatosensory cortex. Reductions in pain were associated with increased activity in the ACC and insula. Decreased pain unpleasantness was associated with orbitofrontal activation and thalamic deactivation.

ACC: Anterior cingulate cortex; DMN: Default mode network; PCC: Posterior cingulate cortex; DMPFC: Dorsomedial prefrontal cortex; mPFC: Medial prefrontal cortex; vLPFC: Ventrolateral prefrontal cortex; vPMC: Ventral posterior medial cortex.

Table 2 Brain regions where structural imaging studies have demonstrated mindfulness related changes

Anterior cingulate cortex[42,51]
Orbitofrontal cortex[41]
Inferior temporal gyrus[49]
Insula[49,53]
Lingual gyrus[45]
Cuneus[45]
Sensorimotor cortex[42,53]
Fusiform gyrus[53]
Cuneus[53]
Corpus callosum[52]
Posterior cingulate cortex[48]
Cerebellum[48]
Hippocampus[19,41,45-49]
Amygdala[43-45]
Putamen[50]
Caudate[44,45]
Thalamus[45]

Taken together, these studies provide convincing evidence that neural mindfulness mechanisms involve the CMS/DMN, insula, hippocampus and amygdala. There is also evidence implicating lateral prefrontal regions, basal ganglia and thalamus.

NEURAL MECHANISMS OF THE COGNITIVE AND EMOTIONAL BENEFITS OF MINDFULNESS

As reviewed elsewhere[5], the literature indicates that mindfulness impacts attention, emotional regulation and thinking patterns. The following sections review evidence suggesting neural mechanisms underlying these effects.

ATTENTION

The development of attentional skills is the central component of mindfulness meditation practice[3,4,54]. Training of attention skills enhances the capability to sustain non-judgmental awareness of one's thinking patterns, emotions, and sensory perceptions[4,55]. This awareness facilitates gain distance from thoughts and emotions such that these become less powerful and compelling. In particular, mindfulness supports the recognition of automatic thinking patterns (discussed below).

Three neural networks, the alerting, orienting and executive, are thought to play specific roles in the attention process[56,57]. The alerting network modulates task-specific alertness and attentional engagement and involves right frontal cortex, including DLPFC and ACC, as well as right parietal cortex[57]. The orienting network controls stimulus selection, which is the capability to select precise information from numerous sensory stimuli. This network includes the frontal eye fields, superior parietal cortex, superior colliculus and temporal parietal junction[57]. Finally, the executive control circuitry mediates control of attention. This function includes top-down control as well as monitoring and resolution of conflict between computations involving planning or decision-making, error detection and regulation of thoughts and feelings[57]. In regard to brain regions involve, the ACC, lateral frontal

Table 3 Brain regions involved with mindfulness mechanisms

Frontal cortex[6,10,11,14,16-18,20,25,28,32-36,39]
  Lateral frontal cortex[11,16,25]
    Ventrolateral prefrontal cortex[16]
    Dorsolateral prefrontal cortex[11]
  Medial frontal cortex[6,10,13,14,17,18,20,25,27,28,33,36]
    Anterior cingulate cortex[10,18,20,25,36]
  Orbitofrontal cortex[10]
Posterior medial cortex[13,22,29-31,33,36,37]
  Posterior cingulate cortex/precuneus[13,22,30,31,33,36,37]
  Ventral posteromedial cortex[29]
Insula[6,10,14,18,23,25,32,35,38]
Temporal cortex[28,33]
Temporoparietal junction[29]
Sensorimotor cortex[6,10,28]
Inferior parietal lobule[6,33]
Parahippocampal gyrus[35]
Amygdala[8,12,16,24,32,35,39]
Basal ganglia[22,28]
Thalamus[10]

cortex, and basal ganglia contribute to executive control processes[56].

Several studies suggest neural mechanisms associated with mindfulness-related improvements in attention. An MBSR study examined the neural processes of deploying attention to control responses to negative beliefs about self in social anxiety disorder[15]. MBSR yielded decreased negative emotion and increased activation in attention modulating parietal regions. In a study to investigate meta-awareness and regulation of mind wandering and related influence on DMN activity, investigators collected fMRI data from a group of Zen meditators and a meditation-naive control group engaging in an attention-to-breathing task[29]. Results indicated the incidence of states of elevated ventral posterior medial cortex (vPMC) activity was lower in meditators and was significantly correlated with performance on a test for sustained attention. Analysis of functional connectivity using the vPMC seed revealed an association between attention performance and the degree of temporal correlation between right temporoparietal junction (TPJ) and vPMC. Another study aimed to evaluate the performance of meditators and non-meditators during an fMRI adapted Stroop Task, which requires impulse and attention control[28]. Non-meditators showed increased activity compared to meditators in the middle temporal, medial frontal, pre and postcentral gyri and basal ganglia during the incongruent conditions. The authors conclude that their results suggest that meditation improves efficiency, perhaps by enhancing the ability to sustain attention and control impulses[28]. A study examined a model[26] that proposes four cognitive cycle intervals relevant for meditation: mind wandering, awareness of the wandering of one's mind, varying of attention, and prolonged attention. Fourteen meditators executed breath-focused meditation during scanning[26]. Study participants were instructed to press a button when they realized their mind had wandered and then return their focus to the breath. Analyses of results indicated brain activity in regions associated with the

default mode during mind wandering, and in the salience network during awareness of mind wandering. Finally the executive network was active when shifting and sustaining attention.

Taken together, these investigation suggest that enhanced attention is associated with neural mechanisms involving attention-related parietal cortical regions[15], vPMC[29], TPJ[29], CMS[28], temporal cortex[28], sensorimotor cortex[28] and basal ganglia[28]. Thus, mindfulness likely impacts all of the three attention networks.

In addition to training general attention processes, mindfulness facilitates the enhancement of interoceptive attention (IA) to visceral bodily sensations as they occur in the present moment. An fMRI study examined functional plasticity in accessing interoceptive representations in MBSR trained individuals[14]. Mindfulness training predicted enhanced activity in anterior insula and diminished recruitment of dorsomedial prefrontal cortex (DMPFC) during IA, as well as changed functional connectivity between the DMPFC and insula.

In summary, mindfulness training appears to modify neural processes in the three attention networks and insula, which result in improved general and interoceptive attention respectively.

AUTOMATIC THOUGHTS AND SELF-REFERENTIAL THINKING

Cognitive neuroscience suggests two general types of mental processes, those that are controlled and those that are automatic. Automatic processes may be innately automatic or become automated as a result of learning and practice. Automated thoughts are initiated unconsciously and are not easy to interrupt or prevent[57]. For example, when attention involuntarily drifts away from an object of conscious attention, the DMN and automatic thinking is engaged as an involuntary process[58]. Objective awareness of automatic thoughts is understood to be a primary mechanism by which mindfulness decreases symptoms of depression, anxiety and stress[5]. Objective awareness allows one to interpret thoughts as "just thoughts" and prevents experiencing irrational negative thinking as fact.

There is compelling evidence that mindfulness impacts DMN neural processes[21,24,26,30,33,37]. Modification of this network likely plays a significant role in the objectification of the experience of automatic thoughts.

Most of the medial cortex acts as a functional unit known as the CMS[59]. The CMS are part of the DMN[60,61] and play a key role in stimulus independent thought (SIT)[58,62]. Decreased activation of the CMS is correlated with decreased SIT[63]. Therefore, the CMS may be the specific portion of the DMN involved with mindfulness-induced modification of automatic thinking.

As reviewed elsewhere[5], self-referential thinking is a type of automatic cognitions particularly relevant for mood and anxiety disorders. The CMS are involved in self-referential thinking[59,62,64]. A study of MBSR for Social anxiety disorder (SAD)[13] used a self-referential en-

coding paradigm, which was administered at baseline and post-intervention in order to examine changes in neural and behavioral responses during fMRI. MBSR produced reductions in negative, as well as increases in positive views of self. MBSR led to increased brain responses in the PCC during the negative self-view. MBSR-related increased DMPFC activity during negative self-view was correlated with diminished social anxiety and augmented mindfulness. These findings suggest that mindfulness specifically attenuates maladaptive habitual self-views – at least in part - by impacting DMN regions and in particular the CMS.

EMOTIONAL REGULATION

A number of studies provide evidence of how mindfulness may contribute to enhanced emotional regulation. An fMRI study compared neural reactivity to provocation of sadness in participants completing 8 wk of mindfulness training (MT) and controls[7]. Sadness caused activation of regions associated with self-referential thinking in the CMS. MT participants had a distinct activation pattern, with enhanced right hemisphere recruitment, including areas associated with body sensation. Another fMRI study examined effects of a short mindfulness intervention during the cued expectation and perception of pictures that were negative or potentially negative[35]. The mindfulness intervention was correlated with increased activation of prefrontal cortex during the expectation of negative pictures. Perception of negative stimuli was associated with reduced activation in amygdala and parahippocampal gyrus. A study of MBCT for bipolar disorder using fMRI[17] revealed improvements in the treatment group in measures of mindfulness, anxiety, affect regulation working memory, spatial memory and verbal fluency. Blood-oxygen level-dependent (BOLD) signal increases occurred in the medial prefrontal cortex (PFC) and parietal lobe. Analysis also revealed a correlation between signal changes in medial PFC and increased mindfulness. A study of MBSR for GAD[16] found changes in amygdala and VLPFC activation as well as increased functional connectivity between amygdala and PFC regions comparing pre- to post-intervention. VLPFC activation and amygdala-prefrontal connectivity changes were correlated with change in Beck Anxiety Inventory scores. Another study of the longitudinal effects of meditation training on amygdala responses examined how 8 wk of meditation training impacts amygdala responses to emotional when in a non-meditative state[12]. Adults with no prior meditation experience took part in Mindful Attention Training, Cognitively-Based Compassion Training or a control intervention. Participants underwent an fMRI experiment pre and post-intervention. In the scanner, they were presented images with positive, negative, and neutral emotional valences while remaining in a non-meditative state. Findings indicated decreased right amygdala activation in the Mindful Attention group in response to im-

ages of all valences. Another fMRI study explored the effects of mindfulness on the neural responses to emotional stimuli[24]. Experienced and novice meditators were scanned as they viewed negative, positive, and neutral pictures in both a mindful state and non-mindful state. The mindful condition attenuated emotional intensity and imaging data indicated that this effect was achieved through distinct neural mechanisms for each group. For the experienced cohort, mindfulness produced deactivation of DMN areas but did not influence responses in brain regions involved in emotional reactivity. For beginners, mindfulness down-regulated the left amygdala during emotional processing. The authors conclude that the long-term practice of mindfulness leads to reduced emotional reactivity by promoting tolerance of emotion and enhanced present-moment awareness. A study investigated MBSR-induced changes in of emotional reactivity and regulation of negative beliefs about self in subjects with seasonal affective disorder (SAD)[8]. Sixteen patients were scanned while reacting to negative beliefs and while regulating negative emotions. MBSR resulted in improved anxiety and depressive symptoms and self-esteem and during a breath-focused attention task. Subjects also showed diminished negative emotion and amygdala activity as well as increased activity in brain regions involved in attentional deployment.

These investigations indicate that mindfulness enhancement of emotional regulation appears involve modification of processing in lateral frontal regions[16] CMS/DMN[7,17,24], regions involved with IA[7] and amygdala[8,12,16,24,35]. Interestingly, there is evidence that these mechanisms may change based upon amount of meditation experience[24]. The CMS are of particular interest in emotional regulation as these regions play a role in emotional processing[65,66] including mediating the experience of sadness[7]. Thus, these areas may represent a key link between self-referential thinking and emotional dysregulation in affective disorders.

CONCLUSION

The studies reviewed herein increase our understanding of the neural processes associated with mindfulness. A limitation of the literature is the fact that multiple methodologies have been utilized and a diverse population studied. Thus direct comparison of studies is not feasible. Nonetheless, the current literature begins to define the neural mechanisms of mindfulness and provides the groundwork for future investigations.

This review of this literature revealed compelling evidence that mindfulness impacts the function of the medial cortex and associated default mode network as well as insula and amygdala. Additionally, mindfulness practice appears to effect lateral frontal regions and basal ganglia, at least in some cases. Structural imaging studies are consistent with these findings and also indicate changes in the hippocampus.

REFERENCES

1. **Grossman P**, Niemann L, Schmidt S, Walach H. Mindfulness-based stress reduction and health benefits. A meta-analysis. *J Psychosom Res* 2004; **57**: 35-43 [PMID: 15256293 DOI: 10.1016/S0022-3999(03)00573-7]

2. **Kabat-Zinn J**, Mindfulness-based interventions in context: past, present, and future. *Clin Psychol Sci Pract* 2003; **10**: 144-156 [DOI: 10.1093/clipsy.bpg016]

3. **Lutz A**, Slagter HA, Dunne JD, Davidson RJ. Attention regulation and monitoring in meditation. *Trends Cogn Sci* 2008; **12**: 163-169 [PMID: 18329323 DOI: 10.1016/j.tics.2008.01.005]

4. **Malinowski P**. Neural mechanisms of attentional control in mindfulness meditation. *Front Neurosci* 2013; **7**: 8 [PMID: 23382709 DOI: 10.3389/fnins.2013.00008]

5. **Marchand WR**. Mindfulness-based stress reduction, mindfulness-based cognitive therapy, and Zen meditation for depression, anxiety, pain, and psychological distress. *J Psychiatr Pract* 2012; **18**: 233-252 [PMID: 22805898 DOI: 10.1097/01.pra.0000416014.53215.86]

6. **Farb NA**, Segal ZV, Mayberg H, Bean J, McKeon D, Fatima Z, Anderson AK. Attending to the present: mindfulness meditation reveals distinct neural modes of self-reference. *Soc Cogn Affect Neurosci* 2007; **2**: 313-322 [PMID: 18985137 DOI: 10.1093/scan/nsm030]

7. **Farb NA**, Anderson AK, Mayberg H, Bean J, McKeon D, Segal ZV. Minding one's emotions: mindfulness training alters the neural expression of sadness. *Emotion* 2010; **10**: 25-33 [PMID: 20141299 DOI: 10.1037/a0017151]

8. **Goldin PR**, Gross JJ. Effects of mindfulness-based stress reduction (MBSR) on emotion regulation in social anxiety disorder. *Emotion* 2010; **10**: 83-91 [PMID: 20141305 DOI: 10.1037/a0018441]

9. **Kilpatrick LA**, Suyenobu BY, Smith SR, Bueller JA, Goodman T, Creswell JD, Tillisch K, Mayer EA, Naliboff BD. Impact of Mindfulness-Based Stress Reduction training on intrinsic brain connectivity. *Neuroimage* 2011; **56**: 290-298 [PMID: 21334442 DOI: 10.1016/j.neuroimage.2011.02.034]

10. **Zeidan F**, Martucci KT, Kraft RA, Gordon NS, McHaffie JG, Coghill RC. Brain mechanisms supporting the modulation of pain by mindfulness meditation. *J Neurosci* 2011; **31**: 5540-5548 [PMID: 21471390 DOI: 10.1523/JNEUROSCI.5791-10.2011]

11. **Allen M**, Dietz M, Blair KS, van Beek M, Rees G, Vestergaard-Poulsen P, Lutz A, Roepstorff A. Cognitive-affective neural plasticity following active-controlled mindfulness intervention. *J Neurosci* 2012; **32**: 15601-15610 [PMID: 23115195 DOI: 10.1523/JNEUROSCI.2957-12.2012]

12. **Desbordes G**, Negi LT, Pace TW, Wallace BA, Raison CL, Schwartz EL. Effects of mindful-attention and compassion meditation training on amygdala response to emotional stimuli in an ordinary, non-meditative state. *Front Hum Neurosci* 2012; **6**: 292 [PMID: 23125828 DOI: 10.3389/fnhum.2012.00292]

13. **Goldin P**, Ziv M, Jazaieri H, Gross JJ. Randomized controlled trial of mindfulness-based stress reduction versus aerobic exercise: effects on the self-referential brain network in social anxiety disorder. *Front Hum Neurosci* 2012; **6**: 295 [PMID: 23133411 DOI: 10.3389/fnhum.2012.00295]

14. **Farb NA**, Segal ZV, Anderson AK. Mindfulness meditation training alters cortical representations of interoceptive attention. *Soc Cogn Affect Neurosci* 2013; **8**: 15-26 [PMID: 22689216 DOI: 10.1093/scan/nss066]

15. **Goldin P**, Ziv M, Jazaieri H, Hahn K, Gross JJ. MBSR vs aerobic exercise in social anxiety: fMRI of emotion regulation of negative self-beliefs. *Soc Cogn Affect Neurosci* 2013; **8**: 65-72 [PMID: 22586252 DOI: 10.1093/scan/nss054]

16. **Hölzel BK**, Hoge EA, Greve DN, Gard T, Creswell JD, Brown KW, Barrett LF, Schwartz C, Vaitl D, Lazar SW. Neural mechanisms of symptom improvements in generalized anxiety disorder following mindfulness training. *Neuroimage Clin* 2013; **2**: 448-458 [PMID: 24179799 DOI: 10.1016/j.nicl.2013.03.011]

17. **Ives-Deliperi VL**, Howells F, Stein DJ, Meintjes EM, Horn N. The effects of mindfulness-based cognitive therapy in patients with bipolar disorder: a controlled functional MRI investigation. *J Affect Disord* 2013; **150**: 1152-1157 [PMID: 23790741 DOI: 10.1016/j.jad.2013.05.074]

18. **Zeidan F**, Martucci KT, Kraft RA, McHaffie JG, Coghill RC. Neural correlates of mindfulness meditation-related anxiety relief. *Soc Cogn Affect Neurosci* 2014; **9**: 751-759 [PMID: 23615765 DOI: 10.1093/scan/nst041]

19. **Wells RE**, Yeh GY, Kerr CE, Wolkin J, Davis RB, Tan Y, Spaeth R, Wall RB, Walsh J, Kaptchuk TJ, Press D, Phillips RS, Kong J. Meditation's impact on default mode network and hippocampus in mild cognitive impairment: a pilot study. *Neurosci Lett* 2013; **556**: 15-19 [PMID: 24120430 DOI: 10.1016/j.neulet.2013.10.001]

20. **Hölzel BK**, Ott U, Hempel H, Hackl A, Wolf K, Stark R, Vaitl D. Differential engagement of anterior cingulate and adjacent medial frontal cortex in adept meditators and non-meditators. *Neurosci Lett* 2007; **421**: 16-21 [PMID: 17548160 DOI: 10.1016/j.neulet.2007.04.074]

21. **Pagnoni G**, Cekic M, Guo Y. "Thinking about not-thinking": neural correlates of conceptual processing during Zen meditation. *PLoS One* 2008; **3**: e3083 [PMID: 18769538 DOI: 10.1371/journal.pone.0003083]

22. **Baerentsen KB**, Stødkilde-Jørgensen H, Sommerlund B, Hartmann T, Damsgaard-Madsen J, Fosnaes M, Green AC. An investigation of brain processes supporting meditation. *Cogn Process* 2010; **11**: 57-84 [PMID: 19876663 DOI: 10.1007/s10339-009-0342-3]

23. **Kirk U**, Downar J, Montague PR. Interoception drives increased rational decision-making in meditators playing the ultimatum game. *Front Neurosci* 2011; **5**: 49 [PMID: 21559066 DOI: 10.3389/fnins.2011.00049]

24. **Taylor VA**, Grant J, Daneault V, Scavone G, Breton E, Roffe-Vidal S, Courtemanche J, Lavarenne AS, Beauregard M. Impact of mindfulness on the neural responses to emotional pictures in experienced and beginner meditators. *Neuroimage* 2011; **57**: 1524-1533 [PMID: 21679770 DOI: 10.1016/j.neuroimage.2011.06.001]

25. **Gard T**, Hölzel BK, Sack AT, Hempel H, Lazar SW, Vaitl D, Ott U. Pain attenuation through mindfulness is associated with decreased cognitive control and increased sensory processing in the brain. *Cereb Cortex* 2012; **22**: 2692-2702 [PMID: 22172578 DOI: 10.1093/cercor/bhr352]

26. **Hasenkamp W**, Wilson-Mendenhall CD, Duncan E, Barsalou LW. Mind wandering and attention during focused meditation: a fine-grained temporal analysis of fluctuating cognitive states. *Neuroimage* 2012; **59**: 750-760 [PMID: 21782031 DOI: 10.1016/j.neuroimage.2011.07.008]

27. **Hasenkamp W**, Barsalou LW. Effects of meditation experience on functional connectivity of distributed brain networks. *Front Hum Neurosci* 2012; **6**: 38 [PMID: 22403536 DOI: 10.3389/fnhum.2012.00038]

28. **Kozasa EH**, Sato JR, Lacerda SS, Barreiros MA, Radvany J, Russell TA, Sanches LG, Mello LE, Amaro E. Meditation training increases brain efficiency in an attention task. *Neuroimage* 2012; **59**: 745-749 [PMID: 21763432 DOI: 10.1016/j.neuroimage.2011.06.088]

29. **Pagnoni G**. Dynamical properties of BOLD activity from the ventral posteromedial cortex associated with meditation and attentional skills. *J Neurosci* 2012; **32**: 5242-5249 [PMID: 22496570 DOI: 10.1523/JNEUROSCI.4135-11.2012]

30. **Garrison KA**, Santoyo JF, Davis JH, Thornhill TA, Kerr CE, Brewer JA. Effortless awareness: using real time neurofeedback to investigate correlates of posterior cingulate cortex activity in meditators' self-report. *Front Hum Neurosci* 2013; **7**: 440 [PMID: 23964222 DOI: 10.3389/fnhum.2013.00440]

31 **Garrison KA**, Scheinost D, Worhunsky PD, Elwafi HM, Thornhill TA, Thompson E, Saron C, Desbordes G, Kober H, Hampson M, Gray JR, Constable RT, Papademetris X, Brewer JA. Real-time fMRI links subjective experience with brain activity during focused attention. *Neuroimage* 2013; **81**: 110-118 [PMID: 23684866 DOI: 10.1016/j.neuroimage.2013.05.030]

32 **Lutz A**, McFarlin DR, Perlman DM, Salomons TV, Davidson RJ. Altered anterior insula activation during anticipation and experience of painful stimuli in expert meditators. *Neuroimage* 2013; **64**: 538-546 [PMID: 23000783 DOI: 10.1016/j.neuroimage.2012.09.030]

33 **Taylor VA**, Daneault V, Grant J, Scavone G, Breton E, Roffe-Vidal S, Courtemanche J, Lavarenne AS, Marrelec G, Benali H, Beauregard M. Impact of meditation training on the default mode network during a restful state. *Soc Cogn Affect Neurosci* 2013; **8**: 4-14 [PMID: 22446298 DOI: 10.1093/scan/nsr087]

34 **Dickenson J**, Berkman ET, Arch J, Lieberman MD. Neural correlates of focused attention during a brief mindfulness induction. *Soc Cogn Affect Neurosci* 2013; **8**: 40-47 [PMID: 22383804 DOI: 10.1093/scan/nss030]

35 **Lutz J**, Herwig U, Opialla S, Hittmeyer A, Jäncke L, Rufer M, Grosse Holtforth M, Brühl AB. Mindfulness and emotion regulation-an fMRI study. *Soc Cogn Affect Neurosci* 2014; **9**: 776-785 [PMID: 23563850 DOI: 10.1093/scan/nst043]

36 **Ives-Deliperi VL**, Solms M, Meintjes EM. The neural substrates of mindfulness: an fMRI investigation. *Soc Neurosci* 2011; **6**: 231-242 [PMID: 20835972 DOI: 10.1080/17470919.2010.513495]

37 **Shaurya Prakash R**, De Leon AA, Klatt M, Malarkey W, Patterson B. Mindfulness disposition and default-mode network connectivity in older adults. *Soc Cogn Affect Neurosci* 2013; **8**: 112-117 [PMID: 23051900 DOI: 10.1093/scan/nss115]

38 **Paul NA**, Stanton SJ, Greeson JM, Smoski MJ, Wang L. Psychological and neural mechanisms of trait mindfulness in reducing depression vulnerability. *Soc Cogn Affect Neurosci* 2013; **8**: 56-64 [PMID: 22717383 DOI: 10.1093/scan/nss070]

39 **Creswell JD**, Way BM, Eisenberger NI, Lieberman MD. Neural correlates of dispositional mindfulness during affect labeling. *Psychosom Med* 2007; **69**: 560-565 [PMID: 17634566 DOI: 10.1097/PSY.0b013e3180f6171f]

40 **Brefczynski-Lewis JA**, Lutz A, Schaefer HS, Levinson DB, Davidson RJ. Neural correlates of attentional expertise in long-term meditation practitioners. *Proc Natl Acad Sci USA* 2007; **104**: 11483-11488 [PMID: 17596341 DOI: 10.1073/pnas.0606552104]

41 **Luders E**, Toga AW, Lepore N, Gaser C. The underlying anatomical correlates of long-term meditation: larger hippocampal and frontal volumes of gray matter. *Neuroimage* 2009; **45**: 672-678 [PMID: 19280691 DOI: 10.1016/j.neuroimage.2008.12.061]

42 **Grant JA**, Courtemanche J, Duerden EG, Duncan GH, Rainville P. Cortical thickness and pain sensitivity in zen meditators. *Emotion* 2010; **10**: 43-53 [PMID: 20141301 DOI: 10.1037/a0018334]

43 **Hölzel BK**, Carmody J, Evans KC, Hoge EA, Dusek JA, Morgan L, Pitman RK, Lazar SW. Stress reduction correlates with structural changes in the amygdala. *Soc Cogn Affect Neurosci* 2010; **5**: 11-17 [PMID: 19776221 DOI: 10.1093/scan/nsp034]

44 **Taren AA**, Creswell JD, Gianaros PJ. Dispositional mindfulness co-varies with smaller amygdala and caudate volumes in community adults. *PLoS One* 2013; **8**: e64574 [PMID: 23717632 DOI: 10.1371/journal.pone.0064574]

45 **Pickut BA**, Van Hecke W, Kerckhofs E, Mariën P, Vanneste S, Cras P, Parizel PM. Mindfulness based intervention in Parkinson's disease leads to structural brain changes on MRI: a randomized controlled longitudinal trial. *Clin Neurol Neurosurg* 2013; **115**: 2419-2425 [PMID: 24184066 DOI: 10.1016/j.clineuro.2013.10.002]

46 **Luders E**, Thompson PM, Kurth F, Hong JY, Phillips OR, Wang Y, Gutman BA, Chou YY, Narr KL, Toga AW. Global and regional alterations of hippocampal anatomy in long-term meditation practitioners. *Hum Brain Mapp* 2013; **34**: 3369-3375 [PMID: 22815233 DOI: 10.1002/hbm.22153]

47 **Luders E**, Kurth F, Toga AW, Narr KL, Gaser C. Meditation effects within the hippocampal complex revealed by voxel-based morphometry and cytoarchitectonic probabilistic mapping. *Front Psychol* 2013; **4**: 398 [PMID: 23847572 DOI: 10.3389/fpsyg.2013.00398]

48 **Hölzel BK**, Carmody J, Vangel M, Congleton C, Yerramsetti SM, Gard T, Lazar SW. Mindfulness practice leads to increases in regional brain gray matter density. *Psychiatry Res* 2011; **191**: 36-43 [PMID: 21071182 DOI: 10.1016/j.pscychresns.2010.08.006]

49 **Hölzel BK**, Ott U, Gard T, Hempel H, Weygandt M, Morgen K, Vaitl D. Investigation of mindfulness meditation practitioners with voxel-based morphometry. *Soc Cogn Affect Neurosci* 2008; **3**: 55-61 [PMID: 19015095 DOI: 10.1093/scan/nsm038]

50 **Pagnoni G**, Cekic M. Age effects on gray matter volume and attentional performance in Zen meditation. *Neurobiol Aging* 2007; **28**: 1623-1627 [PMID: 17655980 DOI: 10.1016/j.neurobiolaging.2007.06.008]

51 **Tang YY**, Lu Q, Fan M, Yang Y, Posner MI. Mechanisms of white matter changes induced by meditation. *Proc Natl Acad Sci USA* 2012; **109**: 10570-10574 [PMID: 22689998 DOI: 10.1073/pnas.1207817109]

52 **Luders E**, Phillips OR, Clark K, Kurth F, Toga AW, Narr KL. Bridging the hemispheres in meditation: thicker callosal regions and enhanced fractional anisotropy (FA) in long-term practitioners. *Neuroimage* 2012; **61**: 181-187 [PMID: 22374478 DOI: 10.1016/j.neuroimage.2012.02.026]

53 **Luders E**, Kurth F, Mayer EA, Toga AW, Narr KL, Gaser C. The unique brain anatomy of meditation practitioners: alterations in cortical gyrification. *Front Hum Neurosci* 2012; **6**: 34 [PMID: 22393318 DOI: 10.3389/fnhum.2012.00034]

54 **Tang YY**, Posner MI. Attention training and attention state training. *Trends Cogn Sci* 2009; **13**: 222-227 [PMID: 19375975 DOI: 10.1016/j.tics.2009.01.009]

55 **Chiesa A**, Malinowski P. Mindfulness-based approaches: are they all the same? *J Clin Psychol* 2011; **67**: 404-424 [PMID: 21254062 DOI: 10.1002/jclp.20776]

56 **Posner MI**, Rothbart MK. Research on attention networks as a model for the integration of psychological science. *Annu Rev Psychol* 2007; **58**: 1-23 [PMID: 17029565 DOI: 10.1146/annurev.psych.58.110405.085516]

57 **Raz A**, Buhle J. Typologies of attentional networks. *Nat Rev Neurosci* 2006; **7**: 367-379 [PMID: 16760917 DOI: 10.1038/nrn1903]

58 **Mason MF**, Norton MI, Van Horn JD, Wegner DM, Grafton ST, Macrae CN. Wandering minds: the default network and stimulus-independent thought. *Science* 2007; **315**: 393-395 [PMID: 17234951 DOI: 10.1126/science.1131295]

59 **Northoff G**, Bermpohl F. Cortical midline structures and the self. *Trends Cogn Sci* 2004; **8**: 102-107 [PMID: 15301749 DOI: 10.1016/j.tics.2004.01.004]

60 **Raichle ME**, MacLeod AM, Snyder AZ, Powers WJ, Gusnard DA, Shulman GL. A default mode of brain function. *Proc Natl Acad Sci USA* 2001; **98**: 676-682 [PMID: 11209064 DOI: 10.1073/pnas.98.2.676]

61 **Gusnard DA**, Raichle ME, Raichle ME. Searching for a baseline: functional imaging and the resting human brain. *Nat Rev Neurosci* 2001; **2**: 685-694 [PMID: 11584306 DOI: 10.1038/35094500]

62 **McGuire PK**, Paulesu E, Frackowiak RS, Frith CD. Brain activity during stimulus independent thought. *Neuroreport* 1996; **7**: 2095-2099 [PMID: 8930966]

63 **McKiernan KA**, D'Angelo BR, Kaufman JN, Binder JR.

Interrupting the „stream of consciousness": an fMRI investigation. *Neuroimage* 2006; **29**: 1185-1191 [PMID: 16269249 DOI: 10.1016/j.neuroimage.2005.09.030]

64   **Northoff G**, Heinzel A, de Greck M, Bermpohl F, Dobrowolny H, Panksepp J. Self-referential processing in our brain--a meta-analysis of imaging studies on the self. *Neuroimage* 2006; **31**: 440-457 [PMID: 16466680 DOI: 10.1016/j.neuroimage.2005.12.002]

65   **Grimm S**, Boesiger P, Beck J, Schuepbach D, Bermpohl F, Walter M, Ernst J, Hell D, Boeker H, Northoff G. Altered negative BOLD responses in the default-mode network during emotion processing in depressed subjects. *Neuropsychopharmacology* 2009; **34**: 932-943 [PMID: 18536699 DOI: 10.1038/npp.2008.81]

66   **Heinzel A**, Bermpohl F, Niese R, Pfennig A, Pascual-Leone A, Schlaug G, Northoff G. How do we modulate our emotions? Parametric fMRI reveals cortical midline structures as regions specifically involved in the processing of emotional valences. *Brain Res Cogn Brain Res* 2005; **25**: 348-358 [PMID: 16081255 DOI: 10.1016/j.cogbrainres.2005.06.009]

MINIREVIEWS

Clinical use of bone-targeting radiopharmaceuticals with focus on alpha-emitters

Hinrich A Wieder, Michael Lassmann, Martin S Allen-Auerbach, Johannes Czernin, Ken Herrmann

Hinrich A Wieder, Department of Radiology, Zentrum für Radiologie und Nuklearmedizin, 41515 Grevenbroich, Germany
Hinrich A Wieder, Department of Nuclear Medicine, Technische Universität München, 81675 Munich, Germany
Michael Lassmann, Ken Herrmann, Department of Nuclear Medicine, University of Würzburg, 97080 Würzburg, Germany
Martin S Allen-Auerbach, Johannes Czernin, Ahmanson Translational Imaging Division, Department of Molecular and Medical Pharmacology, David Geffen School of Medicine at UCLA, Los Angeles, CA 90095, United States
Author contributions: Wieder HA, Lassmann M, Allen-Auerbach M, Czernin J and Herrmann K contributed to development of outline, and revision and approval of manuscript; Wieder HA, Czernin J and Herrmann K contributed to drafting and editing of manuscript; Lassmann M and Allen-Auerbach M contributed to figures.
Correspondence to: Hinrich A Wieder, MD, Department of Radiology, Zentrum für Radiologie und Nuklearmedizin, Zentrum für Radiologie und Nuklearmedizin, Von-Werth-Straße 5, 41515 Grevenbroich, Germany. h@wieder.de
Telephone: +49-2133-664980 Fax: +49-2133-662983
Received: November 27, 2013 Revised: March 20, 2014
Accepted: May 16, 2014
Published online: July 28, 2014

Abstract

Various single or multi-modality therapeutic options are available to treat pain of bone metastasis in patients with prostate cancer. Different radionuclides that emit β-rays such as [153]Samarium and [89]Strontium and achieve palliation are commercially available. In contrast to β-emitters, [223]Radium as a α-emitter has a short path-length. The advantage of the α-emitter is thus a highly localized biological effect that is caused by radiation induced DNA double-strand breaks and subsequent cell killing and/or limited effectiveness of cellular repair mechanisms. Due to the limited range of the α-particles the bone surface to red bone marrow dose ratio is also lower for [223]Radium which is expressed in a lower myelotoxicity. The α emitter [223]Radium dichloride is the first radiopharmaceutical that significantly prolongs life in castrate resistant prostate cancer patients with wide-spread bone metastatic disease. In a phase Ⅲ, randomized, double-blind, placebo-controlled study 921 patients with castration-resistant prostate cancer and bone metastases were randomly assigned. The analysis confirmed the [223]Radium survival benefit compared to the placebo (median, 14.9 mo *vs* 11.3 mo; *P* < 0.001). In addition, the treatment results in pain palliation and thus, improved quality of life and a delay of skeletal related events. At the same time the toxicity profile of [223]Radium was favourable. Since May 2013, [223]Radium dichloride (Xofigo®) is approved by the US Food and Drug Administration.

Core tip: The incidence rate of prostate cancer worldwide is high. Ninety percent of patients dying of prostate cancer have bone metastases with varying symptoms which are significantly impairing their quality of life. [223]Radium is the first therapeutic that results in a survival benefit for patients with bone metastatic, castrate resistant prostate cancer. [223]Radium was also associated with low myelosuppression rates and fewer adverse events.This article provides an overview of the pre-clinical and clinical trials with [223]Radium.

Wieder HA, Lassmann M, Allen-Auerbach M, Czernin J, Herrmann K. Clinical use of bone-targeting radiopharmaceuticals with focus on alpha-emitters. *World J Radiol* 2014; 6(7): 480-485 Available from: URL: http://www.wjgnet.com/1949-8470/full/v6/i7/480.htm DOI: http://dx.doi.org/10.4329/wjr.v6.i7.480

INTRODUCTION

According to estimates from the International Agency

Table 1 Physical characteristics of ⁸⁹Strontium, ¹⁵³Samarium and ²²³Radium

Radionuclide	Half-life	Maximum energy (MeV)	Mean energy (MeV)	Maximum range	γ-Emission (keV)
⁸⁹Sr	50.5 d	1.4 (β)	0.583 (β)	7 mm	None
¹⁵³Sm	1.9 d	0.81 (β)	0.229 (β)	4 mm	103
²²³Ra	11.4 d	5.78 (α) average	-	< 10 μm	154

for Research on Cancer (IARC, GLOBOCAN 2008), the incidence rate of prostate cancer worldwide is 13.6 per 100000 inhabitants per year, with a mortality of 6.1 per 100000 per year[1]. The incidence rate differs quite significantly among the various regions of the world. It is lowest in Central Asia with 4.1 per 100000 and highest in Australia/New Zealand with 104 per 100000[1]. Ninety% of patients dying of prostate cancer have bone metastases[2]. Patients with bone metastases have varying symptoms such as pain, pathological fractures, neurological disorders, spinal cord compression, and bone marrow failure, which are significantly impairing their quality of life[3,4].

An optimal therapy leads to pain reduction, improved quality of life, and prolonged survival. Various single or multi-modality therapeutic options are available to treat bone pain. These include analgesics, hormone therapy, chemotherapy, external beam radiation, biphosphonates, or β-emitting radionuclides.

Combined pain medication and external radiotherapy result in pain relief in up to 70% of patients with localized pain[5]. However, external radiotherapy is only possible to a limited extent in patients with multiple bone metastases and diffuse bone pain.

Different radionuclides that emit β-rays such as ¹⁵³Samarium and ⁸⁹Strontium and achieve palliation are commercially available. ⁸⁹Strontium is a pure β-emitter with a relatively long half-life of 50.5 d. ¹⁵³Samarium has a shorter half-life of 1.9 d and emits β-rays in addition to γ-rays (Table 1). Thus, imaging of the skeletal samarium distribution post therapy is feasible. In more than half of the cases, administration of these radiopharmaceuticals results in a decrease of pain[6-8]. Yet, an effect of this therapy on patient survival is not investigated in randomised phase III studies.

β-emitters with a low linear energy transfer (LET) and a long β-range can lead to a high radiation burden of the bone marrow and thus carry the risk of a significant myelosuppression. This bone marrow suppression may be dose limiting.

In contrast to β-emitters, α-emitters have a short path-length of less than 0.1 mm which increases the local anti-tumour effect without affecting the bone marrow. The α-emitter ²²³Radium dichloride is the first radiopharmaceutical that significantly prolongs life in castrate resistant prostate cancer patients with wide-spread bone metastatic disease. Radium-223 has been developed by the Norwegian company Algeta ASA, in a partnership with Bayer, under the trade name Xofigo®. ²²³Radium dichloride is approved by the US Food and Drug Admin-istration (FDA) and by the European Commission (EC).

This article provides an overview of the pre-clinical and clinical trials with ²²³Radium.

PATIENT EXPOSURE

Lassmann *et al*[9] provided a comprehensive dosimetry calculation of absorbed organ doses after intravenous administration of ²²³Radium chloride for 25 organs or tissues. Bone surface and red bone marrow show the highest dose coefficients followed by liver, colon, and intestines. Six cycles of ²²³Radium at 0.05 MBq/kg[10] (corresponding to 21 MBq for a 70 kg patient), the absorbed a dose to the bone surface was calculated at around 16 Gy with a dose of approximately 1.5 Gy to the bone marrow. Patient-specific dosimetry data have not been published yet.

PHARMACOKINETICS AND PRECLINICAL STUDIES

Radium was discovered in December 1898 by the physicist Marie Curie and her husband Pierre Curie. ²²³Radium decays originates from uranium and has a natural decay balance with uranium. The α-emitter ²²³Radium is water soluble as ²²³Radium chloride. ²²³Radium can be relatively easily gained from ²²⁷Actinium through a cation exchange system. Due to the long half-life of ²²⁷Actinium (21.7 years), it could potentially be used as a long-term generator.

²²³Radium has a half-life of 11.4 d (Table 1) and decays *via* seven daughter nuclides into stable ²⁰⁷Lead-207. The half-life of the daughter nuclides ranges from seconds to minutes. During the decay of ²²³Radium, approximately four α particles and two β particles (electrons) are released. The combined energy of the particles emitted during the decay chain of ²²³Radium and its daughter nuclides is 27.5 MeV, with α-particles emitting 95.3% of the energy and β-particles emitting 3.6%. One point one percent are emitted as gamma rays.

Because of the electric charge and the relatively high mass of 4u, α-particles have a very low penetration depth in organic matter which ranges from 40 to 100 μm which approximately equals the size of micro metastases. α-particles produce high-linear energy-transfer (LET) radiation. The advantage of the α-emitter is thus a highly localized biological effect that is caused by radiation induced DNA double-strand breaks and subsequent cell killing and/or limited effectiveness of cellular repair

mechanisms.

The penetration depth into the surrounding tissue of the β-particles is higher than with ^{223}Radium (Table 1). Due to the limited range of the α-particles the bone surface to red bone marrow dose ratio is also lower for ^{223}Radium which is expressed in a lower myelotoxicity of ^{223}Radium as compared to the "traditional" radiopharmaceuticals.

As a calcium analogue, ^{223}Radium dichloride is absorbed by the bone after intravenous injection without the necessity of a carrier. Initially, approximately 25% of the injected ^{223}Radium dichloride is bound to the bone surface and from there quickly absorbed into the bone volume or returned into blood[9]. Eighty percent of the activity is transferred from the exchangeable bone volume back to the bone surface at a biological half-life of 30 d. The amount of ^{223}Radium dichloride that the bone absorbs depends on the regional bone metabolism. The target of ^{223}Radium dichloride in the bone is calcium hydroxylapatite. The radiopharmaceutical accumulates in regions of osteoblast activity, therefore allowing the simultaneous treatment of multiple bone metastases. In addition to the bones ^{223}Radium dichloride is mainly absorbed from blood into soft tissue, including the liver. Its excretion is predominantly *via* the intestines, *i.e.*, the feces. Renal excretion is minimal. In contrast, ^{153}Samarium and ^{89}Strontium undergo predominantly renal excretion thereby increasing the probability of renal toxicity.

Because of its very limited tissue penetration the environmental risk of ^{223}Radium application is minimal if existent at all. Thus, ^{223}Radium dichloride can be administered safely in an outpatient setting.

In animal experimental studies, ^{223}Radium had the same bone distribution as ^{89}Strontium which suggested that a therapeutically relevant dose of ^{223}Radium could be applied to bone metastases[11]. In addition, ^{223}Radium had a lower myelotoxicity than β-emitters[11]. Rats which received chemotherapy and had biphosphonate resistant bone metastases, showed a longer survival rate when they were treated with ^{223}Radium[12]. This suggested that ^{223}Radium may not only be used for palliation but may in fact prolong life.

PHASE I STUDY

The pharmacokinetics, pharmacodynamics, and biodistribution were investigated in a phase I study in 10 patients with bone metastatic prostate cancer[13]. Three patients received injections of 50 kBq/kg radium, another three received 100 kBq/kg radium, and 4 patients received 250 kBq/kg. After 6 wk, 6 of the 10 patients had another injection of 50 kBq/kg. A rapid clearance of ^{223}Radium from the blood was observed whereby only 0.5% of ^{223}Radium remained in the blood after 24 h. On average, 52% of the ^{223}Radium was cleared *via* the intestines, which was the main route of excretion of ^{223}Radium. The excretion *via* the kidneys was relatively low with a mean

of 4%. No dose limiting toxicity could be verified.

In another phase I study, a total of 25 patients with bone metastatic prostate cancer (*n* = 15) and breast cancer (*n* = 10) received a single dose of 250 kBq/kg ^{223}Radium (46, 93, 163, 213, or 250 kBq/kg)[14]. The goal of this dose escalation study was to investigate the safety profile and the pain response to ^{223}Radium. The pain scale was documented before the first injection and at 1, 4, and 8 wk after the injection. In addition, in 6 patients the distribution of the daughter nuclide ^{219}Radium was imaged with a gamma camera and compared to the pretherapeutic bone scintigraphy.

The patients exhibited mild and reversible myelosuppression. In one patient, a grade 1 thrombocytopenia was observed; 2 patients had a grade 3 neutropenia, and 3 patients showed a grade 3 leukopenia. Four weeks after the injection of ^{223}Radium a pain reduction was observed in most patients (60%). 24 h after the injection, the activity of ^{223}Radium rapidly decreased to below 1% (redundant). Thus, ^{223}Radium was well tolerated at therapeutically relevant doses. The pre- and post-therapeutic gamma camera images showed a good correlation with the ^{223}Radium accumulation in bone metastases.

PHASE II STUDY

In a randomized, double-blind multicentre phase II study the effect of the repeated administration of ^{223}Radium was investigated in patients with symptomatic hormone refractory metastatic prostate cancer. Inclusion criteria were multiple bone metastases or a painful osseous lesion with two consecutive rising PSA values[15]. The endpoints of the study were the efficacy of ^{223}Radium with respect to the decrease of bone-specific alkaline phosphatase (ALK) concentration and the time to the occurrence of a skeletal event. All patients also underwent external beam radiation. Sixty-four patients were recruited of whom 33 received external beam radiation and ^{223}Radium while 31 received external beam radiation and placebo (saline). Patients received up to 4 injections of 50 kBq/kg ^{223}Radium or placebo at intervals of 4 wk. Eight patients in the ^{223}Radium group and 21 patients in the placebo group completed the protocol. The study demonstrated an excellent safety profile for ^{223}Radium. There were no differences in haemotoxicity between the groups and no patient in the ^{223}Radium group terminated the study due to treatment related toxic effects. In the ^{223}Radium group, 3 patients had a grade 2/3 neutropenia, which, however, was reversible.

In addition, there was evidence of biologic effects and efficacy with ^{223}Radium. Patients in the ^{223}Radium arm had a significantly greater reduction in bone-ALP (-65.6%, *P* < 0.0001) than those in the placebo group (-9.3%). The median time to skeletal related events was 124 wk in the ^{223}Radium group *vs* 11 wk in the placebo arm. The median time until PSA progression was 126 wk in the ^{223}Radium group *vs* 8 wk in the placebo group (*P* = 0.048). Four weeks after the last injection, the median
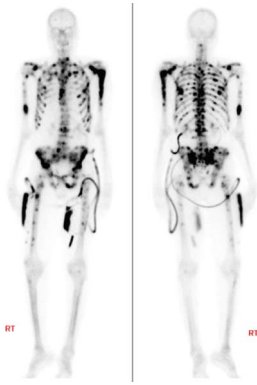
Figure 1 Sixty-one years old male with a history of high-grade Gleason 9 prostate cancer, diagnosed 8 years ago, treated with radiation treatment, prostatectomy, and androgen deprivation therapy. Patient has significant uncontrolled pain throughout the skeleton. Bone scan demonstrates wide spread metastatic disease to the skeleton.

relative change of the PSA was -23.8% in the ^{223}Radium arm, *vs* +44.9% in the placebo group ($P = 0.003$). Importantly, there was a trend toward improved survival in the ^{223}Radium group (65.3 wk) *vs* the placebo group (46.4 wk; $P = 0.066$). Thus, ^{223}Radium was tolerated, reduced serum ALP levels and tended to improve survival. In an additional study, the same authors published the 24 mo follow-up of the patients and confirmed the results of the previous study[16]. They confirmed the excellent safety profile and demonstrated no increased risk for a secondary malignancy. A trend towards improved survival was again demonstrated ($P = 0.056$).

The effect of different dosages of ^{223}Radium on the pain reduction was investigated in another randomized and double-blinded study, involving 100 patients with castration-resistant, bone metastatic prostate cancer[17]. More than 50% of the patients had 20 or more metastases, or a superscan. The patients received single doses of 5, 25, 50, or 100 kBq/kg ^{223}Radium. Patients were classified as responders or non-responders using a bone pain index. Already after 2 wk, a significant pain reduction was evident ($P = 0.35$). After 8 wk, 40%, 63%, 56%, and 71% of the patients were classified as responders in the 5, 25, 50, and 100 kBq/kg groups, respectively. In the group of responders the pain was reduced by a mean of -30, -31, -27, and -28 mm [according to the visual analogue scale (VAS)]. Furthermore, the favourable safety profile of ^{223}Radium was confirmed.

PHASE Ⅲ STUDY AND FDA APPROVAL

A recently published phase Ⅲ trial reported the results about Xofigo® from the Symptomatic Prostate Cancer Patients (ALSYMPCA) study[10]. This multi-national, randomized, double-blind study started in 2008 and by February 2011 921 patients were enrolled. The goal of the study was to compare the efficacy and safety of ^{223}Radium *vs* placebo in patients with castration-resistant prostate cancer and bone metastases.

Patients were included in the study when they showed two or more bone metastases on skeletal scintigraphy, had no visceral metastases, and had been treated with docetaxel or if they were unable to receive docetaxel (Figure 1).

The patients were randomized in a ratio of 2:1 and received intravenous injections of ^{223}Radium (at a dose of 50 kBq per kilogram of body weight) or saline injections as placebo. Patient received 6 injections in 4-wk intervals. Each patient was provided with the best standard of care including local external-beam radiation therapy or treatment with glucocorticoids, antiandrogens, ketoconazole, or estrogens. Chemotherapy, hemibody external radiotherapy, and other systemic radionuclides were not permitted.

The primary end point was overall survival, defined as the time from randomization to the date of death, regardless of cause. The main secondary end points were the time to an increase in the total ALP level, a total alkaline phosphatase response, the time to the first symptomatic skeletal event, normalization of the total alkaline phosphatase level and the time to an increase in the PSA level.

The study was designed to provide a statistical power of 90% to detect a hazard ratio of 0.76 for the risk of death in the ^{223}Radium group *vs* the placebo group with a two-sided alpha significance level of 0.05. In total, 614 patients were enrolled in the ^{223}Radium group and 307 patients in the placebo group. The patients were enrolled in 136 study centres in 19 countries. The baseline patient characteristics in both groups were largely identical.

A pre-defined interim analysis was conducted after 314 deaths had occurred to assess the effect of ^{223}Radium on the primary end point (overall survival). On the basis of this interim analysis, which showed a survival advantage with ^{223}Radium and an acceptable safety profile, early discontinuation of the trial and crossover from placebo to ^{223}Radium was recommended. The authors report in this study the results of an updated descriptive analysis of the efficacy and safety data, performed when 528 deaths had occurred, before any crossover treatment with ^{223}Radium was administered.

The median overall survival was 14.9 mo in the ^{223}Radium group and 11.3 mo in the placebo group. The mortality risk was 30% lower in the ^{223}Radium group than in the placebo group ($P < 0.001$). In total 528 patients died; 333 of the 614 patients in the ^{223}Radium group (54%) and 195 of the 307 patients in the placebo group (64%). A secondary endpoint also confirmed the superiority of ^{223}Radium over the best standard of care. The time to the first symptomatic skeletal event was 15.6 mo in the ^{223}Radium group *vs* 9.8 mo in the placebo group ($P < 0.001$). The time to increases in the total ALP ($P < 0.001$) and PSA levels ($P < 0.001$) was significantly longer in the ^{223}Radium group. Finally, a significantly larger proportion of patients in the ^{223}Radium group showed a response of the total ALP and PSA levels ($\geqslant 30\%$ reduction, $P < 0.001$). Sixteen and 24 wk after initiation of ^{223}Radium

treatment, patients had significantly less pain compared to baseline ($P < 0.001$ and $P = 0.001$, respectively).

No clear difference in the appearance of grade 3 and 4 adverse events (according to the Common Terminology Criteria for Adverse Events) was reported between the two groups. One patient in each group showed grade 3 febrile neutropenia. In the [223]Radium group one grade 5 haematologic adverse event (thrombocytopenia) occured. Serious adverse events that occurred in > 5% of the patients in the [223]Radium or the placebo group were disease progression, bone pain, anaemia, and spinal cord compression. Overall the probability for the appearance of adverse events of all grades was lower in the [223]Radium group than in the placebo group. The quality of life (according to the Functional Assessment of Cancer Therapy-Prostate) improved significantly in the [223]Radium group.

Because of the interim analysis of the ALSYMPCA study, [223]Radium was approved by the FDA as a treatment for patients with bone metastatic castrate-resistant prostate cancer. The approval was given for patients without visceral metastases.

The suggested regimen follows that of the ALSYMPCA study and includes 50 kBq/kg at an interval of 4 wk with a maximum of 6 doses. A simultaneous administration of [223]Radium and chemotherapy is not permitted outside of clinical trials because of the unclear potential of additive effects on myelosuppression.

With its approval the FDA requested additional trials to determine the efficacy and safety of [223]Radium when given at doses > 50 kBq/kg. The FDA also requested to investigate the long term safety, the effects of [223]Radium on healthy bone marrow and the risk of the treatment for developing secondary malignancies.

CONCLUSION

[223]Radium is the first therapeutic that results in a survival benefit for patients with bone metastatic, castrate resistant prostate cancer. In addition, the treatment results in pain palliation and thus, improved quality of life and a delay of skeletal related events. At the same time the toxicity profile of [223]Radium was favourable. Thus [223]Radium may provide a new standard of care for patients with CRPC and bone metastases.

REFERENCES

1 GLOBOCAN 2008. Cancer Fact Sheet Prostate Cancer, 2008
2 **Coleman R**. Management of bone metastases. *Cancer Treat Rev* 1997; **23** Suppl 1: S69-S75 [PMID: 9377604 DOI: 10.1016/S0305-7372(97)90009-8]
3 **Coleman RE**. Clinical features of metastatic bone disease and risk of skeletal morbidity. *Clin Cancer Res* 2006; **12**: 6243s-6249s [PMID: 17062708 DOI: 10.1158/1078-0432.CCR-06-0931]
4 **Lange PH**, Vessella RL. Mechanisms, hypotheses and questions regarding prostate cancer micrometastases to bone. *Cancer Metastasis Rev* 1998; **17**: 331-336 [PMID: 10453276 DOI: 10.1023/A]
5 **Wu JS**, Wong R, Johnston M, Bezjak A, Whelan T. Meta-analysis of dose-fractionation radiotherapy trials for the palliation of painful bone metastases. *Int J Radiat Oncol Biol Phys* 2003; **55**: 594-605 [PMID: 12573746 DOI: 10.1016/S0360-3016(02)04147-0]
6 **Robinson RG**, Preston DF, Schiefelbein M, Baxter KG. Strontium 89 therapy for the palliation of pain due to osseous metastases. *JAMA* 1995; **274**: 420-424 [PMID: 7542352 DOI: 10.1001/jama.1995.03530050068035]
7 **Sartor O**. Prostate cancer and bone: a unique relationship with multiple opportunities for targeted therapy. *Clin Prostate Cancer* 2004; **3**: 71-72 [PMID: 15479486 DOI: 10.3816/CGC.2004.n.015]
8 **Serafini AN**, Houston SJ, Resche I, Quick DP, Grund FM, Ell PJ, Bertrand A, Ahmann FR, Orihuela E, Reid RH, Lerski RA, Collier BD, McKillop JH, Purnell GL, Pecking AP, Thomas FD, Harrison KA. Palliation of pain associated with metastatic bone cancer using samarium-153 lexidronam: a double-blind placebo-controlled clinical trial. *J Clin Oncol* 1998; **16**: 1574-1581 [PMID: 9552068]
9 **Lassmann M**, Nosske D. Dosimetry of 223Ra-chloride: dose to normal organs and tissues. *Eur J Nucl Med Mol Imaging* 2013; **40**: 207-212 [PMID: 23053328 DOI: 10.1007/s00259-012-2265-y]
10 **Parker C**, Nilsson S, Heinrich D, Helle SI, O'Sullivan JM, Fosså SD, Chodacki A, Wiechno P, Logue J, Seke M, Widmark A, Johannessen DC, Hoskin P, Bottomley D, James ND, Solberg A, Syndikus I, Kliment J, Wedel S, Boehmer S, Dall'Oglio M, Franzén L, Coleman R, Vogelzang NJ, O'Bryan-Tear CG, Staudacher K, Garcia-Vargas J, Shan M, Bruland ØS, Sartor O. Alpha emitter radium-223 and survival in metastatic prostate cancer. *N Engl J Med* 2013; **369**: 213-223 [PMID: 23863050 DOI: 10.1056/NEJMoa1213755]
11 **Henriksen G**, Fisher DR, Roeske JC, Bruland ØS, Larsen RH. Targeting of osseous sites with alpha-emitting 223Ra: comparison with the beta-emitter 89Sr in mice. *J Nucl Med* 2003; **44**: 252-259 [PMID: 12571218]
12 **Henriksen G**, Breistøl K, Bruland ØS, Fodstad Ø, Larsen RH. Significant antitumor effect from bone-seeking, alpha-particle-emitting (223)Ra demonstrated in an experimental skeletal metastases model. *Cancer Res* 2002; **62**: 3120-3125 [PMID: 12036923]
13 **Carrasquillo JA**, O'Donoghue JA, Pandit-Taskar N, Humm JL, Rathkopf DE, Slovin SF, Williamson MJ, Lacuna K, Aksnes AK, Larson SM, Scher HI, Morris MJ. Phase I pharmacokinetic and biodistribution study with escalating doses of 223Ra-dichloride in men with castration-resistant metastatic prostate cancer. *Eur J Nucl Med Mol Imaging* 2013; **40**: 1384-1393 [PMID: 23653243 DOI: 10.1007/s00259-013-2427-6]
14 **Nilsson S**, Larsen RH, Fosså SD, Balteskard L, Borch KW, Westlin JE, Salberg G, Bruland OS. First clinical experience with alpha-emitting radium-223 in the treatment of skeletal metastases. *Clin Cancer Res* 2005; **11**: 4451-4459 [PMID: 15958630]
15 **Nilsson S**, Franzén L, Parker C, Tyrrell C, Blom R, Tennvall J, Lennernäs B, Petersson U, Johannessen DC, Sokal M, Pigott K, Yachnin J, Garkavij M, Strang P, Harmenberg J, Bolstad B, Bruland OS. Bone-targeted radium-223 in symptomatic, hormone-refractory prostate cancer: a randomised, multicentre, placebo-controlled phase II study. *Lancet Oncol* 2007; **8**: 587-594 [PMID: 17544845]
16 **Nilsson S**, Franzén L, Parker C, Tyrrell C, Blom R, Tennvall J, Lennernäs B, Petersson U, Johannessen DC, Sokal M, Pigott K, O'Bryan-Tear CG, Thuresson M, Bolstad B, Bruland ØS. Two-year survival follow-up of the randomized, double-blind, placebo-controlled phase II study of radium-223 chloride in patients with castration-resistant prostate cancer and bone metastases. *Clin Genitourin Cancer* 2013; **11**: 20-26 [PMID: 23021204 DOI: 10.1016/j.clgc.2012.07.002]
17 **Nilsson S**, Strang P, Aksnes AK, Franzèn L, Olivier P, Peck-

ing A, Staffurth J, Vasanthan S, Andersson C, Bruland ØS. A randomized, dose-response, multicenter phase II study of radium-223 chloride for the palliation of painful bone metastases in patients with castration-resistant prostate cancer. *Eur J Cancer* 2012; **48**: 678-686 [PMID: 22341993 DOI: 10.1016/j.ejca.2011.12.023]

MINIREVIEWS

Nuclear imaging in detection and monitoring of cardiotoxicity

Carmen D'Amore, Paola Gargiulo, Stefania Paolillo, Angela Maria Pellegrino, Tiziana Formisano, Antonio Mariniello, Giuseppe Della Ratta, Elisabetta Iardino, Marianna D'Amato, Lucia La Mura, Irma Fabiani, Flavia Fusco, Pasquale Perrone Filardi

Carmen D'Amore, Stefania Paolillo, Angela Maria Pellegrino, Tiziana Formisano, Antonio Mariniello, Giuseppe Della Ratta, Elisabetta Iardino, Marianna D'Amato, Lucia La Mura, Irma Fabiani, Flavia Fusco, Pasquale Perrone Filardi, Department of Advanced Biomedical Sciences, Federico II University, 80131 Naples, Italy
Paola Gargiulo, SDN Foundation, Institute of Diagnostic and Nuclear Development, 80129 Naples, Italy
Author contributions: D'Amore C and Gargiulo P contributed to this work, generated the tables and wrote the manuscript; Paollillo S, Pellegrino AM, Formisano T and Mariniello A contributed to the writing of the manuscript; Della Ratta G, Iardino E, D'Amato M, La Mura L, Fabiani I and Fusco F contributed to med-line; and Perrone Filardi P reviewed the manuscript.
Correspondence to: Pasquale Perrone Filardi, MD, PhD, Department of Advanced Biomedical Sciences, Federico II University, Via Pansini, 5, 80131 Naples, Italy. fpperron@unina.it
Telephone: +39-81-7462224 Fax: +39-81-7462224
Received: February 21, 2014 Revised: April 21, 2014
Accepted: May 29, 2014
Published online: July 28, 2014

Abstract

Cardiotoxicity as a result of cancer treatment is a novel and serious public health issue that has a significant impact on a cancer patient's management and outcome. The coexistence of cancer and cardiac disease in the same patient is more common because of aging population and improvements in the efficacy of antitumor agents. Left ventricular dysfunction is the most typical manifestation and can lead to heart failure. Left ventricular ejection fraction measurement by echocardiography and multigated radionuclide angiography is the most common diagnostic approach to detect cardiac damage, but it identifies a late manifestation of myocardial injury. Early non-invasive imaging techniques are needed for the diagnosis and monitoring of cardiotoxic effects. Although echocardiography and cardiac magnetic resonance are the most commonly used imaging techniques for cardiotoxicity assessment, greater attention is focused on new nuclear cardiologic techniques, which can identify high-risk patients in the early stage and visualize the pathophysiologic process at the tissue level before clinical manifestation. The aim of this review is to summarize the role of nuclear imaging techniques in the non-invasive detection of myocardial damage related to antineoplastic therapy at the reversible stage, focusing on the current role and future perspectives of nuclear imaging techniques and molecular radiotracers in detection and monitoring of cardiotoxicity.

Core tip: Cardiomyopathy is a potential complication of various anticancer drugs, such as anthracyclines and biological therapy. Left ventricular dysfunction is the most common manifestation of cardiotoxicity and is monitored with left ventricular ejection fraction measurement, but it is a late manifestation of myocardial injury. Thus, the cardiologist and oncologist should collaborate to identify new non-invasive techniques to detect cardiac dysfunction at an early and potentially reversible stage, before the onset of clinical manifestation. To achieve this aim, nuclear imaging techniques may offer good future perspectives for early detection of myocardial damage using novel molecular tracers.

D'Amore C, Gargiulo P, Paolillo S, Pellegrino AM, Formisano T, Mariniello A, Della Ratta G, Iardino E, D'Amato M, La

INTRODUCTION

Over the last few decades, early diagnosis and development of new antitumor agents have significantly improved the survival of cancer patients. However, conventional and new oncologic drugs frequently have a wide range of cardiac adverse effects, in particular myocardial toxicity. Anthracyclines (doxorubicin, epirubicin), cyclophosphamide, monoclonal antibodies (trastuzumab) and other tyrosine kinase inhibitors (TKIs) are antineoplastic drugs more frequently associated with cardiotoxicity[1]. These drugs may cause irreversible damage, such as that induced by anthracyclines, through free radical production, adrenergic function alteration and cardiac myocyte death due to calcium overload[2,3], or potential completely reversible dysfunction, like that related to TKI administration[4].

Left ventricular (LV) dysfunction is the most typical manifestation of cardiotoxicity and it contributes to increased mortality during chemotherapy[5]. Cardiotoxicity has been defined by the Cardiac Review and Evaluation Committee supervising trastuzumab clinical trials[6] as: (1) a decrease in cardiac LV ejection fraction (EF), either globally or more severe in the septum; (2) the onset of symptoms associated with congestive heart failure (HF); (3) the presence of signs associated with congestive HF; and (4) a reduction in LVEF from baseline of at least 5% to below 55% with signs and symptoms of congestive HF, or a decline in LVEF of at least 10% to below 55% without signs and symptoms of congestive HF. The serial assessment of LVEF is the most common modality for detection of cardiotoxicity and a reduction more than 10% from baseline or a decrease in LVEF below 50% are considered interruption criteria for anticancer drugs administration[7-9]. Notwithstanding, guidelines do not specify the timing and the duration of follow-up and what technique is preferable to assess LV function during and after cancer treatment[10].

Echocardiography (ECHO) plays an important role in evaluation and monitoring of cancer patients treated with cardiotoxic antineoplastic drugs due to its availability and repeatability. Conversely, inter- and intra-observer variability during serial measurement of LVEF and underestimation of myocardial contractile dysfunction should be considered. To overcome these limitations, novel echocardiographic techniques, such as tissue velocity imaging and strain imaging, could be used to detect the presence of myocardial contractile dysfunction before impairment of LVEF[11].

In addition, cardiac magnetic resonance imaging (CMR) is a well recognized imaging technique to screen chemotherapy-related cardiomyopathy[12]. It provides reproducible and noninvasively assessment of LV volume, mass and function[13,14]. Moreover, several studies[13,15,16] emphasized its role in early detection of myocardial damage, however high cost and low availability limit clinical routine use.

Although ECHO and CMR are the two most commonly used imaging techniques for non-invasive chemioterapic myocardial toxicity assessment, nuclear imaging may still have a role in the evaluation and monitoring of cancer patients treated with cardiotoxic drugs. Besides providing sensitive and accurate estimation of LVEF, nuclear imaging techniques using specific radiotracer molecules represent an emerging tool for non-invasive detection of biological processes preceding anatomical involvement and physiological consequences of myocardial damage induced by antineoplastic drugs (Tables 1 and 2).

In this review we will summarize the role of nuclear cardiology in the non-invasive detection of myocardial damage related to antineoplastic therapy, focusing on the current role and future perspectives of nuclear imaging and molecular radiotracers in the assessment of cardiac toxicity.

99MTC-MUGA

Multigated radionuclide angiography (MUGA) is a non-invasive technique using ^{99m}Tc-erythrocytes to visualize the cardiac blood pool through a γ camera with gated acquisition[17]. The series of heart planar images at each stage of the cardiac cycle permit accurate and highly reproducible quantification of LV volumes and LVEF during cancer therapy[18]. However, its use may be hampered by soft tissue attenuation artifacts and may expose patients to ionizing radiation[14,19]. In 28 patients treated with increasing cumulative doses of doxorubicin for non-Hodgkin lymphoma, Nousianen *et al*[20] documented that a MUGA scan had 90% sensitivity and 72% specificity for predicting development of chronic HF. However, the results of this little prospective study were not confirmed by a large retrospective study[21] conducted on 630 patients randomized to increasing dose of doxorubicin or placebo. In fact, Swain *et al*[21] observed that 66% of patients experiencing doxorubicin-related chronic HF showed no clinically relevant decline in LVEF value assessed by MUGA scan from baseline levels (ranging from 0 to 30% of the absolute value), suggesting that it is not accurate in HF prediction.

99mTC GBPS

^{99m}TC gated blood-pool SPECT (single photon emission computed tomography) is a nuclear technique enabling acquisition of 3-dimensional scanned images. ^{99m}TC gated blood-pool SPECT provides information on LVEF, right ventricular EF and wall motion useful for monitoring and personalizing therapy in HF patients[21]. A good cor-

Technique	Tracer	Action
SPECT		
	^{99m}Tc-erythrocyte	Contractile function
	^{111}In-antimyosin	Imaging necrosis/cell death
	^{123}I-MIBG	Neuronal imaging(presynaptic uptake and storage)
	^{111}In-Tz	Therapeutic target imaging
	^{99m}Tc-annessin V	Imaging necrosis/cell death
	^{123}I-BMIPP	Fatty acid use
PET		
	^{18}F-FDG	Glucose metabolism
	Presynaptic tracers	Visualize inhibition of neurotransmission
	true catecholamines	
	^{18}F-6-fluorodopamine	
	^{11}C-epinephrine	
	catecholamine analogs	False neurotransmitters
	^{11}C-HED	
	^{11}C-phenylephrine	
	^{18}F-6-fluoro-metaraminol	
	Postsynaptic tracers	Visualize transmission of sympathetic signal to target tissue
	^{11}C-CGP12177	
	^{11}C-CGP12388	
	^{11}C-GB67	

SPECT: Single photon emission computed tomography; PET: Positron emission tomography; HED: Hydroxyephedrine; FDG: Fluorodeoxyglucose; ^{123}I-BMIPP: [123]I-15-(p-iodophenyl)-3-(R,S)-methylpentadecanoic acid.

relation between gated blood-pool SPECT and MUGA in LVEF estimation was documented[22]. However, gated blood-pool SPECT tends to underestimate LVEF values (33% ± 13%)[23] compared with MUGA (41% ± 14%, P = 0.001), first-pass radionuclide ventriculography (45% ± 13%, P < 0.0001) and echocardiography (37% ± 15%, P = 0.004).

[111]IN-ANTIMYOSIN SPECT

The immunoscintigraphic agent ^{111}In-antimyosin is a specific marker for myocardial cell injury and necrosis, binding to intracellular myosin when sarcolemma disruption occurs and the cell is irreversibly damaged. It has been studied in myocardial infarction, myocarditis, cardiac transplant rejection and anthracycline cardiotoxicity[24].

[111]In-antimyosin SPECT can play a role in subclinical assessment of LV dysfunction as documented in several studies[24,25]. Estorch *et al*[25] showed an increased uptake of ^{111}In-antimyosin after anthracycline chemotherapy (doxorubicin or mitoxantrone) in breast cancer patients without cardiovascular risk factors or previous chemotherapy or mediastinal radiotherapy, and the degree of myocardial antimyosin uptake was associated with changes in LVEF. Moreover, the presence in some patients of radiotracer uptake not associated with a significant reduction in LVEF after chemotherapy suggested the potential use of this technique to detect cellular damage before the onset of LV functional impairment, allowing the identification of patients at risk of HF. Similar results have also been obtained by Carrió *et al*[24], who documented a significant reduction in LVEF after chemotherapy in patients treated with an anthracycline dose of 420-600 mg/m^2 (P < 0.001)

and no significant change in patients treated with a dose of 240-300 mg/m^2. Moreover, patients with heart-to-lung ratio (HLR) ≥ 1.90 at a cumulative anthracycline dose of 240-300 mg/m^2 developed a reduction in LVEF greater than 10% at a subsequent cumulative doxorubicin dose of 420-600 mg/m^2. These data encouraged the use of antimyosin scintigraphy to identify patients with a high risk of developing systolic LV dysfunction when treated with an increasing dose of chemotherapeutic drugs. In addition, Valdés Olmos *et al*[26] observed that patients with a persistent reduction in LVEF after chemotherapy had a significantly higher HLR value (1.83 ± 0.37) than patients with transient LVEF decrease (1.52 ± 0.21; P < 0.01), revealing that cardiac uptake of ^{111}In-antimyosin could also be useful in discriminating between patients with transient and persistent LV dysfunction and in guiding clinical decisions about discontinuation of anthracycline therapy.

^{123}I-METAIODOBENZYLGUANIDINE SPECT

[123]I-metaiodobenzylguanidine (^{123}I-MIBG) SPECT is a promising technique for detection of early anthracycline injury and for identification of patients at high risk of developing cardiotoxicity.

Chemotherapy-induced cardiomyopathy activates a compensatory response that increases adrenergic sympathetic and renin-angiotensin system activity to preserve organ perfusion[27]. In patients with chronic HF, increased norepinephrine (NE) release, depletion of NE deposits and downregulation of human NE transporter (hNET1)

Table 2 Techniques used for detection of anticancer therapy cardiomiopathy

Methods	Advantages	Limits
Echocardiography	Non-invasive	Inter- and intra-observer variability
	Absence of adverse effects	Low sensitivity of EF assessment for early diagnosis
	Analysis of systolic and diastolic function	
	Tissue velocity imaging and strain imaging useful for early detection of subclinical alteration	
Magnetic resonance imaging	Accurate heart anatomic description	Limited availability
	Absence of radiation exposure	High costs
	Accurate and reproducible EF assessment	Not applicable in patients with metallic device
	Cardiac innervation assessment	Low information about its role in the early detection
Multiple-gated acquisition scintigraphy	High sensitivity and specificity EF assessment	Low sensitivity of EF for early diagnosis
	No inter- and intra-observer variability	Less information about diastolic function
		Radiation exposure
Positron emission tomography	Myocardial metabolic and perfusion evaluation	Limited availability

EF: Ejection fraction.

have been shown[28]. ^{123}I-MIBG is a norepinephrine analogue, showing the same uptake, storage and release mechanisms of NE. Unlike NE, MIBG is not metabolized by catechol-o-methyl transferase and monoamine oxidase[29]; so, labelled with ^{123}I, it can be used to generate scintigraphic images of cardiac efferent sympathetic innervation. After ^{123}I-MIBG administration, early (15 min) and late (4 h) post injection images are acquired to determinate heart to mediastinal ratio (H/M) and washout rate (WR). Consequently, increased NE in the cardiac synaptic space and a reduction in the presynaptic space, induced by HF, reduced MIBG cardiac uptake and accelerated the washout rate.

Studies[30,31] conducted in asymptomatic patients treated with anthracyclines revealed that ^{123}I-MIBG was useful for assessment of myocardial adrenergic derangement and identification of patients at risk of developing cardiotoxicity. In addition, in 36 patients undergoing MIBG scintigraphy who had a diagnosis of sarcoma and no history of cardiac disease or previous cancer treatment, Carrió *et al*[30] found an insignificant decrease in LVEF and MIBG uptake at an intermediate cumulative dose of doxorubicin (240-300 mg/mg^2). However, when a high cumulative dose of doxorubicin 420-600 mg/m^2 was used, the experimenters documented a significant impairment of ^{123}I-MIBG uptake ($P < 0.001$) and a reduction in LVEF ($P < 0.05$), and proposed that the degree of H/M reduction was also correlated with the dose of anthracycline administered.

^{111}IN-TRASTUZUMAB SPECT

In cancer patients, anthracyclines can increase the levels of human epidermal growth factor receptor 2 (HER2) expressed by myocytes. In patients pre-treated with anthracyclines, trastuzumab, a chemotherapic agent with a direct effect on HER2, often causes cardiotoxicity, likely as a result of the inhibition of cardiac HER2 that activates the apoptotic pathways and amplifies anthracycline oxidative stress. Thus, ^{111}In-trastuzumab (^{111}In-Tz) SPECT

can be used to evaluate the myocyte HER2 expression and the risk of development LV dysfunction in patients treated with this drug[32].

In a small study, Behr *et al*[33] investigated ^{111}In-Tz scintigraphy in 20 patients with metastatic breast cancer expressing the HER2/neu receptor, pre-treated with anthracyclines and scheduled for administration of Tz as second-line therapy. They documented myocardial ^{111}In-Tz uptake prior to Tz in 7 patients; of these, 6 developed clinical HF (II-IV NYHA class), whereas none of 13 patients without uptake had adverse cardiac events, suggesting that pre-treatment scanning with ^{111}In-Tz could predict cardiotoxicity. In contrast to these results, Perik *et al*[34] documented increased ^{111}In-Tz uptake at the start of trastuzumab therapy only in 1 of 17 studied patients, who had received extensive anthracycline pre-treatment, and normal ^{111}In-Tz uptake at baseline scintigraphy in 3 patients who developed Tz-induced cardiomyopathy.

^{99M}TC-ANNEXIN V SPECT

Apoptosis of myocardial cells plays a critical role in the onset of cardiomyopathy and has been observed in several conditions, such as hypoxia, ischemia, cardiac overload, acute myocardial infarction, anthracycline-induced cardiomyopathy and end-stage HF. In apoptotic cells, the early stage is characterized by activation of proteases and sphingomyelinases and consequent exposure of phosphatidyldserine molecules on the outer surface of the cell membrane. ^{99m}Tc-annexin V has a high affinity for the exposed phosphatidylserine molecule and thus allows imaging of apoptotic cell death[35].

In animals, annexin V scintigraphy has been used to assess acute and chronic doxorubicin-induced cardiomyopathy based on early apoptosis. Increased ^{99m}Tc-annexin V uptake was observed in the myocardium of doxorubicin-treated animals and cardiac oxidative stress was confirmed by histological analysis[36,37].

Further studies are needed of the clinical use of this radiotracer, in particular early identification of myocardial

damage related to antineoplastic drugs.

^{123}I-15-(P-IODOPHENYL)-3-(R,S)-METHYLPENTADECANOIC ACID SPECT

Taxanes are used in the treatment of breast, lung and ovarian cancer, and they can cause ischemia, arrhythmias and HF. Taxanes can impair the microtubular transport system in cardiomyocytes, resulting in failure to store free fatty acids in the cytosol lipid pool and impairment of mitochondrial free fatty acid uptake for beta-oxidation. ^{123}I-15-(p-iodophenyl)-3-(R,S)-methylpentadecanoic acid (^{123}I-BMIPP) scintigraphy has been used to assess this biochemical perturbation in free fatty acid oxidation[38]. Saito *et al*[38] showed significantly lower BMIPP uptake scores after chemotherapy than those before treatment (23.4 ± 3.4 *vs* 26.6 ± 0.8, *P* < 0.001). Moreover, 6 of 25 studied patients, who developed LV dysfunction, also had a significant decrease in total BMIPP uptake scores, suggesting the use of ^{123}I-BMIPP SPECT for detecting of taxane-induced cardiotoxicity. The value of ^{123}I-BMIPP in prediction of cardiotoxicity was also documented in 36 patients with various malignancies treated with doxorubicin[39]. In this study, Saito *et al*[39] showed a significant dose-related reduction in ^{123}I-BMIPP uptake (0.095 ± 0.25 *vs* 0.071 ± 0.019; *P* < 0.001) after doxorubicin chemotherapy and a higher rate of LV dysfunction development in patients with decreased uptake, but with normal LVEF at echocardiography.

POSITRON EMISSION TOMOGRAPHY

Positron emission tomography (PET) is the gold standard technique to assess myocardial metabolism and perfusion due to its high spatial and temporal resolution and high diagnostic sensibility and accuracy. Cardiac PET radiotracers are divided into two categories, those evaluating myocardial perfusion and those evaluating myocardial metabolism.

In the cardio-oncologic field, PET is useful for the diagnosis of metastatic lesion and assessment of the response to chemotherapy. However, fluorine-18-fluorodeoxyglucose (^{18}F-FDG)-PET imaging is used to monitor the response to treatment of primary cardiac lymphoma[40,41] and to evaluate metastatic pericardial involvement[42]. The role of PET in the early detection of cardiotoxicity is still debated. Nony *et al*[43] showed a significant decrease in LVEF (*P* = 0.046) assessed by radionuclide angiography after treatment with doxorubicin, but no significant effect was observed in myocardial blood flow evaluated with PET in 6 female cancer patients without heart disease. Recently, Borde *et al*[44] analyzed changes in myocardial glucose metabolism using FDG-PET and suggested increased glucose utilization was evidence of cellular alteration preceding the cardiotoxicity cascade in patients treated with adriamycin.

Like SPECT, PET imaging can play a key role in the evaluation of cardiac autonomic dysfunction associated with HF[45]. PET provides several advantages over SPECT, with higher spatial and temporal resolution and routinely available attenuation correction. In addition, PET radiotracers more closely resemble the endogenous neurotransmitters than ^{123}MIBG used for SPECT imaging, and the variety of available tracers may allow for more detailed analysis of neuronal signalling[46]. There are two types of presynaptic positron-emitting tracers to assess the presynaptic sympathetic integrity in the heart, radiolabeled catecholamines and radiolabeled catecholamine analogs. The first type behaves identically to endogenous neurotransmitters, thus it is metabolically active and can complicate kinetic data analysis. Catecholamine analogs work as false neurotransmitters and are incapable of following the entire metabolic pathway of true catecholamines. Instead, postsynaptic tracers transmit the sympathetic signal to target tissue. Compared with the availability of presynaptic tracers, only a small number of tracers for postsynaptic neuronal imaging are clinically used. Experimental studies showed a significant reduction in the amount of LV β-adrenoceptors[47] and ^{11}C-hydroxyephedrine in HF catecholamine uptake[48,49] associated with LV dysfunction. Thus, studies are needed to validate this new radiotracer in the cardio-oncology field.

However, the complexity of most of the radiolabeling ligands, the requirement of laborious and specific knowledge, the high cost and the low availability limit clinical use of PET.

CONCLUSION

Cardiotoxicity is one of the principal adverse effects of anticancer therapy of clinical and prognostic importance. LVEF reduction is the most valid criterion to assess the presence of myocardial damage during or after chemotherapy. However, changes in LVEF occur when a critical amount of myocardial damage has taken place and compensatory mechanisms are exhausted[50]. Thus, cardiologists and oncologists should work together to identify new non-invasive, sensitive and non-expensive diagnostic tools that can accurately recognize cardiotoxicity at the subclinical stage to reduce cardiac morbidity and mortality in cancer patients. Further interesting future perspectives in early detection of myocardial damage are offered by nuclear imaging using new molecular tracers which may be able to identify patients at high risk of developing LV dysfunction during and after cancer treatment. Several studies are needed to validate the clinical application of new molecular markers for the identification of early cellular damage.

REFERENCES

1   **Yeh ET**, Tong AT, Lenihan DJ, Yusuf SW, Swafford J, Champion C, Durand JB, Gibbs H, Zafarmand AA, Ewer MS. Cardiovascular complications of cancer therapy: diagnosis, pathogenesis, and management. *Circulation* 2004; **109**: 3122-3131 [PMID: 15226229 DOI: 10.1161/01.

CIR.0000133187.74800.B9]

2   **Smith LA**, Cornelius VR, Plummer CJ, Levitt G, Verrill M, Canney P, Jones A. Cardiotoxicity of anthracycline agents for the treatment of cancer: systematic review and meta-analysis of randomised controlled trials. *BMC Cancer* 2010; **10**: 337 [PMID: 20587042 DOI: 10.1186/1471-2407-10-337]

3   **Olivetti G**, Melissari M, Capasso JM, Anversa P. Cardiomyopathy of the aging human heart. Myocyte loss and reactive cellular hypertrophy. *Circ Res* 1991; **68**: 1560-1568 [PMID: 2036710 DOI: 10.1161/01.RES.68.6.1560]

4   **Ewer MS**, Lippman SM. Type II chemotherapy-related cardiac dysfunction: time to recognize a new entity. *J Clin Oncol* 2005; **23**: 2900-2902 [PMID: 15860848 DOI: 10.1200/JCO.2005.05.827]

5   **Kendal WS**. Dying with cancer: the influence of age, comorbidity, and cancer site. *Cancer* 2008; **112**: 1354-1362 [PMID: 18286532 DOI: 10.1002/cncr.23315]

6   **Seidman A**, Hudis C, Pierri MK, Shak S, Paton V, Ashby M, Murphy M, Stewart SJ, Keefe D. Cardiac dysfunction in the trastuzumab clinical trials experience. *J Clin Oncol* 2002; **20**: 1215-1221 [PMID: 11870163 DOI: 10.1200/JCO.20.5.1215]

7   **Schwartz RG**, McKenzie WB, Alexander J, Sager P, D'Souza A, Manatunga A, Schwartz PE, Berger HJ, Setaro J, Surkin L. Congestive heart failure and left ventricular dysfunction complicating doxorubicin therapy. Seven-year experience using serial radionuclide angiocardiography. *Am J Med* 1987; **82**: 1109-1118 [PMID: 3605130 DOI: 10.1016/0002-9343(87)90212-9]

8   **van Royen N**, Jaffe CC, Krumholz HM, Johnson KM, Lynch PJ, Natale D, Atkinson P, Deman P, Wackers FJ. Comparison and reproducibility of visual echocardiographic and quantitative radionuclide left ventricular ejection fractions. *Am J Cardiol* 1996; **77**: 843-850 [PMID: 8623737 DOI: 10.1016/S0002-9149(97)89179-5]

9   **Mitani I**, Jain D, Joska TM, Burtness B, Zaret BL. Doxorubicin cardiotoxicity: prevention of congestive heart failure with serial cardiac function monitoring with equilibrium radionuclide angiocardiography in the current era. *J Nucl Cardiol* 2003; **10**: 132-139 [PMID: 12673177 DOI: 10.1067/mnc.2003.7]

10   **Eschenhagen T**, Force T, Ewer MS, de Keulenaer GW, Suter TM, Anker SD, Avkiran M, de Azambuja E, Balligand JL, Brutsaert DL, Condorelli G, Hansen A, Heymans S, Hill JA, Hirsch E, Hilfiker-Kleiner D, Janssens S, de Jong S, Neubauer G, Pieske B, Ponikowski P, Pirmohamed M, Rauchhaus M, Sawyer D, Sugden PH, Wojta J, Zannad F, Shah AM. Cardiovascular side effects of cancer therapies: a position statement from the Heart Failure Association of the European Society of Cardiology. *Eur J Heart Fail* 2011; **13**: 1-10 [PMID: 21169385 DOI: 10.1093/eurjhf/hfq213]

11   **Yu CM**, Sanderson JE, Marwick TH, Oh JK. Tissue Doppler imaging a new prognosticator for cardiovascular diseases. *J Am Coll Cardiol* 2007; **49**: 1903-1914 [PMID: 17498573 DOI: 10.1016/j.jacc.2007.01.078]

12   **Hendel RC**, Patel MR, Kramer CM, Poon M, Hendel RC, Carr JC, Gerstad NA, Gillam LD, Hodgson JM, Kim RJ, Kramer CM, Lesser JR, Martin ET, Messer JV, Redberg RF, Rubin GD, Rumsfeld JS, Taylor AJ, Weigold WG, Woodard PK, Brindis RG, Hendel RC, Douglas PS, Peterson ED, Wolk MJ, Allen JM, Patel MR. ACCF/ACR/SCCT/SCMR/ ASNC/NASCI/SCAI/SIR 2006 appropriateness criteria for cardiac computed tomography and cardiac magnetic resonance imaging: a report of the American College of Cardiology Foundation Quality Strategic Directions Committee Appropriateness Criteria Working Group, American College of Radiology, Society of Cardiovascular Computed Tomography, Society for Cardiovascular Magnetic Resonance, American Society of Nuclear Cardiology, North American Society for Cardiac Imaging, Society for Cardiovascular Angiography and Interventions, and Society of Interventional Radiology. *J Am Coll Cardiol* 2006; **48**: 1475-1497 [PMID:

13   **Fallah-Rad N**, Lytwyn M, Fang T, Kirkpatrick I, Jassal DS. Delayed contrast enhancement cardiac magnetic resonance imaging in trastuzumab induced cardiomyopathy. *J Cardiovasc Magn Reson* 2008; **10**: 5 [PMID: 18272009 DOI: 10.1186/1532-429X-10-5]

14   **Walker J**, Bhullar N, Fallah-Rad N, Lytwyn M, Golian M, Fang T, Summers AR, Singal PK, Barac I, Kirkpatrick ID, Jassal DS. Role of three-dimensional echocardiography in breast cancer: comparison with two-dimensional echocardiography, multiple-gated acquisition scans, and cardiac magnetic resonance imaging. *J Clin Oncol* 2010; **28**: 3429-3436 [PMID: 20530277 DOI: 10.1200/JCO.2009.26.7294]

15   **Fallah-Rad N**, Walker JR, Wassef A, Lytwyn M, Bohonis S, Fang T, Tian G, Kirkpatrick ID, Singal PK, Krahn M, Grenier D, Jassal DS. The utility of cardiac biomarkers, tissue velocity and strain imaging, and cardiac magnetic resonance imaging in predicting early left ventricular dysfunction in patients with human epidermal growth factor receptor II-positive breast cancer treated with adjuvant trastuzumab therapy. *J Am Coll Cardiol* 2011; **57**: 2263-2270 [PMID: 21616287 DOI: 10.1016/j.jacc.2010.11.063]

16   **Wassmuth R**, Lentzsch S, Erdbruegger U, Schulz-Menger J, Doerken B, Dietz R, Friedrich MG. Subclinical cardiotoxic effects of anthracyclines as assessed by magnetic resonance imaging-a pilot study. *Am Heart J* 2001; **141**: 1007-1013 [PMID: 11376317 DOI: 10.1067/mhj.2001.115436]

17   **Hesse B**, Lindhardt TB, Acampa W, Anagnostopoulos C, Ballinger J, Bax JJ, Edenbrandt L, Flotats A, Germano G, Stopar TG, Franken P, Kelion A, Kjaer A, Le Guludec D, Ljungberg M, Maenhout AF, Marcassa C, Marving J, McKiddie F, Schaefer WM, Stegger L, Underwood R. EANM/ESC guidelines for radionuclide imaging of cardiac function. *Eur J Nucl Med Mol Imaging* 2008; **35**: 851-885 [PMID: 18224320 DOI: 10.1007/s00259-007-0694-9]

18   **Altena R**, Perik PJ, van Veldhuisen DJ, de Vries EG, Gietema JA. Cardiovascular toxicity caused by cancer treatment: strategies for early detection. *Lancet Oncol* 2009; **10**: 391-399 [PMID: 19341970 DOI: 10.1016/S1470-2045(09)70042-7]

19   **Corapçioglu F**, Sarper N, Berk F, Sahin T, Zengin E, Demir H. Evaluation of anthracycline-induced early left ventricular dysfunction in children with cancer: a comparative study with echocardiography and multigated radionuclide angiography. *Pediatr Hematol Oncol* 2006; **23**: 71-80 [PMID: 16326416 DOI: 10.1080/08880010500313603]

20   **Nousiainen T**, Jantunen E, Vanninen E, Hartikainen J. Early decline in left ventricular ejection fraction predicts doxorubicin cardiotoxicity in lymphoma patients. *Br J Cancer* 2002; **86**: 1697-1700 [PMID: 12087452 DOI: 10.1038/sj.bjc.6600346]

21   **Swain SM**, Whaley FS, Ewer MS. Congestive heart failure in patients treated with doxorubicin: a retrospective analysis of three trials. *Cancer* 2003; **97**: 2869-2879 [PMID: 12767102 DOI: 10.1002/cncr.11407]

22   **Groch MW**, DePuey EG, Belzberg AC, Erwin WD, Kamran M, Barnett CA, Hendel RC, Spies SM, Ali A, Marshall RC. Planar imaging versus gated blood-pool SPECT for the assessment of ventricular performance: a multicenter study. *J Nucl Med* 2001; **42**: 1773-1779 [PMID: 11752072]

23   **Hacker M**, Hoyer X, Kupzyk S, La Fougere C, Kois J, Stempfle HU, Tiling R, Hahn K, Störk S. Clinical validation of the gated blood pool SPECT QBS processing software in congestive heart failure patients: correlation with MUGA, first-pass RNV and 2D-echocardiography. *Int J Cardiovasc Imaging* 2006; **22**: 407-416 [PMID: 16328851 DOI: 10.1007/s10554-005-9031-1]

24   **Carrió I**, Lopez-Pousa A, Estorch M, Duncker D, Berná L, Torres G, de Andrés L. Detection of doxorubicin cardiotoxicity in patients with sarcomas by indium-111-antimyosin monoclonal antibody studies. *J Nucl Med* 1993; **34**: 1503-1507 [PMID: 8355070]

25   **Estorch M**, Carrió I, Martínez-Duncker D, Berná L, Torres G, Alonso C, Ojeda B. Myocyte cell damage after administration of doxorubicin or mitoxantrone in breast cancer patients assessed by indium 111 antimyosin monoclonal antibody studies. *J Clin Oncol* 1993; **11**: 1264-1268 [PMID: 8315423]

26   **Valdés Olmos RA**, ten Bokkel Huinink WW, ten Hoeve RF, van Tinteren H, Bruning PF, van Vlies B, Hoefnagel CA. Usefulness of indium-111 antimyosin scintigraphy in confirming myocardial injury in patients with anthracycline-associated left ventricular dysfunction. *Ann Oncol* 1994; **5**: 617-622 [PMID: 7993837]

27   **Francis GS**, Cohn JN. The autonomic nervous system in congestive heart failure. *Annu Rev Med* 1986; **37**: 235-247 [PMID: 2871803 DOI: 10.1146/annurev.me.37.020186.001315]

28   **Triposkiadis F**, Karayannis G, Giamouzis G, Skoularigis J, Louridas G, Butler J. The sympathetic nervous system in heart failure physiology, pathophysiology, and clinical implications. *J Am Coll Cardiol* 2009; **54**: 1747-1762 [PMID: 19874988 DOI: 10.1016/j.jacc.2009.05.015]

29   **Strashun A**. Adriamycin, congestive cardiomyopathy, and metaiodobenzylguanidine. *J Nucl Med* 1992; **33**: 215-222 [PMID: 1732443]

30   **Carrió I**, Estorch M, Berná L, López-Pousa J, Tabernero J, Torres G. Indium-111-antimyosin and iodine-123-MIBG studies in early assessment of doxorubicin cardiotoxicity. *J Nucl Med* 1995; **36**: 2044-2049 [PMID: 7472595]

31   **Valdés Olmos RA**, ten Bokkel Huinink WW, ten Hoeve RF, van Tinteren H, Bruning PF, van Vlies B, Hoefnagel CA. Assessment of anthracycline-related myocardial adrenergic derangement by [123I]metaiodobenzylguanidine scintigraphy. *Eur J Cancer* 1995; **31A**: 26-31 [PMID: 7695974 DOI: 10.1016/0959-8049(94)00357-B]

32   **de Korte MA**, de Vries EG, Lub-de Hooge MN, Jager PL, Gietema JA, van der Graaf WT, Sluiter WJ, van Veldhuisen DJ, Suter TM, Sleijfer DT, Perik PJ. 111Indium-trastuzumab visualises myocardial human epidermal growth factor receptor 2 expression shortly after anthracycline treatment but not during heart failure: a clue to uncover the mechanisms of trastuzumab-related cardiotoxicity. *Eur J Cancer* 2007; **43**: 2046-2051 [PMID: 17719768]

33   **Behr TM**, Béhé M, Wörmann B. Trastuzumab and breast cancer. *N Engl J Med* 2001; **345**: 995-996 [PMID: 11575295 DOI: 10.1056/NEJM200109273451312]

34   **Perik PJ**, Lub-De Hooge MN, Gietema JA, van der Graaf WT, de Korte MA, Jonkman S, Kosterink JG, van Veldhuisen DJ, Sleijfer DT, Jager PL, de Vries EG. Indium-111-labeled trastuzumab scintigraphy in patients with human epidermal growth factor receptor 2-positive metastatic breast cancer. *J Clin Oncol* 2006; **24**: 2276-2282 [PMID: 16710024 DOI: 10.1200/JCO.2005.03.8448]

35   **Bennink RJ**, van den Hoff MJ, van Hemert FJ, de Bruin KM, Spijkerboer AL, Vanderheyden JL, Steinmetz N, van Eck-Smit BL. Annexin V imaging of acute doxorubicin cardiotoxicity (apoptosis) in rats. *J Nucl Med* 2004; **45**: 842-848 [PMID: 15136635]

36   **Panjrath GS**, Jain D. Monitoring chemotherapy-induced cardiotoxicity: role of cardiac nuclear imaging. *J Nucl Cardiol* 2006; **13**: 415-426 [PMID: 16750786 DOI: 10.1016/j.nuclcard.2006.03.002]

37   **Panjrath GS**, Patel V, Valdiviezo CI, Narula N, Narula J, Jain D. Potentiation of Doxorubicin cardiotoxicity by iron loading in a rodent model. *J Am Coll Cardiol* 2007; **49**: 2457-2464 [PMID: 17599610 DOI: 10.1016/j.jacc.2007.02.060]

38   **Saito K**, Takeda K, Imanaka-Yoshida K, Imai H, Sekine T, Kamikura Y. Assessment of fatty acid metabolism in taxan-induced myocardial damage with iodine-123 BMIPP SPECT: comparative study with myocardial perfusion, left ventricular function, and histopathological findings. *Ann Nucl Med* 2003; **17**: 481-488 [PMID: 14575384 DOI: 10.1007/BF03006439]

39   **Saito K**, Takeda K, Okamoto S, Okamoto R, Makino K, Tameda Y, Nomura Y, Maeda H, Ichihara T, Nakano T. Detection of doxorubicin cardiotoxicity by using iodine-123 BMIPP early dynamic SPECT: quantitative evaluation of early abnormality of fatty acid metabolism with the Rutland method. *J Nucl Cardiol* 2000; **7**: 553-561 [PMID: 11144469 DOI: 10.1067/mnc.2000.108351]

40   **Lee JC**, Platts DG, Huang YT, Slaughter RE. Positron emission tomography combined with computed tomography as an integral component in evaluation of primary cardiac lymphoma. *Clin Cardiol* 2010; **33**: E106-E108 [PMID: 20552627 DOI: 10.1002/clc.20725]

41   **Kaderli AA**, Baran I, Aydin O, Bicer M, Akpinar T, Ozkalemkas F, Yesilbursa D, Gullulu S. Diffuse involvement of the heart and great vessels in primary cardiac lymphoma. *Eur J Echocardiogr* 2010; **11**: 74-76 [PMID: 19759028 DOI: 10.1093/ejechocard/jep111]

42   **Weijs LE**, Arsos G, Baarslag HJ, Wittebol S, de Klerk JM. Pericardial involvement in a non-Hodgkin lymphoma patient: coregistered FDG-PET and CT imaging. *Eur Heart J* 2007; **28**: 2698 [PMID: 17567624]

43   **Nony P**, Guastalla JP, Rebattu P, Landais P, Lievre M, Bontemps L, Itti R, Beaune J, Andre-Fouet X, Janier M. In vivo measurement of myocardial oxidative metabolism and blood flow does not show changes in cancer patients undergoing doxorubicin therapy. *Cancer Chemother Pharmacol* 2000; **45**: 375-380 [PMID: 10803920 DOI: 10.1007/s002800051005]

44   **Borde C**, Kand P, Basu S. Enhanced myocardial fluorodeoxyglucose uptake following Adriamycin-based therapy: Evidence of early chemotherapeutic cardiotoxicity? *World J Radiol* 2012; **4**: 220-223 [PMID: 22761982 DOI: 10.4329/wjr.v4.i5.220]

45   **Lautamäki R**, Tipre D, Bengel FM. Cardiac sympathetic neuronal imaging using PET. *Eur J Nucl Med Mol Imaging* 2007; **34** Suppl 1: S74-S85 [PMID: 17479262 DOI: 10.1007/s00259-007-0442-1]

46   **Langer O**, Halldin C. PET and SPET tracers for mapping the cardiac nervous system. *Eur J Nucl Med Mol Imaging* 2002; **29**: 416-434 [PMID: 12002720 DOI: 10.1007/s002590100640]

47   **Merlet P**, Delforge J, Syrota A, Angevin E, Mazière B, Crouzel C, Valette H, Loisance D, Castaigne A, Randé JL. Positron emission tomography with 11C CGP-12177 to assess beta-adrenergic receptor concentration in idiopathic dilated cardiomyopathy. *Circulation* 1993; **87**: 1169-1178 [PMID: 8096441 DOI: 10.1161/01.CIR.87.4.1169]

48   **Vesalainen RK**, Pietilä M, Tahvanainen KU, Jartti T, Teräs M, Någren K, Lehikoinen P, Huupponen R, Ukkonen H, Saraste M, Knuuti J, Voipio-Pulkki LM. Cardiac positron emission tomography imaging with [11C]hydroxyephedrine, a specific tracer for sympathetic nerve endings, and its functional correlates in congestive heart failure. *Am J Cardiol* 1999; **84**: 568-574 [PMID: 10482157 DOI: 10.1016/S0002-9149(99)00379-3]

49   **Hartmann F**, Ziegler S, Nekolla S, Hadamitzky M, Seyfarth M, Richardt G, Schwaiger M. Regional patterns of myocardial sympathetic denervation in dilated cardiomyopathy: an analysis using carbon-11 hydroxyephedrine and positron emission tomography. *Heart* 1999; **81**: 262-270 [PMID: 10026349]

50   **Popat S**, Smith IE. Therapy Insight: anthracyclines and trastuzumab--the optimal management of cardiotoxic side effects. *Nat Clin Pract Oncol* 2008; **5**: 324-335 [PMID: 18364726 DOI: 10.1038/ncponc1090]

RETROSPECTIVE STUDY

Nuclear imaging to characterize adrenal tumors: Comparison with MRI

Simone Maurea, Pier Paolo Mainenti, Valeria Romeo, Carmine Mollica, Marco Salvatore

Simone Maurea, Pier Paolo Mainenti, Valeria Romeo, Carmine Mollica, Marco Salvatore, Medicina Nucleare e Radiologia, Dipartimento di Scienze Biomediche Avanzate, Università degli Studi di Napoli Federico II (UNINA), 80123 Napoli, Italy

Simone Maurea, Pier Paolo Mainenti, Valeria Romeo, Carmine Mollica, Marco Salvatore, Fondazione SDN (IRCCS), 80123 Napoli, Italy

Simone Maurea, Pier Paolo Mainenti, Valeria Romeo, Carmine Mollica, Marco Salvatore, Istituto di Biostrutture e Bioimmagini (IBB), Consiglio Nazionale delle Ricerche (CNR), 80123 Napoli, Italy

Author contributions: All authors contributed to this work.
Correspondence to: Simone Maurea, MD, PhD, Medicina Nucleare e Radiologia, Dipartimento di Scienze Biomediche Avanzate, Università degli Studi di Napoli Federico II (UNINA), via Ernesto Murolo n. 5, 80123 Napoli, Italy. maurea@unina.it
Telephone: +39-81-7463560-2039 Fax: +39-81-5457081
Received: January 21, 2014   Revised: May 30, 2014
Accepted: June 14, 2014
Published online: July 28, 2014

Abstract

AIM: To describe the role of nuclear imaging modalities using nor-cholesterol, metaiodobenzylguanidine (MIBG) and fluorine-deoxy-glucose (FDG) in adrenal tumors for lesion characterization in comparison with magnetic resonance (MR).

METHODS: Population was classified in group 1 consisting of 30 patients with non-hypersecreting unilateral adrenal masses, in group 2 consisting of 34 patients with hypersecreting ($n = 19$) or non-hypersecreting ($n = 15$) adrenal adenomas and in group 3 consisting of 18 patients with chromaffin-tissue tumors (CTT), of which 14 were pheochromocytomas while 4 were paragangliomas ($n = 4$). All patients underwent MR and nuclear studies (nor-cholesterol, MIBG and FDG). Pathology samples ($n = 63$) or follow-up data in adenomas ($n = 19$) were used as standard of reference for imaging studies interpretation.

RESULTS: In group 1, MR findings were not highly accurate for lesion characterization, while the results of nuclear scans showed abnormal nor-cholesterol, MIBG and FDG concentration in all cases of adenomas, pheos and malignant tumors, respectively. In group 2, no differences in MR parameters were found between hyperfunctioning and non-hyperfunctioning adenomas, while nor-cholesterol uptake was significantly higher in hyperfunctioning compared to non-hyperfunctioning lesions. In group 3, no differences in MR parameters were found between benign and malignant CCT, while MIBG uptake was significantly higher in malignant compared to benign tumors.

CONCLUSION: On the basis of our findings, nuclear imaging modalities using specific target agents are able to better characterize adrenal tumors, compared with MR. In particular, radionuclide techniques are able to identify the nature of adrenal incidentalomas and to differentiate between hypersecreting and non-hypersecreting adenomas as well as between benign and malignant CTT.

Key words: Adrenals; Tumors; Nor-cholesterol; Metaiodobenzylguanidine; Fluorine-deoxy-glucose; Magnetic resonance imaging

Core tip: This manuscript deals with tumor imaging characterization in patients with adrenal tumors; in particular, we discuss our results obtained in three different groups of patients with incidentalomas, adenomas and pheochromocytomas; on the basis of our experience, nuclear imaging modalities using different radiotracers such as labeled nor-cholesterol, metaiodobenzylguanidine and fluorine-deoxy-glucose are able to better characterize, compared with magnetic resonance (MR), adrenal tumors; the functional as well as

metabolic features of radionuclide imaging, compared to anatomical characteristics of MR, may explain the better performance of nuclear imaging in characterizing adrenal tumors.

INTRODUCTION

The high accuracy of imaging madalities as computed tomography (CT) and magnetic resonance (MR) in the evaluation of the abdomen is usually able to detect incidental adrenal abnormalities; in this clinical scenario, the diagnostic goal is the differential diagnosis between benign and malignant lesions for the appropriate therapeutic management[1]. As initial diagnostic evaluation, clinical and laboratory assessment of adrenal function allows to detect hypersecreting adrenal tumors and, thus, to characterize such patients[2]. Conversely, an adrenal mass may not be associated to abnormal hormone hypersecretion or it may produces non-functional agents[1-3]. In these patients, tumor characterization is required; for this purpose, CT and MR well describe anatomic features of adrenal masses and may suggest presumptive imaging criteria for tissue characterization[4-6].

Nuclear adrenal scans with different radiolabeled compounds, which reflect specific metabolic pathway, are helpful to characterize adrenal tumors providing diagnostic information complementary to morphological imaging modalities[7,8]. For this purpose, different radiocompounds that reflects specific biological functions may be considered in nuclear medicine for adrenal radionuclide studies; among these agents, nor-cholesterol, metaiodobenzylguanidine (MIBG) and fluorine-deoxyglucose (FDG) are the more commonly used in the clinical practice[7,9-15]. Furthermore, radiolabeled peptides such as somatostatin analogs have been reported to be able to characterize malignant adrenal lesions, as these express somatostatin receptors[16]. Limited comparative studies between radionuclide and MR imaging are available. A complementary role of MIBG and MR techniques in the diagnostic evaluation of patients with chromaffin-tissue tumors (CTT), such as pheochromocytoma or paraganglioma, has been suggested, although no data regarding the imaging characterization of such tumors are reported[17-19].

In this paper, we show the accuracy of nuclear scans with different radiocompounds in the assessment of adrenal tumors to perform lesion identification in comparison with MR images. The comparative results of nuclear and MR imaging studies in three different groups of patients with adrenal tumors, that is (1) patients with inci-dentalomas; (2) patients with adenomas; and (3) patients with CTT, are reported.

MATERIALS AND METHODS

Patient population
Patients were classified in three groups; in group 1, 30 patients (20 F and 10 M, 51 ± 13 years) with incidental non-hyperfunctioning adrenal tumors, detected on ultrasound and/or CT, were studied; in group 2, 34 patients (20 F and 14 M, 47 ± 15 years) with non-hypersecreting ($n = 15$) or hypersecreting ($n = 19$) adrenal adenomas; group 3 consisted of 18 patients (9 M and 9 M, mean age 37 ± 8 years) with CTT of which 14 were pheochromocytomas and 4 were paragangliomas. Patients with non-hypersecreting adrenal adenomas were separated into groups 1 and 2 for specific comparative diagnostic purposes. All patients underwent MR studies. In group 1, a total of 46 nuclear studies were analyzed using FDG ($n = 11$), MIBG ($n = 15$) and nor-cholesterol ($n = 20$) radiocompounds; in group 2, all patients underwent nor-cholesterol adrenal scintigraphy; in group 3 all patients underwent MIBG imaging. Pathology samples ($n = 63$) or follow-up data in adenomas ($n = 19$) were used as standard of reference for imaging studies interpretation. Informed patient consent was obtained in all cases.

MR imaging
MR was performed with a 3.0 Tesla magnet scan (Trio, Siemens Medical Systems, Hoffman Estates, IL); conventional TSE sequences were used to realize 5 mm contiguous sections of the abdomen in axial, coronal and sagittal views. T1 (TR/TE = 600/15 ms) and T2 (TR/TE = 2000/15-90 ms) images were obtained. T1 images were also acquired after intravenous injection of gadolinium-DTPA (0.2 mL/kg, Magnevist, Schering) using dynamic multi-phase acquisition. The tumor size was measured as maximal diameter (cm). For qualitative evaluation, signal intensity of tumor lesions was analyzed on T2 images as hypo-, iso- or hyper-intensity compared to liver signal intensity. Tumor lesions enhancement of gadolinium (yes or no) as well as signal intensity changes on chemical shift (CS) images were also analyzed. For quantitative analysis, signal intensity ratios (ratios of lesions signal intensity *vs* that of liver, fat, muscle and image background) was measured on T1 and T2-weighted images using region of interest analysis. The regions of interest considered for the analysis were placed on adrenal or lymph node neoplastic lesions as well as on right liver lobe, adrenal bed fat tissue, lumbar para-vertebral muscle tissue, and image background to obtain tumor lesion signal intensity ratios (SIRs).

Nor-cholesterol scintigraphy
Thyroid iodine uptake was blocked before intravenous tracer (37 MBq) injection with a saturated solution of potassium iodide (200 mg per os and per day, starting the day before tracer injection and continuing for 8 d); ad-

renal scanning was performed five and seven days after tracer administration using a large field of view gamma camera with a high-energy collimator (Orbiter, Siemens, Erlangen, Germany) and a 20% window centered at 364 KeV; posterior abdominal acquisitions were performed in preset time for 600 s for each scan. A mild laxative (bisacodyl) was given (10 mg) twice daily beginning 2 d before the first day of imaging to reduce interfering colonic iodine-131 activity. The grading of nor-cholesterol uptake by tumor lesions was visually and semi-quantitatively assessed by two individual and experienced evaluators; in case of disagreement, final interpretation was reached by consensus reading; in particular, nuclear images were assessed using the criteria by Gross *et al*[20]; for the semi-quantitative analysis, a 4-point scoring system was used to quantify nor-cholesterol concentration by adenomas as well as to perform a direct comparison between hypersecreting and non-hypersecreting lesions; the 4-point scoring system was: 0 = background tracer uptake, 1 = just visible tumor activity, 2 = increased tumor activity with faint uptake in the opposite gland and 3 = exclusive tumor activity with no uptake in the opposite gland.

MIBG scintigraphy

Thyroid iodine uptake was blocked before intravenous tracer (37 MBq) injection with a saturated solution of potassium iodide (200 mg per os and per day, starting the day before tracer injection and continuing for 8 d). Anterior and posterior all-body scans as well as abdominal spot views were acquired 24, 48, and 72 h after tracer administration using a dual head rotating gamma camera (ECAM, Siemens Medical Systems, Hoffman Estates, IL) with a high-energy collimator and a 20% window centered at 364 Kev. MIBG uptake was visually and quantitatively assessed in anatomic sites where tumor lesions were detected on MR images. For qualitative analysis, MIBG uptake was graded as mild, moderate, or intense; while for quantitative analysis, MIBG uptake was evaluated on 48 h images using a photographic densitometer (X-Rite Company, MI) for measuring optical density (OD), as previously described[21].

Fluorine-18 FDG PET

PET scan was performed using a EXACT 47 scanner (Siemens, Erlangen, Germany); patients were evaluated fasted since 6 h before tracer administration; patients were placed in the gantry using a computerized program localized on the superior abdomen; before tracer administration, transmission scan for the attenuation correction of emission scans was acquired for 20 min.; patients were intravenously injected with 370 MBq of F-18 FDG; emission scans were performed 30-45 min. after tracer injection; images were reconstructed using filtered back-projection smoothed with a Hann filter with a cutoff frequency of 0.4 cycles/pixels by SUN Workstation System generating PET scans as axial, coronal and sagittal views. The presence of abnormal FDG uptake was visually

evaluated in the superior abdomen where tumor masses were localized by MR, while the grade of FDG uptake by the mass was assessed by two experienced evaluators; in case of disagreement, final interpretation was reached by consensus reading.

RESULTS

Group 1

In this group, pathology examinations (*n* = 19), of which 16 post-surgical histology and 3 fine needle cytology samples, or follow-up controls (*n* = 11) demonstrated 22 benign adrenal tumors, of which 13 adenomas, 3 cysts, 2 myelolipomas, 4 pheochromocytomas (pheos), and 8 malignant adrenal lesions, of which 4 carcinomas, 1 sarcoma and 3 metastases. Qualitative MR analysis demonstrated: high signal intensity on T2 images in adenomas (46%), in pheos (100%) and adrenal malignancies (100%); no contrast enhancement (92%) and clear reduction of signal intensity on CSI (100%) in adenomas; significant contrast enhancement in pheos (100%) and malignant tumors (63%); no changes of signal intensity on CSI in pheos (100%) and malignancies (100%). Quantitative MR evaluation showed: higher signal intensity on T2 and post-contrast images in pheos *vs* adenomas and malignant tumors (*P* < 0.03). Radionuclide qualitative analysis demonstrated abnormal nor-cholesterol uptake only in adenomas (100%) (Figure 1) and, similarly, abnormal MIBG uptake only in pheos (100%) (Figure 2) as well as abnormal FDG uptake only in 100% of malignancies (100%) (Figure 3); no false positive or negative nuclear imaging results occurred.

Group 2

Of 34 patients included in this group, 19 presented hypersecreting and 15 had non-hypersecreting adenomas. In hypersecreting adenomas abnormal plasma amount of cortisol (*n* = 13) or aldosterone (*n* = 6) occurred. Pathology (*n* = 26) or follow-up data (*n* = 8) were obtained. MR detected 16 and 18 regular tumors of left and right adrenals, respectively. There was no significant difference in the quantitative evaluation of SIRs between hypersecreting (Figure 4A) and non-hypersecreting (Figure 1B) adenomas; however, no differences in lesion size (cm) were found between hypersecreting (2.7 ± 0.5) and non-hypersecreting (3.1 ± 0.9) tumors. For radionuclide studies, abnormal nor-cholesterol focal uptake occurred in all patients with adenomas, both hypersecreting and non-hypersecreting, showing exclusive or prevalent uptake. The accuracy of nor-cholesterol scanning was 100%. The semi-quantitative comparison of nor-cholesterol uptake between hypersecreting and non-hypersecreting lesions demonstrated a significant (*P* = 0.01) difference in tracer concentration between hypersecreting (2.8 ± 0.5) (Figure 4B) and non-hypersecreting (2.2 ± 0.6) lesions (Figure 1A).

Group 3

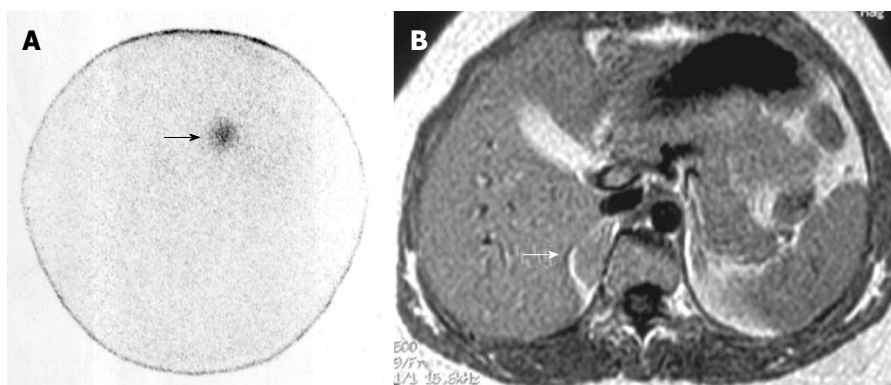Among the 10 patients with benign CTT, 8 had pheo-

Figure 1 Right non-hypersecreting adrenal adenoma. A: Abdominal posterior scan of I-131 nor-cholesterol scintigraphy demonstrates abnormal (faint) focal uptake in the right adrenal (black arrow) where a mass was detected by magnetic resonance (MR); no detectable tracer uptake in the left adrenal bed; B: T1-weighted axial MR detects a small lesion in the right adrenal bed (white arrow) isointense compared to liver signal intensity.

Figure 2 Right benign non-hypersecreting pheochromocytoma. A: Abdominal posterior scan of I-131 metaiodobenzylguanidine scintigraphy demonstrates abnormal (faint) focal uptake in the right adrenal (black arrow) where a small mass was detected by magnetic resonance (MR); no detectable tracer uptake in the left adrenal bed; B: T2-weighted axial MR with fat-suppression detects a small right adrenal lesion hyperintense compared to liver signal intensity (white arrow).
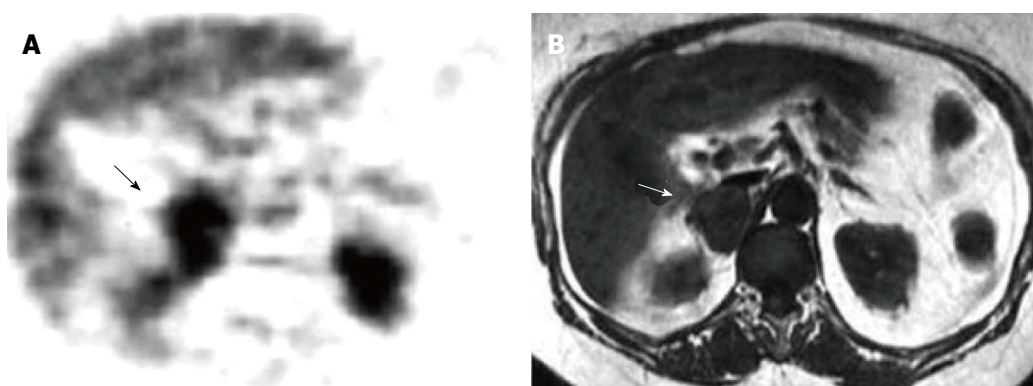
Figure 3 Right adrenal metastasis by melanoma. A: Axial fluorine-18 fludeoxyglucose-positron emission tomography scan detects abnormal focal uptake in the right adrenal region (black arrow) where a large adrenal metastasis was detected by magnetic resonance (MR); diffuse normal liver tracer activity is detectable; physiologic tracer activity is also detectable in kidneys; B: T1-weighted axial MR detects a right adrenal tumor hypointense compared to liver signal intensity (white arrow).

chromocytoma and 2 paraganglioma; while among the 8 patients with malignant CTT, 6 had pheochromocytoma and 2 paraganglioma. In patients with benign CTT, a total of 12 lesions were found since a para-aortic paraganglioma was bilateral and a pheochromocytoma was bilobated. In patients with malignant CTT, a total of 16 lesions were detected and the majority (75%) of these patients showed lymph nodes or bone involvement. At visual analysis, MR imaging and MIBG scintigraphy detected all tumor lesions. At quantitative analysis, MIBG uptake intensity ratio was significantly higher in malignant (Figure 5A) compared to benign (Figure 2A) lesions (5.2 ± 2.4 *vs* 2.9 ± 1.4, $P < 0.01$); on the contrary, at MR imaging no significant difference in tumor signal intensity
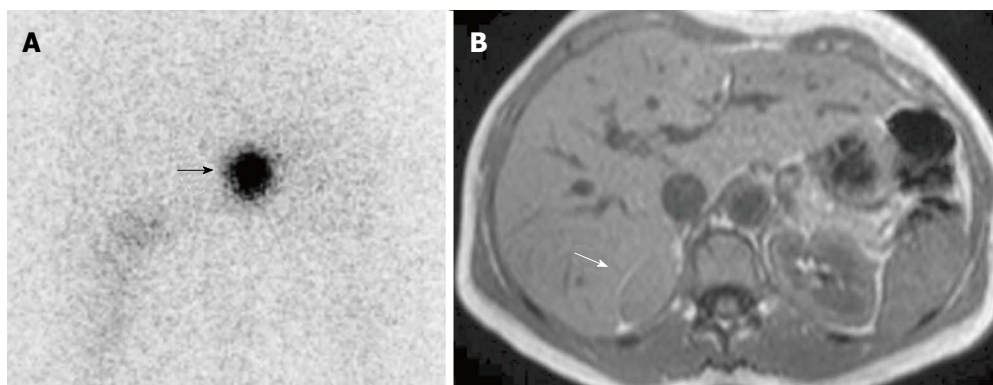
Figure 4 Right hypersecreting adenoma of the adrenal gland. A: Abdominal posterior scan of I-131 nor-cholesterol scintigraphy demonstrates abnormal (intense) focal uptake in the right adrenal (black arrow) where a mass was detected by magnetic resonance (MR); no uptake is detected on the contralateral side; normal bowel uptake is detectable on the left; B: T1-weighted axial MR detects a right adrenal lesion isointense compared to liver signal intensity (white arrow).
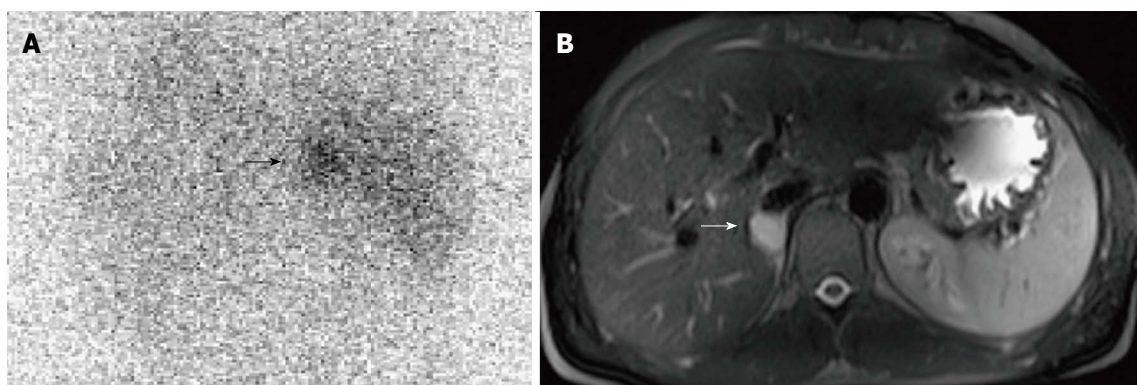

Figure 5 Right malignant hypersecreting pheochromocytoma. A: Abdominal posterior scan of I-131 metaiodobenzylguanidine scintigraphy demonstrates abnormal (intense) focal uptake in the right adrenal (black arrow) where a large mass was detected by magnetic resonance (MR); no detectable tracer uptake in the left adrenal bed; B: T2-weighted axial MR with fat-suppression detects a large right adrenal lesion hyperintense compared to liver signal intensity (white arrow).
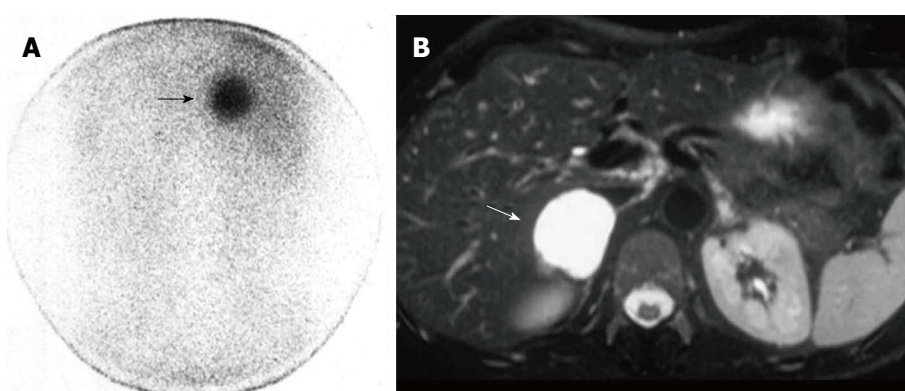
ratios between malignant (Figure 5B) and benign (Figure 2B) lesions was observed; no significant difference in lesion size (cm) was found between benign (3.2 ± 0.5) and malignant (2.8 ± 0.8) tumors.

DISCUSSION

Tumor imaging characterization in patients with adrenal masses is clinically important since diagnostic evaluation currently consists not only of lesion detection, but also of tumor characterization in order to recognize lesion-type, to assess lesion endocrine activity as well as to differentiate between benign and malignant tumors. Advances in imaging techniques allow to reach these purposes. In this paper, we report the results obtained in three different groups of patients with adrenal tumors: (1) patients with incidentalomas; (2) patients with adenomas; and (3) patients with CTT. On the basis of our findings, nuclear imaging modalities using specific target agents are able to better characterize, compared with MR, adrenal tumors. Radionuclide techniques are able to identify the nature of adrenal incidentalomas and to differentiate between hypersecreting and non-hypersecreting adenomas as well as between benign and malignant CTT.

Group 1

Asymptomatic non-hypersecreting adrenal masses have recently increased as a result of the availability of high resolution abdominal imaging modalities as CT and MR[1]. However, CT- and MR- based imaging is useful for tumor detection and the differential diagnosis between benign and malignant lesions, as it provides accurate anatomic details useful for lesion characterization[4-6,22,23]. Despite CT and MR presumptive criteria for tissue characterization, complementary or alternative imaging modalities are still needed. In this setting, radionuclide techniques with different agents are able to *in vivo* characterize adrenal tumors and differentiate between benign and malignant abnormalities[4,7,9,12-14,24-26]; in particular, these agents are not related to each other and are concentrated in adrenal tumors depending by distinct metabolic pathways.

In adrenal adenomas, MR qualitative patterns were represented by signal intensity reduction on CS sequence and transient contrast enhancement with significant wash-out; in particular, CS signal intensity changes was the more appropriate criterion to characterize adenomas[4]. On the other hand, the analysis of signal intensity on T1 and T2 images showed inhomogeneous findings, which did not allow definite adenoma characterization.

For pheos, T2 signal hyper-intensity and significant persistent gadolinium enhancement were both specific, as they were detected in all lesions. In malignant tumors T2 hyperintensity was observed in all lesions, while contrast enhancement was found only in 63% of these cases. These MR features suggest that high signal intensity, visually assessed on T2 scan, is not accurate in differentiating adrenal masses. Furthermore, since CS sequence was not useful to characterize pheos or adrenal malignancies, other technical methods are necessary in this setting. For this purpose, we used MR quantitative analysis to assess the degree of T2 high signal intensity as well as of contrast enhancement; this evaluation demonstrated higher values of these two parameters in pheos compared with adenomas and malignant tumours; however, these latter tumors were not differentiated using these parameters. These findings are concordant with those of other studies[4,6] suggesting that MR imaging offers only some indicative criteria for lesion characterization in patients with non-functioning adrenal tumors. In particular, the reduction of signal intensity on CS sequence seems to be the best marker for adenomas, while the quantitative evaluation of T2 or T1-contrast signal intensity allows to better identify pheos, while no specific MR signs for malignant tumors were selected.

Conversely, nuclear studies demonstrated more specific imaging results in comparison with MR for tumor characterization; in fact, the presence of nor-cholesterol concentration was observed only in adenomas, as well as that of MIBG in pheo and that of FDG in malignant tumors (Figures 1-3). Thus, nuclear imaging using different radiotracers is able to accurately and non-invasively characterize non-functioning adrenal tumors[9,12-14,25,26]; for this purpose, the choice of the radiocompound to perform adrenal scintigraphy is dependent by the clinical scenario. In patients with incidental occurrence of an adrenal mass, nor-cholesterol should be initially used because adenoma is the more frequent lesion; in case of absence of nor-cholesterol by the lesion, MIBG should be used as second choice, while FDG should be selected in case of clinical suspicion of malignant tumors. On the other hand, during the follow-up of oncologic patients with evidence of an adrenal mass, FDG should be initially selected; in case of absence of FDG by the lesion, nor-cholesterol and MIBG should be used as second and third choice, respectively. Currently, radionuclide scans are not frequently considered in the diagnostic management of patients with non-functioning adrenal tumors[27,28]; in particular, the results of nuclear imaging reflect important clinical implications; for example, in case of non-hypersecreting adenoma diagnosed on nor-cholesterol nuclear imaging, surgery is required only for large masses, while lesion size monitoring in follow-up is required in smaller tumors; otherwise, in case of pheo the pre-surgical diagnosis using MIBG scan allows to correctly prepare the patient or in case of malignant tumors the use of FDG PET may allow early diagnosis with subsequent immediate lesion resection with good prognosis.

Therefore, nuclear scans with different radiocompounds represent a powerful diagnostic tool to specifically characterize non-functioning adrenal tumors.

Group 2

The characterization of adrenal adenomas comparing imaging techniques has been investigated in a previous study[29] using quantitative evaluation of nor-cholesterol uptake, CT attenuation value and CS MR signal intensity loss, but no comparative data between hypersecreting and non-hypersecreting lesions were reported. Our results showed that while the analysis of nor-cholesterol activity is able to distinguish between hyperfunctioning and non-hyperfunctioning adenomas, MR signal intensity ratios are not able in this setting. As cholesterol is the precursor molecule of all adrenocortical steroid hormones[30], nor-cholesterol scintigraphy has been clinically used in both hyperfunctioning and non-hyperfunctioning adenomas[31]. The diagnostic accuracy of nor-cholesterol imaging recorded in our study was high (100%) and concordant with previous findings. Interestingly, the analysis of radionuclide images showed a significant difference in nor-cholesterol uptake between hyperfunctioning and non-hyperfuntioning lesions (Figures 1 and 4), which reflects their different biosynthetic activity. Of note, the significantly higher nor-cholesterol concentration observed in hypersecreting adenomas was independent on tumor size. As non-hypersecreting adenomas showed increased nor-cholesterol uptake *vs* normal adrenal glands, but lower nor-cholesterol uptake compared to hypersecreting lesions, nor-cholesterol uptake may be more reliable than peripheral hormone levels to assess the functional index of non-hypersecreting adenomas. In this field, a nuclear diagnostic criterion, using the intensity of nor-cholesterol, of silent pre-clinical adrenal dysfunction has been previously suggested in adenomas when adrenal functional abnormality may be not yet detected by laboratory markers[32]. Semi-quantitative indexes of nor-cholesterol activity in adrenal adenomas have been indicated to be able to evaluate adrenal functional degree, especially when serum hormonal values are not inconclusive. Furthermore, assessment of nor-cholesterol uptake could identify those lesions at risk of causing an overt clinical syndrome as a result of hormonal hyperproduction[33,34], and it may be a powerful instrument to assess the biosynthetic activity of some adenomas, which have been shown to produce relevant amounts of adrenocortical hormones, yet insufficient to cause symptoms.

The comparative results of nor-cholesterol scintigraphy and MR imaging demonstrated a similar diagnostic sensitivity for the identification of cortical adenomas confirming previous studies[7,35]; in particular, MR imaging should be selected since this tecnique is radiation-free as well as it may be performed also without contrast administration using CS sequence. However, when imaging differentiation between hypersecreting and non-hypersecreting adenomas was investigated, no specific MR criteria for this topic were found; in fact, no differences

in MR parameters were observed between these lesions; these findings suggest that MR parameters reflect tumor tissue anatomic features which are not related to endocrine function.

Group 3

Pheochromocytomas are CTT localized in the adrenal medulla with the specific characteristics to secrete catecholamines. The most frequent form is the sporadic with unilateral benign involvement of a single gland, but the possibility of bilateral, extra-adrenal, or multiple localization as well as familiar or malignant forms occur in 10% of cases[36]. The distinction between benign and malignant pheochromocytoma based on histological analysis is challenging, and metastatic disease is the only established criterion for malignancy, according to the World Health Organization classification of solid tumors[36].

Tumor imaging characterization in terms of differentiation between benign and malignant lesions is currently attractive in oncology. Although benign lesions represent the majority of pheochromocytomas, malignancy may occur in 10% of patients as well as benign tumors may also rarely show malignant evolution[36]. Although no reliable CT and/or MR imaging features are available to detect malignant pheocromocytoma, these techniques can show invasive regional tumor growth and/or the presence of distant metastases[4]. Several diagnostic methods, such as biological fluid tests, molecular markers, imaging techniques, and genome studies, have been proposed to differentiate between benign and malignant pheochromocytoma[37,38]. Previous experiences suggested that radiolabeled somatostatin analogs might be used to characterize malignant pheochromocytomas[16,39]. Conversely, MIBG uptake has been demonstrated to reflect the concentration of neurosecretory storage granules in CTT[40]. Lesions that concentrate MIBG can be benign or malignant and the ability of MIBG scan for tumor detection depends on both tumor size and differentiation[7,41]. Our results demonstrated that quantitative analysis of MIBG uptake may differentiate between benign and malignant CTT such as pheochromocytoma and paraganglioma, while MR imaging using signal intensity ratio measurement is not useful for this purpose. In fact, MIBG uptake, measured as tumor lesion OD IR, was significantly higher in malignant lesions compared to benign disease (Figures 2 and 5); this finding could depend by larger size of malignant compared to benign CTT, however no difference in lesion size was found.

MIBG, a physiological analog of nor-epinephrine and guanetidine, shows a specific uptake by chromaffin-tissue cells in adrenal as well as extra-adrenal locations[41-43]; of note, storage catecholamine granules have been demonstrated within adrenal medullary tissue and pheochromocytoma tumor lesions[40]. Since MIBG uptake reflects the concentration of neurosecretory storage granules in chromaffin normal tissue and in the corresponding tumors, the higher MIBG uptake of lesions in patients with malignant compared to those of patients with benign

tumors suggests a higher concentration of catecholamine in malignant pheochromocytoma. Thus, this difference could reflect different functional conditions with malignant lesions being more prone to catecholamine secretion crises compared to benign tumors. This observation might explain the severe hypertensive attacks that frequently occur in patients with malignant pheochromocytoma and might also justify the use of radiolabeled MIBG for therapeutic purposes in such patients when conventional treatments are not effective[44,45].

Previous comparative studies between MIBG and MR imaging demonstrated the complementary role of these techniques in the diagnostic evaluation of patients with pheochromocytoma or paraganglioma[17-19]. In these studies no data regarding the characterization and differentiation between benign and malignant tumors have been reported. Our results showed that there are no specific MR criteria, either on T1- or on T2-scans, to differentiate between benign and malignant CTT; no significant differences in MR signal intensity ratios were observed between tumor lesions of benign and malignant neoplasms; these findings suggest that signal intensity ratios reflects tumor tissue structural characteristics which are not related to metabolic and functional conditions.

In conclusion, nuclear imaging modalities using specific target agents are able to better characterize, compared with MR, adrenal tumors. Radionuclide techniques are able to identify the nature of adrenal incidentalomas and to differentiate between hypersecreting and non-hypersecreting adenomas as well as between benign and malignant CTT.

COMMENTS

Background
Imaging modalities such as computed tomography (CT), magnetic resonance imaging (MRI) and nuclear modalities are actually advanced as well as technically improved suggesting that qualitative and/or quantitative methods might be helpful for this purpose.

Research frontiers
Radionuclide techniques using specific tracers such as labeled nor-cholesterol, metaiodobenzylguanidine (MIBG) and fluorine-deoxy-glucose (FDG) may provide *in vivo* tissue characterization of adrenal tumours being able to differentiate between benign and malignant abnormalities; these agents have no relation to each other and are taken up by individual parts of adrenals on the basis of entirely separate mechanism and are able to differentiate different types of tumours.

Innovations and breakthroughs
Nuclear techniques using specific tracers such as nor-cholesterol, MIBG and FDG are able to provide *in vivo* tissue characterization of adrenal tumors being able to differentiate between benign and malignant lesions. Quantitative analysis of MIBG uptake may differentiate between benign and malignant chromaffin-tissue tumors such as pheochromocytoma and paraganglioma, while MR imaging using signal intensity ratio measurement is not useful in this field.

Terminology
Nuclear imaging: Nuclear imaging is part of nuclear medicine and consists of functional techniques used for diagnostic purposes. Imaging characterization: Imaging characterization consist of techniques able to provide diagnostic criteria and parameters to perform tissue diagnosis in terms of benign or malignant lesions. Adrenal tumors: Adrenal tumors are lesions of adrenal glands located into the retroperitoneum; these lesions may be benign or malignant and, thus, tumor characterization is clinically required for patient appropriate management.

Peer review

This study concerns a comparison of different nuclear imaging methods (norcholesterol, MIBG and FDG) to MR imaging for the diagnostic evaluation of patients with adrenal masses. The results show that nuclear imaging methods in general show higher sensitivity compared to MR in detecting adrenal tumors and should be useful in the clinic. This is well written.

REFERENCES

1　**Kloos RT**, Gross MD, Francis IR, Korobkin M, Shapiro B. Incidentally discovered adrenal masses. *Endocr Rev* 1995; **16**: 460-484 [PMID: 8521790 DOI: 10.1210/edrv-16-4-460]

2　**Ross NS**, Aron DC. Hormonal evaluation of the patient with an incidentally discovered adrenal mass. *N Engl J Med* 1990; **323**: 1401-1405 [PMID: 2233907 DOI: 10.1056/NEJM199011153232007]

3　**Gross MD**, Shapiro B. Clinical review 50: Clinically silent adrenal masses. *J Clin Endocrinol Metab* 1993; **77**: 885-888 [PMID: 8408461 DOI: 10.1210/jcem.77.4.8408461]

4　**Mayo-Smith WW**, Boland GW, Noto RB, Lee MJ. State-of-the-art adrenal imaging. *Radiographics* 2001; **21**: 995-1012 [PMID: 11452074 DOI: 10.1148/radiographics.21.4.g01jl21995]

5　**Korobkin M**, Brodeur FJ, Francis IR, Quint LE, Dunnick NR, Londy F. CT time-attenuation washout curves of adrenal adenomas and nonadenomas. *AJR Am J Roentgenol* 1998; **170**: 747-752 [PMID: 9490968 DOI: 10.2214/ajr.170.3.9490968]

6　**Heinz-Peer G**, Hönigschnabl S, Schneider B, Niederle B, Kaserer K, Lechner G. Characterization of adrenal masses using MR imaging with histopathologic correlation. *AJR Am J Roentgenol* 1999; **173**: 15-22 [PMID: 10397092 DOI: 10.2214/ajr.173.1.10397092]

7　**Ilias I**, Sahdev A, Reznek RH, Grossman AB, Pacak K. The optimal imaging of adrenal tumours: a comparison of different methods. *Endocr Relat Cancer* 2007; **14**: 587-599 [PMID: 17914090 DOI: 10.1677/ERC-07-0045]

8　**Lawson MA**. Role of molecular imaging in management of nonhypersecreting adrenal masses. *J Nucl Med* 2001; **42**: 893-894 [PMID: 11390553]

9　**Maurea S**, Klain M, Mainolfi C, Ziviello M, Salvatore M. The diagnostic role of radionuclide imaging in evaluation of patients with nonhypersecreting adrenal masses. *J Nucl Med* 2001; **42**: 884-892 [PMID: 11390552]

10　**Truong B**, Jolles PR, Mullaney JM. Primary adrenal lymphoma: gallium scintigraphy and correlative imaging. *J Nucl Med* 1997; **38**: 1770-1771 [PMID: 9374351]

11　**Shulkin BL**, Wieland DM, Schwaiger M, Thompson NW, Francis IR, Haka MS, Rosenspire KC, Shapiro B, Sisson JC, Kuhl DE. PET scanning with hydroxyephedrine: an approach to the localization of pheochromocytoma. *J Nucl Med* 1992; **33**: 1125-1131 [PMID: 1597727]

12　**Boland GW**, Goldberg MA, Lee MJ, Mayo-Smith WW, Dixon J, McNicholas MM, Mueller PR. Indeterminate adrenal mass in patients with cancer: evaluation at PET with 2-[F-18]-fluoro-2-deoxy-D-glucose. *Radiology* 1995; **194**: 131-134 [PMID: 7997539 DOI: 10.1148/radiology.194.1.7997539]

13　**Erasmus JJ**, Patz EF, McAdams HP, Murray JG, Herndon J, Coleman RE, Goodman PC. Evaluation of adrenal masses in patients with bronchogenic carcinoma using 18F-fluorodeoxyglucose positron emission tomography. *AJR Am J Roentgenol* 1997; **168**: 1357-1360 [PMID: 9129444 DOI: 10.2214/ajr.168.5.9129444]

14　**Maurea S**, Mainolfi C, Bazzicalupo L, Panico MR, Imparato C, Alfano B, Ziviello M, Salvatore M. Imaging of adrenal tumors using FDG PET: comparison of benign and malignant lesions. *AJR Am J Roentgenol* 1999; **173**: 25-29 [PMID: 10397094]

15　**Bergström M**, Juhlin C, Bonasera TA, Sundin A, Rastad J, Akerström G, Långström B. PET imaging of adrenal cortical tumors with the 11beta-hydroxylase tracer 11C-metomidate. *J Nucl Med* 2000; **41**: 275-282 [PMID: 10688111]

16　**Maurea S**, Lastoria S, Caracò C, Klain M, Varrella P, Acampa W, Muto P, Salvatore M. The role of radiolabeled somatostatin analogs in adrenal imaging. *Nucl Med Biol* 1996; **23**: 677-680 [PMID: 8940709]

17　**Quint LE**, Glazer GM, Francis IR, Shapiro B, Chenevert TL. Pheochromocytoma and paraganglioma: comparison of MR imaging with CT and I-131 MIBG scintigraphy. *Radiology* 1987; **165**: 89-93 [PMID: 3628794 DOI: 10.1148/radiology.165.1.3628794]

18　**Maurea S**, Cuocolo A, Reynolds JC, Tumeh SS, Begley MG, Linehan WM, Norton JA, Walther MM, Keiser HR, Neumann RD. Iodine-131-metaiodobenzylguanidine scintigraphy in preoperative and postoperative evaluation of paragangliomas: comparison with CT and MRI. *J Nucl Med* 1993; **34**: 173-179 [PMID: 8381474]

19　**van Gils AP**, van Erkel AR, Falke TH, Pauwels EK. Magnetic resonance imaging or metaiodobenzylguanidine scintigraphy for the demonstration of paragangliomas? Correlations and disparities. *Eur J Nucl Med* 1994; **21**: 239-253 [PMID: 8200393]

20　**Gross MD**, Shapiro B, Francis IR, Glazer GM, Bree RL, Arcomano MA, Schteingart DE, McLeod MK, Sanfield JA, Thompson NW. Scintigraphic evaluation of clinically silent adrenal masses. *J Nucl Med* 1994; **35**: 1145-1152 [PMID: 8014672]

21　**Maurea S**, Fiumara G, Pellegrino T, Zampella E, Assante R, Mainenti P, Cuocolo A. MIBG molecular imaging for evaluating response to chemotherapy in patients with malignant pheochromocytoma: preliminary results. *Cancer Imaging* 2013; **13**: 155-161 [PMID: 23598367 DOI: 10.1102/1470-7330.2013.0017]

22　**Slapa RZ**, Jakubowski W, Januszewicz A, Kasperlik-Zaluska AA, Dabrowska E, Fijuth J, Feltynowski T, Tarnawski R, Królicki L. Discriminatory power of MRI for differentiation of adrenal non-adenomas vs adenomas evaluated by means of ROC analysis: can biopsy be obviated? *Eur Radiol* 2000; **10**: 95-104 [PMID: 10663723]

23　**Caoili EM**, Korobkin M, Francis IR, Cohan RH, Platt JF, Dunnick NR, Raghupathi KI. Adrenal masses: characterization with combined unenhanced and delayed enhanced CT. *Radiology* 2002; **222**: 629-633 [PMID: 11867777 DOI: 10.1148/radiol.2223010766]

24　**Maurea S**, Lastoria S, Cuocolo A, Celentano L, Salvatore M. The diagnosis of nonfunctioning pheochromocytoma. The role of I-123 MIBG imaging. *Clin Nucl Med* 1995; **20**: 22-24 [PMID: 7895430]

25　**Barzon L**, Scaroni C, Sonino N, Fallo F, Gregianin M, Macrì C, Boscaro M. Incidentally discovered adrenal tumors: endocrine and scintigraphic correlates. *J Clin Endocrinol Metab* 1998; **83**: 55-62 [PMID: 9435416 DOI: 10.1210/jcem.83.1.4501]

26　**Maurea S**, Klain M, Caraco C, Ziviello M, Salvatore M. Diagnostic accuracy of radionuclide imaging using 131I norcholesterol or meta-iodobenzylguanidine in patients with hypersecreting or non-hypersecreting adrenal tumours. *Nucl Med Commun* 2002; **23**: 951-960 [PMID: 12352593]

27　**Young WF**. Management approaches to adrenal incidentalomas. A view from Rochester, Minnesota. *Endocrinol Metab Clin North Am* 2000; **29**: 159-185, x [PMID: 10732270]

28　**Schteingart DE**. Management approaches to adrenal incidentalomas. A view from Ann Arbor, Michigan. *Endocrinol Metab Clin North Am* 2000; **29**: 127-139, ix-x [PMID: 10732268]

29　**Yoh T**, Hosono M, Komeya Y, Im SW, Ashikaga R, Shimono T, Tsuchiya N, Okada M, Hanada K, Yagyu Y, Nishimura Y, Murakami T. Quantitative evaluation of norcholesterol scintigraphy, CT attenuation value, and chemical-shift MR imaging for characterizing adrenal adenomas. *Ann Nucl Med* 2008; **22**: 513-519 [PMID: 18670858 DOI: 10.1007/s12149-008-0143-2]

30   **Soffer LJ,** Dorfam RJ, Gabrilove JL. The human adrenal gland. Lea & Febiger: Philadelphia, 1961: 10-20

31   **Shapiro B,** Gross MD, Sandler MP. Adrenal scintigraphy revisited: a current status report on radiotracers, clinical utility and correlative imaging. In: Annual Nuclear Medicine, Freeman LM, Weissman HS, editors. New York: Raven Press, 1987: 193-232

32   **Dominguez-Gadea L**, Diez L, Piedrola-Maroto G, Crespo A. Scintigraphic diagnosis of subclinical Cushing's syndrome in patients with adrenal incidentalomas. *Nucl Med Commun* 1996; **17**: 29-32 [PMID: 8692469]

33   **La Cava G**, Imperiale A, Olianti C, Gheri GR, Ladu C, Mannelli M, Pupi A. SPECT semiquantitative analysis of adrenocortical (131)I-6 beta iodomethyl-norcholesterol uptake to discriminate subclinical and preclinical functioning adrenal incidentaloma. *J Nucl Med* 2003; **44**: 1057-1064 [PMID: 12843220]

34   **Imperiale A**, Olianti C, Mannelli M, La Cava G, Pupi A. Tomographic evaluation of [131I] 6beta-iodomethyl-norcholesterol standardised uptake trend in clinically silent monolateral and bilateral adrenocortical incidentalomas. *Q J Nucl Med Mol Imaging* 2005; **49**: 287-296 [PMID: 16172575]

35   **Maurea S**, Imbriaco M, D'Angelillo M, Mollica C, Camera L, Salvatore M. Diagnostic accuracy of chemical-shift MR imaging to differentiate between adrenal adenomas and non adenoma adrenal lesions. *Radiol Med* 2006; **111**: 674-686 [PMID: 16791464 DOI: 10.1007/s11547-006-0065-9]

36   **Pacak K**, Eisenhofer G, Ahlman H, Bornstein SR, Gimenez-Roqueplo AP, Grossman AB, Kimura N, Mannelli M, McNicol AM, Tischler AS. Pheochromocytoma: recommendations for clinical practice from the First International Symposium. October 2005. *Nat Clin Pract Endocrinol Metab* 2007; **3**: 92-102 [PMID: 17237836 DOI: 10.1038/ncpendmet0396]

37   **Gao B**, Kong F, Xu Z. Development of differential diagnosis for benign and malignant pheochromocytomas. *Int J Urol* 2008; **15**: 771-777 [PMID: 18651863 DOI: 10.1111/j.1442-2042.2008.02111.x]

38   **Kann PH**, Wirkus B, Behr T, Klose KJ, Meyer S. Endosonographic imaging of benign and malignant pheochromocytomas. *J Clin Endocrinol Metab* 2004; **89**: 1694-1697 [PMID: 15070932 DOI: 10.1210/jc.2003-031709]

39   **van der Harst E**, de Herder WW, Bruining HA, Bonjer HJ, de Krijger RR, Lamberts SW, van de Meiracker AH, Boomsma F, Stijnen T, Krenning EP, Bosman FT, Kwekkeboom DJ. [(123)I]metaiodobenzylguanidine and [(111)In]octreotide uptake in begnign and malignant pheochromocytomas. *J Clin Endocrinol Metab* 2001; **86**: 685-693 [PMID: 11158032 DOI: 10.1210/jcem.86.2.7238]

40   **Bomanji J**, Levison DA, Flatman WD, Horne T, Bouloux PM, Ross G, Britton KE, Besser GM. Uptake of iodine-123 MIBG by pheochromocytomas, paragangliomas, and neuroblastomas: a histopathological comparison. *J Nucl Med* 1987; **28**: 973-978 [PMID: 3585505]

41   **Nguyen HH**, Proye CA, Carnaille B, Combemale F, Pattou FN, Huglo D. Tumour size: the only predictive factor for 131I MIBG uptake in phaeochromocytoma and paraganglioma. *Aust N Z J Surg* 1999; **69**: 350-353 [PMID: 10353549]

42   **McEwan AJ**, Shapiro B, Sisson JC, Beierwaltes WH, Ackery DM. Radio-iodobenzylguanidine for the scintigraphic location and therapy of adrenergic tumors. *Semin Nucl Med* 1985; **15**: 132-153 [PMID: 3890187]

43   **Jaques S**, Tobes MC, Sisson JC. Sodium dependency of uptake of norepinephrine and m-iodobenzylguanidine into cultured human pheochromocytoma cells: evidence for uptake-one. *Cancer Res* 1987; **47**: 3920-3928 [PMID: 3607739]

44   **Loh KC**, Fitzgerald PA, Matthay KK, Yeo PP, Price DC. The treatment of malignant pheochromocytoma with iodine-131 metaiodobenzylguanidine (131I-MIBG): a comprehensive review of 116 reported patients. *J Endocrinol Invest* 1997; **20**: 648-658 [PMID: 9492103]

45   **Rose B**, Matthay KK, Price D, Huberty J, Klencke B, Norton JA, Fitzgerald PA. High-dose 131I-metaiodobenzylguanidine therapy for 12 patients with malignant pheochromocytoma. *Cancer* 2003; **98**: 239-248 [PMID: 12872341 DOI: 10.1002/cncr.11518]

SYSTEMATIC REVIEWS

Usefulness of myocardial positron emission tomography/ nuclear imaging in Takotsubo cardiomyopathy

Marzia Testa, Mauro Feola

Marzia Testa, Mauro Feola, Cardiovascular Rehabilitation, Heart Failure Unit, 12045 Fossano, Italy
Marzia Testa, School of Geriatry, Universita' degli Studi di Torino, Torino 10126, Italy
Author contributions: Testa M wrote the manuscript; Feola M wrote and edited the manuscript.
Correspondence to: Feola Mauro, MD, FESC, Cardiovascular Rehabilitation, Heart Failure Unit, Ospedale SS Trinita', Via Ospedale 4, 12045 Fossano, Italy. m_feola@virgilio.it
Telephone: +39-0172-699365 Fax: +39-0172-699364
Received: January 21, 2014 Revised: May 28, 2014
Accepted: June 14, 2014
Published online: July 28, 2014

Abstract

AIM: To analyse and summarize all the articles related to positron emission tomography and Takotsubo cardiomyopathy (TTC).

METHODS: We performed a systematic review of the existing literature on positron emission tomography/ nuclear imaging and Takotsubo cardiomyopathy using PUBMED database. We combined search terms such as "takotsubo", "takotsubo syndrome", "myocardial positron emission tomography", "positron emission tomography". All case reports were excluded. The list included only four articles which were reviewed by two independent investigators. It was not possible to undertake a formal meta-analysis because of the heterogeneity of the studies; therefore, we made a narrative synthesis of the collected data.

RESULTS: Nuclear medicine techniques can be useful employed in the differential diagnosis of TTC from an acute coronary syndrome (ACS). In fact, transient left ventricular (LV) apical ballooning is a syndrome frequently misdiagnosed as an ACS and can mimic symptoms of myocardial infarction with ST-T segments changes on electrocardiography (ECG), a limited release of myocardial enzyme, mainly reported after sudden emotional or physical stress, and an akinesis or dyskinesis of the left ventricle apex which are completely reversible in a few weeks. In the studies included in this review, nuclear medicine techniques have demonstrated a discrepancy between normal perfusion and a reduced glucose utilization in TTC, commonly known as "inverse flow metabolism mismatch". This suggests that apical ballooning represents a transient metabolic disorder on the cellular level, rather than a structural contractile disease of the myocardium, due to a transient decrease of glucose metabolism that might be related to a coronary microcirculation impairment followed by prolonged myocardial stunning.

CONCLUSION: Nuclear medicine techniques can be usefully used for the diagnosis of TTC and can increase our knowledge of the pathophysiological mechanisms of TTC.

Key words: Takotsubo cardiomyopathy; Cardiac positron emission tomography; Clinical review.

Core tip: Takotsubo cardiomyopathy is a cardiac syndrome with symptoms similar to acute myocardial infarction (MI) including chest pain and electrocardiographic changes, in absence of coronary artery stenosis. This syndrome is characterized by reversible wall-motion abnormalities involving apical and midportion of left ventricle. In the acute phase it is clinically indistinguishable from acute MI but, recently, myocardial positron emission tomography have demonstrated to delineate this syndrome from acute coronary artery disease, also offering a new pathophysiological explanation for this particular syndrome. This clinical review aimed to summarise the most significant experiences on the use of myocardial positron emission tomography in Takotsubo cardiomyopathy.

INTRODUCTION

Transient left ventricular (LV) apical ballooning is a syndrome frequently misdiagnosed as an acute coronary syndrome related to occlusive epicardial coronary artery disease (CAD)[1,2]. It is characterised by a rare form of transient LV dysfunction and dilatation accompanied by chest pain following emotional or physical stress, ischemic electrocardiographic changes, minimal release of cardiac enzymes, wall-motion abnormalities involving the apical and mid-portion of the left ventricle and absence of angiographically detectable coronary artery disease (CAD)[3]. Physiopathology of this particular heart disease, also called Takotsubo cardiomyopathy (TTC), is still unexplained although several mechanisms have been proposed, such as multivessel coronary vasospasm, abnormalities in coronary microvascular function, inflammatory process and catecholamine-mediated cardiotoxicity[4-9].

Recently, nuclear medicine techniques for diagnosis and improvement in pathophysiological explanation of TTC have been used, showing interesting results both for diagnosis and for speculative clinical research. This review aimed to summarise the most significant experiences on the use of myocardial positron emission tomography (PET) in TTC.

MATERIALS AND METHODS

We performed a systematic review of the existing literature on this topic using PUBMED database, combining search terms such as "takotsubo", "takotsubo syndrome", "myocardial positron emission tomography", "positron emission tomography". Case reports were excluded. The list included only four articles which were reviewed by two investigators. A formal meta-analysis was not done because of the heterogeneity of studies, therefore, we undertook a narrative synthesis of the collected data.

RESULTS

Studies' characteristics

Four articles[10-13] were included in our clinical review (see Table 1); one is from Japan, one from Italy, one from France and the last from Austria. The main characteristics of the studies included in this review are reported in Table 1. All publications were written in English. All of them were prospective studies, but just in three of them a period of follow-up was planned (ranged from 30 to 180 d). The studies ranged from 3 to 18 patients; a total of 49 patients were included in this review.

The study of myocardial perfusion.

A total of 37 patients underwent a myocardial perfusion scintigraphy in the acute phase of TTC [14 patients with Thallium-201 (^{201}Tl), 3 with nitrogen 13-ammonia (N13) and 20 with ^{99m}Tc-tetrofosmin (^{99m}Tc) used as radiotracer]. The interval between onset of acute symptoms and single photon emission computed tomography (SPECT) or PET scan imaging varied from 1 to 15 d; in two studies this interval was not clearly reported. In three out of fourteen patients, an early perfusion image demonstrated a decreased ^{201}Tl uptake in a small area of the apex detected with a semiquantitative method. The hypoperfused apex region did not correlate with an angiographic obstructive epicardial coronary stenosis. Normal myocardial perfusion was observed in the other cases studied with ^{201}Tl or ^{99m}Tc. Cimarelli et al[12] found, at the analysis of left ventricle motion, apical akinesis or severe hypokinesis in TTC and severe mid ventricular hypokinesis with preserved apical and basal function in patients with a particular variant of TTC, called "mid-ventricular ballooning syndrome". The quantitative perfusion analysis using the ammonia tracer in PET scan in patients admitted for TTC showed a slight reduction in tracer uptake after adenosine in the apex and apical segments of the left ventricle that normalized at rest. Myocardial blood flow (MBF) and coronary flow reserve (CFR) were evaluated by Feola et al[11] in three female patients obtaining a significant reduction in MBF at rest in the apical segments in comparison to the mid-ventricular and basal LV segments. CFR also reduced in apical and, in 2 cases out of 3, in mid-ventricular segments in comparison to the basal LV segments (Figure 1).

A follow-up SPECT was provided in four patients three months after the acute onset of TTC. In one of them, studied with ^{201}Tl radiotracer, apical abnormality returned to normal. In the other three patients, studied with N13 and stress/rest perfusion scan using adenosine, both MBF and CFR reduction observed in the acute phase recovered, demonstrating as the impairment of MBF and, above all, CFR seemed to be transient and localized in TTC.

The same population studied by Feola et al[11] was also analysed with cardiac magnetic resonance imaging (MRI) that confirmed, in the acute phase, the segmental disturb of LV contraction (hypo/akinesia in apex and periapical segments) determining an important systolic dysfunction. In none areas a delayed enhancement after gadolinium injection either in the acute phase or at 3 mo' follow up phase emerged, suggesting that the damage in the dysfunctional areas was transient and did not include necrotic tissue.

The myocardial glucose metabolism

Myocardial PET using fluorine 18 fluorodeoxyglucose (FDG) was totally used in 39 patients with acute TTC as an indicator of myocardial metabolism. Yoshida et al[10] studied 8 TTC patients, obtaining in 7 out of 8 patients a pattern of severe and diffuse reduced ^{18}F-FDG uptake in left ventricle. Of these seven patients, six exhibited a LV dysfunction at echocardiography examination. Moreover,
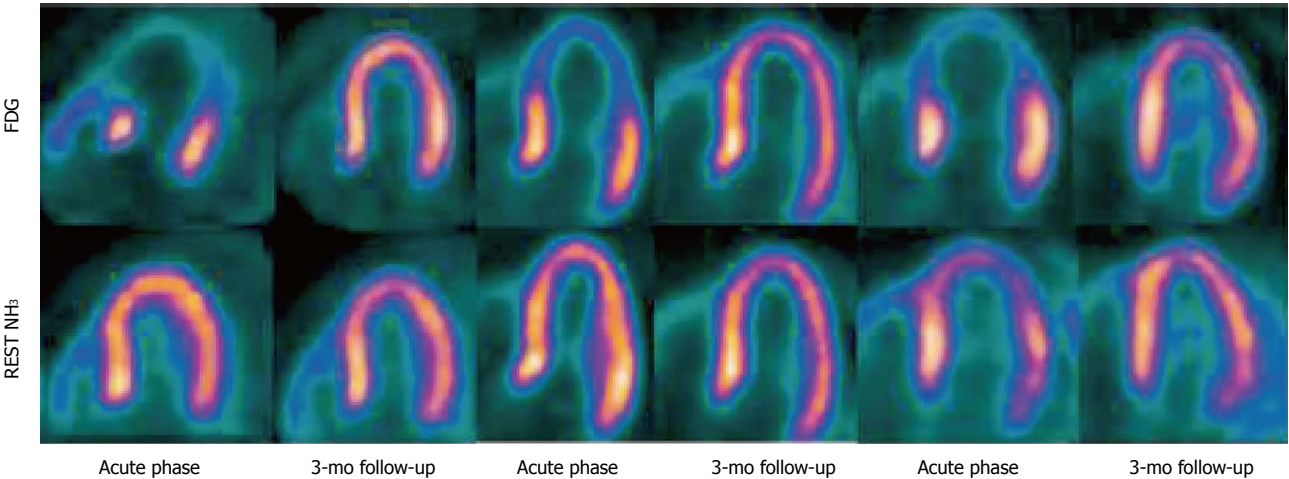
Figure 1 Images representing three different consecutive female patients with diagnosis of Takotsubo cardiomyopathy in which in the acute phase a clear inverse flow/metabolism mismatch emerged (reduction of fluorodeoxyglucose uptake and preserved blood flow obtained with ammonia). The mismatch was reversible and disappeared at 3-mo follow-up. FDG: Fluorodeoxyglucose;

Table 1 Comparison between the four articles

	No of patients (females)	Mean age	LVEF acute phase	Diagnostic techniques used for TTC	MRI (*n*)	SPECT (*n*)	FDG-PET (*n*)	MIBG	Time of follow-up (d)	LVEF follow-up	MRI follow-up (*n*)	SPECT follow-up (*n*)	FDG-PET follow-up (*n*)	MIBG follow-up (*n*)
Yoshida *et al*[10]	15 (12)	72	47.7% ± 6.6%	ECG/CAG/ EchoCG	-	201Tl (10)	8	-	90	-	-	1	-	-
Feola *et al*[11]	3 (3)	75, 3	40.7% ± 5.1%	ECG/CAG/ EchoCG	3	N13 (3)	3	-	90	54%	3	3	3	-
Cimarelli *et al*[12]	18 (13)	67	35% ± 8%	ECG/CAG/ EchoCG	-	99mTc (7) or 201Tl (4)	15	8	30-180	58% ± 6%	-	-	6	2
Rendl *et al*[13]	13 (NR)	NR	52% ± 13%	CAG/ EchoCG	-	99mTc (13)	13	-	60	62% ± 13%	-	NR	11	-
TOTAL (*n*)	49				3	37	39	8			3	4	20	2

NR: Not reported; "-": not examined; LVEF: Left ventricular ejection fraction; TTC: Takotsubo cardiomyopathy; ECG: Electrocardiography; CAG: Coronary angiography; EchoCG: Echocardiography; MRI: Cardiac magnetic resonance; SPECT: Myocardial scintigraphy; FDG-PET: Fluoridesossiglucose myocardial positron emission tomography; MIBG: Iobenguane myocardial scintigraphy.

they observed that the extension of the metabolic defect was much larger and more severe than the perfusion defect with 201Tl. In the other three studies[11-13], most of patients (20/24, 83.3%) showed a severe reduction of metabolic activity in the apex and periapical segments in the acute phase of TTC. This reduction of FDG uptake in the dysfunctional areas recovered at follow-up, following the normalization of left ventricle function. In fact, considering the entire population of TTC studied with PET, FDG-PET was repeated in 20 patients, in a follow-up period variable from 30 to 180 d: in 18/20 cases a complete recovery of FDG uptake emerged, confirming the hypothesis of a complete reversibility of the FDG impairment. The severe reduction of FDG uptake in the dysfunctional myocardial segments has not been completely understood and might be related to a partial volume effect in enlarged, impaired areas or to a specific metabolic impairment of the glucose utilization.

The myocardial innervation

Cimarelli *et al*[12] observed in 8 TTC patients, underwent myocardial 123I-mIBG SPECT, a severe reduction/absence of mIBG uptake in the dysfunctional segments of apical or mid-ventricular regions. Four out of eight patients repeated 123I-mIBG SPECT six months after acute symptoms, demonstrating an improvement of tracer uptake in apical segments. Furthermore, analysing the 4 patients underwent myocardial SPECT, 123I-mIBG SPECT and 18F-FDG PET, they concluded that dysfunctional but normally perfused LV segments were characterized by severe decrease of 123I-mIBG and 18F-FDG uptake. Moreover, the distribution of 123I-mIBG and 18F-FDG uptake defects was largely overlapping. These data added an interesting element in the pathophysiology of TTC syndrome, highlighting as the dysfunctioning segments presented a pattern of severe denervation and metabolic glucose uptake that ameliorated and even normalized in the follow-up following the improvement of myocardial function.

DISCUSSION

TCC is a severe, reversible form of left ventricular dys-

function in patients with normal coronary angiography. Because the onset of this syndrome is very similar to that of an ACS, it is really important to differentiate one from the other, also considering the different treatment that should be undertaken.

TTC is often preceded by emotional or physical stress and this have suggested the hypothesis of catecholamine-mediated multivessel epicardial spasm, microvascular coronary spasm[2] or possible direct catecholamine-mediated myocyte injury[6] as possible pathophysiological mechanisms. The multivessel spasm may be responsible for a self-limited ischemic event able to generate stunned myocardium but not long enough to cause myocardial necrosis[7].

Nuclear medicine techniques have been successfully employed in the differential diagnosis of TTC from ACS and have demonstrated a discrepancy between normal perfusion and reduced ^{18}F-FDG uptake in TTC[8,9]. This association is commonly known as "inverse metabolic-perfusion mismatch" and represented a transient metabolic disorder at the cellular level, demonstrated by evidence of tissue's impairment metabolism in the dysfunctioning left ventricle with preserved MBF at rest[10-13]. Moreover, PET imaging, using the quantitative analysis, confirmed the light impairment of MBF in dysfunctioning LV segments in the acute phase together with a clearly reduction of CFR after vasodilator stimuli. These MBF modifications recovered completely in the follow-up, probably justifying the favourable clinical prognosis in those patients. Further studies and a larger patient population are needed to confirm these findings.

COMMENTS

Background
Takotsubo cardiomyopathy (TTC) is a severe, reversible form of left ventricular dysfunction that can mimic symptoms similar to acute myocardial infarction (MI) in absence of coronary artery stenosis. Because the onset of this syndrome is very similar to that of an acute coronary syndrome (ACS), it is really important to differentiate one from the other, also considering the different treatment that should be undertaken.

Research frontiers
Recently, nuclear medicine techniques, such as myocardial positron emission tomography (PET), have demonstrated to delineate this syndrome from acute coronary artery disease, also offering a new pathophysiological explanation for this particular syndrome. This clinical review aimed to summarise the most significant experiences on use of myocardial positron emission tomography in TTC.

Innovations and breakthroughs
Recent reports on use of PET in TTC have highlighted a discrepancy between normal myocardial perfusion and reduced glucose utilization in this particular syndrome, commonly known as "inverse flow metabolism mismatch". This suggests that TTC represents a transient metabolic disorder on the cellular level, rather than a structural contractile disease of the myocardium, due to a transient decrease of glucose metabolism that might be related to a coronary microcirculation impairment. In an other study this interesting finding has been associated to a severe denervation of the myocardium.

Applications
Nuclear medicine techniques have been successfully employed in the differential diagnosis of TTC from ACS and have offered a new pathophysiological explanation for this particular syndrome, useful in improving the knowledge of this poorly understood syndrome.

Terminology
Takotsubo cardiomyopathy: syndrome, mainly reported after sudden emotional or physical stress, characterized by chest pain, changes on electrocardiography, limited release of myocardial enzyme and reversible wall-motion abnormalities involving apical and midportion of left ventricle. PET: a nuclear medicine, functional imaging technique that can use biologically active molecules (*e.g.*, glucose); their uptake, showed in the tissue, indicate the presence of metabolic activity.

Peer review
In this article the authors aimed to summarize the results of four articles on the use of myocardial PET in Takotsubo cardiomiopathy. It is a good work.

REFERENCES

1   **Bybee KA**, Kara T, Prasad A, Lerman A, Barsness GW, Wright RS, Rihal CS. Systematic review: transient left ventricular apical ballooning: a syndrome that mimics ST-segment elevation myocardial infarction. *Ann Intern Med* 2004; **141**: 858-865 [PMID: 15583228 DOI: 10.7326/0003-4819-141-11-200412070-00010]

2   **Abe Y**, Kondo M, Matsuoka R, Araki M, Dohyama K, Tanio H. Assessment of clinical features in transient left ventricular apical ballooning. *J Am Coll Cardiol* 2003; **41**: 737-742 [PMID: 12628715]

3   **Dote K**, Sato H, Tateishi H, Uchida T, Ishihara M. [Myocardial stunning due to simultaneous multivessel coronary spasms: a review of 5 cases]. *J Cardiol* 1991; **21**: 203-214 [PMID: 1841907]

4   **Gianni M**, Dentali F, Grandi AM, Sumner G, Hiralal R, Lonn E. Apical ballooning syndrome or takotsubo cardiomyopathy: a systematic review. *Eur Heart J* 2006; **27**: 1523-1529 [PMID: 16720686 DOI: 10.1093/eurheartj/ehl032]

5   **Nef HM**, Möllmann H, Elsässer A. Tako-tsubo cardiomyopathy (apical ballooning). *Heart* 2007; **93**: 1309-1315 [PMID: 17890711]

6   **Mann DL**, Kent RL, Parsons B, Cooper G. Adrenergic effects on the biology of the adult mammalian cardiocyte. *Circulation* 1992; **85**: 790-804 [PMID: 1370925 DOI: 10.1161/01.CIR.85.2.790]

7   **Tsubokawa A**, Lee JD, Shimizu H, Nakano A, Uzui H, Takeuchi M, Tsuchida T, Yonekura Y, Ishii Y, Ueda T. Recovery of perfusion, glucose utilization and fatty acid utilization in stunned myocardium. *J Nucl Med* 1997; **38**: 1835-1837 [PMID: 9430454]

8   **Bybee KA**, Murphy J, Prasad A, Wright RS, Lerman A, Rihal CS, Chareonthaitawee P. Acute impairment of regional myocardial glucose uptake in the apical ballooning (takotsubo) syndrome. *J Nucl Cardiol* 2006; **13**: 244-250 [PMID: 16580961 DOI: 10.1007/BF02971249]

9   **Obunai K**, Misra D, Van Tosh A, Bergmann SR. Metabolic evidence of myocardial stunning in takotsubo cardiomyopathy: a positron emission tomography study. *J Nucl Cardiol* 2005; **12**: 742-744 [PMID: 16344237 DOI: 10.1016/j.nuclcard.2005.06.087]

10   **Yoshida T**, Hibino T, Kako N, Murai S, Oguri M, Kato K, Yajima K, Ohte N, Yokoi K, Kimura G. A pathophysiologic study of tako-tsubo cardiomyopathy with F-18 fluorodeoxyglucose positron emission tomography. *Eur Heart J* 2007; **28**: 2598-2604 [PMID: 17921529 DOI: 10.1093/eurheartj/ehm401]

11   **Feola M**, Chauvie S, Rosso GL, Biggi A, Ribichini F, Bobbio M. Reversible impairment of coronary flow reserve in takotsubo cardiomyopathy: a myocardial PET study. *J Nucl Cardiol* 2008; **15**: 811-817 [PMID: 18984457 DOI: 10.1007/BF03007363]

12   **Cimarelli S**, Sauer F, Morel O, Ohlmann P, Constantinesco A, Imperiale A. Transient left ventricular dysfunction syndrome: patho-physiological bases through nuclear medicine

imaging. *Int J Cardiol* 2010; **144**: 212-218 [PMID: 19443060 DOI: 10.1016/j.ijcard.2009.04.025]

13   **Rendl G**, Rettenbacher L, Keinrath P, Altenberger J, Schuler J, Heigert M, Pichler M, Pirich C. Different pattern of re-gional metabolic abnormalities in Takotsubo cardiomyopa-thy as evidenced by F-18 FDG PET-CT. *Wien Klin Wochen-schr* 2010; **122**: 184-185 [PMID: 20361383 DOI: 10.1007/s00508-010-1356-7]

CASE REPORT

Bilateral squamosal suture synostosis: A rare form of isolated craniosynostosis in Crouzon syndrome

Yasmeen K Tandon, Michael Rubin, Mohamed Kahlifa, Gaby Doumit, Lena Naffaa

Yasmeen K Tandon, Department of Radiology, Case Western Reserve University-Metro Health Medical Center, Cleveland, OH 44109, United States

Michael Rubin, Lena Naffaa, Department of Radiology, Akron Children's Hospital, One Perkins Square, Akron, OH 44308, United States

Mohamed Kahlifa, Department of Medical Genetics, Akron Children's Hospital, One Perkins Square, Akron, OH 44308, United States

Gaby Doumit, Department of Plastic Surgery, Cleveland Clinic, Cleveland, OH 44195, United States

Author contributions: Tandon YK, Rubin M, Kahlifa M, Doumit G and Naffaa L contributed equally to this work; Tandon YK, Naffaa L, Rubin M and Doumit G interpreted images in this study; Tandon YK, Rubin M, Kahlifa, Doumit G and Naffaa L and wrote the paper; Tandon YK, Rubin M, Kahlifa, Doumit G and Naffaa L gave final approval of the version to be published.

Correspondence to: Yasmeen K Tandon, MD, Department of Radiology, Case Western Reserve University-Metro Health Medical Center, 2500 Metro Health Dr, Cleveland, OH 44109, United States. ytandon@neomed.edu

Telephone: +1-216-7784016   Fax: +1-216-7784375

Received: April 5, 2014   Revised: June 1, 2014
Accepted: June 14, 2014
Published online: July 28, 2014

Abstract

Craniosynostosis is a pathologic condition which is characterized by the premature fusion of cranial sutures. It may occur alone or in association with other anomalies making up various syndromes. Crouzon syndrome is the most common craniosynostosis syndrome. Bicoronal sutures fusion is most commonly involved in Crouzon syndrome. There have only been a handful of cases of squamosal suture synostosis described in the surgery literature with the few ones described in Crouzon syndrome associated with other types of craniosynostosis. To the best of our knowledge, we are presenting the first case of isolated bilateral squamosal suture synostosis in a patient with Crouzon syndrome in a radiology journal with emphasis on its radiological appearance.

Core tip: We report the unique case of isolated bilateral squamosal suture synostosis in a 13-mo old patient with Crouzon syndrome. Although bicoronal sutures are most commonly involved in patients with Crouzon syndrome, it is important to be familiar with this rare entity of craniosynostosis in order to prevent misdiagnosis or delayed surgical treatment.

INTRODUCTION

Crouzon syndrome is a very rare autosomal dominant craniofacial dysostosis that occurs in approximately 16 in 1 million live births[1-3]. It was described in 1912 by a French neurologist, Octave Crouzon, in a mother and son exhibiting a triad of skull deformities, facial anomalies and exophthalmos[4]. Typically Crouzon syndrome has been associated with bicoronal synostosis leading to a characteristic tall, flattened forehead. Midface hypoplasia, a beaked nose, and proptosis have also been described as characteristic features[5,6].

To the best of our knowledge, there have been no cases of Crouzon syndrome associated with isolated bilateral squamosal suture craniosynostosis described in the literature. We report the radiological appearance of bilateral premature squamosal craniosynostosis found in a 13 mo-old female with Crouzon syndrome during her work
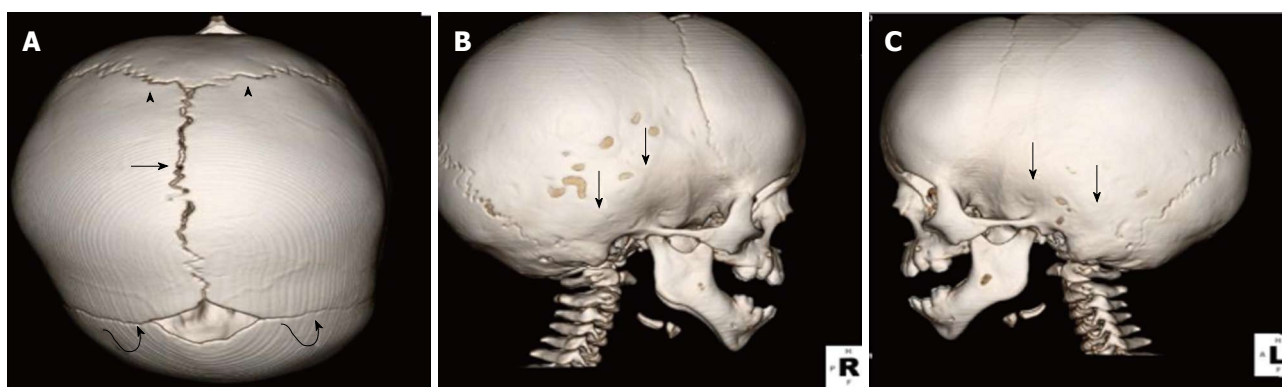
Figure 1 3 D computed tomographic image. A: Of the skull demonstrating normal appearance to the coronal (curved arrows), sagittal (straight arrow), and lambdoid sutures (arrow heads); B, C: Of the cranium demonstrating bony bridging of bilateral squamosal sutures consistent with premature craniosynostosis. The approximate region of the normal squamosal sutures is indicated by straight arrows.
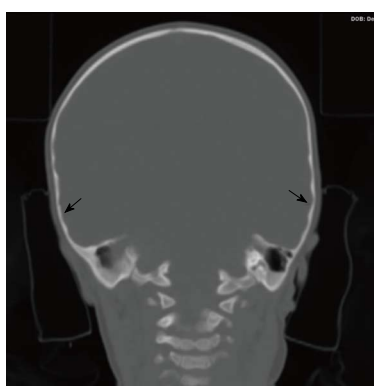

Figure 2 Coronal computed tomography image of the brain demonstrating a local thumb printing/ beaten copper appearance (straight arrows) of the inner cortex in the region of bilateral squamosal fusion.

up for skull deformity.

CASE REPORT

The patient was a 13 mo-old female who was born at 37 wk gestation and had a normal neonatal course. The patient's father carried a diagnosis of Crouzon syndrome. Her family history was otherwise unremarkable. Her past surgical history includes bilateral tear duct probing for bilateral nasolacrimal obstruction. On physical exam, the patient was noted to have macrocephaly (> 97% percentile for age) associated with a prominent forehead and relatively narrowed temples, proptosis, low set ears, orbital hypertelorism and the right cheek was higher and fuller than the left cheek. Given the family history of Crouzon syndrome and the patient's dysmorphic features, Crouzon syndrome was suspected. Genetic testing was done to confirm diagnosis and a mutation in the FGFR2 gene was noted. The patient was then referred to our radiology department to have a head CT performed to rule out craniosynostosis.

CT of the head without intravenous contrast was performed in our institution for further evaluation using the following technique: GE Medical Systems, Pitch: 0.625:1,

Pixel spacing: 0.400 mm/0.400 mm, Kvp 120, mA 109, rotate time: 0.8, ST 3.75 mm, FOV 20 cm, Tilt 0, W: 90, L: 40. Two dimensional images (2D) in the sagittal and coronal planes were reformatted at ST of 3 mm as well as three dimensional images of the skull (3D). The 3D images demonstrate normal appearance of the bilateral coronal and lambdoid sutures and normal appearance of the sagittal suture (Figure 1A). The metopic suture is not visualized, having normally fused. However, there is premature fusion of the squamosal sutures bilaterally (Figure 1B). Coronal 2D reformatted image (Figure 2) shows the local thumb printing (beaten copper) appearance of the inner cortex in the region of bilateral squamosal suture fusion.

The correction of the craniofacial deformities in a patient with Crouzon syndrome and bilateral squamosal craniosynostosis is accomplished through a series of operations over time with respect to the growth and development of the craniofacial skeleton. Around the first year of age, the patient will undergo subtotal cranial vault remodeling to release the fused sutures and correct the skull shape deformities. Subsequently, at around 7 years of age, the patient will be scheduled to undergo either a facial bipartition or Lefort III advancement to correct the hypertelorism or midface hypoplasia. At skeletal maturity, the patient will undergo orthognatic surgery to correct malocclusion when necessary.

DISCUSSION

The development of the human calvaria is a complex process that is still not completely understood. There are 5 primary ossification centers which meet to form 6 main sutures. When this process occurs normally, it culminates to a normally shaped adult head[7].

Craniosynostosis is a pathologic condition which is characterized by the premature fusion of cranial sutures which results in deformity of the vault and cranial base and is often associated with neurological sequelae secondary to alteration in cranial volume and restriction in brain growth. It may occur alone or in association with

other anomalies making up various syndromes[8].

Craniosynostosis is estimated to affect approximately 1 in 2500 children[9,10]. Different etiologies of craniosynostosis include metabolic anomalies, teratogens, genetic anomalies, and abnormal intrauterine pressures[11].

Among the craniosynostosis that are attributed to genetics, most have been associated with a mutation involving 1 of 3 fibroblast growth factor receptors (FGFRs) which include FGFR1, FGFR2, or FGFR3[11]. In the majority of cases, Crouzon syndrome is caused by mutations in the fibroblast growth factor 2 (FGFR2) gene on chromosome 10q26[1,12,13]. However, in patients with Crouzon syndrome and acanthosis nigricans, FGFR3 mutations have also been identified[14]. *FGFR* gene family mutations have also been found in patients with other syndromic craniosynostosis including Pfeiffer syndrome, Jackson-Weiss syndrome, Apert, and Saethre-Chotzen's syndromes[15,16].

Our patient tested positive for FGFR2 mutation which is also found in Pfeiffer and Apert Syndromes[17]. Pfeiffer and Aper syndromes share common features with Crouzon syndrome including craniosynostosis, hypertelorism, proptosis, maxillary bone hypoplasia and autosomal dominance inheritance. However Pfeiffer and Apert syndromes are acrocephalosyndactyly syndromes associated with brachydactyly and syndactyly which our patient did not have and which helped in confirming the diagnosis of Crouzon syndrome[18,19].

The gold standard imaging modality in diagnosing craniosynostosis is CT scan with 3D surface-rendered reconstruction[20]. MRI has no significant role in the diagnosis of craniosynostosis or facial anomalies associated with Crouzon syndrome as it has poor details to bones. MRI of the brain may be indicated in the future only if patient develops neurologic symptoms.

The sagittal suture is most commonly affected in non syndromic craniosynostosis and is estimated to be affected in 40%-60% of cases[21]. This is followed by the coronal suture that is affected in 20%-30% of the cases and the metopic suture in less than 10% of the cases[21]. The pattern of suture involvement determines the shape of the skull defect[21]. There have been more than 100 different types of syndromes which have been identified to be associated with craniosynostosis[9,10].

Crouzon syndrome is one of the most common of the craniosynostosis syndromes[21]. It account for up to 4.8% of all cases of craniosynostosis[13]. The coronal and sagittal sutures are most commonly involved in Crouzon syndrome[13].

There have only been a handful of cases of squamosal suture synostosis described in the surgery literature, the few described in Crouzon patients were always associated with other type of craniosynostosis[10,22]. This is the first reported case of isolated squamosal suture synostosis in a patient with Crouzon syndrome. The squamosal suture arches posteriorly from the pterion and connects the temporal squama with the inferior border of the parietal bone[10].

The treatment of craniosynostosis syndromes requires a multidisciplinary team including plastic surgeons, pediatricians, ENT specialist, radiologists, neurosurgeons, and clinical genetic specialist[23,24]. Surgical correction is undertaken to correct craniofacial deformities and functional problems such as elevated intracranial pressure, airway obstruction, ocular exposure and malocclusion. Surgical techniques that are commonly utilized include fronto-orbital advancement or cranial vault remodeling in first year of life to correct craniosynostosis[25]. Hypertelorism is usually corrected with facial bipartition at age 7. Distraction osteogenesis is commonly used with midface osteotomies to correct midface hypoplasia as it has multiple advantages over conventional mid-facial advancement such as the monobloc or LeFort Ⅲ. Distraction techniques have been shown to reduce operating time, reduce blood loss, reduce infection, eliminate need of bone graft, and allow for large advancement of the midface. Class Ⅲ malocclusion which is commonly seen in syndromic craniosynostosis patients is corrected at skeletal maturity with a Lefort I advancement or double jaw surgery[26-32].

In a conclusion, although squamosal suture craniosynostosis is an extremely rare entity, especially when associated with Crouzon syndrome, it is extremely important for the radiologist to be familiar with its radiological appearance in order to prevent misdiagnosis and delayed treatment.

COMMENTS

Case characteristics
Thirteen-month-old female patient with Crouzon syndrome was found to have isolated bilateral squamosal suture synostosis.

Clinical diagnosis
The patient was noted to have macrocephaly associated with a prominent forehead and relatively narrowed temples, proptosis, low set ears, orbital hypertelorism and asymmetry in appearance of the cheeks.

Differential diagnosis
Pfeiffer and Apert syndromes.

Laboratory diagnosis
Mutation in the *FGFR2* gene was noted.

Imaging diagnosis
Computed tomography finding: The three dimensional (3D) images demonstrate normal appearance of the bilateral coronal and lambdoid sutures and normal appearance to the sagittal suture. However, there is bony bridging in the region of squamosal sutures bilaterally indicating premature synostosis. Coronal 2D reformatted image shows the local thumb printing (beaten copper) appearance of the inner cortex in the region of bilateral squamosal suture fusion.

Treatment
The treatment of craniosynostosis syndromes requires a multidisciplinary team including plastic surgeons, pediatricians, ENT specialists, radiologists, neurosurgeons, and clinical genetic specialists. A series of corrective operations will be performed over time.

Experiences and lessons
The authors report the unique case of isolated bilateral squamosal suture synostosis in a patient with Crouzon syndrome. Although bicoronal sutures are most commonly involved in patients with Crouzon syndrome, it is important to be familiar with this rare entity of craniosynostosis in order to prevent misdiagnosis or delayed surgical treatment.

Peer review
This is a simple case report on a young patient with Crouzon syndrome. It is

concise, well written and well illustrated.

REFERENCES

1   **Reardon W**, Winter RM, Rutland P, Pulleyn LJ, Jones BM, Malcolm S. Mutations in the fibroblast growth factor receptor 2 gene cause Crouzon syndrome. *Nat Genet* 1994; **8**: 98-103 [PMID: 7987400 DOI: 10.1038/ng0994-98]

2   **Mulliken JB**, Steinberger D, Kunze S, Müller U. Molecular diagnosis of bilateral coronal synostosis. *Plast Reconstr Surg* 1999; **104**: 1603-1615 [PMID: 10541159 DOI: 10.1097/00006534-199911000-00001]

3   **Cohen MM**, Kreiborg S. Birth prevalence studies of the Crouzon syndrome: comparison of direct and indirect methods. *Clin Genet* 1992; **41**: 12-15 [PMID: 1633640 DOI: 10.1111/j.1399-0004.1992.tb03620.x]

4   **Babic GS,** Babic RR. Ophthalmological and Radiological picture of Crouzon syndrome-A case report. *Acta Medica Medianae* 2009; **48**: 37-40

5   **Kreiborg S**, Cohen MM. Is craniofacial morphology in Apert and Crouzon syndromes the same? *Acta Odontol Scand* 1998; **56**: 339-341 [PMID: 10066112 DOI: 10.1080/000163598428275]

6   **Kreiborg S**. Craniofacial growth in plagiocephaly and Crouzon syndrome. *Scand J Plast Reconstr Surg* 1981; **15**: 187-197 [PMID: 7347002 DOI: 10.3109/02844318109103433]

7   **Podda S**, Ciminello FS, Wolfe SA. "Congenital Synostoses." Medscape. Cited: 2014-03-20. Available from: URL: http://emedicine.medscape.com/article/1280365-overview

8   **Gorlin RJ,** Cohen MM, Hennekam RC. Syndromes with craniosynostosis: General aspects and well known syndromes. In: Syndromes of the Head and Neck, 4th ed. New York: Oxford university press, 2001: 654-670

9   **Silva DL**, Neto FX, Carneiro SG, Palheta AC, Monteiro MC, Cunha SC, Nunes CT. Crouzon's Syndrome: Literature Review. *Intl Arch Otorhinolaryngol* 2008; **12**: 436-441

10 **Ranger A**, Chaudhary N, Matic D. Craniosynostosis involving the squamous temporal sutures: a rare and possibly underreported etiology for cranial vault asymmetry. *J Craniofac Surg* 2010; **21**: 1547-1550 [PMID: 20856046 DOI: 10.1097/SCS.0b013e3181ebe62f]

11 **Aleck K**. Craniosynostosis syndromes in the genomic era. *Semin Pediatr Neurol* 2004; **11**: 256-261 [PMID: 15828709 DOI: 10.1016/j.spen.2004.10.005]

12 **Rutland P**, Pulleyn LJ, Reardon W, Baraitser M, Hayward R, Jones B, Malcolm S, Winter RM, Oldridge M, Slaney SF. Identical mutations in the FGFR2 gene cause both Pfeiffer and Crouzon syndrome phenotypes. *Nat Genet* 1995; **9**: 173-176 [PMID: 7719345 DOI: 10.1038/ng0295-173]

13 **Guledgud M**, Patil K, Pai E, Deshpande P. Crouzon Syndrome. *Int J Contemp Dent* 2011; **2**: 80-83

14 **Meyers GA**, Orlow SJ, Munro IR, Przylepa KA, Jabs EW. Fibroblast growth factor receptor 3 (FGFR3) transmembrane mutation in Crouzon syndrome with acanthosis nigricans. *Nat Genet* 1995; **11**: 462-464 [PMID: 7493034 DOI: 10.1038/ng1295-462]

15 **Nagase T**, Nagase M, Hirose S, Ohmori K. Crouzon syndrome with acanthosis nigricans: case report and mutational analysis. *Cleft Palate Craniofac J* 2000; **37**: 78-82 [PMID: 10670894]

16 **Maloth S,** Padamashree S, Rema J, Yalsangi S, Ramadoss T, Kalladka M. Diagnosis of Crouzon's syndrome. *Hong Kong Dent J* 2010; **7**: 95-100

17 **Passos-Bueno MR**, Wilcox WR, Jabs EW, Sertié AL, Alonso LG, Kitoh H. Clinical spectrum of fibroblast growth factor receptor mutations. *Hum Mutat* 1999; **14**: 115-125 [PMID: 10425034]

18 **Pfeiffer RA**. [Dominant hereditary acrocephalosyndactylia]. *Z Kinderheilkd* 1964; **90**: 301-320 [PMID: 14316612 DOI: 10.1007/BF00447500]

19 **Kaplan LC**. Clinical assessment and multispecialty management of Apert syndrome. *Clin Plast Surg* 1991; **18**: 217-225 [PMID: 2065483]

20 **Vannier MW**, Hildebolt CF, Marsh JL, Pilgram TK, McAlister WH, Shackelford GD, Offutt CJ, Knapp RH. Craniosynostosis: diagnostic value of three-dimensional CT reconstruction. *Radiology* 1989; **173**: 669-673 [PMID: 2813770]

21 **Panigrahi I**. Craniosynostosis genetics: The mystery unfolds. *Indian J Hum Genet* 2011; **17**: 48-53 [PMID: 22090712 DOI: 10.4103/0971-6866.86171]

22 **Smartt JM**, Singh DJ, Reid RR, Hellinger JC, Hsu VM, Bartlett SP. Squamosal suture synostosis: a cause of atypical skull asymmetry. *Plast Reconstr Surg* 2012; **130**: 165-176 [PMID: 22418716 DOI: 10.1097/PRS.0b013e318254b271]

23 **Kawamoto HK**, Heller JB, Heller MM, Urrego A, Gabbay JS, Wasson KL, Bradley JP. Craniofrontonasal dysplasia: a surgical treatment algorithm. *Plast Reconstr Surg* 2007; **120**: 1943-1956 [PMID: 18090758 DOI: 10.1097/01.prs.0000287286.12944.9f]

24 **Clayman MA**, Murad GJ, Steele MH, Seagle MB, Pincus DW. History of craniosynostosis surgery and the evolution of minimally invasive endoscopic techniques: the University of Florida experience. *Ann Plast Surg* 2007; **58**: 285-287 [PMID: 17471133 DOI: 10.1097/01.sap.0000250846.12958.05]

25 **Kirmi O**, Lo SJ, Johnson D, Anslow P. Craniosynostosis: a radiological and surgical perspective. *Semin Ultrasound CT MR* 2009; **30**: 492-512 [PMID: 20099636 DOI: 10.1053/j.sult.2009.08.002]

26 **Shand JM**, Smith KS, Heggie AA. The role of distraction osteogenesis in the management of craniofacial syndromes. *Oral Maxillofac Surg Clin North Am* 2004; **16**: 525-540 [PMID: 18088752 DOI: 10.1016/j.coms.2004.07.004]

27 **Nout E**, Cesteleyn LL, van der Wal KG, van Adrichem LN, Mathijssen IM, Wolvius EB. Advancement of the midface, from conventional Le Fort III osteotomy to Le Fort III distraction: review of the literature. *Int J Oral Maxillofac Surg* 2008; **37**: 781-789 [PMID: 18486452 DOI: 10.1016/j.ijom.2008.04.006]

28 **Fearon JA**. Halo distraction of the Le Fort III in syndromic craniosynostosis: a long-term assessment. *Plast Reconstr Surg* 2005; **115**: 1524-1536 [PMID: 15861055 DOI: 10.1097/01.PRS.0000160271.08827.15]

29 **Yu JC**, Fearon J, Havlik RJ, Buchman SR, Polley JW. Distraction Osteogenesis of the Craniofacial Skeleton. *Plast Reconstr Surg* 2004; **114**: 1E-20E [PMID: 15220559 DOI: 10.1097/01.PRS.0000128965.52013.95]

30 **Fearon JA**. The Le Fort III osteotomy: to distract or not to distract? *Plast Reconstr Surg* 2001; **107**: 1091-1103; discussion 1104-1106 [PMID: 11373547 DOI: 10.1097/00006534-200104150-00001]

31 **Cedars MG**, Linck DL, Chin M, Toth BA. Advancement of the midface using distraction techniques. *Plast Reconstr Surg* 1999; **103**: 429-441 [PMID: 9950528 DOI: 10.1097/00006534-199902000-00010]

32 **Moore MH,** Abbott AH. Extradural deadspace after infant fronto-orbital advancement in Apert syndrome. *Cleft Palate Craniofac J* 1996; **33**: 202-205 [PMID: 8734719]

CASE REPORT

Aicardi syndrome: Neonatal diagnosis by means of transfontanellar ultrasound

Claudio Rodrigues Pires, Edward Araujo Júnior, Adriano Czapkowski, Sebastião Marques Zanforlin Filho

Claudio Rodrigues Pires, Edward Araujo Júnior, Adriano Czapkowski, Sebastião Marques Zanforlin Filho, Referral Center for Teaching of Diagnostic Imaging (CETRUS), São Paulo, SP 05303-000, Brazil

Author contributions: Pires CR contributed to design and data collection; Araujo Júnior E contributed to written of the article; Czapkowski A and Zanforlin Filho SM contributed to review this paper; Zanforlin Filho SM contributed to supervision this paper.

Correspondence to: Edward Araujo Júnior, PhD, Professor, Referral Center for Teaching of Diagnostic Imaging (CETRUS), Rua Carlos Weber, 956 apt. 113 Visage, São Paulo, SP 05303-000, Brazil. araujojred@terra.com.br
Telephone: +55-11-37965944 Fax: +55-11-37965944

Abstract

Aicardi syndrome is a rare genetic disease characterized by a characteristic classical trio of neurological clinical abnormalities (spasms), agenesis of the corpus callosum and ophthalmological abnormalities (chorioretinal lacunae). The diagnosis can be suspected by prenatal ultrasound with color Doppler identifying the agenesis of the corpus callosum. Usually, the diagnosis is confirmed in the neonate period by transfontanellar ultrasound and ophthalmological examination. We present a case of newborn with Aicardi syndrome, being the transfontanellar identified partial dysgenesis of the corpus callosum and a cyst in the inter-hemispheric fissure. Ophthalmological examination showed bilateral chorioretinal lacunae.

Key words: Aicardi syndrome; Neonate; Agenesis of the corpus callosum; Chorioretinal lacunae; Transfontanellar ultrasound

Core tip: Aicardi syndrome is a rare genetic disease characterized by a characteristic classical trio of neurological clinical abnormalities (spasms), agenesis of the corpus callosum and ophthalmological abnormalities (chorioretinal lacunae). The diagnosis can be suspected by prenatal ultrasound with color Doppler identifying the agenesis of the corpus callosum. Usually, the diagnosis is confirmed in the neonate period by transfontanellar ultrasound and ophthalmological examination. Tranfontanellar ultrasound is a cheap and affordable method, with similar accuracy of magnetic resonance imaging.

INTRODUCTION

Aicardi syndrome is a rare genetic disease that was described for the first time in 1965, by Aicardi *et al*[1], who studied 117 cases of spasms in infants and discovered eight new cases that comprised this syndrome. This syndrome is formed by a characteristic classical trio of neurological clinical abnormalities (spasms), agenesis of the corpus callosum and ophthalmological abnormalities (chorioretinal lacunae). Here, we describe a case of Aicardi syndrome diagnosed in the immediate postnatal period by means of transfontanellar ultrasonography, and illustrate the main abnormalities of this case.

CASE REPORT

A female newborn of gestational age 39 wk and Apgar score 8/9 started to show a condition of spasms in
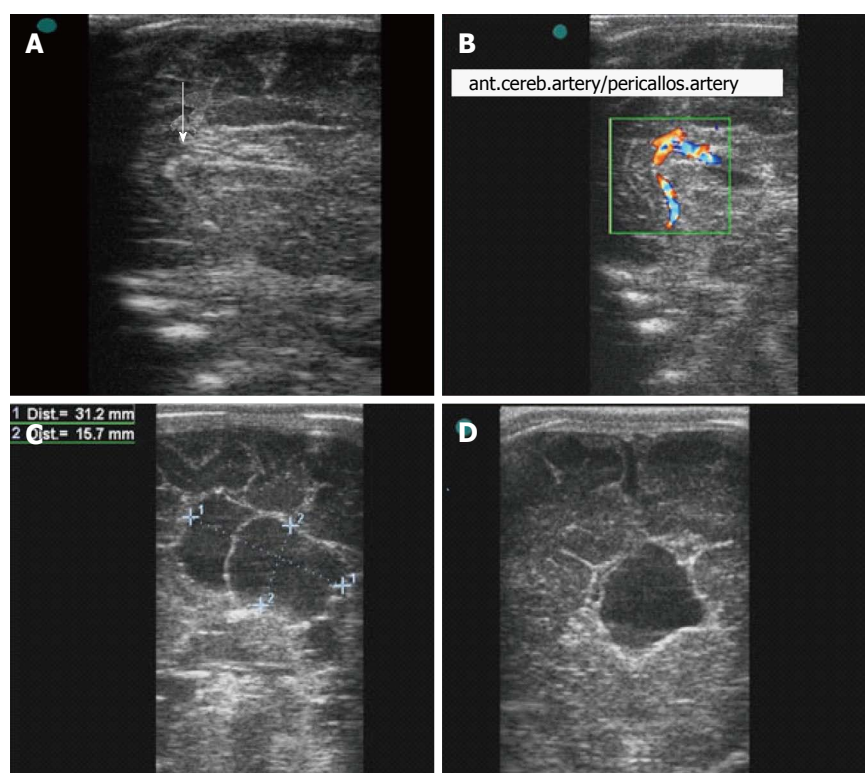
Figure 1 Transfontanellar ultrasonography.
A: In the sagittal plane, showing the knee of the corpus callosum (with arrow); the spleen and posterior segment were not observed; B: In the sagittal plane, showing partial agenesis of the corpus callosum with the aid of color Doppler on the pericallosal artery; C: In the parasagittal plane, showing a cyst in the inter-hemispherical fissure; D:In the coronal plane, showing a cyst in the inter-hemispherical fissure and porencephaly.

flexion, during the immediate postnatal period. Prenatal ultrasonographic examinations had not shown any alterations at the cephalic pole. Physical examination showed that the cranial circumference was at the lower limit of normality, and ophthalmological examination showed chorioretinal lacunae bilaterally (Figure 1A, B). The ultrasonographic examination was done using the Vivid 3 apparatus (General Electric Healthcare, Zipf, Austria), by means of a multifrequency linear transducer, through the anterior transfontanellar route. Partial dysgenesis of the corpus callosum was seen (Figure 1C, D), with a cyst in the inter-hemispheric fissure measuring 31.2 mm × 18.9 mm × 15.7 mm and porencephaly (Figure 2), without evidence of ventricular dilatation. No other encephalic morphological abnormalities were observed.

DISCUSSION

The majority of the cases of Aicardi syndrome have been reported in females, but two cases in males with 47,XXY karyotypes have also been observed. There is still no consensus regarding its etiology, but the most likely hypothesis is that it comes from a short-arm mutation linked to chromosome X, which presents in a heterozygous form in females and is lethal to males[2]. However, there are some evidences of genomic rearrangements involved in the etiology of Aicardi syndrome. Bursztejn *et al*[3] reported an 8-year-old girl with an initial diagnosis of Aicardi syndrome who subsequently found to carry a de novo 11.73-Mb terminal deletion of 1p36 chromosome band and emphasized the phenotypic overlap between the 2 disorders. Prontera *et al*[4] reported a case of a girl with 21-year-old presenting Aicardi syndrome with a 6q

deletion; 12q duplication, derived from a maternal 6q; 12q translocation. Spennato *et al*[5] described a case of a 36-year-old female patient, carrier of a 45,X0/46,XX mosaicism, showing a complex clinical picture including the signs of both Turner and Aicardi syndromes.

The most frequent neurological alterations, which start in the first year of life, include tonic convulsive or limited clonic spasms. The spasms are predominantly asymmetrical, with hemiparesis or hemiplegia on the side that is more affected. These spasms are usually the first manifestation for screening of Aicardi syndrome. The cranial circumference at birth may be within the limits of normality, although a certain degree of microcephaly may be observed[6].

Among the main ophthalmological abnormalities of Aicardi syndrome, choroidal filling defects of varying sizes, shapes, colors and location can be highlighted. Some characteristics are more frequently observed, such as peripapillary chorioretinal lacunae, of white color with rounded edges, although they can also be yellowish, pinkish and shiny, and can be multilobular. Other ophthalmological abnormalities that have been reported include: coloboma, detachment of the retina, hypoplasia of the optic nerve, macular scars, remnant pupil membranes, pseudoglioma, cataracts, retro-bulbar cysts, synechiae and microphthalmia[7]. Sutton *et al*[8] assessed the frequency of ophthalmologic finding of Aicardi syndrome in 20 girls. The most common findings were chorioretinal lacunae in 66 (88%) of 75 eyes and optic nerve abnormalities in 61 (81%) of 75 eyes. Other less common findings included persistent pupillary membrane in 4 (5%) of 79 eyes and anterior synechiae in 1 of 79 eyes (1%).

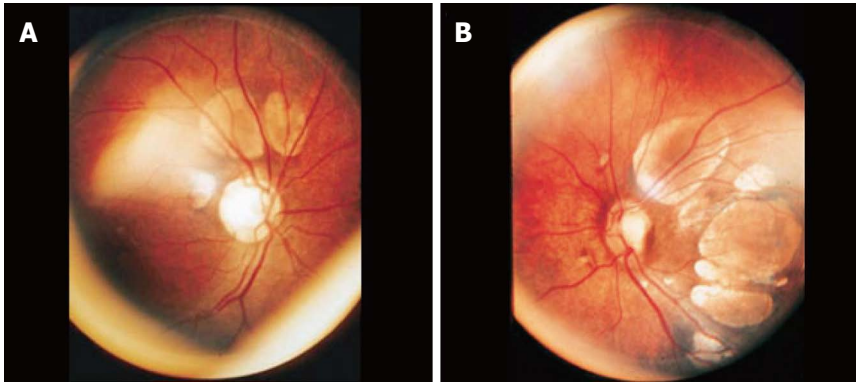Classical craniofacial features in Aicardi syndrome

Figure 2 Fundoscopy. A: Showing chorioretinal lacunae in the supra-papillary and temporal para-macular region; B: Showing chorioretinal lacunae at the posterior pole, including the macular area.

that have been described include a small philtrum with upturned nasal tip and decreased angle of the nasal bridge, big ears, prominent premaxilla and sparse eyebrows on lateral aspects, but these were not present in our case[8]. Skeletal anomalies such as fused vertebrae, hemi-vertebrae, blocked vertebrae and absent ribs could be present, which may lead to scoliosis[9].

Imaging diagnostic methods may reveal conditions ranging from classical findings like partial or total agenesis of the corpus callosum to other findings like ventricular dilatation, hydrocephaly and cortical heterotopy[10]. Dysgenesis of the corpus callosum may occur together with other midline abnormalities, such as Chiari II malformation, holoprosencephaly, Dandy-Walker malformation, septo-optic dysplasia and median facial cleft syndrome.

Magnetic resonance imaging (MRI) is the gold-standard examination for diagnosing this syndrome. In the largest study on Aicardi syndrome so far produced, 95% of the 23 patients (all the cases were female) presented frontal/perisylvian polymicrogyria and single or multiple intracranial cysts. These cysts were on the midline in 81% of the cases[10]. Hopkins *et al*[11] assessed the relationship between laterality of brain and ocular lesions in Aicardi syndrome. These authors assessed 26 subjects between 3 mo and 19 years old. Ocular and brain MRI asymmetry was found in 18% (4/22) and 58% (15/26) of subjects, respectively, with more right sided brain lesions than left. A significant correlation between sidedness of brain disease and microphthalmos was observed. Singh *et al*[12] described a case of Aicardi syndrome in a 4.5-mo-old baby. MRI revealed hypogenesis of the corpus callosum, polymicrogyria, interhemispheric cyst and periventricular nodular subependymal grey matter heterotopia along the body of the left lateral ventricle.

MRI is the imaging method used for confirming the diagnosis, although transfontanellar ultrasonography can also be chosen for screening, confirming the diagnosis and follow-up, with similar results. Ultrasound is relatively inexpensive and accessible; there are no contraindications and the images are obtained non-invasively.

In summary, we have presented a classical case of Aicardi syndrome that was diagnosed during the neonatal period by means of transfontanellar ultrasonography. This method may provide sufficient support for making an early diagnosis of this syndrome, without radioactive and anesthetic risks, as well as the facility of being performed on the hospital bed.

COMMENTS

Case characteristics
A female newborn of gestational age 39 wk and Apgar score 8/9 started to show a condition of spasms in flexion, during the immediate postnatal period.

Clinical diagnosis
Physical examination showed that the cranial circumference was at the lower limit of normality, and ophthalmological examination showed chorioretinal lacunae bilaterally.

Imaging diagnosis
Magnetic resonance imaging is the imaging method used for confirming the diagnosis.

Related reports
The majority of the cases of Aicardi syndrome have been reported in females, but two cases in males with 47,XXY karyotypes have also been observed.

Peer review
This paper is beneficial for the clinical practitioners. A systematic approach to find more compulsory information leads to provide more beneficial manuscript.

REFERENCES

1 **Aicardi J**, Levfebrve J, Lerique-Koechlin A. A new syndrome spasm in flexion, callosal agenesis, ocular abnormalities. *Electroencephalogr Clin Neurophysiol* 1965; **19**: 609-610

2 **Curatolo P**, Libutti G, Dallapiccola B. Aicardi syndrome in a male infant. *J Pediatr* 1980; **96**: 286-287 [PMID: 7351599 DOI: 10.1016/S0022-3476(80)80830-4]

3 **Bursztejn AC**, Bronner M, Peudenier S, Grégoire MJ, Jonveaux P, Nemos C. Molecular characterization of a monosomy 1p36 presenting as an Aicardi syndrome phenocopy. *Am J Med Genet A* 2009; **149A**: 2493-2500 [PMID: 19842196 DOI: 10.1002/ajmg.a.33051]

4 **Prontera P**, Bartocci A, Ottaviani V, Isidori I, Rogaia D, Ardisia C, Guercini G, Mencarelli A, Donti E. Aicardi syndrome associated with autosomal genomic imbalance: coincidence or evidence for autosomal inheritance with sex-limited expression? *Mol Syndromol* 2013; **4**: 197-202 [PMID: 23801936 DOI: 10.1159/000350040]

5 **Spennato P**, La Porta A, Varone A, Ruggiero C, Buono S, Cinalli G. Aicardi and Turner syndrome in a 45,X0/46,XX female. *Clin Neurol Neurosurg* 2013; **115**: 820-822 [PMID: 22898088 DOI: 10.1016/j.clineuro.2012.07.030]

6 **Aicardi J**. Aicardi syndrome. *Brain Dev* 2005; **27**: 164-171 [PMID: 15737696 DOI: 10.1016/j.braindev.2003.11.011]

7 **Costa PP**, Haas PC, Yamasoto E, Quilião ME. [Aicardi's syndrome: a description of two cases][Article in Portuguese]. *Arq Bras Oftalmol* 2004; **67**: 341-343 [DOI: 10.1590/

S0004-27492004000200028]

8   **Sutton VR**, Hopkins BJ, Eble TN, Gambhir N, Lewis RA, Van den Veyver IB. Facial and physical features of Aicardi syndrome: infants to teenagers. *Am J Med Genet A* 2005; **138A**: 254-258 [PMID: 16158440 DOI: 10.1002/ajmg.a.30963]

9   **Donnenfeld AE**, Packer RJ, Zackai EH, Chee CM, Sellinger B, Emanuel BS. Clinical, cytogenetic, and pedigree findings in 18 cases of Aicardi syndrome. *Am J Med Genet* 1989; **32**: 461-467 [PMID: 2773986 DOI: 10.1002/ajmg.1320320405]

10   **Fruhman G**, Eble TN, Gambhir N, Sutton VR, Van den Veyver IB, Lewis RA. Ophthalmologic findings in Aicardi syndrome. *J AAPOS* 2012; **16**: 238-241 [PMID: 22681940 DOI: 10.1016/j.jaapos.2012.01.008]

11   **Hopkins B**, Sutton VR, Lewis RA, Van den Veyver I, Clark G. Neuroimaging aspects of Aicardi syndrome. *Am J Med Genet A* 2008; **146A**: 2871-2878 [PMID: 18925666 DOI: 10.1002/ajmg.a.32537]

12   **Singh P**, Goraya JS, Saggar K, Ahluwalia A. Aicardi syndrome. *Singapore Med J* 2012; **53**: e153-e155 [PMID: 22815034]

CASE REPORT

Differentiation of true anophthalmia from clinical anophthalmia using neuroradiological imaging

Ali Riza Cenk Celebi, Hadi Sasani

Ali Riza Cenk Celebi, Ophthalmology Clinic, Republic of Turkey Ministry of Health, Nigde State Hospital, Nigde 51000, Turkey

Hadi Sasani, Department of Radiology, Florence Nightingale Hospital, Istanbul Bilim University, Istanbul 34394, Turkey

Author contributions: Celebi ARC prepared the manuscript; Sasani H edited the manuscript.

Correspondence to: Ali Riza Cenk Celebi, MD, Ophthalmology Clinic, Republic of Turkey Ministry of Health, Nigde State Hospital, Feridun Zeren Street, Nigde 51000, Turkey. arcenkcelebi@gmail.com

Telephone: +90-388-2210020 Fax: +90-388-2322220
Received: March 30, 2014   Revised: May 9, 2014
Accepted: June 18, 2014
Published online: July 28, 2014

Abstract

Anophthalmia is a condition of the absence of an eye and the presence of a small eye within the orbit. It is associated with many known syndromes. Clinical findings, as well as imaging modalities and genetic analysis, are important in making the diagnosis. Imaging modalities are crucial scanning methods. Cryptophthalmos, cyclopia, synophthalmia and congenital cystic eye should be considered in differential diagnoses. We report two clinical anophthalmic siblings, emphasizing the importance of neuroradiological and orbital imaging findings in distinguishing true congenital anophthalmia from clinical anophthalmia.

Core tip: Anophthalmia is a condition of the absence of an eye and the presence of a small eye within the orbit. Imaging modalities and genetic analysis are crucial for correct diagnosis and differential diagnosis. In this article, two clinical anophthalmic siblings cases are reported, emphasizing the importance of neuroradiological and orbital imaging findings in distinguishing true congenital anophthalmia from clinical anophthalmia. Anophthalmia is associated with many known syndromes. Clinical findings, as well as imaging modalities and genetic analysis, are important in making the diagnosis. Imaging modalities are crucial scanning methods. Cryptophthalmos, cyclopia, synophthalmia and congenital cystic eye should be considered in differential diagnoses. We report two clinical anophthalmic siblings, emphasizing the importance of neuroradiological and orbital imaging findings in distinguishing true congenital anophthalmia from clinical anophthalmia.

Celebi ARC, Sasani H. Differentiation of true anophthalmia from clinical anophthalmia using neuroradiological imaging. *World J Radiol* 2014; 6(7): 515-518 Available from: URL: http://www.wjgnet.com/1949-8470/full/v6/i7/515.htm DOI: http://dx.doi.org/10.4329/wjr.v6.i7.515

INTRODUCTION

The prevalence of congenital anophthalmia ranges from 3 to 14 per 100000 population. It is the result of insufficient development or complete regression of the optic vesicle[1]. However, it is always confused with the term clinical anophthalmia or severe microphthalmia. It is clinically difficult to distinguish severe microphthalmia from anophthalmia in routine ophthalmology practice. Small conjunctival fornices, narrowed palpebral fissure range and common hypoplasia of the periocular soft tissues frequently accompany microphthalmia or anophthalmia. Microphthalmia refers to reduction in the size of the globe because of the congenital developmental disorder or acquired causes. Microphthalmia is classified as severe, simple and complex depending on the anatomical

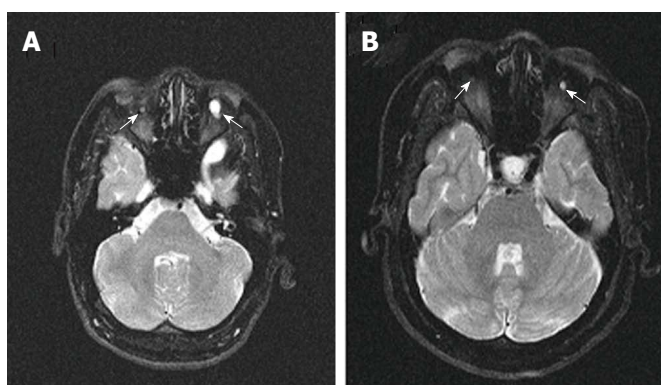**Figure 1 Clinical appearance of siblings.**

Figure 2 Axial fat-suppressed T2-weighted magnetic resonance imaging. A: Axial fat-suppressed T2-weighted magnetic resonance imaging (MRI) of the male patient showed bilateral cystic structures that are synonymous with rudimentary eyeballs (white arrows); B: Axial fat-suppressed T2-weighted MRI of the female patient showed bilateral cystic structures that are synonymous with rudimentary eyeballs (white arrows).
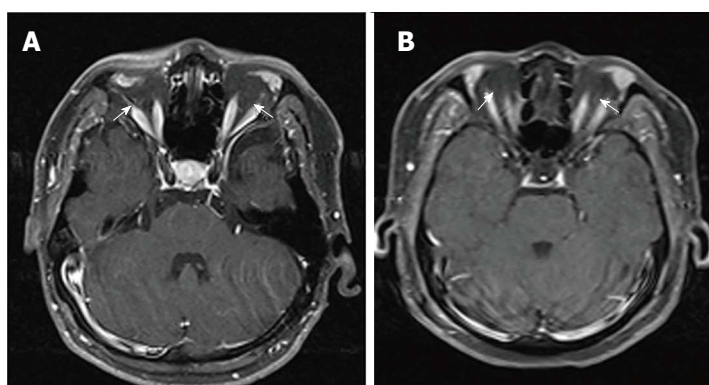

Figure 3 Post-contrast fat-suppressed T1-weighted axial magnetic resonance imaging of each patient show bilateral hypoplastic optic nerves between extraocular muscle groups (white arrows).

appearance of the globe and the degree of reduction in the axial length. Severe microphthalmia is a considerable reduction in the size of the globe in terms of total axial length at birth under 10 mm or under 12 mm after 1 year of age[2].

CASE REPORT

Two siblings, one a 27-year-old male (Figure 1A) and the other a 40-year-old female (Figure 1B), with anophthalmia attended the ophthalmology clinic. They were 2 of 9 siblings in a family. There was no consanguinity between their dead parents and the other siblings did not have anophthalmia or microphthalmia. Systematic physical examination and laboratory workup, including thoracoabdominal magnetic resonance imaging (MRI), were normal and the two siblings were considered to have isolated anophthalmia. Brain MRI was performed to exclude any accompanying central nervous system malformation. T1-weighted images (WI), T2-WI and post-contrast T1-WI were obtained at axial, sagittal and coronal planes. Orbital MRI was also performed to show intraorbital structures. In both cases, the globes were found to be quite small and cystic in appearance. Cornea, lens and sclera were not observed (Figure 2). Axial length of the globe was 4 mm on the right and 11 mm on the left of 27-year-old male (Figure 2A) and in the 40-year-old female, the right globe was 2 mm and the left globe was 4 mm (Figure 2B). Although both optic nerves were hypoplastic in the intraconal orbital space, the optic nerves were not found at the distal optic canal in both patients (Figure 3). In these two cases, the lacrimal glands, extraocular muscles and the eyelids were observed. Brain MRI did not show any accompanying central nervous system abnormality.

DISCUSSION

The spectrum of clinical anophthalmia includes severe microphthalmia, in which a small amount of ocular tissue can be found in the orbit on neuroimaging, even although the globe may appear to be absent externally[3]. Once the diagnosis has been established, systematic examination with both ocular and systemic imaging tests (ultrasonography, computed tomography, MRI) should be performed to rule out additional neurological, renal, cardiac or other associations[2]. Cases associated with other congenital systemic abnormalities have been reported in many syndromes, such as Fraser, Fryns, Waardenburg or Matthew-Wood[4]. Many microphthalmia patients have additional congenital ocular anomalies and associated neurological abnormalities[5]. A study conducted by Jacquemin *et al*[6] concluded that patients with clinical anophthalmia share a similar constellation of neurological, somatic and neuroradiological abnormalities as patients with microphthalmia. However, Schittkowski *et al*[7] mentioned that anophthalmia is a poorer prognostic factor than microphthalmia in terms of its association with a wide range of systemic diseases and they also described that patients with bilateral anophthalmia are characterized mainly by additional intracranial anomalies. Brunquell *et al*[8] described a case of anophthalmia in which severe developmental disorders and locomotor defects were recognized.

Albernaz *et al*[9] reported imaging findings of a clinical anophthalmia case series in which there were a variety of intraorbital, intracranial and craniofacial anomalies. The high rate of intracranial anomalies in their patients with bilateral anophthalmia suggests overall maldevelopment of the forebrain structures and failure of formation or degeneration of the optic vesicles during early gestation. MR imaging of anophthalmia cases showed amorphous tissues of isointense signal intensity with muscle on T1-WI and markedly hypointense on T2-WI. The imaging characteristics were probably due to fibrosis. These imaging features provide distinction of anophthalmia from severe microphthalmia, which is a condition of identifying a tiny globe with the normal signal intensity of the vitreous and lens[9].

However, in both of our case series, there was no syndromic condition present. Orbital and brain MRI helped us to discern the cases to be clinical anophthalmia or true anophthalmia without the need of histopathological studies. In our patients there was a bilateral hypoplastic optic nerve in the intraconal orbital space. The optic nerve was not found at the distal optic canal in both patients. There were no other central nervous system abnormalities in the brain MRI, including the posterior visual pathways. The signal intensities of rudimentary eyeballs were hypointense on T1-WI and iso-hyperintense on T2-WI due to their contents.

For depiction of the rudimentary optic nerves, optic tracts and intraorbital contents, as well as concomitant intracranial pathologies such as partial agenesis of the corpus callosum and microgyria, MRI is superior to CT[10].

In summary, we believe that the findings of orbital and brain MRI in patients diagnosed with anophthalmia has an important role in diagnosis and differentiation of cases as true anophthalmia or clinical anophthalmia.

COMMENTS

Background
This manuscript reported two clinical anophthalmic siblings and emphasized the importance of neuroradiological imaging findings in distinguishing true congenital anophthalmia from clinical anophthalmia.

Research frontiers
The main limitation of the study is its nature of being a case report. More comprehensive clinical studies with anophthalmic patients are needed to emphasize the importance of neuroradiological imaging.

Innovations and breakthroughs
Anophthalmia without any systemic manifestations can be seen. Clinicians must cooperate with radiologists in cases of anophthalmia, whether true anophthalmia or severe microphthalmia.

Applications
Clinicians are strongly advised to investigate for systemic abnormalities in cases of anophthalmia. Neuroradiological imaging has an important role in diagnosing central nervous system associations with anophthalmia.

Terminology
Anophthalmia is the result of insufficient development or complete regression of the optic vesicle.

Peer review
The manuscript presents a rare case of two siblings with anophthalmia, demonstrating the importance of neuroradiological imaging in making the diagnosis and differentiating the case as true anophthalmia or clinical anophthalmia. It also provides a literature review regarding the intraorbital, intracranial and craniofacial anomalies associated with anophthalmia.

REFERENCES

1   **Verma AS**, Fitzpatrick DR. Anophthalmia and microphthalmia. *Orphanet J Rare Dis* 2007; **2**: 47 [PMID: 18039390 DOI: 10.1186/1750-1172-2-47]
2   **Mafee MF.** Section 2 Eye and Orbit Part 1 The Eye Pathology Congenital Anomalies. In: Mafee MF, Valvassori GE, Becker M, editors. Imaging of the Head and Neck. New York: Thieme, 2005: 146-147
3   **O'Keefe M**, Webb M, Pashby RC, Wagman RD. Clinical anophthalmos. *Br J Ophthalmol* 1987; **71**: 635-638 [PMID: 3651379 DOI: 10.1136/bjo.71.8.635]
4   **Makhoul IR**, Soudack M, Kochavi O, Guilburd JN, Maimon S, Gershoni-Baruch R. Anophthalmia-plus syndrome: a clinical report and review of the literature. *Am J Med Genet A* 2007; **143**: 64-68 [PMID: 17152069]
5   **Tucker S**, Jones B, Collin R. Systemic anomalies in 77 patients with congenital anophthalmos or microphthalmos. *Eye* (Lond) 1996; **10** (Pt 3): 310-314 [PMID: 8796154 DOI: 10.1038/eye.1996.65]
6   **Jacquemin C**, Mullaney PB, Bosley TM. Ophthalmological and intracranial anomalies in patients with clinical anophthalmos. *Eye* (Lond) 2000; **14** (Pt 1): 82-87 [PMID: 10755107 DOI: 10.1038/eye.2000.18]
7   **Schittkowski MP**, Guthoff RF. Systemic and ophthalmological anomalies in congenital anophthalmic or microphthalmic patients. *Br J Ophthalmol* 2010; **94**: 487-493 [PMID: 19822908 DOI: 10.1136/bjo.2009.163436]
8   **Brunquell PJ**, Papale JH, Horton JC, Williams RS, Zgrabik MJ, Albert DM, Hedley-Whyte ET. Sex-linked hereditary bilateral anophthalmos. Pathologic and radiologic correlation.

Arch Ophthalmol 1984; **102**: 108-113 [PMID: 6538407 DOI: 10.1001/archopht.1984.01040030092044]

9   **Albernaz VS**, Castillo M, Hudgins PA, Mukherji SK. Imaging findings in patients with clinical anophthalmos. *AJNR*

Am J Neuroradiol 1997; **18**: 555-561 [PMID: 9090423]

10   **Daxecker F**, Felber S. Magnetic resonance imaging features of congenital anophthalmia. *Ophthalmologica* 1993; **206**: 139-142 [PMID: 8272336 DOI: 10.1159/000310379]
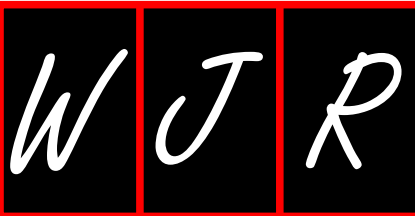
INSTRUCTIONS TO AUTHORS

GENERAL INFORMATION

World Journal of Radiology (*World J Radiol*, *WJR*, online ISSN 1949-8470, DOI: 10.4329) is a peer-reviewed open access (OA) academic journal that aims to guide clinical practice and improve diagnostic and therapeutic skills of clinicians.

Aim and scope

WJR covers topics concerning diagnostic radiology, radiation oncology, radiologic physics, neuroradiology, nuclear radiology, pediatric radiology, vascular/interventional radiology, medical imaging achieved by various modalities and related methods analysis. The current columns of *WJR* include editorial, frontier, diagnostic advances, therapeutics advances, field of vision, mini-reviews, review, topic highlight, medical ethics, original articles, case report, clinical case conference (clinicopathological conference), and autobiography.

We encourage authors to submit their manuscripts to *WJR*. We will give priority to manuscripts that are supported by major national and international foundations and those that are of great basic and clinical significance.

WJR is edited and published by Baishideng Publishing Group (BPG). BPG has a strong professional editorial team composed of science editors, language editors and electronic editors. BPG currently publishes 43 OA clinical medical journals, including 42 in English, has a total of 15471 editorial board members or peer reviewers, and is a world first-class publisher.

Columns

The columns in the issues of *WJR* will include: (1) Editorial: The editorial board members are invited to make comments on an important topic in their field in terms of its current research status and future directions to lead the development of this discipline; (2) Frontier: The editorial board members are invited to select a highly cited cutting-edge original paper of his/her own to summarize major findings, the problems that have been resolved and remain to be resolved, and future research directions to help readers understand his/her important academic point of view and future research directions in the field; (3) Diagnostic Advances: The editorial board members are invited to write high-quality diagnostic advances in their field to improve the diagnostic skills of readers. The topic covers general clinical diagnosis, differential diagnosis, pathological diagnosis, laboratory diagnosis, imaging diagnosis, endoscopic diagnosis, biotechnological diagnosis, functional diagnosis, and physical diagnosis; (4) Therapeutics Advances: The editorial board members are invited to write high-quality therapeutic advances in their field to help improve the therapeutic skills of readers. The topic covers medication therapy, psychotherapy, physical therapy, replacement therapy, interventional therapy, minimally invasive therapy, endoscopic therapy, transplantation therapy, and surgical therapy; (5) Field of Vision: The editorial board members are invited to write commentaries on classic articles, hot topic articles, or latest articles to keep readers at the forefront of research and increase their levels of clinical research. Classic articles refer to papers that are included in Web of Knowledge and have received a large number of citations (ranking in the top 1%) after being published for more than years, reflecting the quality and impact of papers. Hot topic articles refer to papers that are included in Web of Knowledge and have received a large number of citations after being published for no more than 2 years, reflecting cutting-edge trends in scientific research. Latest articles refer to the latest published high-quality papers that are included in PubMed, reflecting the latest research trends. These commentary articles should focus on the status quo of research, the most important research topics, the problems that have now been resolved and remain to be resolved, and future research directions. Basic information about the article to be commented (including authors, article title, journal name, year, volume, and inclusive page numbers); (6) Minireviews: The editorial board members are invited to write short reviews on recent advances and trends in research of molecular biology, genomics, and related cutting-edge technologies to provide readers with the latest knowledge and help improve their diagnostic and therapeutic skills; (7) Review: To make a systematic review to focus on the status quo of research, the most important research topics, the problems that have now been resolved and remain to be resolved, and future research directions; (8) Topic Highlight: The editorial board members are invited to write a series of articles (7-10 articles) to comment and discuss a hot topic to help improve the diagnostic and therapeutic skills of readers; (9) Medical Ethics: The editorial board members are invited to write articles about medical ethics to increase readers' knowledge of medical ethics. The topic covers international ethics guidelines, animal studies, clinical trials, organ transplantation, *etc.*; (10) Clinical Case Conference or Clinicopathological Conference: The editorial board members are invited to contribute high-quality clinical case conference; (11) Original Articles: To report innovative and original findings in radiology; (12) Research Report: To briefly report the novel and innovative findings in radiology; (13) Meta-Analysis: Covers the systematic review, mixedtreatment comparison, meta-regression, and overview of reviews, in order to summarize a given quantitative effect, *e.g.*, the clinical effectiveness and safety of clinical treatments by combining data from two or more randomized controlled trials, thereby providing more precise and externally valid estimates than those which would stem from each individual dataset if analyzed separately from the others; (15) Letters to the Editor: To discuss and make reply to the contributions published in *WJR*, or to introduce and comment on a controversial issue of general interest; (16) Book Reviews: To introduce and comment on quality monographs of radiology; and (17) Autobiography: The editorial board members are invited to write their autobiography to provide readers with stories of success or failure in their scientific research career. The topic covers their basic personal information and information about when they started doing research work, where and how they did research work, what they have achieved, and their lessons from success or failure.

Name of journal

World Journal of Radiology

ISSN

ISSN 1949-8470 (online)

Launch date

December 31, 2009

Frequency

Monthly

Editor-in-Chief

Kai U Juergens, MD, Associate Professor, MRT und PET/CT, Nuklearmedizin Bremen Mitte, ZEMODI - Zentrum für morpholo-

gische und molekulare Diagnostik, Bremen 28177, Germany

Edwin JR van Beek, MD, PhD, Professor, Clinical Research Imaging Centre and Department of Medical Radiology, University of Edinburgh, Edinburgh EH16 4TJ, United Kingdom

Thomas J Vogl, MD, Professor, Reader in Health Technology Assessment, Department of Diagnostic and Interventional Radiology, Johann Wolfgang Goethe University of Frankfurt, Frankfurt 60590, Germany

SPECIAL STATEMENT
All articles published in journals owned by the BPG represent the views and opinions of their authors, and not the views, opinions or policies of the BPG, except where otherwise explicitly indicated.

Biostatistical editing
Statisital review is performed after peer review. We invite an expert in Biomedical Statistics to evaluate the statistical method used in the paper, including *t*-test (group or paired comparisons), chi-squared test, Ridit, probit, logit, regression (linear, curvilinear, or stepwise), correlation, analysis of variance, analysis of covariance, *etc*. The reviewing points include: (1) Statistical methods should be described when they are used to verify the results; (2) Whether the statistical techniques are suitable or correct; (3) Only homogeneous data can be averaged. Standard deviations are preferred to standard errors. Give the number of observations and subjects (*n*). Losses in observations, such as drop-outs from the study should be reported; (4) Values such as ED50, LD50, IC50 should have their 95% confidence limits calculated and compared by weighted probit analysis (Bliss and Finney); and (5) The word 'significantly' should be replaced by its synonyms (if it indicates extent) or the *P* value (if it indicates statistical significance).

Conflict-of-interest statement
In the interests of transparency and to help reviewers assess any potential bias, *WJR* requires authors of all papers to declare any competing commercial, personal, political, intellectual, or religious interests in relation to the submitted work. Referees are also asked to indi-cate any potential conflict they might have reviewing a particular paper. Before submitting, authors are suggested to read "Uniform Requirements for Manuscripts Submitted to Biomedical Journals: Ethical Considerations in the Conduct and Reporting of Research: Conflicts of Interest" from International Committee of Medical Journal Editors (ICMJE), which is available at: http://www.icmje.org/ethical_4conflicts.html.

Sample wording: [Name of individual] has received fees for serving as a speaker, a consultant and an advisory board member for [names of organizations], and has received research funding from [names of organization]. [Name of individual] is an employee of [name of organization]. [Name of individual] owns stocks and shares in [name of organization]. [Name of individual] owns patent [patent identification and brief description].

Statement of informed consent
Manuscripts should contain a statement to the effect that all human studies have been reviewed by the appropriate ethics committee or it should be stated clearly in the text that all persons gave their informed consent prior to their inclusion in the study. Details that might disclose the identity of the subjects under study should be omitted. Authors should also draw attention to the Code of Ethics of the World Medical Association (Declaration of Helsinki, 1964, as revised in 2004).

Statement of human and animal rights
When reporting the results from experiments, authors should follow the highest standards and the trial should conform to Good Clinical Practice (for example, US Food and Drug Administration Good Clinical Practice in FDA-Regulated Clinical Trials; UK Medicines Research Council Guidelines for Good Clinical Practice in Clinical Trials) and/or the World Medical Association Declaration of Helsinki. Generally, we suggest authors follow the lead investigator's national standard. If doubt exists whether the research was conducted in accordance with the above standards, the authors must explain the rationale for their approach and demonstrate that the institutional review body explicitly approved the doubtful aspects of the study.

Before submitting, authors should make their study approved by the relevant research ethics committee or institutional review board. If human participants were involved, manuscripts must be accompanied by a statement that the experiments were undertaken with the understanding and appropriate informed consent of each. Any personal item or information will not be published without explicit consents from the involved patients. If experimental animals were used, the materials and methods (experimental procedures) section must clearly indicate that appropriate measures were taken to minimize pain or discomfort, and details of animal care should be provided.

SUBMISSION OF MANUSCRIPTS
Manuscripts should be typed in 1.5 line spacing and 12 pt. Book Antiqua with ample margins. Number all pages consecutively, and start each of the following sections on a new page: Title Page, Abstract, Introduction, Materials and Methods, Results, Discussion, Acknowledgements, References, Tables, Figures, and Figure Legends. Neither the editors nor the publisher are responsible for the opinions expressed by contributors. Manuscripts formally accepted for publication become the permanent property of BPG, and may not be reproduced by any means, in whole or in part, without the written permission of both the authors and the publisher. We reserve the right to copy-edit and put onto our website accepted manuscripts. Authors should follow the relevant guidelines for the care and use of laboratory animals of their institution or national animal welfare committee. For the sake of transparency in regard to the performance and reporting of clinical trials, we endorse the policy of the ICMJE to refuse to publish papers on clinical trial results if the trial was not recorded in a publicly-accessible registry at its outset. The only register now available, to our knowledge, is http://www.clinicaltrials.gov sponsored by the United States National Library of Medicine and we encourage all potential contributors to register with it. However, in the case that other registers

become available you will be duly notified. A letter of recommendation from each author's organization should be provided with the contributed article to ensure the privacy and secrecy of research is protected.

Authors should retain one copy of the text, tables, photographs and illustrations because rejected manuscripts will not be returned to the author(s) and the editors will not be responsible for loss or damage to photographs and illustrations sustained during mailing.

Online submissions

Manuscripts should be submitted through the Online Submission System at: http://www.wjgnet.com/esps/. Authors are highly recommended to consult the ONLINE INSTRUCTIONS TO AUTHORS (http://www.wjgnet.com/1948-5204/g_info_20100312180518.htm) before attempting to submit online. For assistance, authors encountering problems with the Online Submission System may send an email describing the problem to bpgoffice@wjgnet.com, or by telephone: +86-10-85381891. If you submit your manuscript online, do not make a postal contribution. Repeated online submission for the same manuscript is strictly prohibited.

MANUSCRIPT PREPARATION

All contributions should be written in English. All articles must be submitted using word-processing software. All submissions must be typed in 1.5 line spacing and 12 pt. Book Antiqua with ample margins. Style should conform to our house format. Required information for each of the manuscript sections is as follows:

Title page

Title: Title should be less than 12 words.

Running title: A short running title of less than 6 words should be provided.

Authorship: Authorship credit should be in accordance with the standard proposed by International Committee of Medical Journal Editors, based on (1) substantial contributions to conception and design, acquisition of data, or analysis and interpretation of data; (2) drafting the article or revising it critically for important intellectual content; and (3) final approval of the version to be published. Authors should meet conditions 1, 2, and 3.

Institution: Author names should be given first, then the complete name of institution, city, province and postcode. For example, Xu-Chen Zhang, Li-Xin Mei, Department of Pathology, Chengde Medical College, Chengde 067000, Hebei Province, China. One author may be represented from two institutions, for example, George Sgourakis, Department of General, Visceral, and Transplantation Surgery, Essen 45122, Germany; George Sgourakis, 2nd Surgical Department, Korgialenio-Benakio Red Cross Hospital, Athens 15451, Greece

Author contributions: The format of this section should be: Author contributions: Wang CL and Liang L contributed equally to this work; Wang CL, Liang L, Fu JF, Zou CC, Hong F and Wu XM designed the research; Wang CL, Zou CC, Hong F and Wu XM performed the research; Xue JZ and Lu JR contributed new reagents/analytic tools; Wang CL, Liang L and Fu JF analyzed the data; and Wang CL, Liang L and Fu JF wrote the paper.

Supportive foundations: The complete name and number of supportive foundations should be provided, e.g. Supported by National Natural Science Foundation of China, No. 30224801

Correspondence to: Only one corresponding address should be provided. Author names should be given first, then author title, affiliation, the complete name of institution, city, postcode, province, country, and email. All the letters in the email should be in lower case. A space interval should be inserted between country name and email address. For example, Montgomery Bissell, MD, Professor of Medi-

cine, Chief, Liver Center, Gastroenterology Division, University of California, Box 0538, San Francisco, CA 94143, United States. montgomery.bissell@ucsf.edu

Telephone and fax: Telephone and fax should consist of +, country number, district number and telephone or fax number, e.g. Telephone: +86-10-85381891 Fax: +86-10-85381893

Peer reviewers: All articles received are subject to peer review. Normally, three experts are invited for each article. Decision on acceptance is made only when at least two experts recommend publication of an article. All peer-reviewers are acknowledged on Express Submission and Peer-review System website.

Abstract

There are unstructured abstracts (no less than 200 words) and structured abstracts. The specific requirements for structured abstracts are as follows:

An informative, structured abstract should accompany each manuscript. Abstracts of original contributions should be structured into the following sections: AIM (no more than 20 words; Only the purpose of the study should be included. Please write the Aim in the form of "To investigate/study/…"), METHODS (no less than 140 words for Original Articles; and no less than 80 words for Brief Articles), RESULTS (no less than 150 words for Original Articles and no less than 120 words for Brief Articles; You should present P values where appropriate and must provide relevant data to illustrate how they were obtained, e.g. 6.92 ± 3.86 vs 3.61 ± 1.67, $P < 0.001$), and CONCLUSION (no more than 26 words).

Key words

Please list 5-10 key words, selected mainly from *Index Medicus*, which reflect the content of the study.

Core tip

Please write a summary of less than 100 words to outline the most innovative and important arguments and core contents in your paper to attract readers.

Text

For articles of these sections, original articles and brief articles, the main text should be structured into the following sections: INTRODUCTION, MATERIALS AND METHODS, RESULTS and DISCUSSION, and should include appropriate Figures and Tables. Data should be presented in the main text or in Figures and Tables, but not in both. The main text format of these sections, editorial, topic highlight, case report, letters to the editors, can be found at: http://www.wjgnet.com/1948-5204/g_info_list.htm.

Illustrations

Figures should be numbered as 1, 2, 3, *etc*., and mentioned clearly in the main text. Provide a brief title for each figure on a separate page. Detailed legends should not be provided under the figures. This part should be added into the text where the figures are applicable. Keeping all elements compiled is necessary in line-art image. Scale bars should be used rather than magnification factors, with the length of the bar defined in the legend rather than on the bar itself. File names should identify the figure and panel. Avoid layering type directly over shaded or textured areas. Please use uniform legends for the same subjects. For example: Figure 1 Pathological changes in atrophic gastritis after treatment. A: ...; B: ...; C: ...; D: ...; E: ...; F: ...; G: …*etc*. It is our principle to publish high resolution-figures for the E-versions.

Tables

Three-line tables should be numbered 1, 2, 3, *etc*., and mentioned clearly in the main text. Provide a brief title for each table. Detailed legends should not be included under tables, but rather added into the text where applicable. The information should complement, but not duplicate the text. Use one horizontal line under the title, a second under column heads, and a third below the Table, above any footnotes. Vertical and italic lines should be omitted.

Notes in tables and illustrations

Data that are not statistically significant should not be noted. $^{a}P < 0.05$, $^{b}P < 0.01$ should be noted ($P > 0.05$ should not be noted). If there are other series of P values, $^{c}P < 0.05$ and $^{d}P < 0.01$ are used. A third series of P values can be expressed as $^{e}P < 0.05$ and $^{f}P < 0.01$. Other notes in tables or under illustrations should be expressed as ^{1}F, ^{2}F, ^{3}F; or sometimes as other symbols with a superscript (Arabic numerals) in the upper left corner. In a multi-curve illustration, each curve should be labeled with ●, ○, ■, □, ▲, △, *etc.*, in a certain sequence.

Acknowledgments

Brief acknowledgments of persons who have made genuine contributions to the manuscript and who endorse the data and conclusions should be included. Authors are responsible for obtaining written permission to use any copyrighted text and/or illustrations.

REFERENCES

Coding system

The author should number the references in Arabic numerals according to the citation order in the text. Put reference numbers in square brackets in superscript at the end of citation content or after the cited author's name. For citation content which is part of the narration, the coding number and square brackets should be typeset normally. For example, "Crohn's disease (CD) is associated with increased intestinal permeability[1,2]". If references are cited directly in the text, they should be put together within the text, for example, "From references[19,22-24], we know that..."

When the authors write the references, please ensure that the order in text is the same as in the references section, and also ensure the spelling accuracy of the first author's name. Do not list the same citation twice.

PMID and DOI

Pleased provide PubMed citation numbers to the reference list, e.g. PMID and DOI, which can be found at http://www.ncbi.nlm.nih.gov/sites/entrez?db=pubmed and http://www.crossref.org/SimpleTextQuery/, respectively. The numbers will be used in E-version of this journal.

Style for journal references

Authors: the name of the first author should be typed in bold-faced letters. The family name of all authors should be typed with the initial letter capitalized, followed by their abbreviated first and middle initials. (For example, Lian-Sheng Ma is abbreviated as Ma LS, Bo-Rong Pan as Pan BR). The title of the cited article and italicized journal title (journal title should be in its abbreviated form as shown in PubMed), publication date, volume number (in black), start page, and end page [PMID: 11819634   DOI: 10.3748/wjg.13.5396].

Style for book references

Authors: the name of the first author should be typed in bold-faced letters. The surname of all authors should be typed with the initial letter capitalized, followed by their abbreviated middle and first initials. (For example, Lian-Sheng Ma is abbreviated as Ma LS, Bo-Rong Pan as Pan BR) Book title. Publication number. Publication place: Publication press, Year: start page and end page.

Format

Journals

English journal article (list all authors and include the PMID where applicable)

1   **Jung EM**, Clevert DA, Schreyer AG, Schmitt S, Rennert J, Kubale R, Feuerbach S, Jung F. Evaluation of quantitative contrast harmonic imaging to assess malignancy of liver tumors: A prospective controlled two-center study. *World J Gastroenterol* 2007; **13**: 6356-6364 [PMID: 18081224   DOI: 10.3748/wjg.13.6356]

Chinese journal article (list all authors and include the PMID where applicable)

2   **Lin GZ**, Wang XZ, Wang P, Lin J, Yang FD. Immunologic effect of Jianpi Yishen decoction in treatment of Pixu-diarrhoea.

Shijie Huaren Xiaohua Zazhi 1999; **7**: 285-287

In press

3   **Tian D**, Araki H, Stahl E, Bergelson J, Kreitman M. Signature of balancing selection in Arabidopsis. *Proc Natl Acad Sci USA* 2006; In press

Organization as author

4   **Diabetes Prevention Program Research Group**. Hypertension, insulin, and proinsulin in participants with impaired glucose tolerance. *Hypertension* 2002; **40**: 679-686 [PMID: 12411462 DOI:10.1161/01.HYP.0000035706.28494.09]

Both personal authors and an organization as author

5   **Vallancien G**, Emberton M, Harving N, van Moorselaar RJ; Alf-One Study Group. Sexual dysfunction in 1, 274 European men suffering from lower urinary tract symptoms. *J Urol* 2003; **169**: 2257-2261 [PMID: 12771764   DOI:10.1097/01.ju.0000067940.76090.73]

No author given

6   21st century heart solution may have a sting in the tail. *BMJ* 2002; **325**: 184 [PMID: 12142303   DOI:10.1136/bmj.325.7357.184]

Volume with supplement

7   **Geraud G**, Spierings EL, Keywood C. Tolerability and safety of frovatriptan with short- and long-term use for treatment of migraine and in comparison with sumatriptan. *Headache* 2002; **42** Suppl 2: S93-99 [PMID: 12028325   DOI:10.1046/j.1526-4610.42.s2.7.x]

Issue with no volume

8   **Banit DM**, Kaufer H, Hartford JM. Intraoperative frozen section analysis in revision total joint arthroplasty. *Clin Orthop Relat Res* 2002; (**401**): 230-238 [PMID: 12151900   DOI:10.1097/00003086-200208000-00026]

No volume or issue

9   Outreach: Bringing HIV-positive individuals into care. *HRSA Careaction* 2002; 1-6 [PMID: 12154804]

Books

Personal author(s)

10   **Sherlock S**, Dooley J. Diseases of the liver and billiary system. 9th ed. Oxford: Blackwell Sci Pub, 1993: 258-296

Chapter in a book (list all authors)

11   **Lam SK**. Academic investigator's perspectives of medical treatment for peptic ulcer. In: Swabb EA, Azabo S. Ulcer disease: investigation and basis for therapy. New York: Marcel Dekker, 1991: 431-450

Author(s) and editor(s)

12   **Breedlove GK**, Schorfheide AM. Adolescent pregnancy. 2nd ed. Wieczorek RR, editor. White Plains (NY): March of Dimes Education Services, 2001: 20-34

Conference proceedings

13   **Harnden P**, Joffe JK, Jones WG, editors. Germ cell tumours V. Proceedings of the 5th Germ cell tumours Conference; 2001 Sep 13-15; Leeds, UK. New York: Springer, 2002: 30-56

Conference paper

14   **Christensen S**, Oppacher F. An analysis of Koza's computational effort statistic for genetic programming. In: Foster JA, Lutton E, Miller J, Ryan C, Tettamanzi AG, editors. Genetic programming. EuroGP 2002: Proceedings of the 5th European Conference on Genetic Programming; 2002 Apr 3-5; Kinsdale, Ireland. Berlin: Springer, 2002: 182-191

Electronic journal (list all authors)

15   Morse SS. Factors in the emergence of infectious diseases. Emerg Infect Dis serial online, 1995-01-03, cited 1996-06-05; 1(1): 24 screens. Available from: URL: http://www.cdc.gov/ncidod/eid/index.htm

Patent (list all authors)

16   **Pagedas AC**, inventor; Ancel Surgical R&D Inc., assignee. Flexible endoscopic grasping and cutting device and positioning tool assembly. United States patent US 20020103498. 2002 Aug 1

Statistical data

Write as mean ± SD or mean ± SE.

Statistical expression

Express t test as t (in italics), F test as F (in italics), chi square test as χ^2 (in Greek), related coefficient as r (in italics), degree of freedom as υ (in Greek), sample number as n (in italics), and probability as P (in italics).

Units

Use SI units. For example: body mass, m (B) = 78 kg; blood pressure, p (B) = 16.2/12.3 kPa; incubation time, t (incubation) = 96 h, blood glucose concentration, c (glucose) 6.4 ± 2.1 mmol/L; blood CEA mass concentration, p (CEA) = 8.6 24.5 μg/L; CO_2 volume fraction, 50 mL/L CO_2, not 5% CO_2; likewise for 40 g/L formaldehyde, not 10% formalin; and mass fraction, 8 ng/g, *etc.* Arabic numerals such as 23, 243, 641 should be read 23 243 641.

The format for how to accurately write common units and quantums can be found at: http://www.wjgnet.com/1948-5204/g_info_20100312183048.htm.

Abbreviations

Standard abbreviations should be defined in the abstract and on first mention in the text. In general, terms should not be abbreviated unless they are used repeatedly and the abbreviation is helpful to the reader. Permissible abbreviations are listed in Units, Symbols and Abbreviations: A Guide for Biological and Medical Editors and Authors (Ed. Baron DN, 1988) published by The Royal Society of Medicine, London. Certain commonly used abbreviations, such as DNA, RNA, HIV, LD50, PCR, HBV, ECG, WBC, RBC, CT, ESR, CSF, IgG, ELISA, PBS, ATP, EDTA, mAb, can be used directly without further explanation.

Italics

Quantities: t time or temperature, c concentration, A area, l length, m mass, V volume.
Genotypes: *gyrA*, *arg* 1, *c myc*, *c fos*, *etc.*
Restriction enzymes: *Eco*RI, *Hin*dI, *Bam*HI, *Kbo* I, *Kpn* I, *etc.*
Biology: *H. pylori*, *E coli*, *etc.*

Examples for paper writing

All types of articles' writing style and requirement will be found in the link: http://www.wjgnet.com/esps/NavigationInfo.aspx?id=15

SUBMISSION OF THE REVISED MANUSCRIPTS AFTER ACCEPTED

Authors must revise their manuscript carefully according to the revision policies of BPG. The revised version, along with the signed copyright transfer agreement, responses to the reviewers, and English language Grade B certificate (for non-native speakers of English), should be submitted to the online system via the link contained in the e-mail sent by the editor. If you have any questions about the revision, please send e-mail to esps@wjgnet.com.

Language evaluation

The language of a manuscript will be graded before it is sent for revision. (1) Grade A: priority publishing; (2) Grade B: minor language polishing; (3) Grade C: a great deal of language polishing needed; and (4) Grade D: rejected. Revised articles should reach Grade A or B.

Copyright assignment form

Please download a Copyright assignment form from http://www.wjgnet.com/1948-5204/g_info_20100312182928.htm.

Responses to reviewers

Please revise your article according to the comments/suggestions provided by the reviewers. The format for responses to the reviewers' comments can be found at: http://www.wjgnet.com/1948-5204/g_info_20100312182841.htm.

Proof of financial support

For papers supported by a foundation, authors should provide a copy of the approval document and serial number of the foundation.

STATEMENT ABOUT ANONYMOUS PUBLICATION OF THE PEER REVIEWERS' COMMENTS

In order to increase the quality of peer review, push authors to carefully revise their manuscripts based on the peer reviewers' comments, and promote academic interactions among peer reviewers, authors and readers, we decide to anonymously publish the reviewers' comments and author's responses at the same time the manuscript is published online.

PUBLICATION FEE

WJR is an international, peer-reviewed, OA online journal. Articles published by this journal are distributed under the terms of the Creative Commons Attribution Non-commercial License, which permits use, distribution, and reproduction in any medium and format, provided the original work is properly cited. The use is non-commercial and is otherwise in compliance with the license. Authors of accepted articles must pay a publication fee. Publication fee: 698 USD per article. All invited articles are published free of charge.

Baishideng®